Evaluating the Effects of Selective Laser Sintering Processing Parameters on the Melt Pool Dimensions of Tungsten Carbide through Numerical Thermal Modeling

by

Carlo Martin Olivier

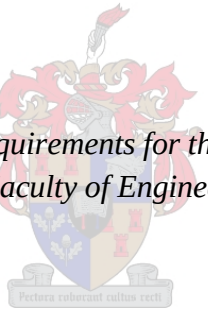

Thesis presented in fulfilment of the requirements for the degree of Master of Engineering (Engineering Management) in the Faculty of Engineering at Stellenbosch University

Supervisor: Prof. G.A. Oosthuizen
Co-supervisor: Prof. N. Sacks

April 2019

Declaration

By submitting this thesis electronically, I declare that the entirety of the work contained therein is my own, original work, that I am the sole author thereof (save to the extent explicitly otherwise stated), that reproduction and publication thereof by Stellenbosch University will not infringe any third party rights and that I have not infringed any third party rights and that I have not previously in its entirety or in part submitted it for any qualification.

April 2019

Abstract

The selective laser sintering (SLS) industry is a relatively novel industry within the broad spectrum of available additive manufacturing (AM) technologies. This layer wise processing technology has gained popularity over recent years, due to its ability to produce low volume, highly complex components made from difficult to process metal materials.

A major driver for this industry is the development of materials for new or improved applications. However, each time manufacturers want to add a new material to their machine, a specific set of processing parameters needs to be developed for that material in order to ensure that high density, high strength components are produced. The primary aim of this developing technology is to produce high quality, low costs components, yet it still struggles to overcome inefficiencies relating to the product development phase. Currently, large quantities of raw material are wasted during the machine-material calibration stage in the SLS industry.

The aim of this study was to investigate the possibility of improving or replacing the current inefficient research and development (R&D) methods of the SLS industry with numerical modeling. In this study, a numerical thermal model was developed, which manufacturers can use in their production facility, in order to predict changes in the melt pool geometry for new or unconventional materials by changing certain processing parameters. This will allow them to make decisions regarding other machine input parameters such as the scan track hatch spacing and layer thickness before performing any physical calibration tests.

Tungsten carbide (WC) was selected as the main processing material for this study, as it is still a relatively novel addition to this technology field. WC has an array of unique material properties, which makes it ideal for application in industries such as the mining, tooling and oil and gas industries.

A numerical thermal model was used to develop a feasible set of processing parameters specifically for processing tungsten carbide. The results from the numerical model were validated by comparing the simulated melt pool geometry to that of experimentally produced samples. The simulation was able to predict the change in the melt pool geometry with the change in processing parameters successfully. However, the result comparisons revealed that there were still deviations present between the simulated and the actual measurements. The highest deviations between the simulated and actual melt pool geometry measurements were found to be 24% and 50% for the scan track width and penetration depth, respectively. Additionally, a cost comparison revealed that the simulated calibration method was 46.5% more affordable than that of the conventional calibration techniques used in the industry.

Although, the findings of this study are not enough to suggest that numerical modeling should replace traditional calibration methods completely, it rather motivates using numerical thermal modeling in addition to current techniques in order to assist with decision making and reduce the scope of the calibration process. This scope reduction may lead to cost savings and increased sustainability, which will ultimately improve the efficiency of the SLS process chain.

Opsomming

Die selektiewe laserstraalsintering (SLS) industrie is ‘n relatiewe nuwe industrie in die breë spektrum van beskikbare byvoegende vervaardingtegnologië (AM). Hierdie tegnologie, wat staatmaak op die laag-vir-laag opbou van materiaal, het oor die laaste paar jare in gewildheid gegroei wat grotendeels toegeskryf kan word aan die tegnologie se vermoeë om komponente met ‘n hoë vlak van kompleksiteit te vervaardig vanuit materiale wat normaalweg moeilik is om te verwerk.

‘n Groot dryfmiddel agter hierdie industrie is die ontwikkeling van materiale vir nuwe of verbeterde toepassings. Tog, elke keer as vervaardigers nuwe materiaal tot hulle masjiene wil toevoeg, moet hulle eers ‘n stel spesifieke prosesparameters ontwikkel wat sal versker dat hulle komponente met ‘n hoë digtheid en sterkte kan produseer. Die primêre doel van hierdie ontwikkelende tegnologie is om hoë kwaliteit, lae koste komponente te vervaardig, maar dit sukkel nog om ondoeltreffenhede in die produkontwikkelingfase te oorkom. Huidiglik word daar groot hoeveelhede rou materiaal tydens die masjienkalibrasiefase in die SLS industrie gemors.

Die doel van hierdie studie was om die moontlikheid te ondersoek om die huidige ondoeltreffende navorsing en ontwikkelings (R&D) metodes van die SLS industrie met dié van numeriese metodes te vervang. In hierdie studie is ‘n numeriese termiese model ontwikkel wat vervaardigers in hulle vervaardingingsfasiliteite kan geburik om die veranderinge in die smeltpoelgeometrie vir nuwe of onkonvensionele materiale met 'n verandering in sekere prosessparameters te kan bepaal. Hierdie sal hulle in staat stel om besluite te maak met betrekking tot die masjien intree parameters soos die skandeerspoorspasieëring en laag dikte, voordat enige fisiese kalibrasietoets uigevoer word.

Wolframkarbied (WC) is gekies as die hoof vervaardigingsmatriaal vir hierdie studie aangesien dit nog ‘n relatiewe nuwe toevoeging tot die tegnologieveld is. WC het ‘n hele klomp unieke materiaaleienskappe wat dit ideaal maak vir industrietoepassings soos mynbou, implemente, olie en gas.

'n Numeriese termiese model is gebruik om ‘n uitvoerbare stel prosesparameters, wat spesifiek op wolframkarbied van toepassing is, te ontwikkel. Die resultate van die numerise model is gevalideer deur die gesimuleerde smeltpoelgeometrie met dié van eksperimentele monsters te vergelyk. Die simulasie was in staat om die smeltpoelgeometrie met die verandering in prosesparameters suksesvol te voorspel. Tog, het die resultate van die vergelykings getoon dat daar nogsteeds afwykings tussen die gesimuleerde en werklike afmeetings teenwoording is. Die grootste afwykings tussen die gesimuleerde en werklike smeltpoelgeometrieafmeetings is gevind om tussen 24% en 50% vir die skandeerspoorwydte en penetrasiediepte, onderskeidelik te wees. Daarbenewens het ‘n kostevergelyking getoon dat die gesimuleerde kalibrasiemetode 46.5% goedkoper as die tradisionele kalibrasietegnieke van die industrie is.

Alhoewel die bevindinge nie genoeg is om aan te beveel dat numeriese modelleering heeltemal die tradisionele kalibrasiemetodes moet vervang nie, dien dit eerder as motiveering dat numeriese modelleering tot toevoeging van huidige kalibrasiemetodes kan dien met die doel om die omvang van die kalibrasieproses te verklein. Hierdie verkleining in omvang mag moontlik tot kostebesparings en ‘n verbetering in volhoubaarheid lei, om tot einde die doeltreffendheid van die SLS prosesketting te verbeter.

Acknowledgements

The author would firstly like to thank his project advisors, Professors Gert Adriaan Oosthuizen and Natasha Sacks for their academic guidance and leadership roles in this study. Without their assistance in the fields of business management, manufacturing process chains and material sciences, this project would not have been possible. The advisors granted the author the freedom to make the project his own and perform experiments and observations on his own accord.

The support of the DST-NRF Centre of Excellence in Strong Materials (CoE-SM) towards this research is hereby acknowledged. Opinions expressed and conclusions arrived at, are those of the author and are not necessarily to be attributed to the CoE-SM.

Thanks are also due to the Department of Industrial Engineering at the University of Stellenbosch for providing the author with a research space during the time of his studies.

The author also acknowledges all those involved in the technical side of this study. This includes the personnel at Centre for Rapid Prototyping and Manufacturing (CRPM) at the Central University of Technology and Stellenbosch Technology Centre (STC) for their assistance at producing the experimental samples as well as the researchers of the Central Analytical Facility (CAF), who provided their assistance with the scanning electron microscope. The author appreciates the inputs of all members of industry and academic institutions involved in this study.

Finally, the author would like to express his gratitude for the unfailing love, financial support and continuous encouragement received from his family during this study. This accomplishment would not have been possible without them. Thank you.

Table of Contents

Table of Figures

List of Tables

Nomenclature

List of Symbols

Symbol	Symbol Name	Unit
A	Constant surface area	$[m^2]$
α	Absorptivity	$dimensionless$
Δ	Difference	$dimensionless$
c_p	Specific heat (constant pressure)	$\left[\frac{J}{kg\ K}\right]$
$\dot{E}$	Energy transfer	$\left[\frac{J}{s}\right]$
ε	Emissivity	$dimensionless$
f	Factor	$dimensionless$
h	Heat transfer coefficient	$\left[\frac{W}{m^2 K}\right]$
h	Height	$[m]$
Hv	Vickers hardness	$[HV]$
k	Thermal conductivity	$\left[\frac{W}{m\ K}\right]$
l	Length	$[m]$
σ	Stefan-Boltzmann constant	$\left[\frac{W}{m^2 K^4}\right]$
P	Laser power	$[W]$
ρ	Density	$\left[\frac{kg}{m^3}\right]$
$\dot{q}$	Irradiance	$\left[\frac{J}{kg\ s}\right]$
r	Radius	$[m]$
T	Temperature	[°C, K or °F]
t	Time duration	$[m]$
v	Scanning speed	$\left[\frac{m}{s}\right]$
w	Width	$[m]$
wt.%	Weight percentage	[%]

Acronyms and Abbreviations

Shortened form	Full description
AM	Additive manufacturing
ANOVA	Analysis of variance
ASTM	American Society for Testing Materials
BCC	Body-centred cubic
BEP	Break-even point
BET	Break-even time
CAD	Computer aided design
CAFE	Cellular automata finite element
Co	Cobalt
CPUT	Cape Peninsula University of Technology
CRPM	Centre for Rapid Prototyping and Manufacturing
CUT	Central University of Technology
DEM	Discrete element method
EBM	Electron beam melting
EDX	Energy dispersive X-ray spectroscopy
FCC	Face-centred cubic
FEA	Finite element analysis
FEM	Finite element methods
FVM	Finite volume method
GARPA	Global Alliance of Rapid Prototyping Associations
HAZ	Heat affected zone
HMLD	Hard metal lung disease
LMD	Laser metal deposition
LPS	Liquid phase sintering
MMC	Mitsubishi Material Corporation
MR	Manufacturing release
OEM	Original equipment manufacturer
PBF	Powder bed fusion
PM	Powder metallurgy
RAPDASA	Rapid product development association of South Africa
RM	Rapid manufacturing
RF	Return factor
ROI	Return on investment
ROS	Return on sales
RP	Rapid prototyping
RSM	Response surface methodology
RT	Rapid tooling
SAM	Sustainability of Additive Manufacturing
SEM	Scanning electron microscope
SFF	Solid free-form fabrication
SLM	Selective laser melting
SLS	Selective laser sintering
SM	Subtractive manufacturing
SMEs	Small and medium-sized enterprises
STL	Standard triangle language
US	University of Stellenbosch
WC	Tungsten carbide

Chapter 1: Introduction

Overview

The chapter introduces the research problem and provides a brief overview of the research field. The research problem contains various aspects of areas such as additive manufacturing (AM), business management, selective laser sintering (SLS), tungsten carbide (WC) and finite element methods (FEM). Research objectives are identified which aim to solve smaller sections of the greater research problem. A background study not only highlights past research achievements, it also provides valuable information required to solve the research problem. The chapter also identifies the novelty of the research, it defines the project scope and it lists the most important limitations and assumptions. Finally, an overview is provided about the research approach, strategy and schedule.

1.1 Background and Motivation

Additive manufacturing (AM) is a technology process where 3D objects are created by adding material in incremental layers. The AM field comprises a wide range of technologies and processes that are able to produce components of a variety of shapes, sizes and materials (Staden, 2015). AM technologies were developed in the late 1980's with the initial intention of producing prototypes in shorter lead times as compared to conventional subtractive manufacturing (SM) methods (Kruth, 1991). However, developments in recent years have allowed AM technologies to expand from rapid prototyping (RP) applications toward more rapid manufacturing (RM), short production runs and mass customisation uses (Bak, 2003). Currently, the technology is revolutionising the manufacturing industry as the ability to produce products shifts from large manufacturing bodies to everyday consumers (Hagedorn-Hansen, 2017).

The benefits of AM include inexpensive complexity, less material waste and minimal previous manufacturing skill or knowledge is required. While the disadvantages include slow build rates, unpredictable material properties and a current lack of manufacturing standards (ACNA, 2014). AM has been widely adopted by the aerospace, automotive, tooling and biomedical industries alike (Wong & Hernandez, 2012). It is predicted that AM will penetrate even more markets in coming years with the development of new technologies, strategies and applications.

One of the main limitations of AM is the inability to produce components from certain materials. During the initial stages of development, AM was limited to produce parts made from polymers for rapid prototyping purposes using the stereolithography technology. The introduction of powder bed fusion (PBF) technologies such as selective laser melting and sintering (SLM/SLS) has led to the production of components made from powdered metals (Singh, 2016). However, not all metals have yet been developed and certified to be included in the range of AM materials. Currently AM technology has the capability to produce components from a range of materials including metals, polymers, ceramics, wax and biomaterial (Kearney, 2015).

As with most industries, research and development (R&D) plays an important role in the competitiveness of a business. However, R&D is expensive in terms of time and resources (monetary and human), which is why some businesses would rather avoid developing technologies themselves and rather wait until innovations mature before introducing it to their processes. The real value of R&D lies in time-to-market (Basu, 2018). The quicker a product can be developed, the quicker it can be brought to market and repay for its initial R&D investment. Hence, the R&D efficiency becomes essential when competing against similar manufacturers in a global market. Machine technology, materials and applications development are all examples of R&D focus areas in AM.

One material with particular interest for the AM industry is tungsten carbide (WC). The material is known as a cermet (ceramic plus metal) and exhibits an excellent combination of high-strength and wear resistance properties. In the past, tungsten carbide cobalt (WC-Co) powder has been shaped using the conventional sintering method, where heat and pressure is applied to a die press, in order to produce a solid object. However, these objects are limited in complexity, hence the need exists for a manufacturing process, such as SLS, able to overcome this limitation. Traditionally, cemented tungsten carbides have been used in highly abrasive environments such as cutting tools (inserts), mining drill bits (compacts) and other equipment for industrial applications (Upadhyaya, 1998).

The selective laser sintering manufacturing technique might increase the achievable complexity of WC components; however, the quality and material properties might be worse than those of conventional manufacturing techniques. This is mainly due to the lack of applied pressure during the SLS process, which leads to imperfections such as micro cracks, internal porosity, and layer separation (delamination) (Manakari, Parande & Gupta, 2016).

The selective laser sintering process is based on the effective heat transfer between the scanning laser and the particles of the powder bed. The heat transfer process is complex and incorporates principles of radiation, convection and conduction, which are unique for each build material (Gusarov & Kruth, 2005). A better understanding of the impact of the SLS processing parameters (laser intensity, scanning speed, scanning strategy etc.) on end-product quality, may result in the increase acceptance of this manufacturing technique (Moletsane *et al.*, 2016).

However, manufacturers cannot simply add novel stock material such as WC-Co to the SLS technology and expect good quality components. Each material varies in material properties (melting temperature, thermal conductivity, specific heat, etc.); therefore, a rigorous R&D process is required in order to determine adequate processing parameters unique to the material.

1.2 Research Aim and Objectives

The project aim establishes what research is required in order to solve a specific research problem. This research problem is deconstructed into smaller objectives. The objectives narrow the scope of the proposed study.

1.2.1 Problem Statement

Owing to the novelty of the SLS technology, machine specific material processing parameters standards are still absent for new or unconventional powdered materials. Hence, manufacturers and researchers need to follow a time consuming and resource intensive trial-and-error calibration process in order to identify the machine-material specific processing parameters required to produce near full dense components from novel or unconventional SLS powders, such as WC-Co. The researchers risk producing parts with internal pores and poor interlayer bonding, if they are unable to determine the extent of the heat affected zones caused by the scanning laser beam. This calibration process delays the full-scale production, which ultimately, affects the overall production process chain negatively. It is clear that a need exists for a tool or method able to predict the material behaviour during SLS processing of such powders. Modern tools such as numerical modeling have made it possible to integrate mathematics, material properties and transient heat transfer principles.

1.2.2 Research Novelty

Although previous studies have been conducted on numerical modeling of SLM/SLS powder technologies and melt pool formation, very limited research has been conducted on the finite element analysis of melt pool geometry of the tungsten carbide powder material when heated in a laser sintering process. The novelty in this case is the use of the material in combination with the SLS technology. Recent research have extensively explored the finite element analyses of Ti-6Al-4V (Fu & Guo, 2014) and aluminium (Loh *et al.*, 2015) powders with a great deal of success. However, due to the material properties of WC being completely different to those of Ti-6Al-4V and aluminium, these similar studies will only serve as a guideline to approach such numerical models.

1.2.3 Research Objectives

For better research management the research problem is divided into smaller, clearly defined focus areas, known as research objectives. The study aims to address all the objectives in order to solve the research problem successfully. The following research objectives have been developed in order to solve the research problem:

1. Determine the effect of SLS process parameter variation, specifically laser power and scanning speed, on the *simulated* melt pool dimensions (width and depth).

2. Determine the effect of SLS process parameter variation, specifically laser power and scanning speed, on the *actual* melt pool dimensions (width and depth).

3. Identify the error between the simulated model and the actual build.

4. Provide a cost comparison between the traditional and adjusted R&D process.

Ultimately, this study will investigate the possibility of using a predictive heat transfer model to identify possible material specific processing parameters suitable for producing WC-Co scan tracks with sufficient quality. The aim is to improve the efficiency of the research and development (R&D) process chain of the SLS industry by reducing or even eliminating the technology's dependence on the extensive trial-and-error material calibration tests. The study aims to balance the three pillars of the Iron Triangle (shown in Figure 1.1(a)) on a machine and process level.

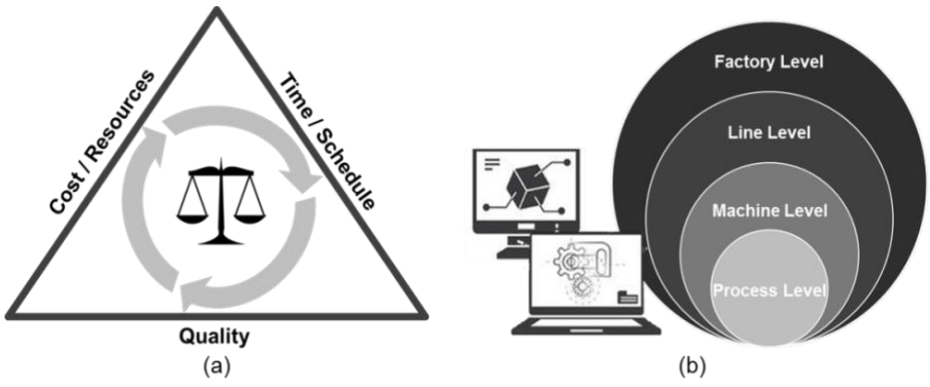

Figure 1.1: Importance of efficiency in a process chain. (a) The balancing act of the Iron Triangle is used by management to make strategic business decisions. (b) Efficiency can be implemented in different levels of a process chain. Adapted from Apostolos *et al.*, 2013.

1.3 Scope and Limitations

The aim of this research project is for the researcher to obtain a master's degree in a limited time frame, hence some basic assumptions need to be formulated in order to narrow the scope of the research.

1.3.1 Scope

The study will be limited to the SLS process only. This eliminates the need to investigate other powder bed fusion technologies. As the SLS process is a multi-physical, multi-scale process, it can be replicated using various numerical modeling techniques. These include computational fluid dynamics (CFD), discrete element methods (DEM), finite element analysis (FEA) etc. However, for this study only a finite element analysis will be performed. Only the thermal effects of laser processing will be evaluated, hence residual stresses, powder distribution and other phenomena will be ignored. The model will also be limited to a single-track, single-layer simulation in order to save computational time. The material will also be simplified to have a constant binder content with only certain material properties varying with temperature.

1.3.2 Assumptions

1. The single layer of powder particles in the powder bed will be modelled as a solid continuum. This assumption allows the heat transfer model to be simulated using a finite element analysis (FEA).

2. An uncoupled heat transfer analysis will be used to solve the thermal field for the single-layer, single-track simulation.

3. Owing to the novelty of the powdered material and the scarcity of reliable material property data, the temperature dependent material properties (thermal conductivity and specific heat) will be approximated using appropriate composition equations.

4. SLS requires a range of different process parameters, which, as mentioned previously, need to be calibrated for each material in order to ensure acceptable part quality. However, in this study most parameters will be assumed to be fixed, while only varying the laser power and scanning speed parameters.

1.3.3 Limitations

The research project is limited by aspects such as time, cost and equipment.

- Time: The deadline for the research is set at November 2018, which is close to two years after the intended start of the project.

- Cost: The project expenditure is limited by funds available to the researcher. A project cost analysis is provided in Appendix A.

- Equipment: A full section will be devoted to the experimental equipment used. Only equipment owned by the university can be used freely by the researcher. Any additional equipment not available at the university will need to be outsourced at an added cost to the project.

1.4 Contribution

The research will certainly benefit the additive manufacturing industry, especially developments in SLS technologies. Numerical modeling may prove to be a valuable tool to predict unknown material behaviour before embarking on a time and resource intensive trial-and-error calibration in order to determine the material and machine specific process parameters for a certain material.

Designers will be able to simulate the melt pool geometry and predict heat affected zones (HAZ) in known problem areas, allowing adjustments to be made before components are even built. This in turn saves time on prototyping and unnecessary expenditure on material. Understanding the effects of certain parameters on the melt pool geometrical features will greatly improve the parameter selection process. Researchers may use simulations to predict the required hatch spacing and layer thickness depending on the melt pool dimensions.

Additive manufacturing of novel or less developed materials such as tungsten carbide will lead to the development of new, more complex designs, which will drive innovation towards finding novel applications for the material. Additive manufacturing may replace the conventional manufacturing processes used to produce tungsten carbide parts all together due to higher process efficiency, improved component quality and lower production cost.

The schematic in Figure 1.2 displays the possible positive influence the technique may have on the current R&D process chain used in industry. Currently, designers are investing heavily in experimental procedures, which may reveal adequate processing parameters for materials designated for powder bed fusion processing. The “design of experiments” step is the most costly and time consuming of the experimental procedures, as this step requires an in depth understanding of both the material and machine properties. Once this step has been completed, a physical screening experiment is needed to identify suitable process parameters. These parameters need to be validated using response analysis techniques. Only after the response analysis has been completed, can designers start optimising the identified parameters for processing. This process can be shortened greatly with numerical simulation process, as numerical modeling may be able to reduce the experimental screening procedure. The model results need only to be validated and optimised before the final parameters are identified. The simulation screening process in SLM processing has been suggested by Yadroitsev, Krakhmalev & Yadroitsava (2015).

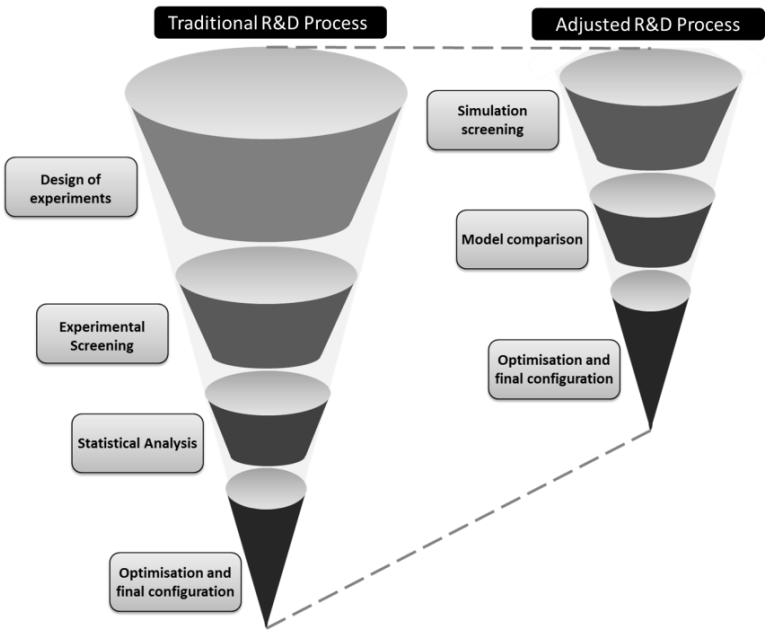

Figure 1.2: Employing numerical simulations to improve the efficiency of the SLS R&D process chain (Olivier, 2018).

1.5 Proposed Research Plan

A structured research plan aids to reach the research objectives effectively within a proposed time frame. It can be used to set deadlines and monitor progress.

1.5.1 Approach

The research approach will be broken down into four main stages, namely:

1. **Research preparation:** This includes setting up the research topic, defining the scope, listing all the research objectives and constructing a basic outline of the final research report.
2. **Literature and background study:** A holistic theoretical background study should provide the necessary understanding of all the research fields involved in the project scope. Literature such as books, journal papers, theses and dissertations are processed in order to collect the relevant information.
3. **Practical experimentation:** Implementation of knowledge gained through the background study is applied in numerical models and experiments as an effort to solve the research problem.
4. **Validation and conclusion:** Comparing the theoretical to the practical is essential. This process is required in order to validate whether the findings are sufficient to solve the research problem. The methods, reasoning and findings are then communicated in a final research report.

1.6 Document Overview

The document overview provides the research report structure. The schematic shown in Figure 1.3 can be used for assistance to navigate through the research report. It highlights only the most important headings of each section of the report and indicates the separation between the background overview and the research novelty.

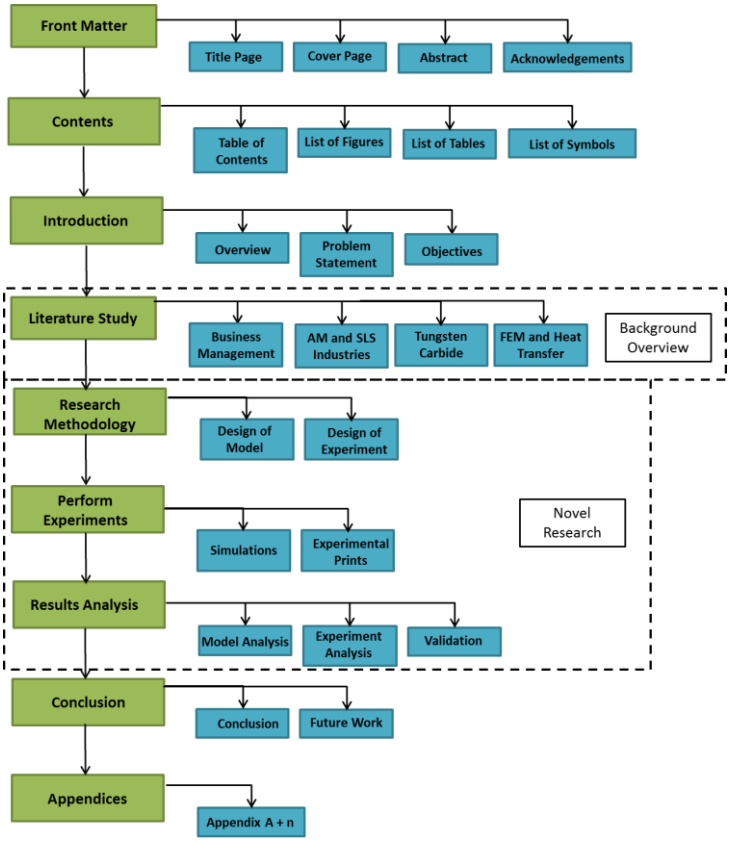

Figure 1.3: Research document overview

Chapter 2: Research and Development Process Efficiency

Overview

This chapter explores the link between R&D process efficiency and business management. It proves why process efficiency is important to key business concepts such as asset management, profit margin and brand promotion. In addition, this chapter investigates the different ways process efficiency can contribute to sustainability in a business. Sustainability includes sustainable manufacturing, which forms part of the umbrella concept of sustainable development. Sustainability can be applied to all manufacturing industries including novel industries such as additive manufacturing.

2.1 Efficiency vs Effectiveness

Efficiency is often mistaken for effectiveness although these are two different concepts. According to the BusinessDictionary (2018) efficiency is defined as the comparison of what is actually produced or performed with what can be achieved with the same consumption of resources (money, labour, time, etc.). It is an important factor in the determination of productivity. Effectiveness is defined as the degree of which objectives are achieved and the extent to which targeted problems are solved. In contrast to efficiency, effectiveness is determined without reference to costs and whereas efficiency means *doing the thing right* whereas effectiveness means *doing the right thing*.

The difference between efficiency and effectiveness can be explained by the analogy of a dartboard, as shown in Figure 2.1. If a dart player wishes to throw a bullseye, he needs to aim for the target area in the centre of the dartboard. He has the choice of different dart sizes for his throw. Large arrowhead darts are more likely to hit the target, as their arrowheads cover a larger area and they require less skill to throw. However, these darts are heavy and require more effort from the dart player to throw. Smaller darts are less likely to hit the target as they cover a smaller area and require more skill to throw. However, these darts are lighter and require less effort to throw.

If the player fails to hit the any part of the dartboard with an arbitrarily sized dart, he is neither effective nor efficient. He needs to adjust his technique or choice of dart. If the player hits the centre of the target with a large and heavy dart he is effective at hitting the target, however the arrowhead is so large that it even spreads over the boundaries of the bullseye area. Although this technique is effective, it is not efficient. He needs to reduce the size of his dart. If he hits the dartboard close to the centre of the dartboard with the new, lighter dart, he is efficient but not effective. He needs to adjust his technique. If the player finally hits the bullseye with the smallest dart size, he is effective as well as efficient as it required very little effort to throw the smaller dart.

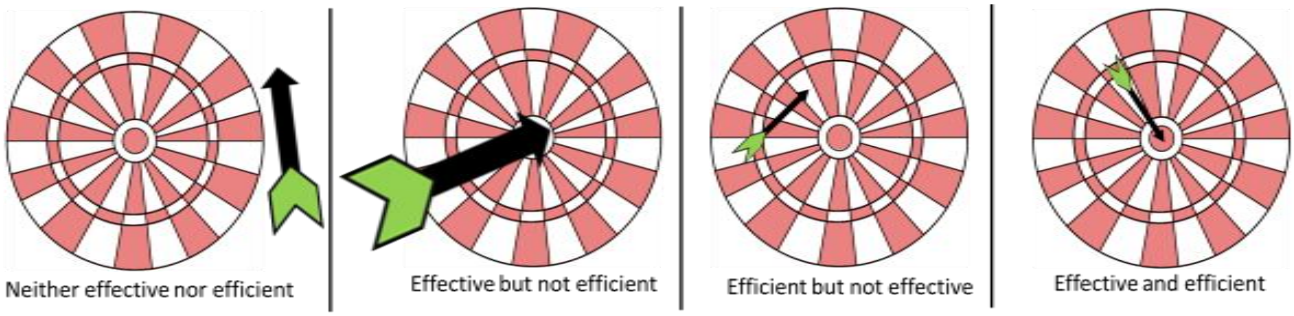

Figure 2.1: Efficiency vs effectiveness dartboard analogy (Olivier, 2018).

2.2 Linking R&D Process Efficiency to Business Management

For today's business enterprises to survive, they must juggle fierce global competition, reduce their operating costs, and rapidly develop new products and services. Businesses must constantly reconsider, adapt and optimise the way they manage their organisation's operating systems in order to keep up with a constantly evolving business environment (Georgakopoulos, Hornick & Sheth, 1995). The reduction in new product development cycle-times and improvements in product quality have become important strategic objectives for many technology driven firms. However, these goals often conflict and organisations struggle to make investments without return on investment (ROI) certainties.

Research and development (R&D) plays an essential role in maintaining the competitiveness and relevance of a business. It provides a platform for creativity and innovation to flourish within an organisation. R&D can act as a catalyst for increasing growth in a business by introducing innovative products to the market. It is also a measure organisations take in order to address future problems before they are realised (Basu, 2018).

It is easier for well-established high-tech firms to invest in innovation than it is for start-ups. This is due to resources constraints. Financial institutions are less likely to support small firms with their R&D activities than for larger organisations due to inherent uncertainty and risks involved, even though it has proven to promote growth in both instances (Teece, 1986).

A study by Stam and Wennberg (2009) into the advantages of R&D for technology firms proved that R&D promotes interfirm alliances, exploits external knowledge, and leads to further product development after realising the initial R&D benefits. Even if innovation investments do not benefit a firm directly, they may provide valuable new knowledge about productive possibilities that other firms will take into account in their own R&D strategies, which will benefit society as a collective. This is the basis of the collective intelligence concept, where innovation arises from the collaboration, collective efforts, and competition between individuals. This theme is also supported by the Europe 2020 Strategy (Stam & Wennberg, 2009).

The true test of R&D lies in its efficiency or its time-to-market. Businesses exist for the sake of making profits. Hence, unless the R&D efforts in the lab cannot be scaled up within a reasonable time-frame, little can be expected in terms of the functional credit to be assigned to R&D (Basu, 2018). Cohen, Eliasberg and Ho (1996) cite a McKinsey report, which said that a company loses 33% of its after tax profit when a new product is shipped six months late, as compared to losses of 3.5% when a company overspends by 50% on the product development. At the IT firm, Hewlett-Packard (HP), over 50% of sales come from products introduced over the last three months. This proves that time and associated costs are the most important measure of the R&D success.

The benefits of an efficient R&D process can be explained using the Return Map, shown in Figure 2.2, developed by HP for a new pocket calculator (House & Price, 1991). This is a tool used by HP in order to represent the contribution graphically of all team members who are working toward developing a new product in terms of time and money. The graph represents the return on investment of a new developed product over a given time span. The costs and revenues are displayed in logarithmic format as revenues increase exponentially after a product is released. The graph can be divided into three stages: the initial product feasibility investigation, product development and the manufacturing and sales stage. The three lines on the chart represent the investment cost, which increases up and to the point of manufacturing release (MR), the sales generated once the product is released to market, and the profit made of the sales once the manufacturing costs are deducted.

Business managers who consider R&D are almost always interested in the break-even-point (BEP). At this critical point the product will start earning a return on its investment. The scale of this return is based on the return factor (RF), which is a relation between profit and time. R&D influences the development stage. Although all three stages influence the final BEP time, it is critically important that the R&D is as efficient as possible, in terms of the time and associated costs. If the development stage (time) can be shortened, the total R&D investment costs will be less. Correspondingly, the sales and profits from sales will also start earlier, resulting in a sooner BEP and a greater overall RF. Hence, the R&D process efficiency can be critical to a business's success.

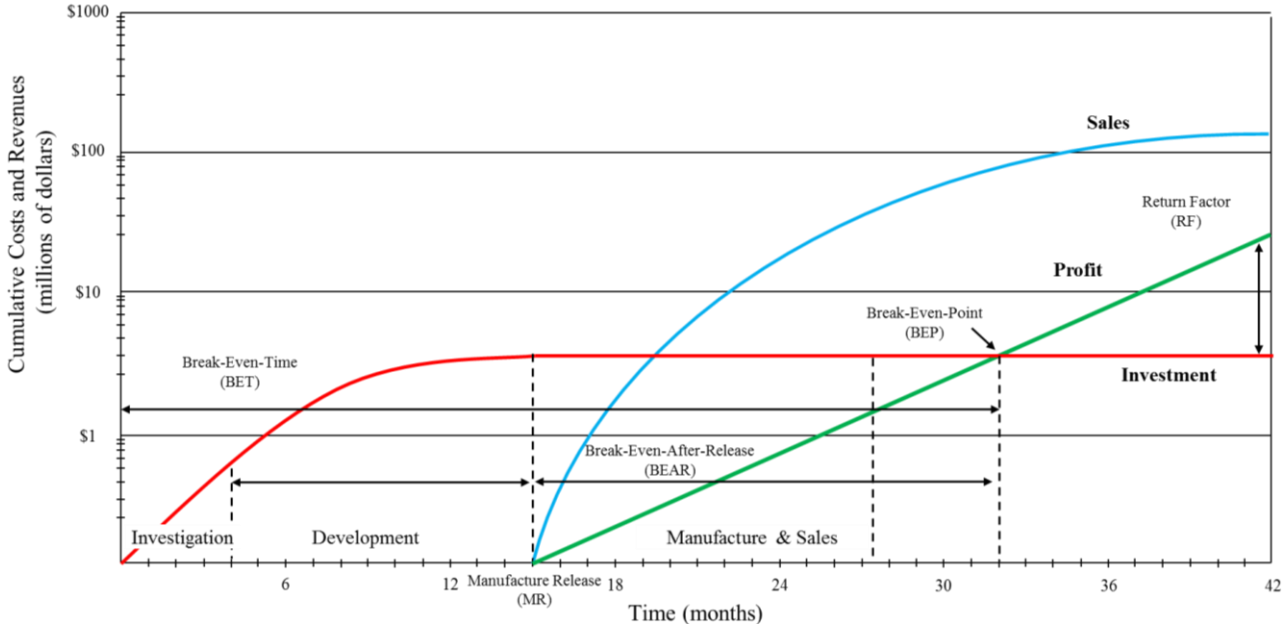

Figure 2.2: R&D return map based on a new HP pocket calculator, adapted from House and Price (1991).

2.2.1 R&D in the Different Manufacturing Process Levels

Research and development can be applied to various process levels within a manufacturing process chain. Management should continuously investigate areas within the functions of its business to improve. A sensible method is to consider all inputs and outputs needed for the business to be successful. A process chain can be constructed, which may assist in identifying opportunities for improvements. The scope and level of improvement of a certain process can vary, ranging from large supply chain management decisions to small changes made at a scientific level. The different levels, where changes to a process might influence the entire workflow efficiency, are shown in Figure 2.3. The levels include the supply chain management level, production system level, technology level, and the physical level (Fysikopoulos *et al.*, 2014)

Process efficiency looks at reducing the cost while increasing the output of certain tasks in the process chain in order to increase value in a business. The capabilities of an enterprise can be enhanced significantly by adopting new technologies, processes, and people. However, the introduction of a new process may not necessarily lead to an increase in efficiency, as organisations still need to adapt to the new technology. Yet, it is assumed that the new processes will lead to better operating performances over time (Jones & Linderman, 2014). However, it is important to note that improving efficiency should not be the only focus of R&D. Research and Development objectives focusing on product quality and availability are still essential to ensure revenues are secured. Many organisations concentrate too much on reducing cost in order to improve efficiency that they forget about paying attention to other essential business values, resulting in losses (Ndolo, 2014).

Motivation to improve the process chain at each level include

Supply chain level

This level includes all peripheral systems that support the functions of the factory. R&D at this level aims to:

- Reduce transport costs
- Reduce lead-times
- Reduce storage costs

Examples: Different transportation methods, cheaper logistic options, different suppliers, safety stock modeling, etc.

Production system level

This level concerns the performance of a group of different machines or other peripheral devices that may be required for the proper functioning of a production line. R&D at this level aims to:

- Enhance profit margins
- Increase asset turn over
- Manage debt and capitalisation

Examples: Automation, new technologies, new processes, factory layout, etc.

Technology level

This level includes all machining peripherals that ensure proper processing conditions. R&D at this level aims to:

- Maximise production rates
- Minimise operational costs
- Increase asset operational life
- Improve output quality

Examples: Process parameter changes, component changes, operator training methods, etc.

Physical level

This level refers to the efficiency associated with the physical mechanisms of the process itself. R&D at this level aims to:

- Improve product quality
- Reduce material waste

Examples: Changes made to methods and materials used at this level.

In a manufacturing context, the Comparative Integral Manufacturing Efficiency is technique used to measure the overall efficiency of the manufacturing process. The method uses the process outputs such as the process effectiveness, component quality and availability and divides it by all resource inputs (Kuznetsov, Koriath & Kalyashina, 2017). It can be written symbolically as:

$$E_p = \frac{Outputs}{Inputs} \tag{2.1}$$

Where E_p is the process efficiency. The overall efficiency of the system, E_{tot}, is equal to the product of the efficiencies of all processes in the system.

$$E_{tot} = \prod_{q=1}^{k} E_p^k \tag{2.2}$$

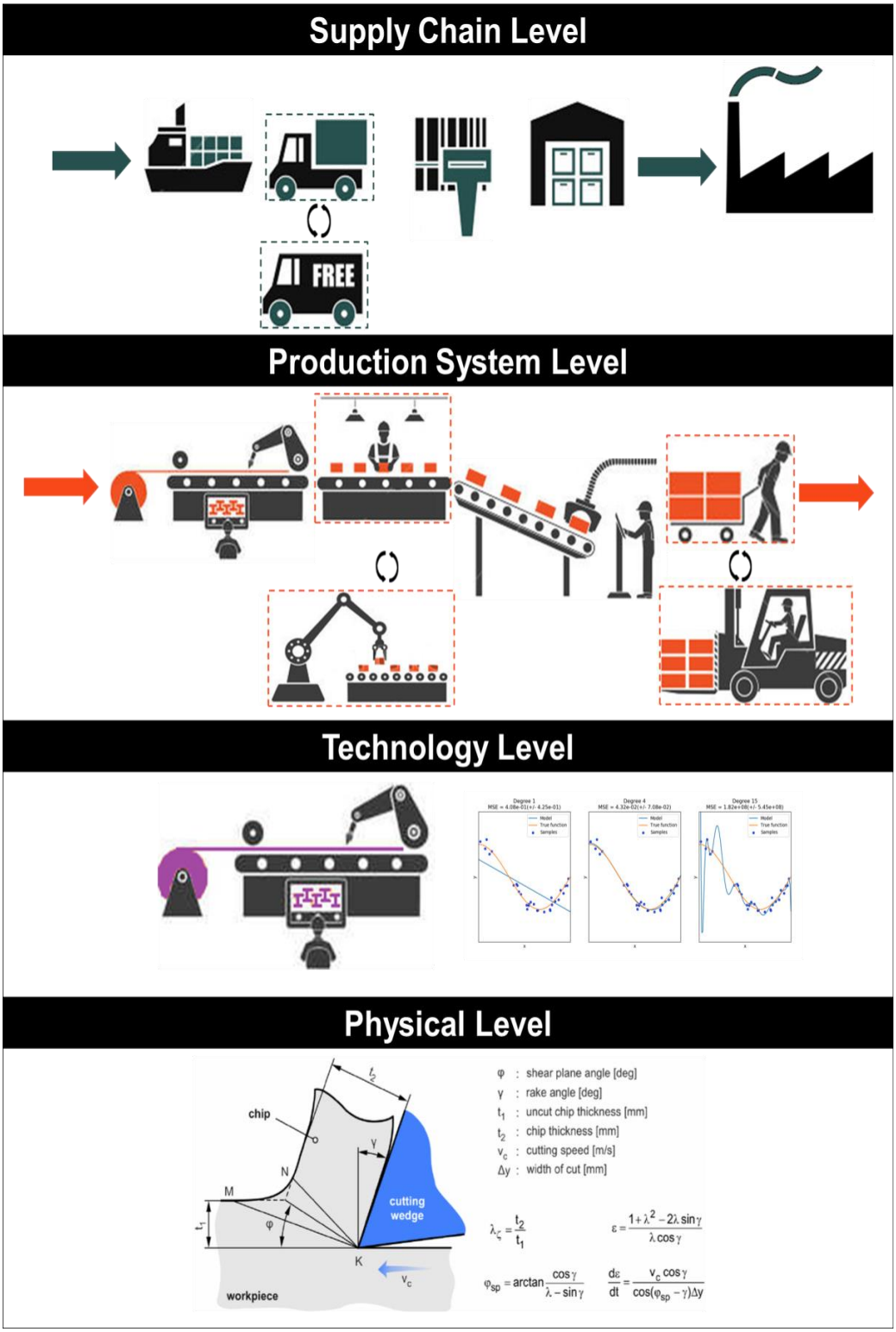

Figure 2.3: Different levels where the process efficiency can be improved (Olivier, 2018).

2.3 Sustainable Additive Manufacturing

Sustainability of Additive Manufacturing (SAM) is one concept, which cannot be ignored when investigating methods in order to improve the R&D efficiency within the AM industry. The term sustainable development is best defined as development that meets the needs of the present without compromising the ability of future generations to meet their own needs (Brundtland, 1987). Moreover, sustainable manufacturing refers to sustainability in a manufacturing context. The International Trade Administration (2010) defines sustainable manufacturing as the creation of manufactured products, which uses processes that minimise negative environmental impacts, conserve energy and natural resources and are safe for communities, employees and consumers and are economically sound.

The astronomical growth in legislation related to environmental matters, a decreased availability of raw materials, increases in waste disposal costs, and changes in customer preferences have significantly increased the interest in, and pressures toward environmentally conscious manufacturing. Manufacturing organisations sometimes find it difficult to remain competitive within a global market whilst adhering to the various environmental outcomes set by their respective governments (Pil & Rothenberg, 2003). However, there is evidence that using a more sustainable manufacturing process has direct benefits to the financial wellbeing of an organisation (Rodriguez, Ricart & Sanchez, 2002).

A sustainable industry is one where the economic and social impacts are maximised, while reducing all harmful effects on the environment. This balancing act is called the Triple Bottom Line. It can be condensed using the 3P's principle, which accounts for Planet, People and Profit. Since the Rio Earth Summit in 1992, the concept of sustainable development has been increasingly accepted as a way to manage businesses by carefully balancing environmental, economic and social responsibilities. The essential aspects of environmental conservation include the sensible utilisation of natural resources and the responsible disposal of wastes (Lange, 2002). A schematic for the Triple Bottom Line is shown if in Figure 2.4. It can be noted that sustainability lies in the so called 'sweet spot', where all aspects of the Triple Bottom Line are satisfied.

Figure 2.4: Sustainability and the Triple Bottom Line. Adapted from Lange (2002).

Environmental Conservation

AM generates less waste than conventional subtractive manufacturing methods. Waste elimination is one of the most effective methods to increase the profitability of a business while improving its environmental performance. Waste reduction is a key concept of lean manufacturing. Lean manufacturing targets the so-called seven deadly wastes, which include: (1) Waiting, (2) overproduction, (3) over-processing or inappropriate processing, (4), excess motion, (5) unnecessary inventory, (6) transportation (7) product defects (Heilala *et al.*, 2010).

AM is highly material efficient, as it only consumes the quantity of material required for building the component. AM material wastes are mostly generated during post-processing operations such as removing support structures and improving the surface finish. However, this is negligible compared to conventional machining technologies. AM also has the possibility to drastically reduce distribution costs. Using AM technologies will also shorten the current manufacturing value chain, which directly influences the industry's environmental and financial performance (Group, 2018).

Another important measurement of sustainability in the life cycle of a product, which links with the pillar of environmental conservation, is the 6R principle. The aspects of the 6R principle include *reduce, reuse, recycle, recover, redesign and remanufacture*. Serres *et al.* (2011) performed an environmental assessment on laser metal deposition (LMD) and compared its life-cycle to the environmental impact with conventional machining, The results confirmed that the total environmental impact of conventional machining was greater than that of the AM technology, which had an impact reduction of 70%. However, there is currently no uniformity agreed upon quantitative method to evaluate the environmental impacts of the AM processes (Huang, Liu, Mokasdar & Hou, 2013).

Economic growth

AM provides economic benefits for established and emerging organisations, alike. New applications for AM products are constantly being developed as research strives for advancements in materials and technologies. New applications present opportunities for economic growth in the form of new products and improvement on older products, resulting in increased sales. Developing industries such as AM stimulate investment and job creation.

AM technologies will dramatically reduce the value stream of manufacturing, minimising the overall production time and cost while still maintaining the product's end value. Some AM technologies have the capability of completely eliminating certain supply chain operations (Sreenivasan, Goel & Bourell, 2010).

AM technology provides two opportunities aimed at improving the conventional manufacturing supply chain: (1) products require fewer parts and (2) products can be manufactured closer to the end customer. The net effect is a reduction in warehousing, transportation and packaging costs. AM improves the responsiveness of an agile supply chain. A build-to-order strategy can be adopted to ensure a stock-out will not occur. The predominant cost in the AM industry is machine and material costs, not labour, which makes it economical to locate production facilities closer to the end customer (Huang *et al.*, 2013).

Social Development

Traditionally technological innovation and entrepreneurship are seen as drivers for jobs and competitiveness and economic prosperity. However, innovation is also an important driver for inclusiveness and social development. Social sustainability is difficult to measure due to its intangible nature and the perceived benefits to society. Social entrepreneurship holds the potential

to solve development challenges such as clean water, sanitation, health-care services, and many more. Social entrepreneurship brings communities closer through support systems like crowdfunding and idea sharing platforms. Emerging technologies, such as AM, allow communities to leapfrog development paradigms that were previously seen as impossible to solve (Desai, 2015).

There is agreement that AM provides substantial possibilities for improving the quality of life of future generations. One example where AM technology has already made a big impact is in the medical science industry. Custom-made implants are now manufactured for a fraction of the price, allowing medical care to patients who could previously not afford implants. AM technology has been used for a variety of medical applications such as knee, skull, elbow and hip joint implants. (Huang *et al.*, 2013). Dentistry is the fastest growing industry for AM implants (Bhargav *et al.*, 2017). Other applications of AM will be discussed further in the following section.

Past research have mainly focused on investigating the effects of replacing current subtractive manufacturing methods with AM technologies. However very few researchers have conducted sustainability studies on the AM processes themselves (Diegel *et al.*, 2010). A Life cycle assessment (LCA) is an internationally accepted method of systematically evaluating the environmental impact of processes, products, and activities. A significant amount of studies have performed LCAs on subtractive machining. However, very few have focused primarily on AM. The main reason for this has been attributed to the variety of AM processes. A comprehensive review study by Peng *et al.,* (2018) investigated the current status of SAM research. The review identified five gaps and priorities in current SAM research:

1. Improve systematic integration and management.
2. Focus on both energy and quality.
3. Push the development of intelligent machinery.
4. Attach importance to material preparation and recycling.
5. Develop innovative applications using AM.

This study, which aims at reducing resource waste during the calibration stage of selective laser sintering process, will address the 4th point made in the study by Peng *et al.*, (2018).

2.4 Chapter Relevance towards Research

The chapter highlighted the importance of R&D efficiency in any manufacturing industry. Efficiency plays a key role in business success and global competitiveness. It also discussed the different process levels in the manufacturing process chain where R&D can be implemented. Therefore, it is important to focus on every level of the process chain and not only on a high, overhead level. In the current study, efforts are made to improve the efficiency of the machine parameters required to produce a specific material. Hence, this detailed study is more focused on the lower machine and process levels. This chapter also discussed sustainability of AM and the influence on a business's performance. Ultimately, the results from this research study may be used to improve the R&D process efficiency, which is tied to the sustainability of the laser processing industry.

Chapter 3: Selective Laser Sintering Additive Manufacturing

Overview

This chapter focuses on the developments, workings and applications of the powder bed fusion (PBF) technology, with a particular focus on the selective laser sintering (SLS) process. The initial introduction discusses how the PBF technology fits into the AM environment as well as some of its major advantages and disadvantages. A brief overview is given of the various PBF processes currently available to industry. A broader review is presented on the workings of SLS process, as this is the principle technology investigated in the research report. Hence, it is important to understand the workings of the SLS machine in order to understand the effect changes in system parameters have on the processed powder. The chapter discusses the current material calibration techniques used to find suitable processing parameters for new materials. Finally, the chapter discusses developments and possible future applications of the PBF technology in industries worldwide, including South Africa.

3.1 Powder Bed Fusion Overview

Additive manufacturing (AM) has the ability to turn data into things. Digital fabrication allows individuals to design and produce tangible objects on demand, whenever and wherever they need them. AM has the power to transform the digital to physical interface for product design, development and manufacturing (Kearney, 2015). Currently, AM technologies are paving the way toward introducing the next global industrial revolution (Berman, 2012).

Powder bed fusion (PBF) is an umbrella term used to describe all processes that employ an energy source (laser or electron beam) to consolidate powder particles in order to create 3D parts. PBF technologies include electron beam melting (EBM), selective laser melting (SLM) and selective laser sintering (SLS). This AM technology opposes the conventional subtractive manufacturing (SM) techniques, such as turning, milling, drilling and other various other processes, which have dominated the manufacturing environment since ancient times (Sames *et al.*, 2016). PBF technology is generally regarded as being the most versatile of the AM technologies due to its wide range of material processing capabilities (Staden, 2015). The variety of materials that could be used include plastics, pure metals, metal alloys, combinations of metals and polymers, and combinations of metals and ceramics (Wong & Hernandez, 2012).

Laser based AM techniques such as SLM and SLS generally involve complex, non-equilibrium physical and a chemical metallurgical processes, which exhibit multiple modes of heat- and mass transfer, and in some instances also chemical reactions. The microstructural features (surface texture, grain size, phase, etc.) and the resultant mechanical properties (strength, residual stress, hardness, etc.) are generally difficult to optimise with current AM technologies (Gu *et al.*, 2012).

Whilst new technologies are continuously being developed, the American Society for Testing and Materials F42 (ASTM) has classified the technologies according to the method they use to add material (Li, Wu & Myant, 2016). Table 3.1 lists the categories and materials, which can be processed using the various AM methods.

Table 3.1: Categories and material capabilities of current AM technologies, adapted from (Li, Wu and Myant, 2016).

Materials	AM Technologies						
	Powder bed fusion	Direct energy deposition	Material jetting	Binder jetting	Material extrusion	Vat photo - polymerisation	Sheet lamination
Polymers	✓	✗	✓	✓	✓	✓	✗
Metals	✓	✓	∞	✓	∞	✓	∞
Ceramics	✗	✗	∞	✓	✓	∞	✗
Composites	✓	✗	✗	✗	✓	✗	✓
Biological	✗	✗	✗	✗	∞	✗	✗
Legend	Commercially available	✓	In R&D stage		∞	Not currently developed	✗

Currently, the PBF category (shown in Figure 3.1) can be broken down even further into more specific binding mechanism classifications. The classification analysis done by Kruth, Mercelis and Van Vaerenbergh (2005) is shown in Figure 3.1.

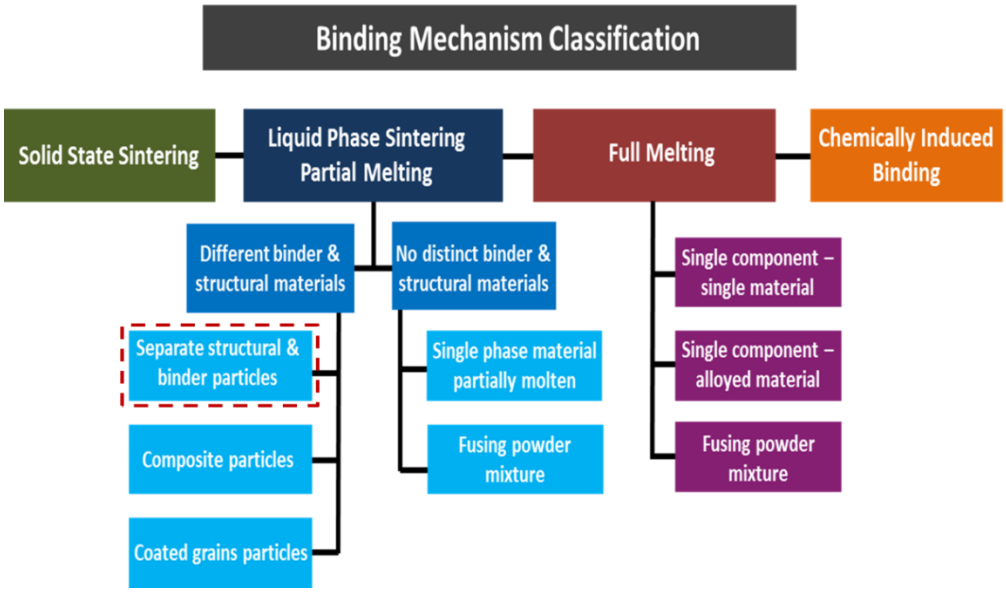

Figure 3.1: Binding mechanism classification for PBF technologies, adapted from Kruth, Mercelis and Van Vaerenbergh (2005).

The classification not only distinguishes between the powder binding methods, but also specifies the different powder compositions and their role in the binding process. In order to limit the scope of the research, this study will primarily investigate the role SLS process parameters play in the consolidation of tungsten carbide with a binder. This particular process is indicated by the red dashed block in Figure 3.1.

The PBF technology has unique material and process benefits, which makes it an important technology for future developments. Table 3.2 lists some of the distinct features of this additive manufacturing process.

Table 3.2: Major advantages and disadvantages of powder bed fusion technologies.

Advantages		
Aspect	**Effect**	**Reference**
Processing	Elimination of extensive post-machining processes as development moves towards net shape parts.	(Król, Dobrzański, Reimann, Czaja & Reimann, 2013; Olakanmi, Cochrane & Dalgarno, 2015)
Material	A wide variety of materials can be processed, including metals.	(Wong & Hernandez, 2012)
Complexity	Complexity is free and unlimited. No need to build support structures.	(Kruth, Mercelis, Van, Froyen, Rombouts, Vaerenbergh & Froyen, 2005; Miller, Morris & Colvin, 2016)
Efficiency	Unprocessed powder is removed and reused.	(Seyda, Kaufmann & Emmelmann, 2012)
Disadvantage		
Aspect	**Effect**	**Reference**
Processing	Powder bed fusion equipment and material are expensive compared to subtractive technologies.	(Berry, Brown-T, Connellf, Craven&, Effordll, Radjenovic & Smith, 1997)
Quality	Porosity and surface roughness are still issues faced by the technology.	(Gu *et al.*, 2012; Yasa & Kruth, 2011)
Knowledge	Each material has its own unique process parameters which need to be controlled to ensure quality parts.	(Fu & Guo, 2014)

3.2 Powder Bed Fusion Technologies

As mentioned in Table 3.2 the major challenges of the PFB technology includes reducing porosity, improving surface quality and minimising thermal crack formation in components. These defects are the main causes of premature part failure within high fatigue components. In order to manufacture more reliable parts with long term consistent mechanical properties, researchers have been developing, improving and reviewing PBF technologies continuously in pursuit of fully dense components with minimal surface defects (Leuders *et al.*, 2013).

3.2.1 Electron Beam Technology

In 2000, researchers in Sweden developed another PBF technique, known as electron beam melting (EBM). Electrons are generated in a gun and accelerated with a 60 kV potential power source and brought to focus by electromagnetic lenses which then electromagnetically scan the powder surface according to information sent from an embedded CAD file (Murr *et al.*, 2012). Although EBM and SLS both use the same powder bed principle for layer-wise selective melting, there are significant differences in the hardware set-up. The EBM system is essentially a high-powered scanning electron microscope (SEM) that needs an electron beam column, filament and magnetic coils to collimate and deflect the beam spatially. In the EBM system the piston powder replenishment system is replaced by a series of hoppers which use gravity to deposit new powder layers (Sames *et al.*, 2016). Another main difference of EBM is the vacuum build environment instead of the inert gas environment used by most laser technologies (Loeber *et al.*, 2011). Advantages of EBM include reduced heat affected zones (smaller melt pools) and the elimination of oxidation due to the vacuum environment (Safdar *et al.*, 2012). However, EBM is limited to certain metals and it has a slightly lower resolution than the SLM/SLS processes. EBM has a minimum feature size of 100-200 µm compared to the 30 - 00 µm of SLM (Amatoa *et al.*, 2012). Figure 3.2 shows the surface of an EBM component.

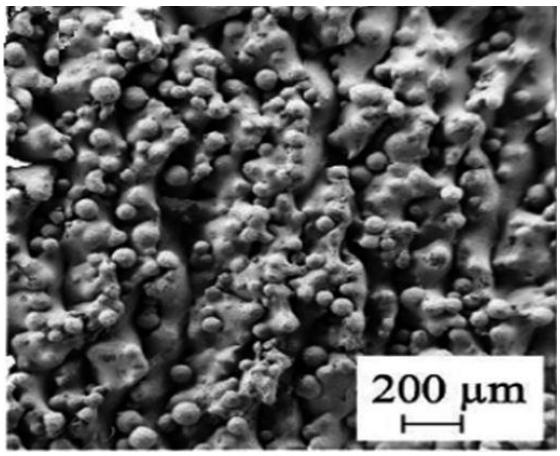

Figure 3.2: Surface morphology of Ti-6Al-4V produced with EBM (Townsend *et al.*, 2016).

3.2.2 Laser Technology

Selective laser melting (SLM) and selective lasers sintering (SLS) are regarded as some of the most important AM technologies for the future, due to their ability to produce components from almost any type of pre-alloyed metal powder (Wong & Hernandez, 2012). SLS and SLM are essentially the same manufacturing technique, as both processes employ a laser as heat source, which selectively consolidates powder particles in order to form 3D objects. The difference between the two processes lies in binding mechanism between the powder caused by the process parameters (Kruth, Mercelis & Van Vaerenbergh, 2005). A comparison of the surface morphology of the two process are shown in Figure 3.3.

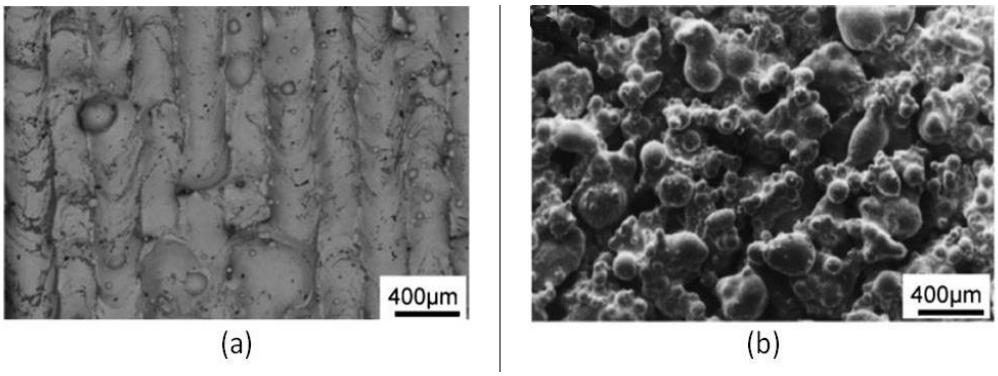

Figure 3.3: SLM/SLS surface morphology comparison. SEM images comparing the surface morphologies of M2 high speed steel processed with (a) SLM and (b) SLS technologies, adapted from (Gu *et al.*, 2012).

A good summary of processing quality can be found when measuring the relative density and surface roughness values achieved by a PBF process. Table 3.3 gives a comparison of these values for the three PBF processes discussed previously.

Table 3.3: PBF quality comparison. A comparison of density and surface roughness values achieved of Ti-6Al-4V components produced with various PBF technologies

PBF Process	Relative Density	Surface Roughness	Reference
EBM	98.0 %	30 - 40 µm	(Loeber *et al.*, 2011; Yang *et al.*, 2016)
SLM	99.7 %	7 - 15 µm	(Leuders *et al.*, 2013; Pyka, *et al.*, 2013)
SLS	71.3 %	35 µm	(Maszybrocka *et al.*, 2017; Traini *et al.*, 2008)

3.3 Selective Laser Sintering

During the SLS process, the laser heats the powder to a specific temperature, which is sufficient to fuse the particles together, but not high enough to completely melt all powder particles. The standard process of sintering hardmetals requires a mixture of two powders: one called the structural powder (e.g. WC, Ti, etc.) and another known as the binder powder (e.g. copper, bronze, nickel, etc.). The binder powder has a low melting point and forms the matrix between the unmelted high-melting-point structural powder particles during sintering. When the binder powder melts, there is rapid bonding of the powders due to the capillary forces exerted on the liquid. The first stage of liquid phase sintering (LPS) is called the rearrangement stage, followed by the second solution precipitation stage and the third stage called solid state sintering, which causes further densification (Wang *et al.*, 2002a). The various stages of liquid phase sintering are shown in Figure 3.4.

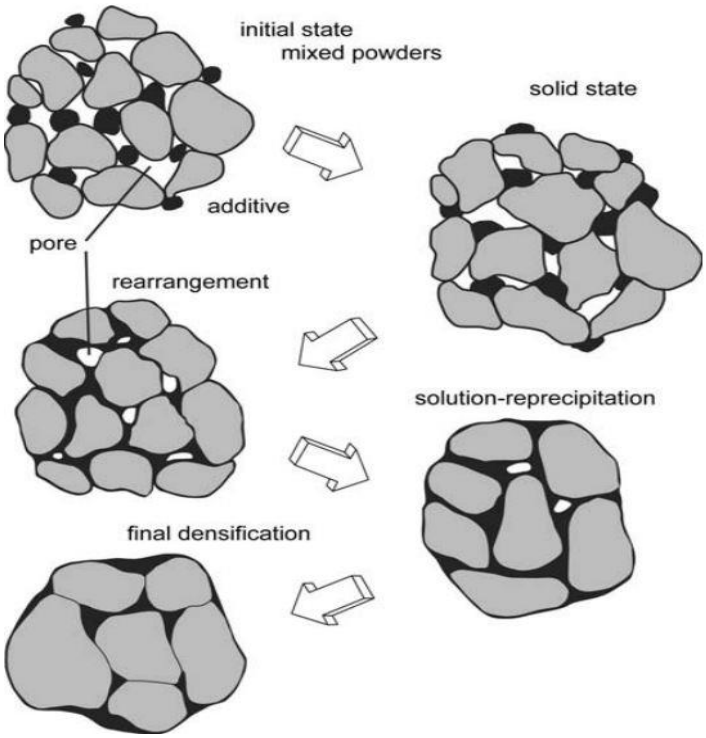

Figure 3.4: Schematic representation of the various steps during the development of liquid phase sintering (German *et al.*, 2009).

3.3.1 Development of SLS

The first functional SLS machine was developed by Carl R. Deckard and Joseph J. Beaman at the University of Texas at Austin in 1989 (Ashley, 1991). The machine used a low power laser (less than 100W) to build components from low-melting-point materials such as polymers, waxes, ceramic-binder mixtures and low-melting-point metals (Das *et al.*, 1991). As with most AM processes, rapid prototyping (RP) was the first application of the SLS and SLM technology. It is clear that the current application and developments in existing technology, justifies the transition from RP to AM. This transition is due to the culmination of a number of evolutionary developments in processes and materials as well as a steady reduction in cost of the technology (Campbell, Bourell & Gibson, 2012). Figures 3.5 and 3.6 display the chronological development and the original design of the SLS/SLM technology, respectively.

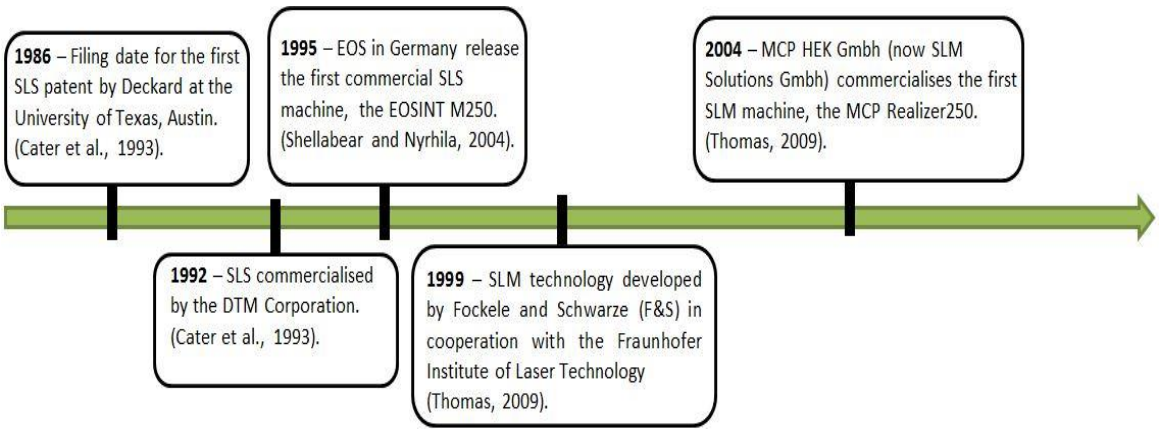

Figure 3.5: SLM/SLS timeline. A brief timeline of the major developments in the SLS/SLM technology.

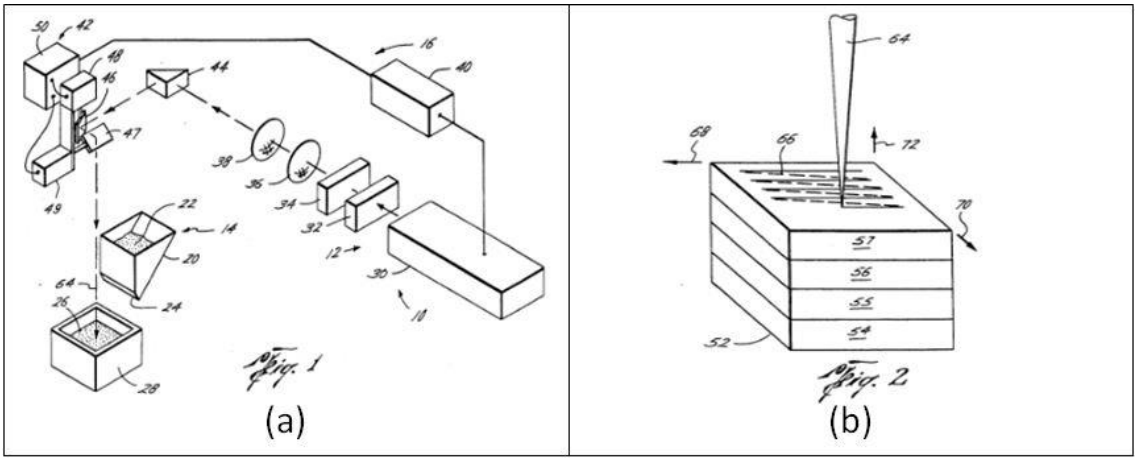

Figure 3.6: Original SLS patent. Hand illustrations displaying the basic workings of the (a) laser positioning system and (b) powder melting and layering method in the original SLS patent by Deckard (1990).

3.3.2 Workings of SLS

Software

Similar to other AM processes, information about the designed component is collected from a computer-aided design (CAD) file and converted into standard triangle language (STL) file format for the SLS machine to read. There are other types of files, but the STL file is the standard for every additive manufacturing process. The STL file creation process mainly converts the continuous geometry in the CAD file into a header, small triangles, or coordinates triplet list of x, y, and z coordinates and the normal vector to the triangles (Wong & Hernandez, 2012). This process can be inaccurate therefore the smaller the triangles, the closer the component will be to the original design. By using software to generate a component, allows designers to transfer the processing information to any place in the world, perhaps even outer space. Therefore, AM is also called digital manufacturing, solid free-form fabrication (SFF), or e-manufacturing (Gu *et al.*, 2012)

Parameter selection

The user selects the process parameters according to the specific powdered material intended for processing. Adjustments to the process parameters lead to variations in the resulting build quality. Process parameters affect quality aspects such as dimensional accuracy, mechanical strength, porosity, surface roughness, processing time etc. (Mierzejewska, 2015). Each material is unique

(material properties, particle size, shape and distribution), hence the material specific parameters need to be fully understood and carefully selected in order to build parts of acceptable quality (Van Staden *et al.*, 2016). Thus far, the establishment of process and material specific parameters has been difficult. Researchers have made attempts to determine optimal configuration parameters for specific AM process-material combinations, however there has been a lack of general conclusions of wider applicability (Townsend *et al.*, 2016). Table 3.4 lists the range of parameters that the user can adjust according to the material.

Table 3.4: Standard selection of SLS process parameters, adapted from Kruth *et al.*, (2005).

Material	Laser	Scan	Environment
Composition	Mode	Scan speed	Preheating
Powder density	Wave length	Hatch spacing	Pressure
Morphology	Power	Layer thickness	Gas type
Particle size distribution	Frequency	Scan strategy	O_2 level
Thermal properties	Pulse width	Scan sectors	Humidity
Flow properties	Offset	Pulse distance	
	Spot size	Scaling factors	

Powder, environment and layering

The environment in the build chamber needs to be controlled perfectly in order to limit the formation of the thermal stresses and surface oxidation of components. The melting occurs within an inert environment of either argon, nitrogen or in special cases helium (Loeber *et al.*, 2011). The powder is placed in the build chamber, which is first pumped down to a vacuum pressure of about 100 Pa and then filled with an inert gas to a pressure of 0.5 bar, which reduces the initial oxygen amount to around 0.02 % (Wang *et al.*, 2002b). Over-pressurising the build chamber prevents atmospheric oxygen to leak back into the chamber. Oxygen will react with the melting powder, resulting in oxidation and even a fire (Hagedorn-Hansen, 2017).

Before starting a new build, the user fills the powder feed piston with the adequate amount of new or recycled powder, which was recovered from previous build. The user is also required to install a component known as the build plate or base substrate. The plate is needed; as SLS builds require a solid, clean surface as a build foundation. The plate may be dulled through a sandblasting process in order to limit initial layer laser reflection (Hagedorn-Hansen, 2017). Certain points of reference will be created by the SLS machine on the build plate, therefore the plate must be perfectly flat and firmly secured to the build platform (Van Staden *et al.*, 2016). The build plate may be pre-heated to temperatures ranging between 100-300℃ in order to lower the thermal gradient during processing (Murr *et al.*, 2012). A higher preheating temperature results in less crack formation (Kempen *et al.*, 2013)

The laser selectively melts the powder according to the geometric information stored in the STL file about a specific powder layer. The unmelted powder is left untouched as it provides support for subsequent layers. After a layer scan is completed, the build platform is lowered down in the z-direction by a distance equal to one single powder layer. This distance is called the layer thickness and is generally between 20-100 µm thick (Ruan *et al.*, 2006). The powder feed piston is raised up in the z-direction, pushing fresh powder to the build surface. A powder roller or scraper mechanism transfers the powder from the feed piston's surface to the build platform. The roller distributes the powder equally on the lowered build platform, creating a new, levelled powder layer. The next layer scan is initiated and the newly deposited powder layer is fused to underlying layers by careful controlling processing parameters such as laser power, scanning speed and scan spacing (Loh *et al.*, 2015). A schematic of the workings of a SLM/SLS system is shown in Figure 3.7. The thickness of

the powder layer is critically important. A too thin layer will cause the binder in the powder to overheat and evaporate, whereas a too thick layer will increase the risk of delamination. The ideal powder layer thickness needs to be determined experimentally (Kempen et al, 2014).

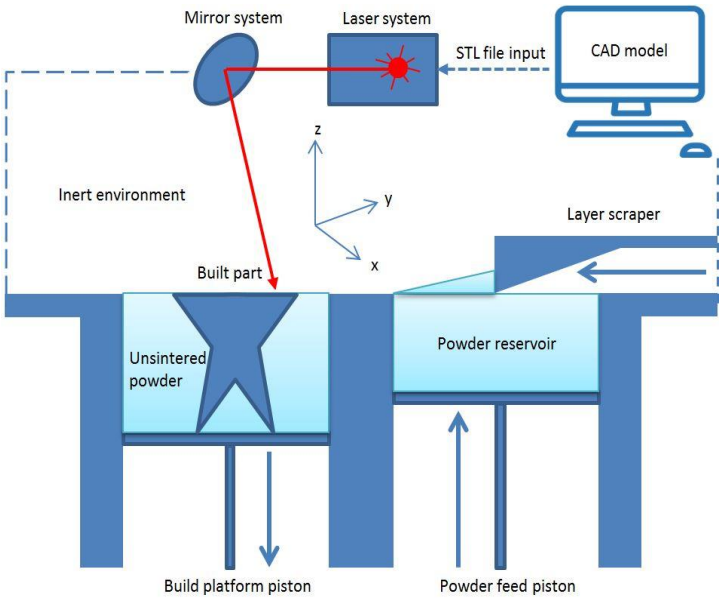

Figure 3.7: Schematic of the basic workings of a SLS machine.

Laser and mirrors

In the past, laser powder bed fusion systems used either a single CO_2 or Nd:YAG laser. These are standard Gaussian lasers, which are also implemented in other laser machining operations such as laser welding and laser cutting. However, in recent years, improvements in positioning systems, materials and other process parameters, meant the laser technology became a limiting factor. Recent developments have led to an improvement in laser technology, which notably improves the laser beam's quality and available resolution. Ytterbium fibre and disc lasers systems are regarded as the future standard laser technologies. SLS systems have developed to incorporate more powerful and multiple sets of lasers (Shellabear & Nyrhilä, 2004). The laser positioning system is shown in a schematic in Figure 3.8.

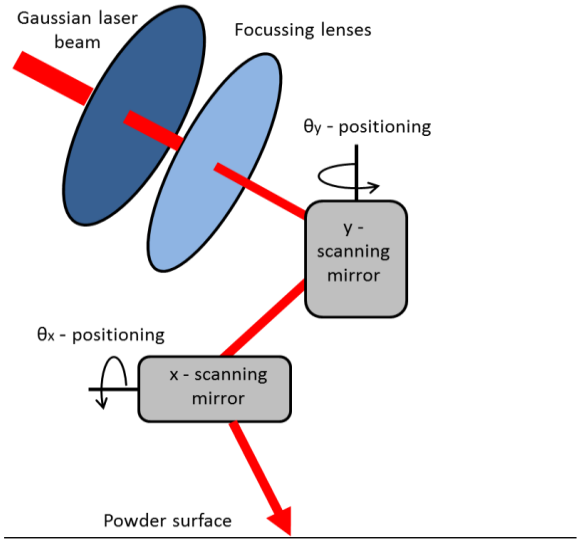

Figure 3.8: Mirror and lens laser positioning system used for laser fusion technologies

The SLS laser positioning system consists of a series of lenses and reflecting mirrors (Sames *et al.*, 2016). Galvanometers move laser-grade mirrors with low mass and inertia in order to deflect the laser beam according to the specific geometry received from the STL file. In a two-mirror setup, the focused laser beam is projected onto the first mirror which then reflects the beam to the second beam where it is positioned and reflected to the powder bed's surface (Deckard, 1990). A series of lenses control the focus spot of the laser beam on the surface of the powder bed. A smaller focus spot will generally yield better geometric accuracy of the laser-fused components. The laser spot size will greatly affect the dimensions of the melt pool that will form on the powder surface (Thomas, 2009).

3.3.3 Material and Parameter Calibration

A wide range of materials have been developed for use in SLS. A number of those materials make SLS superior to other techniques when the characteristics of materials are dependent on the type of process (Kumar, 2003). The development of materials for niche applications is a significant driving force for the SLS industry (Yap, *et al.*,2015). Another promising field of research is the optimisation of processing parameters. The combination of new material and processing parameters in the laser sintering process requires extensive experimental processing trials, otherwise known as material calibration (Kumar, 2003). SLS material calibration strategies include single track scans (Hauser, Chillds & Dalgarno, 1999), multi-track, multi-layer scans (Song & Koenig, 1997), and even full 3D objects (Beard, Ghita & Evans, 2011). Examples of these strategies are shown in Figure 3.9.

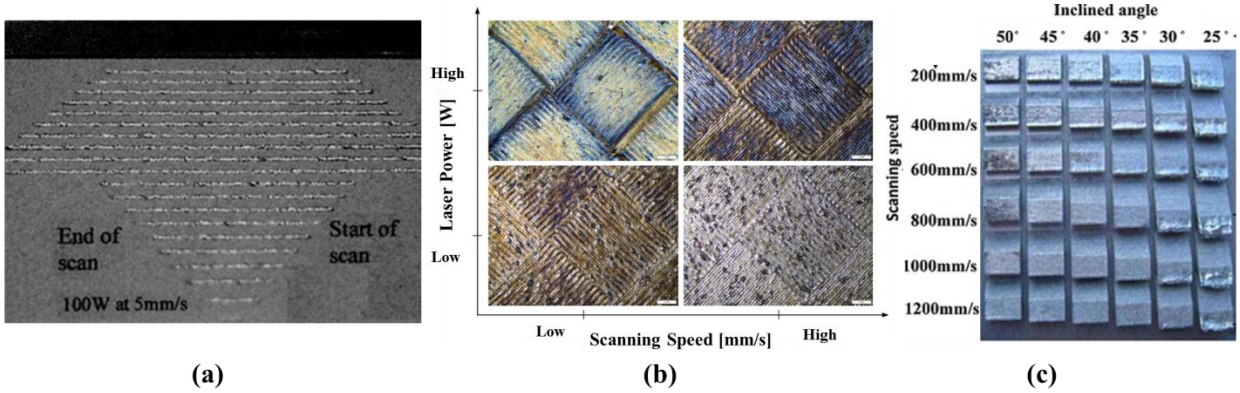

Figure 3.9: Experimental calibration strategies ranging from (a) single track scans, multiple-track and layer scans, and (c) full 3D objects. Adapted from Hauser *et al.*, (1999), Van Staden *et al.*, (2016), and Wang *et al.*, (2017).

Currently, the material calibration process is still very much trial-and-error and dependent on the user's experience. Moreover, the range of testable process parameters increases with the improvement of the laser source specifications. Hence, time and material wastage is inevitable before an optimum set of process parameter is identified (Loh *et al.*, 2015). Ramirez-Cedillo (2018) developed a set of experimental guidelines, which aim to reduce the extent of the experimental tests. However, the need still exists for calibration methods, which may replace current experimental procedures completely.

3.3.4 Applications of SLS

PBF technologies have long past the time when they were solely implemented for RP functions, as the focus now turns toward rapid manufacturing (RM) of net-shape or near net-shape components. The adoption of SLM/SLS produced parts in industry applications is steadily increasing as the need for cheaper, more complex, lightweight components grows. Although AM technologies have not developed to the extent where it can replace all components in a system, rather some non-critical parts can now be produced faster and at a fraction of the cost of conventional manufacturing

processes. One concept that has made AM attractive to industry, is the idea of producing hybrid components where conventional techniques may be used to manufacture components to a certain point after which AM techniques are used to produce the more complex geometries (Hagedorn-Hansen, 2017). The main driving industries of the SLS technology are described in the following section.

Aerospace

One of the main driving industries behind the development of the SLS technology and materials, is the aerospace industry. The reason for this is SLS's ability to fabricate lightweight, complex geometrical components from hard to machine materials for aero-based structural and engine components (Gu *et al.*, 2012). It is expected that PBF AM processes could bring about significant performance improvements and cost reductions for aerospace component manufacturing. Various aerospace companies such as General Electric Aviation, a large company in the aerospace filed, have already started to mass produce AM components in non-critical structural parts (Huang *et al.*, 2016).

A study by (Seabra *et al.*, 2016) investigated the feasibility of replacing aluminium with Ti-6Al-4V SLM manufactured aerospace components in order to reduce weight while maintaining functionality yielded good results. This further motivates the increasingly important role the AM industry will play in the improvement of aerospace technology.

Automotive

The adoption of AM in the automotive industry has closely resembled the route taken by the aerospace industry. At first the technology was solely implemented for rapid prototyping purposes, but with the continuous development in manufacturing processes and materials, the industry later decided to incorporate the benefits of the technology in end parts (Singh, 2016). The industry exploited the technology in order to push products to market quicker, thus having the competitive advantages. Small changes in time and development costs, results in larger downstream savings of vehicle development (Campbell *et al.*, 2012). Functional automotive components that have been manufactured with SLM/SLS technologies include intake manifolds, turbocharger compressors, wheels rims, and oil pumps.

Tool and Die

Another large application field of the PBF technology is the tool and mould-making industry, where tool inserts of complex, large dimensions and/or with integrated (conformal) cooling channels can be manufactured with relative ease (Brecher & Ozdemir, 2016). Additive manufactured drills or inserts with such integrated cooling channels have the potential to increase production greatly (Uhlmann, Bergmann & Gridin, 2015). The AM tool industry is also referred to as rapid tooling (RT), and can be categorised as direct or indirect tooling. Indirect tooling refers to the process where moulds for moulding or casting is produced with AM techniques. While direct tooling refers to the AM process of producing net shape tools such as inserts and dies. This is where the real challenge lies for the RT application field as AM produced tools compete directly with standard proven tools in terms of performance and total life cycle (Rosochowski & Matuszak, 2000). The tool and die industry demands components with high accuracies and sufficient mechanical and thermal properties and in order to withstand the moulding forces (Shellabear & Nyrhilä, 2004). The adoption rate of PBF technologies has been steadily increasing with the development of new tooling materials such as titanium, tool steel alloys and tungsten carbides (Van Staden *et al.*, 2016). SLS is the leading additive process for manufacturing injection tools due to its high precision (Ruan *et al.*, 2006). Tools currently produced using SLM/SLS technologies include sheet metal press tools, pressure dies, and cast tools (Levy, Schindel & Kruth, 2003).

Biomedical

The recent shift of the SLM/SLS technology towards rapid manufacturing paved the way for the development of fully functional, biocompatible dental implants and prostheses, rather than visually anatomically correct models or single-purpose surgical guides. In this way devices can be customised and implanted directly into a patient's body to suit the specific needs of the individual (Campbell *et al.*, 2012). The medical application of the technology ranges from surgical instruments for heart-tissue removal, dental implants, orthopaedic prosthetics and reconstructive surgery (Seneci *et al.*, 2015).

By utilising AM technologies, medical practitioners are not limited to shape and complexity of implants. Researchers, such as Fujibayashi, Neo, Kim, Kokubo and Nakamura (2004) have proven that porosity within implants act to stimulate new bone growth. Hence, medical practitioners now have the option to create a prostheses from an osteopromotive porous-controlled material (Wong & Hernandez, 2012) or include internal reservoir in implants for the delayed delivery of medication such as antibiotics directly to critical areas (Busse, 2016).

3.4 Selective Laser Sintering in South Africa

South Africa was introduced to the AM technology in 1994, after the abolishment of the Apartheid system and the subsequent lifting of sanctions against the nation. However, little attention was paid to the development of new manufacturing industries, as most research efforts had concentrated on the mining and defence industries. Sanctions meant the country's manufacturing industry lacked the advancements made by their US and European rivals. The government knew that it would be a slow and costly process to close the technology gap, however one that needed to be followed as it identified the manufacturing industry as a crucial contribution to increasing wealth and improving employment opportunities for its citizens. The Department of Higher Education (DHE) engaged in a more collaborative approach with local industries in order to fast-track development (Campbell & de Beer, 2005).

Although South Africa was initially excluded from the development of AM technologies and RP applications, enough knowledge was available for the government to identify specific South African industries where the technology could be implemented. The initial industry applications identified included automotive components, jewellery masters, medical visualisations, industrial design models low-volume tooling and rapid manufacturing of functional components (Campbell & de Beer, 2005). However, the tremendous cost of the technology and materials meant that AM was reserved for certain selection of research institutions, never reaching the public. In 2005 South African government launched a series of "Fab Labs" within communities, in an effort to encourage innovation through its National Advanced Manufacturing Technology Strategy (Gershenfeld, 2012).

There was a also a developing need for an AM association where new developments (such as machines, materials and applications) in the field could be discussed. RAPDASA (the Rapid Product Development Association of South Africa) was established in 1999, and consists of a variety of research organisations and industrial companies. RAPDASA is involved in a range of activities, including an annual conference, aimed at encouraging the further development and usage of AM technologies. More importantly it also provides valuable international links through partnerships with the Global Alliance of Rapid Prototyping Associations (GARPA) (Campbell *et al.*, 2012).

Currently, South Africa has looked toward AM technologies as a way to revolutionise its industries, particularly the medical, automotive, aerospace, mining, and tooling industries. Research has also increased to a level where nearly 50% of South African universities having in-house AM facilities (Campbell *et al.,* 2012). A list of universities currently researching AM technologies and applications are shown in Table 3.5.

Table 3.5: The various AM research fields and the institutions facilitating the research in South Africa. Adapted from Campbell *et al.,* (2012).

Applications	Collaborators
Advanced tooling	SU, CUT, VUT, NWU
Footwear	VUT, NWU
Medical Implants & devices	CUT, SU, VUT, UCT, UJ
Aerostructures	CUT, VUT, UJ
Direct end use (SMME focus)	CUT, VUT, SU

3.5 Chapter Relevance towards Research

This chapter is important as it gives a substantial introduction to the technology process. It discussed the technology, terminology and mechanism surrounding laser additive manufacturing. It also differentiated between the similar AM processes such as SLS, SLM and EBM. The chapter motivates the research problem by describing the current wasteful material calibration techniques used in industry. Finally, the chapter looks at current and developing applications of the technology, which adds motivation to the importance of this study.

Chapter 4: Tungsten Carbide and Its Applications

Overview

The main novelty of the research study is the use of tungsten carbide in the selective laser sintering environment. It is of critical importance that the material characteristics be understood before any attempt is made to incorporate the material in a new processing technique. This chapter will briefly discuss the history and development of tungsten carbide in industry applications. However, the main focus of this chapter will be the specific material properties that influence processing during selective laser sintering.

4.1 General Information

Tungsten carbide (WC) is a refractory, interstitial, group VI, transition metal carbide. The material is characterised by its hardness, wear resistance, high melting point and chemical inert properties. Since its discovery in 1906 by Henri Moissan (Lassner & Schubert, 2005) it has become an important industrial material with numerous applications in grinding, drilling and cutting tools, and many others (Pierson, 1996).

4.2 Metallurgy

In order to understand the origin of unique characteristics of WC a basic understanding of the metallurgical composition of the material is essential.

The term *carbide* is applied to compounds formed from the combination of carbon and other elements. Tungsten carbide, for example, is the combination of tungsten and carbon (W + C). A *refractory* refers to a material with a high melting point $T_m > 1800℃$ and a high degree of chemical stability. Only the interstitial and covalent carbides fulfil these two characteristics.

Refractory carbides consist of two structurally different types, namely interstitial carbides and covalent carbides. *Interstitial* carbides are crystalline compounds of a host-metal and carbon with a large difference in electronegativity between the two elements. The host-metal atoms are arranged in close packed structure with the carbon atoms occupying specific interstitial positions in that packed structure. Interstitial carbides are characterised by high electrical and thermal conductivities in addition to the high melting point, hardness and chemical stability. In a *covalent* carbide, the carbon atom is only slightly smaller than the metal atom resulting in a small difference in electronegativity between the two elements (Pierson, 1996). As WC is an interstitial carbide no further reference will be made to the other bonding mechanisms. The location of the tungsten on the periodic table in the refractory interstitial carbide group of metals is displayed in Figure 4.1.

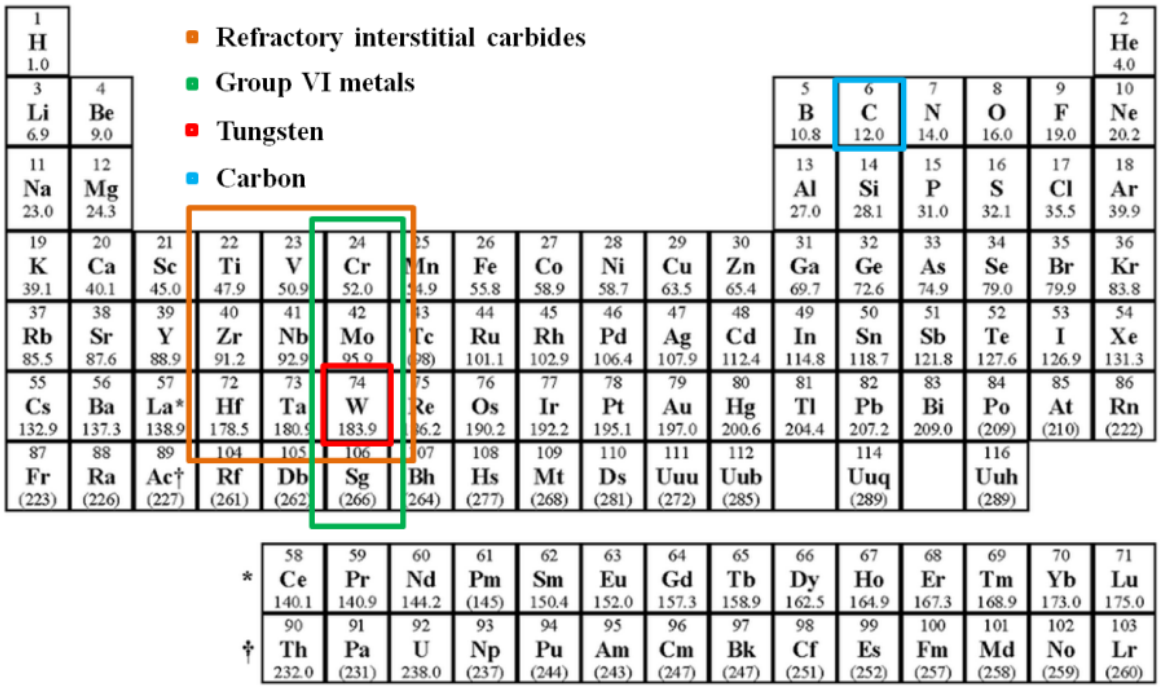

Figure 4.1: Periodic table used for explaining the formation of tungsten carbide. Adapted from Upadhyaya (1998).

Carbon

Carbon has the symbol C and is the sixth most abundant element in the universe. The carbon atom has 6 electrons (Z number) and electron quantum numbers of the ground state can be written as $1s^2 2s^2 2p^2$. The carbon 12 isotope has 6 neutrons in its nucleus. Carbon is found in different crystal structures (allotropes) depending on the temperature and external pressure of its environment (EDinformatics, 1999). A diagram of the carbon atom is shown in Figure 4.2.

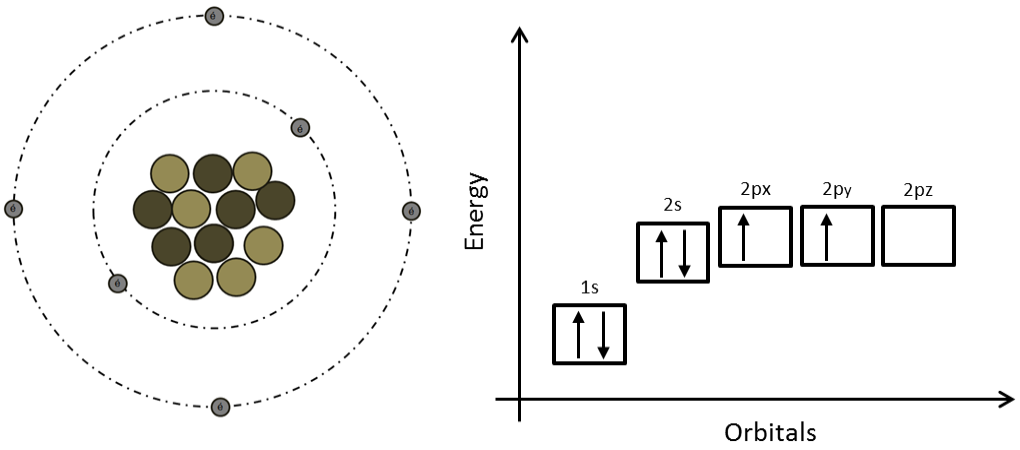

Figure 4.2: Carbon atom and electron quantum numbers. Adapted from Silberberg (2013).

However, there are only two valence electrons in the 2p orbital in the ground state atom structure as shown in Figure 4.2. Valence electrons are the only ones available for bonding to other atoms. Hence, the ground state does not account for the various types of bounds found in carbon compounds or molecules such as carbides where four valence electrons are needed instead of regular two. A carbon hybrid state exists where the one electron in the 2s orbital is promoted to the higher 2p orbital resulting in the carbon hybrid sp^3 orbital with four valence electrons. The hybridised atom is finally ready to bond with other atoms to form compounds such as carbides (Pierson, 1996).

Tungsten

Tungsten, also known as Wolfram, has the symbol W on the periodic table. It can be obtained through processing various naturally occurring minerals, such as ferberite ($FeWO_{4)}$, scheelite ($CaWO_4$) and wolframite ((Fe,Mn) WO_4). Tungsten is generally obtained as a dull grey powder, which is difficult to melt. It is very ductile in its purest form, which makes it easy to be drawn and cut. Tungsten has the highest melting and boiling temperatures of any known metal at 3400℃ and 5700℃, respectively (Emsley, 2001).

Tungsten is in a class known as transition elements. Normally, electrons gradually fill the inner orbitals before the next is occupied. This does not apply to transition elements, which can have partially filled inner shells. This trait plays an important role in the formation of interstitial carbides.

The metals forming the interstitial carbides are in the early d-block of the transition elements. The d-shell of the transition elements are only partially filled. The bonding (valence) electrons consists of the electrons in the outermost s-shell as well as the d-electrons from the inner unfilled d-shell. In the case of the three metals of the sixth period (Hf, Ta, W), the inner 5d shell is partially filled, while the 5f and 5g shells remain empty. They are known as the 5d transition elements. Table 4.1 lists the electron quantum number of this period of transition metal and highlights the valence electrons in bold (Pierson, 1996).

Table 4.1: Electron configuration of the metals in the sixth period. Valence electrons are highlighted in bold.

Shells and Subshells																	
Element	**Z**	**K**	**L**		**M**			**N**				**O**					**P**
		1s	2s	2p	3s	3p	3d	4s	4p	4d	4f	5s	5p	5d	5f	5g	6s
H	72	2	2	6	2	6	10	2	6	10	14	2	6	**2**	-	-	2
Ta	73	2	2	6	2	6	10	2	6	10	14	2	6	**3**	-	-	2
W	74	2	2	6	2	6	10	2	6	10	14	2	6	**4**	-	-	2

The bonding in interstitial carbides, such as WC, is not straightforward and involves a combination of covalent, metallic and ionic bonding mechanisms.

Tungsten carbide

Tungsten carbide is known as a transition metal carbide and is grey in colour. The compound consists of tungsten atoms bonded with carbon. In the carbide form, the material is hard and brittle while the host metal (tungsten) is softer and more malleable.

Pure tungsten has a body-centred cubic (bcc) crystalline structure whereas WC has a simple hexagonal (hex) unit cell structure. The carbon (non-metallic) atoms occupy certain interstitial sites within the tungsten (metal) lattice producing the interstitial carbide. The interstitial sites are triagonal prisms forming a sequence of layers over one another. The atomic structure of the carbide is shown in Figure 4.3.

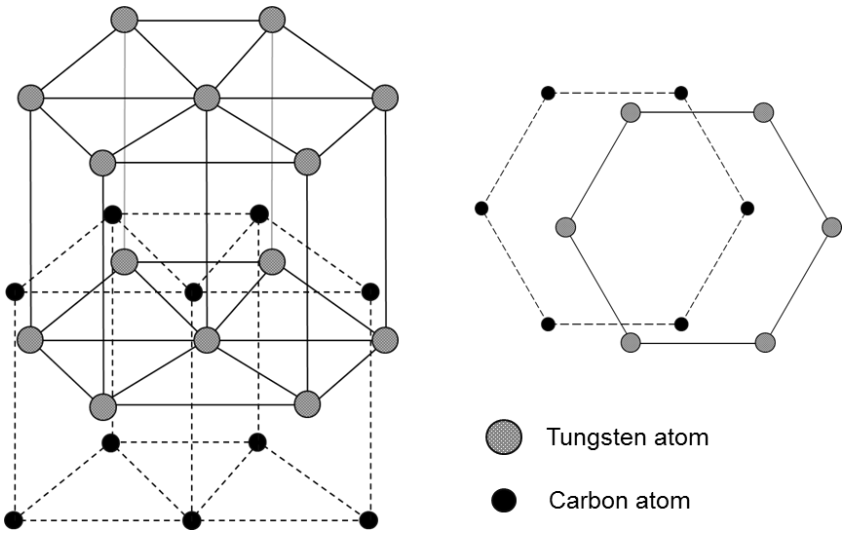

Figure 4.3: Simple hexagonal structure of the tungsten carbide crystal. Adapted from Pierson (1996).

Tungsten carbide is produced by the direct carburisation of tungsten carbide metal with carbon such as graphite or lamp black at temperatures of 1400 - 2000℃ in a vacuum or hydrogen (inert gas) environment. At these elevated temperatures, the tungsten is at risk to react with atmospheric oxygen and form ammonium paratungstate or tungstic oxide. Grain size control is critical and is determined by the processing parameters (Pierson, 1996).

4.3 Material Properties of WC

Tungsten carbide, like most carbides, is a hard and brittle material with a high melting point, which makes it ideal to use in certain industrial applications. However, WC has some unique characteristics that distinguishes it from other carbides and makes it a high value material.

Tungsten carbide has the highest thermal conductivity of any of the transition-metal carbides. Hence, WC can be considered an excellent thermal conductor. It is also the hardest carbide and is able to retain its hardness up to approximately 800℃. A summary of the general material properties are given in Table 4.2.

Table 4.2: General material properties of tungsten carbide (at room temperature) (Pierson, 1996).

Property	Value	Unit
Melting Point	2870	[℃]
Density	15 800	[kg / m^3]
Hardness	1700	[Hv]
Young's Modulus	620-720	[GPa]
Shear Modulus	262	[GPa]
Transverse Rapture Strength	550	[MPa]
Poison's Ratio	0.18	-
Coefficient of Thermal Expansion	6.0×10^{-6}	[$℃^{-1}$]
Thermal Conductivity	63	[W / m K]
Specific Heat Capacity	132	[J / kg K]

4.4 Powder Metallurgy

The powder metallurgy (PM) can be applied as a net shaping process similar to casting. However, unlike casting, which can only be applied to metals with a lower melting temperature, powder techniques are applicable to almost all materials (German, 2005).

Powder metallurgy is an ancient technique used to combine two types of powderised materials in order to achieve certain characteristics. The technique was revived in the late 19th century in order to produce refractory and precious metals. The technology only experienced major growth through the developments of World War II.

The principle of the PM technology is the production of different constituent powders and their consolidation into solid forms by the application of pressure at temperatures below the melting point of the major constituent.

In 1922 researchers of the OSRAM group combined the brittle tungsten carbide with a more ductile metal binder. After sintering the powder mixtures, a material of both high strength and toughness was obtained. Sintered hard metals, based on tungsten carbide bonded with cobalt, were first commercially produced by Krupp in Germany in 1926 (Capus, 2000). Cemented WC is known as a hardmetal although it is not truly a metal. It is also referred to as a cermet, which comes from the combination of a ceramic and a metal.

The hardness and toughness of the cermet/hardmetal can be adjusted by changing the fraction of constituents in the powder mixture. For cutting applications for example, the powder needs to consist of at least 80% of the hard WC. However, low binder content will yield a highly brittle material (Sandvik Coramant, 2016).

4.4.1 Types of Binders

Owing to its brittleness, researchers have discovered that by introducing a malleable metal binder to the sintered WC-cermet, the ductility and toughness of the composite can be increased considerably. Researchers have investigated the effects of various metal binders on WC-cermet characteristics. In past years, cobalt has been the predominant metal binder used commercially, however the cemented carbide industry has stressed on reducing the dependency on cobalt and focus on developing other elements as the possible metal binder. The reasons behind this concern are the sensitivity to cobalt price fluctuations and development of compounds with new properties (Uhrenius, Pastor & Pauty, 1997).

WC-Co

As mentioned previously, cobalt (Co) has been the predominant metal binder for WC in industry. The majority of previous research has focused on improving WC-Co by studying the failure mechanisms of wear, crack propagation and hot deformation (Tracey, 1992). The preference of cobalt to other binders is believed to be due to higher solubility of WC in Co. Secondly, Co has superior comminuation characteristics, which subsequently, leads to a more desirable microstructure during sintering of the powdered mixtures (Upadhyaya, 1998). Additional features, which give the WC-Co alloy good properties, include good toughness, high modulus of elasticity, good thermal conductivity and magnetism.

The sintering temperature for the most commonly used commercial hardmetal (WC-10Co) is **1496**℃ (Wang *et al.*, 2002a). In a WC-Co-C system, an eutectic liquid forms at 1320℃, i.e. WC dissolved in a cobalt matrix. The stoichiometric composition, which can be seen in the phase

diagram in Figure 4.4, is at all temperatures within the two-phase fields WC + liquid or WC + face-centred cubic (fcc)-Co. Owing to the fact that Co is the most commonly used binder in industry, this research project will focus on developing WC-Co for the AM environment.

The influence of the Co binder content on the hardness and toughness of sintered WC-Co is shown in Figure 4.5. It is clear that as the weight percentage (wt%) of Co increases, the fracture toughness increases correspondingly, however the hardness decreases. Industry makes use of this phenomenon in order to select a binder composition, which suits their specific application.

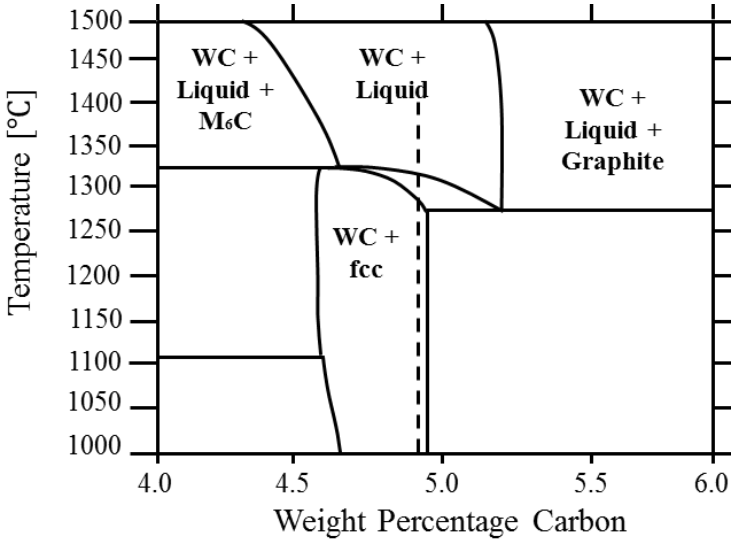

Figure 4.4: Phase diagram of the W-Co-C system. The dashed line indicates the stoichiometric WC + Co composition at 20 wt. % Co adapted from Uhrenius *et al.*, (1997).

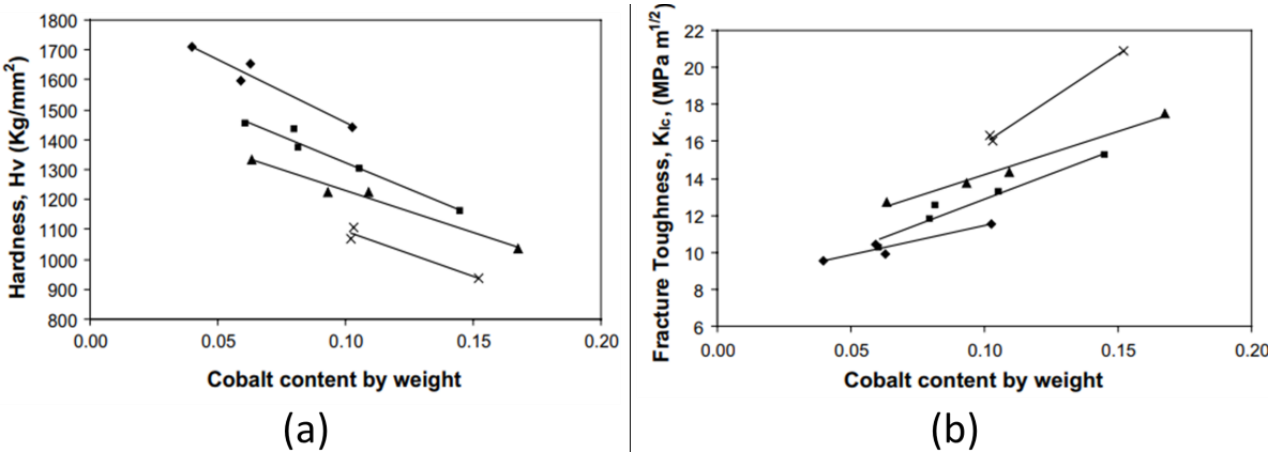

Figure 4.5: Influence of the Co binder. A comparison of the influence of the Co binder content on (a) hardness and (b) fracture toughness of sintered WC-Co (Fang, 2004).

The general properties of WC-Co at room temperature given in Table 4.3 vary significantly from that of pure WC in Table 4.2. There is a clear difference in the hardness and transverse fracture toughness values. A further in depth discussion on the temperature dependent properties of WC-Co powder is given in Chapter 8.

Table 4.3: Properties of as-sintered WC-5Co at room temperature (Siwak & Garbiec, 2016).

Property	Value	Unit
Density	13500	[kg / m^3]
Hardness	1550	[Hv]
Young's Modulus	610	[GPa]
Transverse Rapture Strength	3712	[MPa]
Coefficient of Thermal Expansion	5.0×10^{-6}	[$°C^{-1}$]
Thermal Conductivity	60-80	[W / m K]
Specific Heat Capacity	200	[J / kg K]

A hardness comparison of the most common WC binders are given in the graph in Figure 4.6. It is interesting to note that a high binder, such as 20 wt.%, decreases the Vickers hardness (Hv) value to almost 1000 HV compared to that of the 1550 Hv of WC-5Co in Table 4.3.

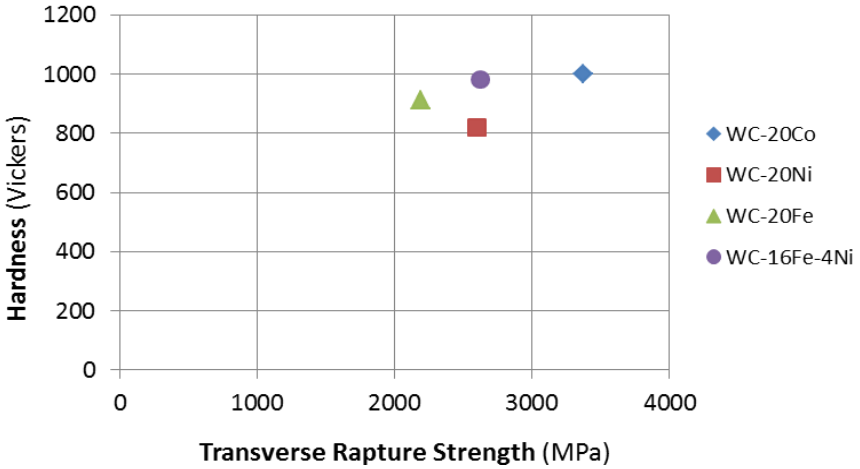

Figure 4.6: A comparison of the material properties of various WC binders, adapted from Tracey (1992).

WC-Ni

Nickel (Ni) has received the most attention as an alternative binder to Co (Fernandes & Senos, 2011). Although nickel also has excellent wetting abilities, the lowest temperature at which the liquid forms (around 1350°C) is higher than that of the W-Co-C system (Upadhyaya, 1998). The material properties of the compound have also been found to be inferior to those found in cobalt-based binders. The reason for this is the alloy produced by mixing WC with the pure element would not result in the plain two- phase WC + fcc-binder structure when cooling to room temperature after sintering as shown in Figure 4.7. Cooling to room temperature will lead to graphite precipitating, resulting in a significantly lower yield strength and work hardening rate compared to those of WC-Co systems (Viswanadham, Lindquist & Peck, 1983).

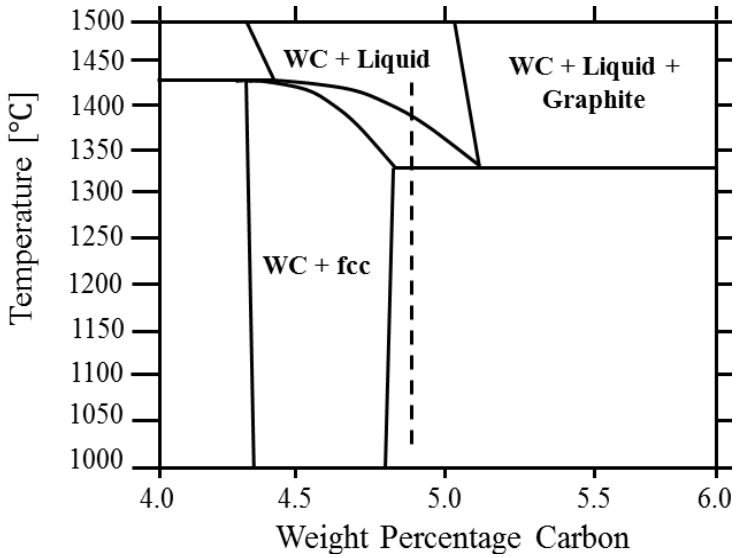

Figure 4.7: Phase diagram of the W-C-Ni system. The dashed line shows the stoichiometric composition of WC + Ni at 20 wt. % Ni adapted from Uhrenius *et al.,* (1997).

The focus on nickel as a binder has also been motivated by results showing higher corrosion and oxidation resistance. A possible solution to improve the material properties of the alloy is to select more suitable compositions from a carbon control point, grain size refinement and processing methods (Kim *et al.,* 2006). Nickel as a binder material is almost exclusively used in die and wear components due to its good corrosion resistance (Fernandes & Senos, 2011).

Kim *et al.* (2006) showed by using a high-frequency induction-heated sintering method, WC-Ni samples of 98.5% density could be achieved. The samples produced using this processing technique had good machanical properties relative to those of WC-Co. The results of the study is shown in Table 4.4.

Table 4.4: Influence of binder contents on material properties of the WC-Ni alloy (Kim *et al.,* 2006).

Binder contents [wt. %]	**Vickers harness** [kg / mm^2]	**Fracture toughness** [MPa / $m^{½}$]
8	1950	13
10	1810	13.5
12	1690	14.4

WC-Fe

Iron (Fe) has also been cited as a possible binder due to its favourable wetting properties. Gustafson (1987) concluded that Fe provides the lowest temperature for the liquid phase formation at 1350℃ and the highest solubility of WC in the liquid phase. However, on cooling, the stoichiometric composition is in the three-phase region WC + M_6C + Fe (fcc) and the embrittled η-phase (M_6C) will form (Fernandes & Senos, 2011).

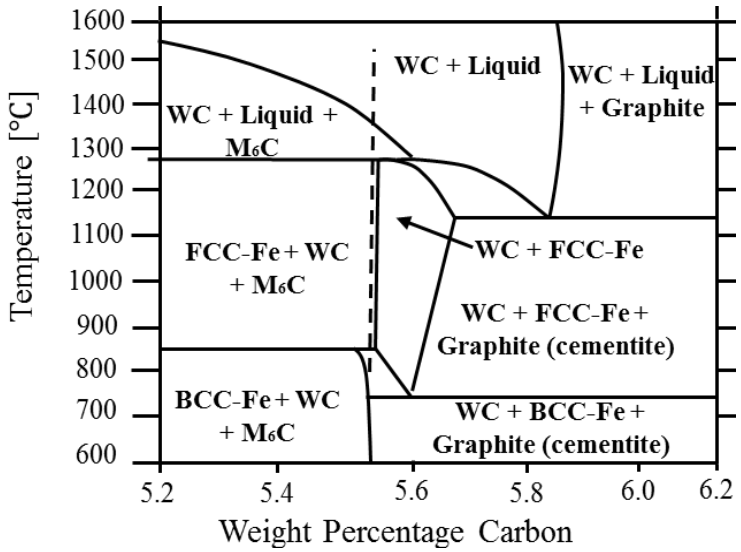

Figure 4.8: Phase diagram of the W-Fe-C system. The dashed line shows the stoichiometric composition of WC + Fe at 20 wt. % Fe adapted from Uhrenius *et al.*, (1997).

WC-Fe-Ni

Current research is investigating the possibility of using a combination of Fe-Ni as a possible alternative binder to Co. Material properties have been comparable and in some cases superior to those of the conventional WC-Co alloy. Furthermore, by controlling the Fe:Ni ratio, carbon content and thermodynamic treatments, the desired degree of metastability in the binder phase can be achieved, thereby avoiding the formation of unwanted M_6C and graphite. Transformation-toughening results in much higher toughness values than that of conventional WC-Co, without a significant difference in hardness (Liu, 2014).

Other binder possibilities

Other binders, which included elements such as TiC (Neikov *et al.*, 2009), Cr, Cr-Fe (Fernandes & Senos, 2011), Ni-Fe-Cr (Tracey, 1992), Ni-Cr, Ni-Fe (Fernandes *et al.*, 2008), Ni-Cr-Mo and Ni-Cr-Mo-Al (Almond & Roebuck, 1988) have been cited as possible alternatives to Co.

4.5 Material Processing

The review of the current hardmetal processing techniques highlights potential advantages of introducing additive manufacturing to the carbide industry. The steps of conventional hardmetal manufacturing are detailed in the following section described by Neikov *et al.*, (2009).

4.5.1 Conventional Processing

Raw materials

The first step in the process is blending of the grade powders (hardmetal and low melting temperature binder). The desired properties of WC-Co can be obtained by varying the WC particle size and the percentage of the cobalt. Moreover, a general rule is the finer the carbide grade and the lower the Co content, the harder, but less tough the alloy will be. A solid lubricant, such as wax or paraffin is added to the powder mix.

Forming

The powder is consolidated using a variety of compaction techniques depending on the intended application of the carbide, e.g. uniaxial pressing is used for mining and construction applications, whereas wear and metal forming tools are formed using cold isostatic pressing. Unlike most other metal powders, hardmetal powders do not deform during the compacting process. Generally, hardmetals can be compressed even above 65% of the theoretical density. The density of the compacts before sintering is referred to as the green density as the low temperature binder is still in its solid particle phase.

Sintering

Using a batch or semi-continuous type graphite furnace the compacts are first heated to approximately 500℃ in a vacuum or hydrogen atmosphere in order to remove the lubricant from the powder compact. After removing the lubricant, the compacts are sintered in a vacuum of 0.1 Pa at a final sinter temperature ranging from 1350 to 1600℃, depending on the cobalt binder content and desired microstructure. This melts the Co and binds the carbide particles together. The mechanics behind liquid phase sintering have been discussed in Section 3.3 Shrinkage of the compact ranges from 17% to 25% and provides a practically pore-free fully dense material.

Secondary operations

A large portion of hardmetal components are machined after sintering to adhere to certain geometrical tolerances or surface finish requirements. The sintered parts are shaped by means of metal-bonded diamond or silicon carbide abrasive wheels, turned with a single-point tool or lapped with a diamond-comprising slurry. These post-processing operations are both expensive and time-consuming.

4.5.2 Additive Manufacturing

Additive manufacturing is seen as a novel process for producing near-net-shaped WC parts. The production of special, interior contoured tools made from cemented tungsten carbide is a time and cost-intensive multistage process. An alternative for flexible, economic and automated production is provided by laser-based, additive manufacturing technologies. In this shortened process chain, near-net-shape and special interior contoured tools can be manufactured in small batch sizes (Uhlmann *et al.*, 2015). Past researchers have applied both the SLS and SLM technology processes to WC-Co powders with various degrees of success.

SLS

At IPT, Aachen, 3D pyramid parts were made from WC-12Co wt.% Co using SLS followed by a cobalt infiltration process. The maximum density achieved was 89.5%. A study by Kumar (2009) produced WC-Co moulds using the SLS technology. However, the maximum green density (no infiltration) achieved varied between 58% and 63% for the WC-12Co and WC-9Co powders, respectively. After infiltration, the maximum final densities ranged between 76% and 95% for the WC-12Co and WC-9Co powders, respectively.

SLM

In a study undertaken by Uhlmann, Bergmann and Gridin (2015) the processing parameters required to produce WC-17Co parts using the SLM technology was investigated. The researchers discovered that in order to melt the WC and Co binder simultaneously, the powder temperature

needed to exceed 2900℃. However, at this elevated temperature, the cobalt binder evaporates, leaving behind the embrittled tungsten carbide grains. Hence, this processing technology still requires more development before functional parts can be produced.

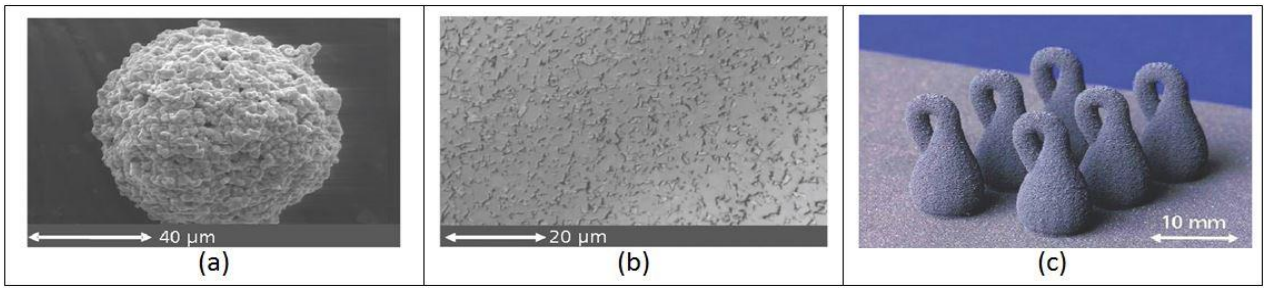

Figure 4.9: Examples of processed WC-Co. (a) A single WC powdered particle. (b) Microstructure of cemented WC-Co. WC particles are distributed uniformly in the CO matrix. (c) WC-Co parts produced with SLS (Kruth *et al.*, 2007).

4.5.3 Toxicity

The exposure to WC powder has been linked to various cases of respiratory complications. This occupational health condition is known as hard metal lung disease (HMLD), however it has also been described as WC pneumoconiosis (Nemery & Abraham, 2007). The rare lung disease can occur in workers who are engaged in the manufacturing, utilization or maintenance of tools composed of a hard metal such as WC-Co. Long lasting exposure may lead to the deterioration of lung function, e.g. shortness of breath, asthma with wheezing or a non-productive cough (Upadhyaya, 1998). There are various known cases of workers contracting the disease when working with particulate WC without the use of a protective dust mask (Terui *et al.*, 2015).

Caution should be taken during the following processes of the powder preparation stage:

- Weighing
- Milling
- Sieving
- Granulating

Ideally, powder preparation should be performed in a well-ventilated environment with the operator protected with a dust mask.

4.6 Applications

Approximately 50% of all carbide production is used for metal cutting applications. However, WC has been used for various other applications as detailed in this section.

Tools

WC-Co inserts are used in various material cutting operations such as milling and turning. Nitride coated cemented WC, which is even more wear resistant than WC, currently represents 80-90% of all cutting tool inserts. The success as a tool material is attributed to the unique combination of wear resistance, toughness and ability to produce complex geometries (Sandvik Coramant, 2016). Drawing and extrusion dies are another common application of tungsten carbide tools.

The Sandvik Group is currently the leading supplier of equipment and tools in the mining and construction industry and manufactures a major portion of the WC tool inserts used today. The tools

vary in composition and geometry, depending on the intended area of application. The dependency of material composition on the application of the WC tool insert is shown in the graph in Figure 4.10, whereas examples of WC tool inserts are displayed in Figure 4.11.

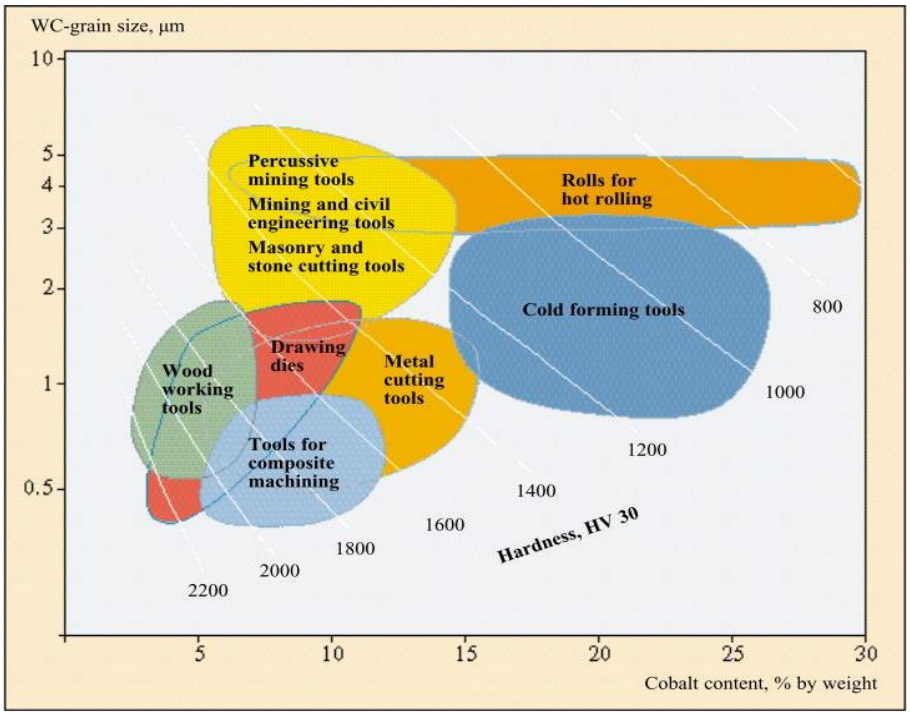

Figure 4.10: The variation of tooling applications depends largely on the composition of the cemented tungsten carbide (Sandvik Coramant, 2016).

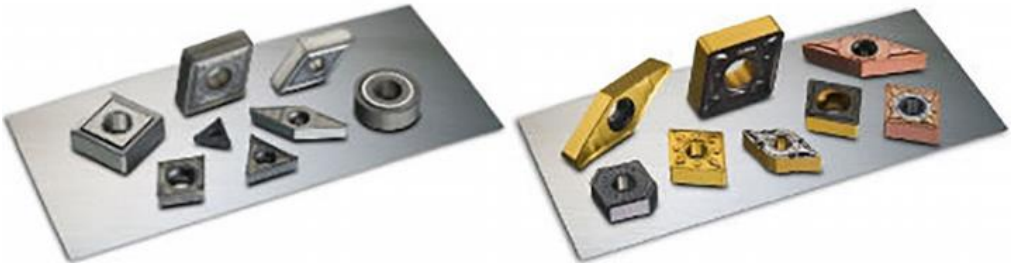

Figure 4.11: Cemented WC tool inserts. Uncoated (left) and coated (right) (Sandvik Coramant, 2016).

Mining, Oil and Gas

In percussive rock drilling there are two types of tools, namely tools with brazed inserts and tools with pressed button inserts. The hard WC crushes rock when it is hammered against the surface of the rock face. The wear resistance of the cemented WC-Co can be increased by decreasing the cobalt content. However, a lower cobalt content increases the risk of breakages caused by brazing stresses. Hence, the most commonly employed drill bits use the button technology, as these are suitable to use with a lower binder containing tungsten carbide (Fisher, Hartzell & Akerman, 1988).

Coatings

Hardfacing is the application of a hard, wear-resistant material to the surface of a component by means of thermal spraying, welding or a similar process with the main purpose of reducing wear. Tungsten carbide mixtures are applied to machine parts in order to improve their resistance.

Tungsten carbide powders for thermal spray coatings usually contain a cobalt content of between 6 to 18%. WC-Co thermal spray coatings particle sizes range from 5 to 150 µm (Neikov *et al.*, 2009).

Other

X-ray tubes for medical use have a tungsten emitter coil and the screens, which are used to view the X-rays, rely on magnesium or calcium tungstate phosphor to convert the X-rays into visible blue light. Other everyday applications include microwave ovens and television sets. Tungsten carbide has also been used in ball-point pens, darts and even golf clubs (Pierson, 1996).

4.7 Tungsten Carbide in South Africa

Much emphasis has been placed on South Africa's domestic production of a wide variety of raw materials, and it has frequently been cited that, although South Africa is a major producer of many metals and ores in the world context, it is nevertheless a relatively small producer of processed mineral products. Previously, South Africa's reserves and production of tungsten ore (scheelite and wolframite) were insignificant and totally inadequate to support the domestic consumption of tungsten carbide. However, the decision was made by Boart to establish a plant for the production of tungsten carbide in Springs, South Africa. The Boart International Springs Centre has since become the largest manufacturer of tungsten carbide in the southern hemisphere (Robinson & Belowt, 1990).

The South African manufacturing industry faces specific challenges such as a relatively limited market as well as competition from the East. It would be advantageous for the South African manufacturing industry to consider using its available tungsten carbide stocks in conventional and niche applications such as AM as the need for customised industrial tools increases (Van Staden *et al.*, 2016).

4.8 Chapter Relevance towards Research

The chapter introduced the primary material of this study, which is tungsten carbide cobalt. It started by providing information on its discovery, composition, properties, and current and developing industry applications. However, the most relevant information regarding this current research study is the details about the material properties needed to construct the numerical model. Properties such as the thermal conductivity, specific heat, and melting and boiling point are essential to the success of a numerical thermal model of the laser sintering process.

Chapter 5: Selective Laser Sintering Heat Transfer

Overview

Heat transfer between a moving laser beam and a metal powder mixture is extremely difficult to measure experimentally. A better method of investigating this phenomenon is by simulating the process using numerical techniques. In this chapter a mathematical model will be discussed, which will aim at simulating the heat transfer process between a moving Gaussian laser heat source and metal powder particles using known heat transfer principles. This numerical model will provide the basis for the simulated models developed later in the project.

5.1 Heat Transfer

5.1.1 Heat Transfer Description

The heat source from the SLS process is different from that of conventional sintering. The SLS process uses a unidirectional, localized, continually moving laser beam (Wiria, Leong & Chua, 2010). The laser beam moves over the top surface of a loose powder layer at a constant scanning speed along the positive x-direction. A fraction of the laser energy is absorbed by the powder and causes the low-melting-temperature binder to melt into a melt pool. The liquid binder now surrounds the high-melting-temperature structural particles. After the laser moves away, the liquid pool cools and solidifies into dense part (Xiao & Zhang, 2008). The four main stages of heat transfer are:

1. Energy input and absorption
2. Heating of the powder bed
3. Binder melting and sintering
4. Cooling of the sintered sample

The heat transfer prcess is modelled as a transient heat conduction problem. The heat transfer diagram in Figure 5.1 tries to simplify the laser sintering process.

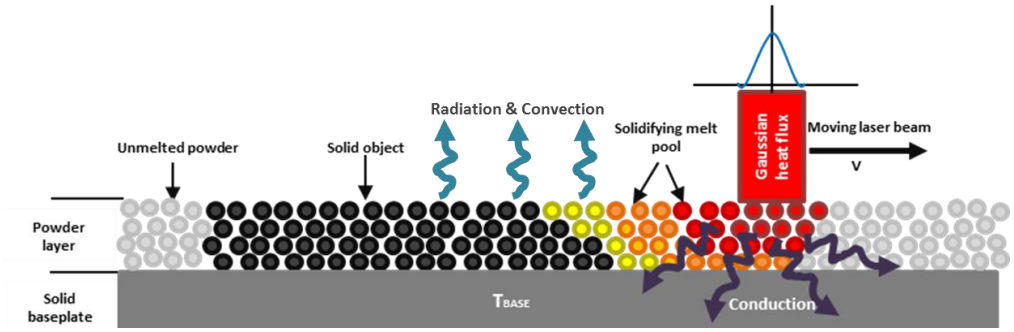

Figure 5.1: Heat transfer diagram of the SLS process (Olivier, 2018).

Later on a series of thermal equations are obtained using the heat transfer model. Ultimately, these equations are discretised and implemented in a numerical model, which is able to solve the heat transfer problem for the entire thermal field.

5.1.2 Absorption

Before discussing the specifics of the laser heat source, it is important to understand the concept of absorption. When the laser radiation strikes the surface, part of it is reflected, part of it is absorbed

and any remaining part is transmitted through the powder layer, as illustrated in Figure 5.2. The radiation heat flux incident on a surface is known as irradiation.

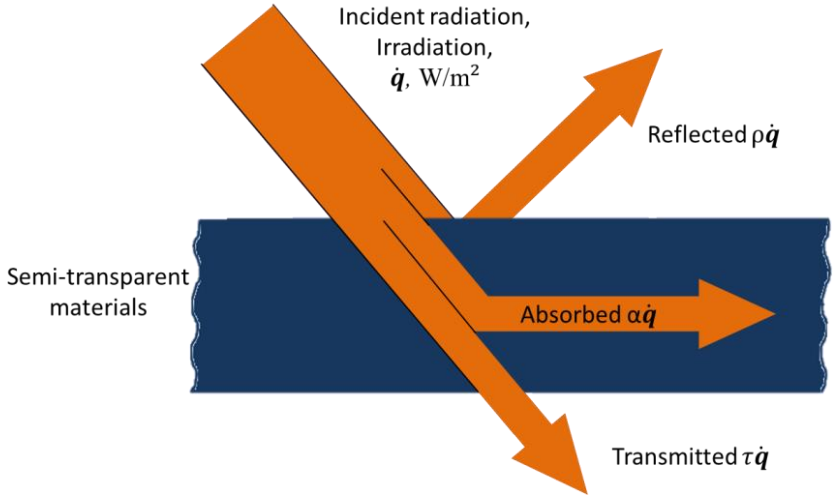

Figure 5.2: Absorptivity, reflectivity, and transmissivity through a semi-transparent material. Adapted from Cengel and Ghajarm (2015).

The First Law of Thermodynamics requires that the sum of the absorbed, reflected, and transmitted irradiation be equal to the incident irradiation (Cengel & Ghajar, 2015). Hence,

$$\dot{q}_{abs} + \dot{q}_{ref} + \dot{q}_{trans} = \dot{q} \tag{5.1}$$

When dividing each term in Equation 5.1 by $\dot{q}$, yields

$$\alpha + \rho + \tau = 1 \tag{5.2}$$

These values are material dependent and have to be determined experimentally. For this study transmitted irradiation was assumed to be negligible.

The absorption of energy in the powder bed is described by the total energy incoupling. It should be noted that the total energy incoupling is different from that of the material absorption coefficient as it is not only influenced by the material properties (reflection/absorption), but also by the powder characteristics (mixture ratio, mean particle size, shape and distribution) (Wang *et al.*, 2002b). The total energy incoupling is described by the following equation:

$$Total\ energy\ incoupling = \frac{Absorbed\ energy}{Input\ energy} \times 100 \qquad [\%] \tag{5.3}$$

A study by Wang *et al.* (2002b) found that the average total energy incoupling for WC-9Co powder was 80.02%. The absorption profile ("energy penetration") of the laser beam as a function of powder bed depth in the y-direction is shown in Figure 5.3.

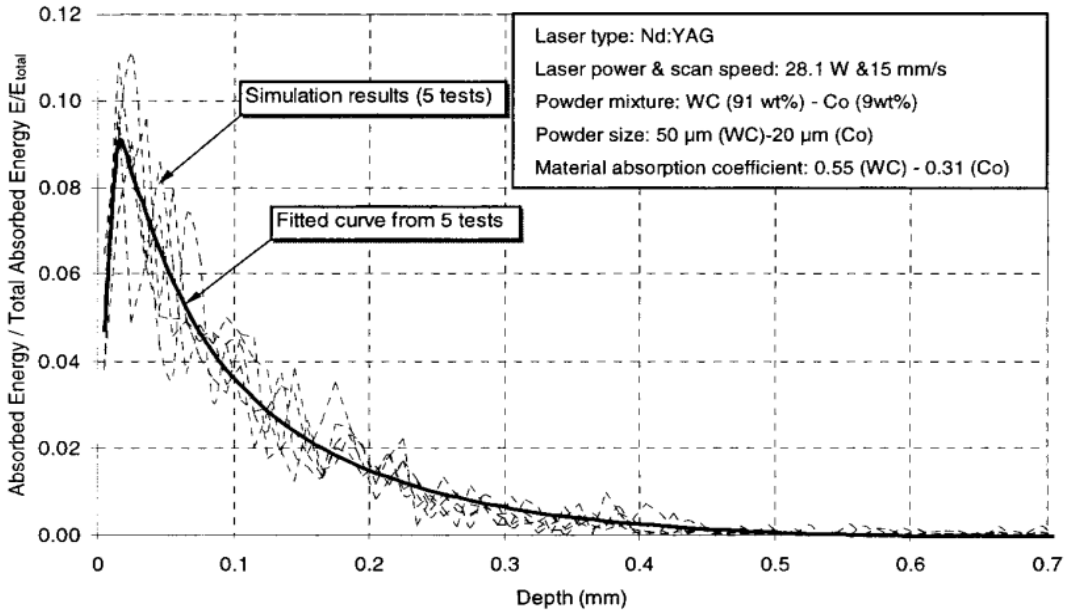

Figure 5.3: Absorption profile of laser beam energy in powdered WC-Co (Wang *et al.*, 2002b).

5.1.3 Moving Heat Source

Various heat flux models have been developed to simulate the intensity of the moving heat source such as the uniform, cylindrical and Gaussian models. However, the Gaussian, as per Equation 5.4, is the most widely implemented distribution (Teng *et al.*, 2014). The equation describing the Gaussian surface distribution is given as:

$$\dot{q}_{laser}\,(x,y,t) = \frac{\alpha P}{\pi r^2} exp\left[-\frac{(x-vt)^2+y^2}{r^2}\right] \qquad \left[\frac{W}{m^2}\right] \tag{5.4}$$

Where $\dot{q}_{laser}$ is the applied heat flux, α is the energy absorption coefficient, $P\ (W)$ is the laser power, $r\ (m)$ is the spot radius at the top surface, $v\ \left(\frac{m}{s}\right)$ is the velocity of the moving laser and $t\ (s)$ is the travel time. The x and y are distances (m) from the centre of the laser beam. A 3D and 2D representation of the Gaussian surface distribution is given in Figures 5.5 and 5.6, respectively.

As will be discussed in the following sections, the majority of the thermal heat is absorbed within the first several microns of powder. Therefore, many researchers including Luo and Zhao (2017) have considered the scanning laser beam to be a surface-based heat source. The difference between a surface and a volumetric heat source is shown in the schematic in Figure 5.4.

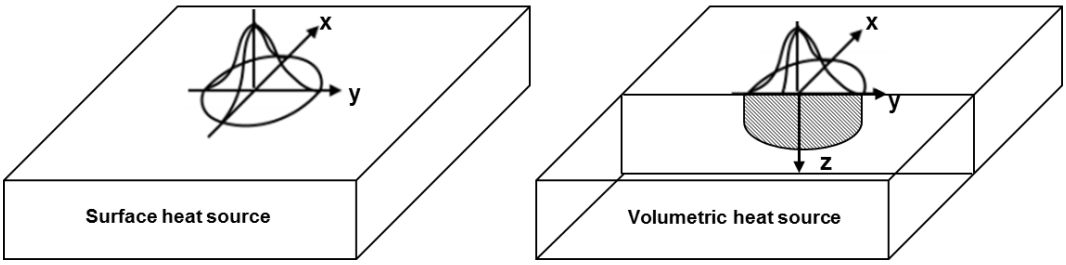

Figure 5.4: Difference between a surface and a volumetric heat source adapted from Heinze *et al.* (2014).

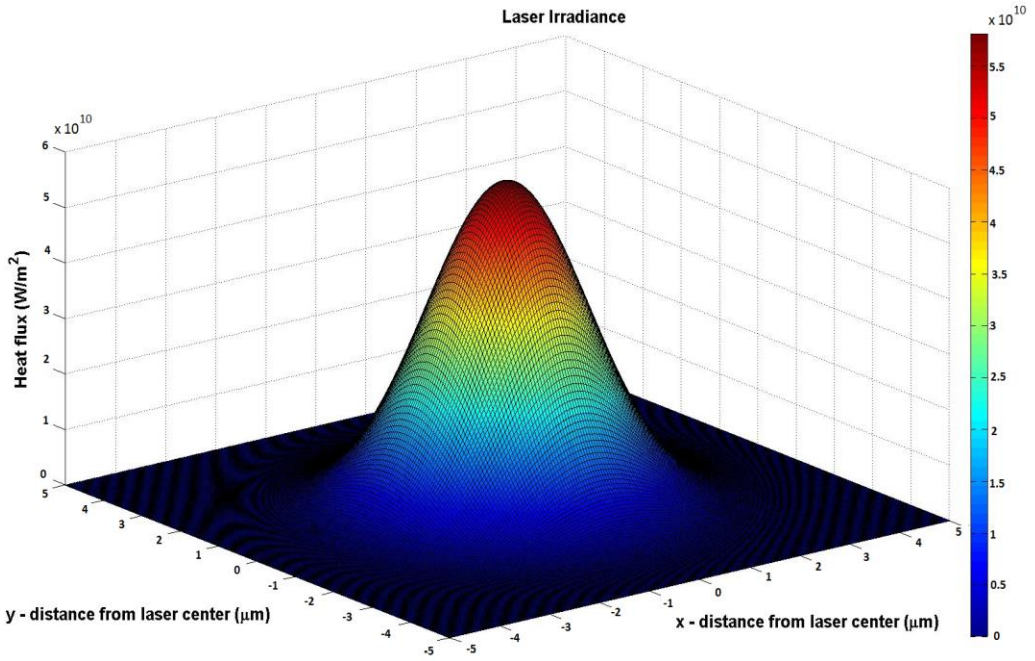

Figure 5.5: 3D Gaussian heat flux distribution. Adapted from (Teng *et al.*, 2014)

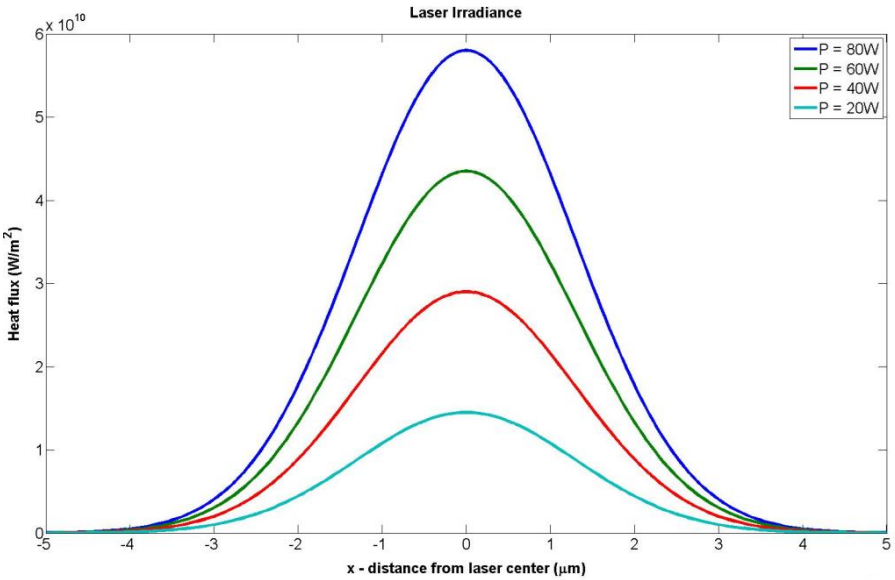

Figure 5.6: 2D Gaussian distribution with a variation in laser input power. Adapted from (Teng *et al.*, 2014)

However, to reduce geometrical errors, the beam has been modelled as a volume-based heat source using Goldak's double ellipsoidal heat distribution equation (Goldak, Chakravarti & Bibby, 1984) such that:

$$\dot{q}_{laser}(x,y,z,t) = \frac{6\sqrt{3}\eta P f}{abc\pi\sqrt{\pi}} exp\left(-\frac{3(x+v\cdot t)^2}{a^2} - \frac{3y^2}{b^2} - \frac{3z^2}{c^2}\right) \quad \left[\frac{W}{m^3}\right] \tag{5.5}$$

Where f is a shape factor for either the front or the back side of the melt pool, η the heat source efficiency and powder absorption, and a, b, and c represents the length of the semi-axis of the ellipsoid along the x,y and z directions, respectively. Goldak's double ellipsoidal volumetric distribution is shown in Figure 5.7.

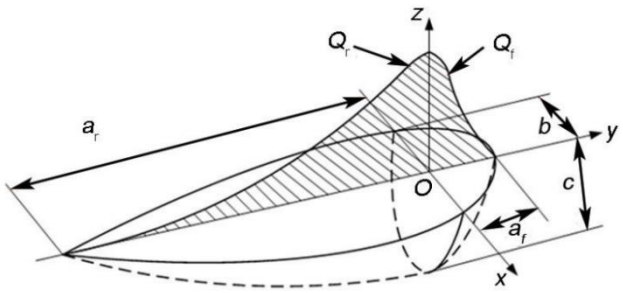

Figure 5.7: Schematic representation of Goldak's double ellipsoidal volumetric heat source (Goldak *et al.*, 1984).

5.1.4 Governing Heat Transfer Equation SLS Processing

In order to fully understand the physics involved during laser processing, the governing equations need to be investigated. Fundamental modeling of thermal behaviour, such as conduction, convection and radiation, will be used in this study in order to describe the physical heat transfer phenomena occurring in the SLS powder bed during sintering and derive the governing equations. The following derivation of the heat transfer process in SLS processing of powder materials has been published by Cengel and Ghajar (2015) and Wiria, Leong and Chua, (2010).

A good place to start is to consider the total energy entering and leaving the system through the surface of the powder bed. This is known as the conservation of energy principle. Heat flows in a solid body by *conduction*, whereas heat is transferred to or from a solid body through an adjacent fluid by *convection* or without an adjacent fluid through *radiation* (Cook *et al*., 2002). The SLS environment can be modelled as a control volume with the top surface of the powder bed as the control surface as seen in Figure 5.8.

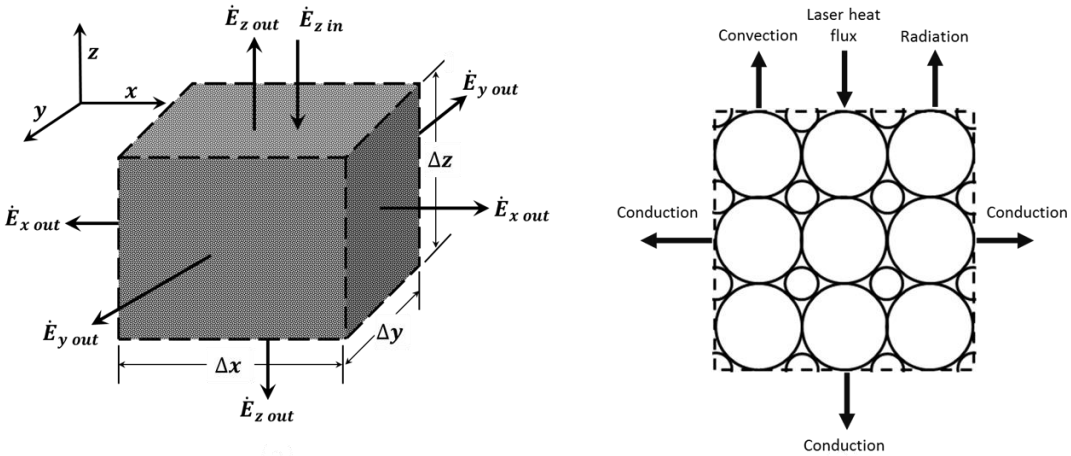

Figure 5.8: Simplified control volume of the powder bed. Adapted from Cengel and Ghajar (2015).

The First Law of Thermodynamics equation is given as:

$$\begin{pmatrix} Total\ energy \\ entering\ the \\ system \end{pmatrix} + \begin{pmatrix} Total\ energy \\ generated\ in\ the \\ system \end{pmatrix} - \begin{pmatrix} Total\ energy \\ leaving\ the \\ system \end{pmatrix} = \begin{pmatrix} Change\ in\ the \\ total\ energy \\ of\ the\ system \end{pmatrix} \tag{5.6}$$

$$\dot{E}_{in} + \dot{E}_g - \dot{E}_{out} = \frac{dE_{st}}{dt} = \dot{E}_{st} \tag{5.7}$$

Heat transfer = Conduction (internal) + boundary conditions (external)

Where $\dot{E}_{in}$, is the energy inflow by laser, $\dot{E}_{out}$ is the energy outflow, which comes from heat transfer due to conduction, convection and radiation from the powder bed to the atmosphere during cooling. $\dot{E}_g$ represents the energy generated in the control volume, such as chemical or electromagnetic energy. $\dot{E}_{st}$ represents the energy stored, which is related to any changes that happen within the control volume and may be due to kinetic, potential or internal energies of its content.

In order to simplify the governing equation, the following assumptions and conditions are made for the heat transfer process in an SLS powder bed:

1. The generated energy term $\dot{E}_g$ may be ignored as there is no energy generation in the powder bed.
2. Owing to the symmetry of the spherical powder particles, the change of temperature in each powder particle is only across its radius, r.
3. Due to the fast scanning speeds and small laser spot size, convection and radiation heat transfer between particles is small and thus negligible.
4. Due to the enormous size difference between the laser beam and a single powder particle, the temperature of the powder particle's surface, T_{surf} is approximately equal to the surrounding temperature, T_∞ ($T_{surf} \approx T_\infty$).
5. The laser power is constant and does not change during the sintering process.

For a 3D transient case, the stored energy term in Equation 5.7 is expressed in terms of the rate of change of the thermal energy of a medium per unit volume, $\rho c_p \frac{\partial T}{\partial t}$. For a unit volume the $\dot{E}_{st}$:

$$\dot{E}_{st} = \rho c_p \frac{\partial T}{\partial t} dxdydz \tag{5.8}$$

Expanding the terms in Equation 5.8 in terms of heat conduction in a 3D volume, gives:

$$\frac{\partial}{\partial x}\left(k\frac{\partial T}{\partial x}\right) + \frac{\partial}{\partial y}\left(k\frac{\partial T}{\partial y}\right) + \frac{\partial}{\partial z}\left(k\frac{\partial T}{\partial z}\right) = \rho c_p \frac{\partial T}{\partial t} \tag{5.9}$$

Where k, ρ and c_p are the temperature dependent material thermal conductivity, density and specific heat at constant pressure, respectively.

To simplify the derivation of the governing equations, the energy balance is formulated to a single spherical particle. The spherical coordinate system such as shown in Figure 5.9 is proposed for the description of heat flux conduction in a control volume of powder particles.

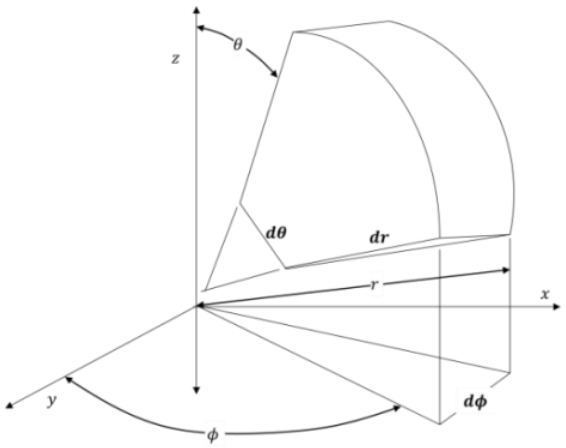

Figure 5.9: Control volume for a spherical element. Adapted from Cengel and Ghajar (2015).

Coordinate transformation can be used to transform from the rectangular to spherical coordinate system, where:

$$x = r\cos\phi\sin\theta,\ y = r\sin\phi\sin\theta \text{ and } z = \cos\theta$$

Transforming the heat equation in Equation 5.9 to the spherical coordinates system gives:

$$\dot{q}_{laser} + \frac{1}{r^2}\frac{\partial}{\partial r}\left(kr^2\frac{\partial T}{\partial r}\right) + \frac{1}{r^2 sin^2\theta}\frac{\partial}{\partial\theta}\left(k\frac{\partial T}{\partial\phi}\right) + \frac{1}{r^2 sin^2\theta}\frac{\partial}{\partial\theta}\left(k\ sin\theta\frac{\partial T}{\partial\theta}\right) = \rho c_p\frac{\partial T}{\partial t} \tag{5.10}$$

Finally, after considering all assumptions, the governing equation in Equation 5.10 for modeling the SLS process reduces to:

$$\dot{q} + \frac{2k}{r}\frac{\partial T}{\partial r} + k\frac{\partial^2 T}{\partial r^2} = \rho c_\rho\frac{\partial T}{\partial t} \tag{5.11}$$

Boundary conditions

Boundary conditions are dependent on the specific temperature analysis case.

$T = T(x,t)$ Prescribed temperature (5.12)

$q = h(T - T_0)$ Surface convection (5.13)

$q = \varepsilon\sigma((T - T^{abs\ zero})^4 - (T^0 - T^{abs\ zero})^4)$ Radiation (5.14)

Where $h = h(x,t)$ is the film coefficient, $T^0 = T^0(x,t)$ is the sink temperature, ε is the emissivity, and σ the Stefan-Boltzmann constant.

5.2 Chapter Relevance towards Research

The chapter investigated the heat transfer principles involved in the selective laser sintering. It discussed the heat distribution profiles various past researchers used in their respective studies. This is important as the loading condition influences the final shape of the simulate melt pool. Ultimately, a heat transfer model with specific boundary conditions was developed, which can be used in the numerical thermal model.

Chapter 6: Numerical Modeling of Laser Processing

Overview

Heat transfer between a moving laser beam and a metal powder mixture is extremely difficult to measure experimentally. An alternative technique to investigate this phenomenon is to simulate the process using numerical methods. This chapter will provide insights to the numerical studies performed by past researchers in the SLS/SLM technology environments. This chapter also discusses some of the findings of a literature review performed by the author, which was presented at the Rapid Product Development Association of South Africa (RAPDASA) conference in November 2017 (Olivier *et al.*, 2017).

6.1 Numerical Methods

Numerical modeling is a good approach in applications where there are (1) high levels of uncertainty due to sparse data sets and (2) environments where the real-life processes are resource intensive and time consuming (Duzevik, 2017). Other benefits of numerical modeling in the additive manufacturing industry are listed below.

1. Simulations can be performed anywhere in the world with the correct software, processing power and network connection.

2. Multiphysical phenomena, which are difficult or even impossible to measure in real time, can be controlled and studied.

3. The process can easily be visualised as it provides insights to environments that are otherwise too dangerous, small or fast.

4. It removes blind guessing as machine calibrations can be made using the results obtained from numerical models.

5. Multiple iterations can be performed within a day depending on complexity reducing time and material wastage

6. It increases the first-time-right components, leading to a shorter time to market.

The first numerical models describing laser processing phenomena appeared in the early 1980's. These numerical models were initially developed in order to investigate various welding phenomena, such as fluid flow in the laser melt, melt pool surface tension and convection as well as the effects of laser scan parameters on the fluid flow (Basu & Date, 1990). The findings of these early models are still relevant and provide a basis for modern PBF analyses.

Numerical simulations, which aim to simulate phenomena during SLM/SLS processing have be undertaken by several past researchers. In the quantitative systematic review, Olivier et al. (2017), reviewed a total of 45 publications focused on recreating the selective laser melting process. The reviewed publications only included numerical studies published within the past five years (2012-2017) at the time of submission.

The main objective of these numerical models is to replicate the multi-physical SLM process as accurately as possible. These simulations incorporate various mathematical formulations in order to

develop accurate numerical replications of physical phenomena such as thermal history, residual stress, melt pool (isotherm) characteristics etc. (Lopez-Botello *et al*., 2017)

.

Owing to the overwhelming complexity of simulating, all the phenomena present during SLS/SLM processing, researchers make use of certain approximations in order to limit the scope of their numerical models. However, different approaches lead to variations in results, even when investigating similar phenomena using identical material properties and process parameters. Depending on the application, large variations in simulated results can be problematic.

6.2 Simulated Phenomenon

SLM/SLS includes aspects of optics, laser physics, heat and mass transfer, mechanics, metallurgy as well as other fields of science (Yadroitsava *et al*., 2015). SLM phenomena currently investigated using numerical modeling include the temperature distribution, melt pool characteristics, residual stresses, microstructure and powder configuration. However, researchers are not limited to the scope of their simulations as most of the reviewed publications include multi-physical phenomena in their models. The results of the quantitative review in Figure 6.1 displays the number of occurrences each of the simulated phenomenon has in literature.

6.2.1 Temperature Distribution

The most common numerically modelled phenomenon in the reviewed literature is the temperature distribution with 41% of the occurrences. The temperature distribution results from the laser heat input on the top surface of the powder bed and plays an important role in both the mechanical and physical (geometric accuracy, surface roughness, etc.) properties of fabricated components (Vijay & Rao, 2013). The temperature distribution can be used to predict the thermal penetration through successive powder layers and thermal history between scan tracks during multi-track, multi-layer processing (Foroozmehr *et al*., 2016). The temperature distribution from numerical models can be validated using infrared cameras (Riedlbauer *et al*., 2014), thermocouples (Dunbar *et al*., 2016) and micrograph analyses of the solidified microstructure (Gu & He, 2016).

6.2.2 Melt Pool (isotherm) Geometry

The second most commonly simulated phenomenon with 30% of the occurrences is the melt pool geometry. These simulations primarily investigate the characteristic shape of the melt pool while disregarding the flow mechanics developed within the isotherm. The melt pool is highly sensitive to SLM input parameters such as laser scanning speed, laser power (Sun *et al*., 2015), scanning length (Cheng & Chou, 2015), power absorptivity (Khairallah *et al*., 2016) and the laser spot size (Romano, Ladani & Sadowski, 2016).

6.2.3 Residual Stress

Residual stress is another commonly simulated phenomenon, as it is primarily caused by high thermal gradients between successive layers and tracks (Hussein *et al*., 2013). Residual stress leads to unwanted abnormalities in components such as deformation and cracks (Li & Gu, 2014). Numerical simulations replicating residual stresses may provide valuable insights to geometries requiring better support structures, which counter or withstand the build-up of internal stresses (Hussein *et al*., 2013). Residual stress is validated experimentally by measuring part distortion (Li, Liu & Guo, 2016), neutron diffraction (Szost *et al*., 2016) and micrograph analysis of crack geometry and orientation (Gu & He, 2016).

6.2.4 Powder Configuration

Numerical modeling of the of the powder configuration is important as it influences the sub-surface porosity and resulting surface structure of SLM components. Powder particle packing configuration is influenced by numerous factors such as powder size distribution, powder morphology, layer thickness and packing density. The particle distribution models in the past simulated the phenomenon using randomly packed configurations or particle raining models, where the particles are dropped into position within a tightly packed configuration (Panwisawas *et al.*, 2017a). Powder configuration techniques include powder bed density (Gürtler *et al.*, 2014) and surface morphology measurements (Panwisawas *et al.*, 2017a).

6.2.5 Melt Pool Flow Dynamics

Melt pool flow dynamics simulations focus on replicating the physics, which influence the characteristics of fluid in the molten powder. The models include thermo-fluid principles (Leitz *et al.*, 2016) and individual powder particle interactions (Khairallah *et al.*, 2016). The models aim at predicting suitable process parameters which limit the formation of defects such as balling and keyholes (Lee & Zhang, 2015). The melt pool flow dynamics are validated by observing the surfaces morphology of single track scan tracks (van Belle, Vansteenkiste & Boyer, 2013).

6.2.6 Microstructure

The numerical modeling techniques used to predict the microstructural grain formation in SLM have only recently been developed and accounted for only 3% of the occurrences in reviewed literature. The majority of microstructure investigations focused only on experimental observations (Lopez-Botello *et al.*, 2017). Microstructural inhomogeneity is a major concern in SLM components. Hence the challenge is to control the microstructure evolution during SLM processing (Zinoviev *et al.*, 2016). The developed models use the simulated temperature profiles to predict microstructure formation. Microstructure formation is validated by measuring the average grain size experimentally in the etched micrographs of samples and comparing it to the simulations (Lopez-Botello *et al.*, 2017).

6.2.7 Relative Density

Only a single numerical model in the reviewed literature aimed at predicting the relative density in SLM processed components. Porosity in SLM parts is one of the primary challenges facing this AM technology. The relative density can give a good indication of the total porosity within the process parts. A numerical model can be used to establish the relationship between process parameters and the internal density of SLM components (Dai & Gu, 2014). Relative density is validated through quantitative measurements of the observed pores in the micrographs of SLM process parts (Dai & Gu, 2014).

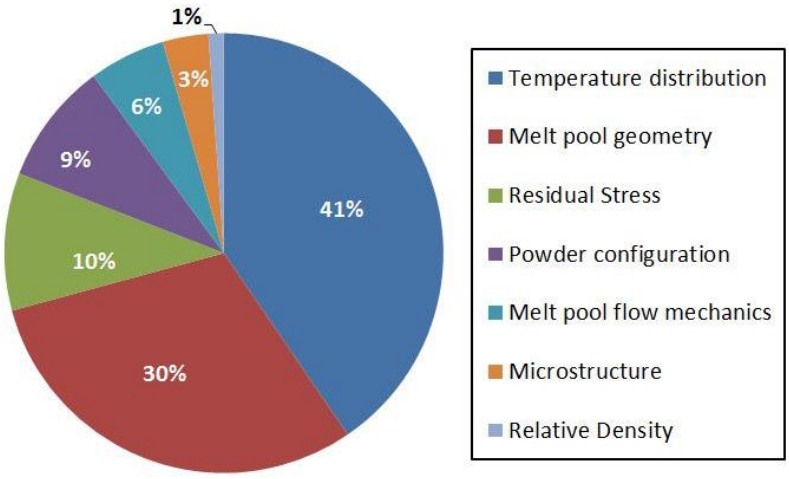

Figure 6.1: Number of occurrences of SLM Phenomenon in the reviewed past literature (Olivier *et al.*, 2017).

6.3 Analysis Techniques

Researchers use various numerical modeling techniques depending on the SLM phenomenon under investigation. The observed analysis techniques in the reviewed literature include finite element analysis, computational fluid dynamics, the discrete element methods and a technique known as cellular automata finite element (CAFE). The occurrences of the publications implementing each of the different analysis techniques for their SLM numerical models are shown in the summary of the quantitative review in Figure 6.2.

6.3.1 Finite Element Analysis

The finite element analysis (FEA), also known as the finite element method (FEM) is a numerical technique used to find approximate solutions to field problems (i.e. stress, displacement, heat transfer, etc.). The term field refers to a domain of interest, such as a physical structure. The FEA technique works on the principle of dividing a domain in to discrete units known as finite elements (Cook *et al.*, 2002). The elements have distinct shapes such as 2-dimensional triangles, quadrilaterals, 3- dimensional tetrahedral wedges and bricks (Dantzig & Rappaz, 2016). The specific arrangement of the elements is called a mesh. Each of the elements in the mesh contains a subset of equations to the original problem, which is solved at the connecting nodes. The systematic solution of each of the unknown nodal values, recombine into the global system of equations in order to supply a final spatial distribution of the original field problem (i.e. temperature) (Maidana, 2014). The FEA is commonly used to simulate the residual stress and temperature distributions in SLM layers and components. The analysis technique occurred most often in the reviewed literature and is also used in combination with fluid analysis in some of the publications as seen in Figure 6.2.

6.3.2 Computational Fluid Dynamics

The main application of the computational fluid dynamics (CFD) technique is to investigate the mechanics of fluids (Bhaskaran & Collins, 2002). The finite volume method (FVM) is the preferred method used in CFD. The FVM is a numerical method, which transforms partial differential equations of the conservation laws (mass, momentum and energy) over differential volumes into discrete algebraic equations of the finite volumes (elements). The characteristics of the FVM have made it possible to use om numerical models of a variety of applications involving fluid flow, heat and mass transfer (Moukalled, Mangani & Darwish, 2015). The CFD technique is used to predict the flow mechanics in the melt pools formed during the laser-powder interaction. The technique has been used in combination with the FEA and particle analysis methods (Gürtler *et al.*, 2013), (Lee & Zhang, 2015).

6.3.3 Discrete Element Method

The discrete element method (DEM) is a numerical modeling approach developed in order to approximate particle material behaviour (Luding, Lätzel & Herrmann, 2001). The method incorporates various aspects such as interaction laws between individual particles and particle properties, which are used in order to predict the behaviour of the bulk medium. Computational time increases with the amount of particles, however, advances in computing power and more effective numerical algorithms have enabled numerical simulations of millions of particles on a single processor (Govender *et* al., 2017). Past SLM models have implemented the DEM in order to investigate the effects of particle size and placement on the density and surface quality of laser processed components. As mentioned previously. The DEM has been used in combination with other analysis techniques such as CFD.

6.3.4 CAFE Method

The cellular automata finite element (CAFE) method can be used to simulate and predict the microstructure evolution during the metal solidification stage in laser based additive manufacturing processes (Zhang *et al*., 2013). The finite element calculation of the thermal fields is coupled with the a cellular automata grain growth model in order to predict dendritic grain growth during melt pool solidification (Panwisawas *et al.*, 2017a). Only two researchers in the reviewed literature used this novel simulation technique for their SLM microstructure evolution predictions. These numerical models are primarily 2D simulations, which yielded good correlations with the experimental results.

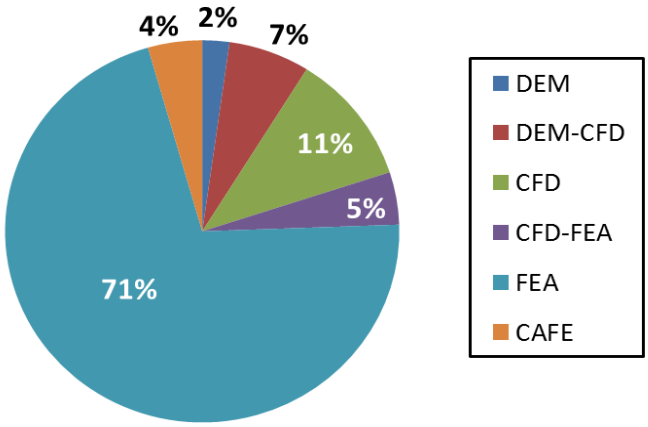

Figure 6.2: Share of analysis techniques in past research (Olivier *et al.*, 2017).

6.4 Simulation Scales

Due to the multi-physical nature of SLM processing, certain phenomena can only be studied on small scales, whereas other phenomena affect the entire component and need to be evaluated over the bulk material. Hence, SLM numerical models vary in simulation scales.

PBF simulations have been defined by various past researchers in literature (Sames *et al.*, 2016), (Lee & Zhang, 2015), (Li *et al.*, 2016). This study uses the scale definition as defined by Sames *et al*. (2016). However, there have been various models, which incorporate multi-physics and hence simulate the phenomena using multiple scales. The multi-scales identified in the reviewed literature are distinguished as being either micro-meso, meso-macro or micro-meso-macro. A graphical representation along with examples of multi-scale simulations is displayed in Figure 6.3.

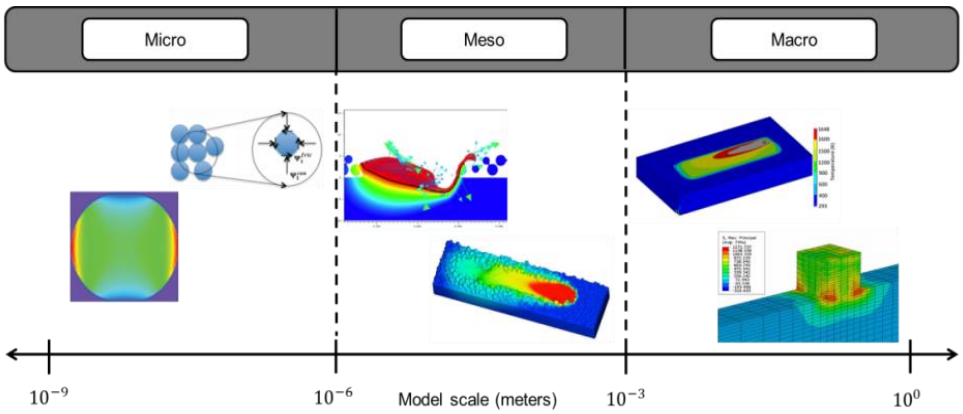

Figure 6.3: SLM simulation scale categories (Olivier *et al.*, 2017).

The definition and application of each of the simulation scales are provided below. The summary of the occurrences of the simulation scales used by the reviewed literature is provided in Figure 6.4.

6.4.1 Micro-Scale (10^{-9}-10^{-6} m)

These models focus primarily on the physics and phenomenon surrounding the individual particles. It assigns the properties of the intrinsic bulk material to single particles. Heat transfer principles are then applied to the individual particles in order to predict the particles' reaction to changes in environmental conditions. The physics of the single particles can be extrapolated and applied to continuum simulations (Sames *et al.*, 2016).

6.4.2 Micro-Meso Scale

These models combine particle level physics with the fluid principles of the melt pool (Gürtler *et al.*, 2014). Hence, these simulations predict the laser-powder interaction with much greater detail.

6.4.3 Meso-Scale (10^{-6}-10^{-3} m)

These models are used to predict the continuum melting and solidification dynamics. The models are based on continuum mass, momentum and energy conservation equations. The continuum properties rely on the weighted volumetric fractions of the powder phase constituents (Gürtler *et al.*, 2014).

6.4.4 Meso-Macro Scale

An example of such a scale would be a numerical model, which firstly simulates the melt pool geometry and extrapolates it to a multiple track simulation in order to see the effect of the geometry during large scale processing.

6.4.5 Macro-Scale (10^{-3}-10^{0} m)

These models include thermo-mechanical simulations, which are used to evaluate the effect parameter changes has on certain phenomena such as residual stress and temperature distributions within continuous powder layers in the global model (Li, Fu, *et al.*, 2016). The continuous nature of the material requires homogenised properties such as the effective beam absorptivity, thermal conductivity, specific heat, laser penetration depth, etc. (Sames *et al.*, 2016).

6.4.6 Micro-Meso-Macro-Scale

These models aim to replicate all the physical phenomena occurring during the SLM simulation process. This theoretical case was not identified in the publications in the review. This fully multiscale process would include aspects concerning the powder configuration (size, shape and distribution), melt pool characteristics and flow dynamics, residual stresses and temperature distribution through all layers of the components.

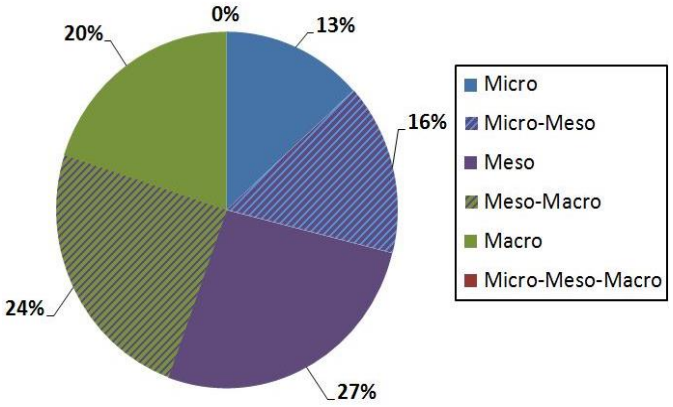

Figure 6.4: The distribution of the simulation scales in reviewed literature (Olivier *et al.*, 2017).

6.5 Simulation Software

Another important aspect of the numerical models documented in the quantitative review is the various numerical software used to perform the SLM simulations. Most software packages specialise primarily on a specific analysis field, whereas others have the ability to simulate multi-physics phenomena. Simulation software differ from each other in a variety of areas such as mesh setups, material setup methods, post processing etc. (Zeng *et al.*, 2014). It may be found that researchers simulate the same SLM phenomena with similar processing parameters and material properties, however they yield different results using different software packages.

The most commonly used simulation packages identified in the review include ANSYS®, ABAQUS® and COMSOL Multiphysics®. These packages predominantly use the FEA technique to predict phenomena such as temperature distribution, residual stresses and melt pool geometry during SLM processing. The number of occurrences of these software packages corresponds to the large share of publications using the FEA to simulate SLM phenomena. Other software packages identified in literature using the FEA technique include MSC Marc®, Cubes Diablo® and SYSWELD®.

The reviewed literature, which investigate phenomenon such as melt pool flow principles and particle configuration mainly use packages based on the CFD technique. These include OpenFOAM®, Flow-3D® and FLUENT®, with OpenFOAM® being the most common. The summary of the occurrences of each of the identified software packages found in the reviewed literature is shown in Figure 6.5.

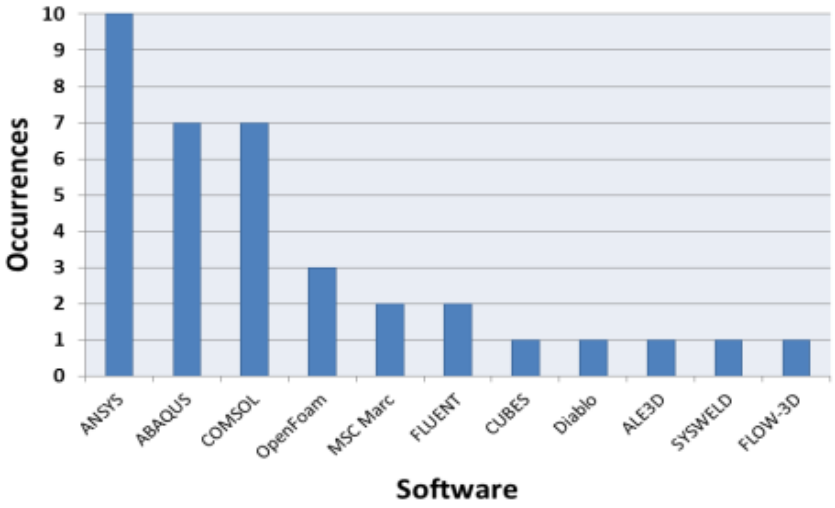

Figure 6.5: Numerical modeling software packages used for past SLM simulations (Olivier *et al.*, 2017).

6.6 Physical Model

SLM numerical models have evolved as the computational capabilities of processing systems have improved over time. The first SLM simulations focused primarily on predicting phenomenon in two-dimensions (2D). However, these models gradually incorporated more complex SLM phenomena, which resulted in the expansion of the simulations in the three-dimensional (3D) space. The final goal of PBF numerical simulations is to replicate the additive manufacturing process of full 3D models, including all complex geometrical features.

Currently, SLM models vary in geometrical complexity. The models reviewed in past literature are characterised according to their dimensional complexity and the amount of tracks and layers present. In the quantitative review, each numerical model was characterised according to the geometry categories in Figure 6.6.

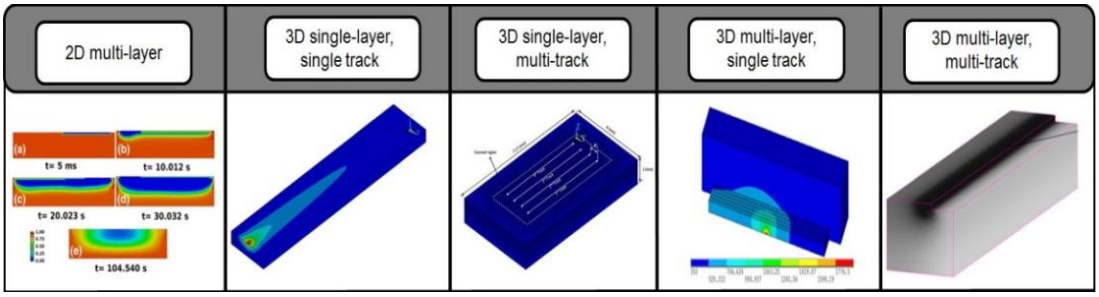

Figure 6.6: Model geometrical complexity observed in reviewed literature (Olivier *et al.*, 2017).

A brief description of each of the geometry classifications is given below and the occurrences of each geometry in past literature is shown in Figure 6.7.

6.6.1 2D Multi-Layer

2D multi-layer numerical models provide a cross-sectional view of the SLM build process. Not many of these models were identified in the reviewed literature, with only 13% of researchers using this setup. This low distribution may be due to the advances in computational processing, which has made it easier to simulate more complex 3D models. The 2D models reviewed were constructed using novel simulation aspects, such as difficult to predict phenomenon or new computational methods (CAFE).

6.6.2 3D Single Layer, Single Track

Although this is the most basic of the three-dimensional setups, single layer, single track numerical models include great detail on the melt pool characteristics and flow dynamics. These were the most common model identified in FEA and CFD simulations, occurring in 35% of the reviewed literature.

6.6.3 3D Single Layer, Multi-Track

Single track, multi-layer models provide insight to the developed thermal history between tracks of a single powder layer caused by the variation in SLM process parameters. Results from these models are useful when considering increasing the hatch spacing while still achieving consolidation between the scan tracks.

6.6.4 3D Multi-Layer, Single-Track

Multi-layer, single layer models are used to provide insight to the developed thermal history between the multiple layers of a single scanned track caused by the variation of SLM process parameters. Multi-layer simulations are used, for example to determine the layer thickness required for adequate inter-layer bonding. This was the least common model setup identified in the reviewed literature with a distribution of only 7% in the reviewed literature.

6.6.5 3D Multi-Layer, Multi-Track

This is the most complex of the geometrical model setups. It incorporates multiple layers and tracks in order to simulate true full scale processing. These simulations require great effort to set up and are computationally expensive, however the results can be used to predict a variety of phenomena. Only 18% of models in the reviewed literature used this particular setup. Most of the simulations featured only basic rectangular shaped models, with the exception of Kundakcioglu (2016), who produced a fully 3D, complex geometrical model.

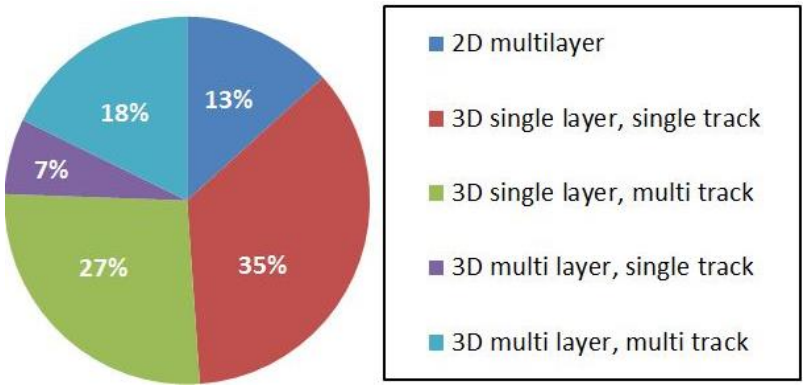

Figure 6.7: Distribution of each of the physical model geometries in the reviewed literature (Olivier *et al.*, 2017).

6.7 Chapter Reverence Towards Research

The chapter provided a detailed background overview of the current focus areas within the laser fusion additive manufacturing research field. This study showed that the type of phenomena under investigation strongly influences the selection of numerical technique, software, simulation scale and model complexity. It also highlighted certain gaps and challenges in current research. The results from this chapter are used to motivate decisions made elsewhere in this study.

Chapter 7: Research and Experimental Methodology

Overview

The chapter utilises the literature study performed in the previous chapters and structures the information in such a way that the requirements needed to meet the original project objectives become clear. A project path is created, which makes it easier to see what information is needed for each part of the planned experimental section and how the information will assist meeting the end goal. This chapter can be used as a guideline for the following sections as most of the experimental study is developed here.

7.1 Research Methodology Breakdown

The research methodology can be broken down in smaller sections by using the problem statement. It is clear from the problem statement that there are three main areas to consider for the research study. These include:

1. Improving the R&D Process Efficiency of the SLS manufacturing industry

2. Using simulation to model heat transfer during laser processing of WC-Co

3. Validating the simulation with experimental WC-Co builds

The important aspects to consider in each of these areas are investigated in greater detail by using information gathered during the literature study.

7.1.1 Improving the R&D Process Efficiency of the SLS Manufacturing Industry

The current R&D process chain of the SLS industry in shown in Figure 7.1. Each of the previous chapters have provided detailed background information on all relevant sections of this process chain. They have also motivated the necessity of improving the efficiency of the current method of performing the material calibration tests. It has been decided to use a numerical thermal model to predict the feasible material processing parameters to process WC-Co. The results may

1. Show a *good* correlation between the numerical model and the experimental results. In this case, it would be suggested that numerical modeling replace current calibration methods.

2. Show a *moderate* correlation between the numerical model and the experimental results. In this case, it would be suggested that numerical modeling reduce the extent of current calibration methods. However, results are still required to be validated.

3. Show *no* correlation between the numerical model and the experimental results. In this case, it would be suggested that numerical modeling should not replace current calibration methods.

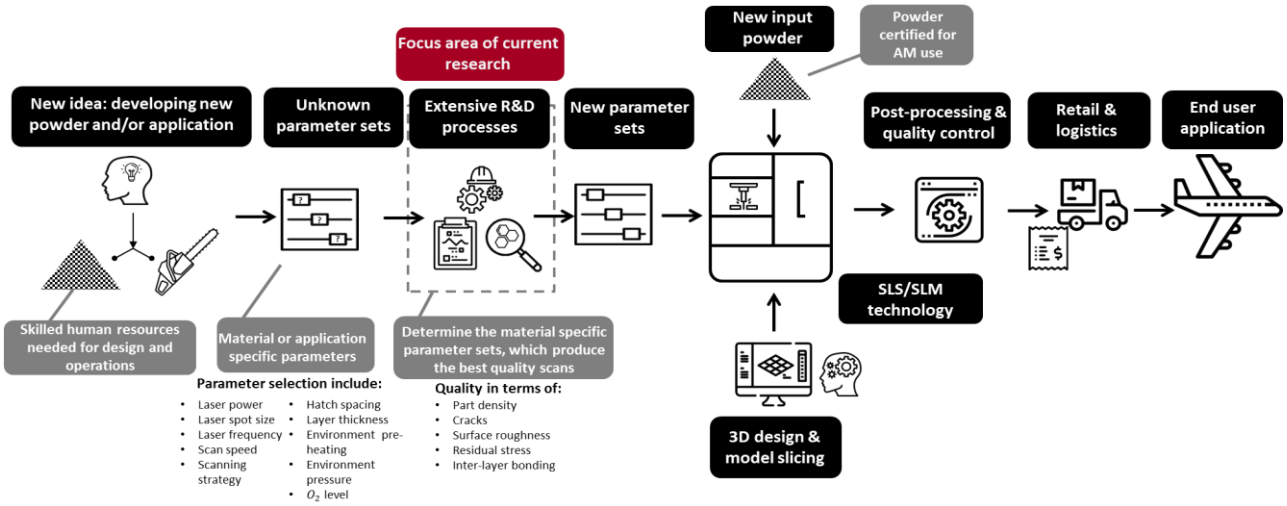

Figure 7.1: Current R&D process chain of the SLS industry (Olivier, 2018).

7.2 Experimental Methodology

This study focuses on developing an alternative method to test the process parameters of SLS processing materials. Rather than performing traditional calibration tests, the research aims to develop an effective numerical model, which can simulate SLS processing. The experimental section can be divided into two sections, namely one simulating the SLS process and the other validating the results with experimental tests. The experimental section of this research study is explained in the flow chart in Figure 7.2.

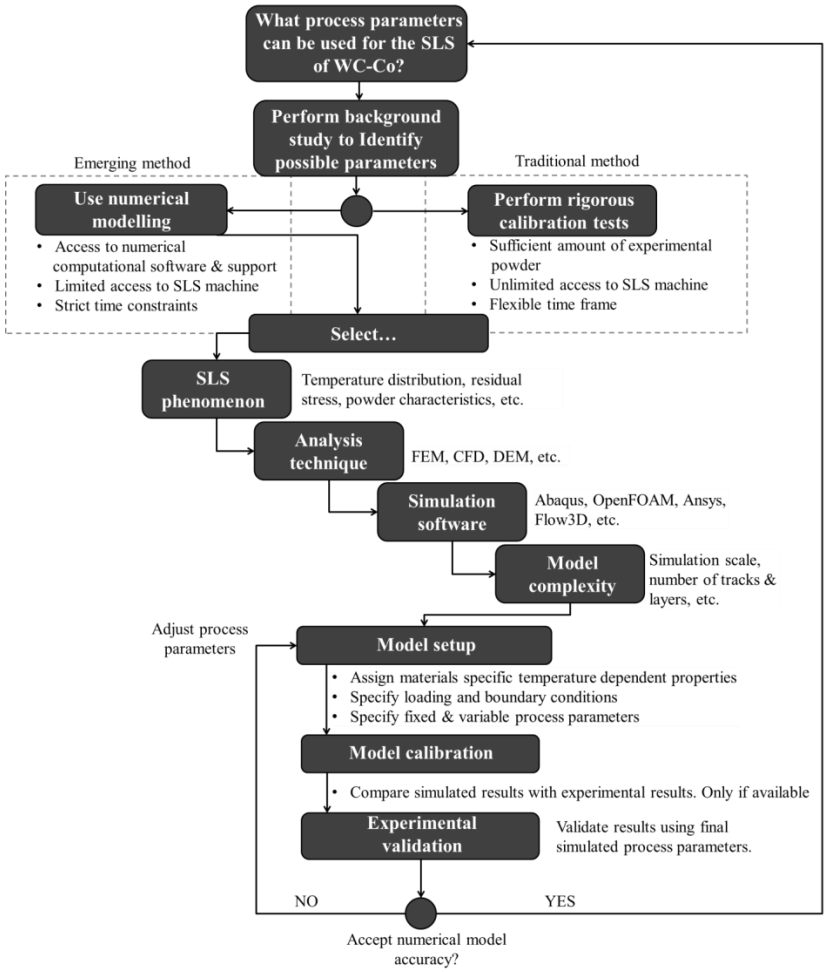

Figure 7.2: Flow chart explaining the methodology used for the research study (Olivier, 2018).

7.2.1 Simulating Laser Processing

SLS is a complex multi-phenomena, multi-scale process. Ideally, all the variables influencing laser processing of powdered materials should be included in the simulation in order to produce an accurate representation of the SLS process. However, such a simulation is extremely difficult to construct, as it requires a combination of numerical methods, which becomes computationally challenging. Due to the complexity of simulating this multi-phenomena process, past researchers have included certain limitations to their numerical models. Different modeling approaches lead to variations in results, even when investigating the same phenomenon with consistent material properties and process parameters. It is therefore critical to state exactly what assumptions and considerations were made in order to produce the model. The basic steps and considerations of setting up a numerical model are given in Figure 7.3.

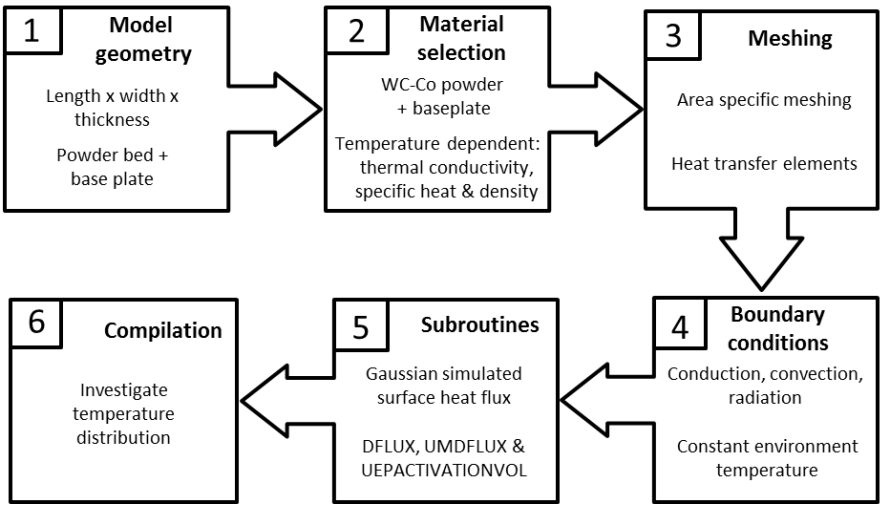

Figure 7.3: Basic simulation steps (Olivier, 2018).

Limitations and considerations

Although assumptions and limitations reduce the accuracy of numerical models in comparison to experimental samples, the results are still useful as they provide insight to processes, which cannot be studied from direct measurements. SLS phenomena such as temperature distribution and melt pool flow dynamics are difficult, if not impossible, to study without the use of numerical methods. The following section lists the considerations and limitations made in the study.

The numerical model used in this study is based on previous models of past literature. The more characteristics the designer includes in the model, the more complex the simulation will become. The characteristics of these models are described in Chapter 6.

A *single track, single layer* simulation will be performed. The model will consist out of two sections, namely a top powder layer and a bottom base substrate (base plate). The sections will be assigned with their respective material properties in order to predict the temperature distribution. A laser profile script will allow the input heat flux to resemble that of the actual laser. *Laser power* and *scanning speed* have been selected as the two variables of the simulation process. All other process parameters will be kept constant.

Table 7.1 lists the simulation characteristics observed from past SLS/SLM numerical models. A green check mark signifies the characteristic will be included in the developed mode, whereas a red cross indicates that it will not feature in the simulation.

Table 7.1: Numerical model design considerations.

Simulation Software		Numerical methods		Simulation Scale		Phenomenon		Physical Model	
ABAQUS	✓	Finite Element Analysis (FEA)	✓	Micro	×	Temperature distribution	✓	2D multi-layer	×
ANSYS	×	Computational Fluid Dynamics (CFD)	×	Micro-meso	×	Melt pool geometry	✓	3D single layer, single track	✓
COMSOL Multi-physics	×	Discrete Element Methods (DEM)	×	Meso	×	Residual stress	×	3D single layer, multi-track	×
OpenFoam	×	Cellular Automata Finite Element Method (CAFE)	×	Meso-macro	✓	Powder configuration	×	3D multi-layer, multi-track	×
MSC Marc	×			Macro	×	Melt pool flow dynamics	×		
FLUENT	×			Micro-meso-macro	×	Micro-structure	×		
						Relative density	×		

Design of Experiments: Parameter sets

An initial parameter screening estimation is performed during the simulation step in order to reduce the broad range of possible parameters. The selection will be based on the resulting maximum temperature (response) caused by a variation of the laser power and scanning speed (factors) in the simulated environment. The parameters will be varied in three levels, namely, high, medium and low. This is known as a 2x3 factorial experiment. The parameter levels selected for the screening simulation will be based on the SLS machine capabilities as well as experimental results from previous researchers using similar materials. An example of this simulated parameter screening technique is shown in Figure 7.4. This technique is similar to that suggested by Yadroitsev *et al.*, (2015), where the region containing the feasible material specific parameter set is found by determining the maximum model temperature at various parameter sets. The parameter selection process will be discussed in greater detail in the following section.

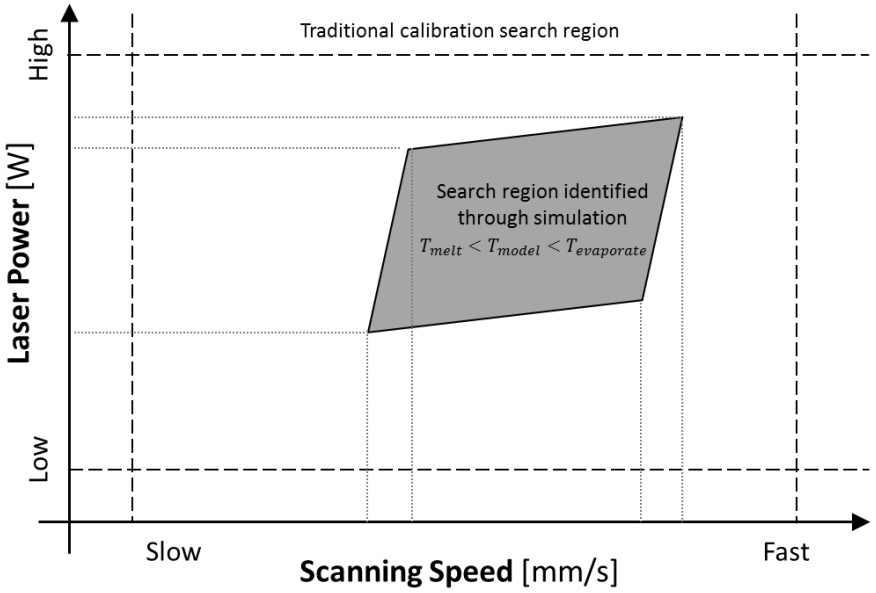

Figure 7.4: Simulation can be used to reduce the parameter screening region tested with traditional methods (Olivier, 2018).

7.2.2 Experimental Validation

The only method to determine whether the numerical model is a useful addition to the calibration step is by comparing the simulated model results to experimental builds. These builds will be produced using the same input parameters identified during the simulation step. If there is a good correlation between the simulated and experimental results, it will indicate that numerical modeling may be a feasible tool to aid in the material calibration process. Currently there are three institutions in South Africa with laser fusion machines, which are able to provide support for R&D purposes. These machines are listed in Table 7.2.

Table 7.2: Laser fusion machines in South Africa.

Institution	Machine
Stellenbosch Technology Centre (STC), University of Stellenbosch (US)	M2 LaserCusing
Centre for Rapid Prototyping and Manufacturing (CRPM), Central University of Technology (CUT)	EOSINT M280
Metal Heart	SLM Solutions

The experimental builds will use the same geometry as modelled in the simulation. It will consist of a rectangular base plate with a single layer of powdered WC-Co spread uniformly over its surface. The laser will perform a single pass scan of the top layer, thereby sintering a single track in the powder. The excess unprocessed powder will be removed, leaving behind the solid single track WC-Co structure on the base plate. The schematics displayed in Figure 7.5 provide a good introduction to the terminology used when describing the different features of single- and multiple track SLS scans. A schematic of the experimental process is shown in Figure 7.6.

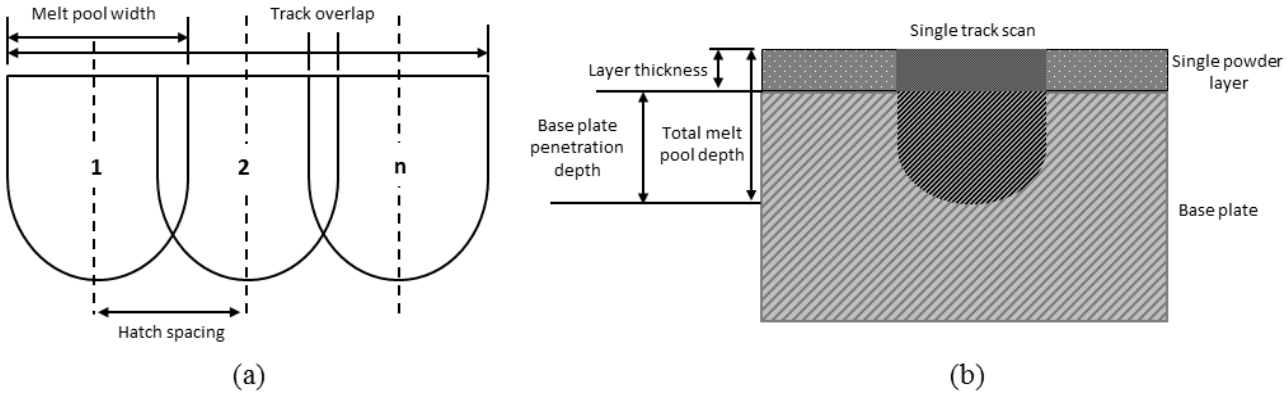

Figure 7.5: Scan track terminology diagram. (a) The scan track width and (b) depth are important geometrical features to understand in the SLS industry (Olivier, 2018).

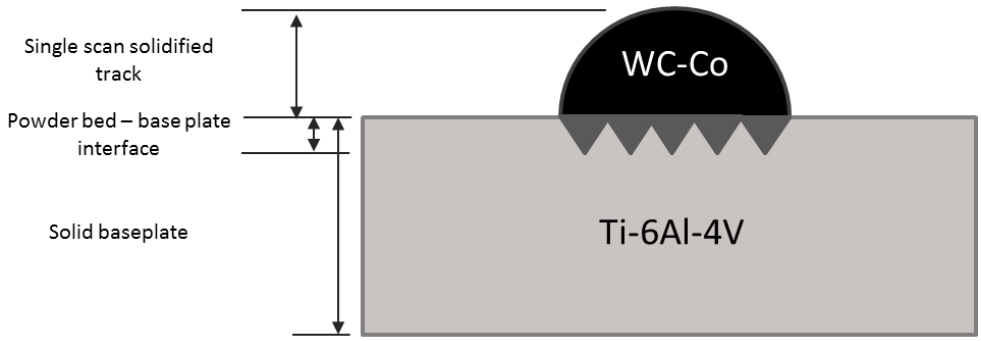

Figure 7.6: Schematic of the expected samples produced for the experimental validation (Olivier, 2018).

Base substrates

Two different materials will be used for the building platform, known as the base substrate or base plate. As mentioned previously, the base plate provides a solid, flat foundation for the initial scan track to be laid onto. In this study, a maraging tool steel (European 1.207) and a titanium alloy (Ti-6Al-4V) were selected for the base substrates. These are two completely different alloy metals, each with a unique set of material properties. The motivation behind using two different base substrate materials lies with the fact that it provides additional validation to the numerical model, if the results agree when using a variety of material properties.

Once the SLS samples have been produced, the next step is to investigate the experimental results in order to compare them to the predicted simulated outcome. In order to investigate the quality of the single track scans, the characteristics of the samples need to be determine analytically. A series of techniques can be used to investigate certain characteristics of the processed samples. Firstly, the sample needs to be prepped for microscopic analysis. A clean and even surface is needed for this analysis. Hence, the sample will be sectioned using wire-cutting techniques. The samples will be cleaned and mounted in resin in order to make them more manageable. Grinding, polishing and etching will allow sample measurements to be performed using optical microscopy. Table 7.3 lists the investigated characteristics of the samples as well as the corresponding techniques used to investigate the characteristics.

Table 7.3: Experimental characteristic analysis and techniques.

Characteristic	Technique	Institute
Geometry	SEM	CAF US
Composition analysis	EDX	CAF US
Porosity	Optical Microscopy	US

Chapter 8: Simulation Model and Design

Chapter Overview

Simulation is defined as the imitation of the operation of a real-world system or processes over time. Simulation offers great potential for improving processes, perfecting products, minimising environmental impacts, reducing product realisation costs and improving design-to-manufacturing cycle time. All numerical modeling methods are sensitive to the input data quality. This chapter outlines the steps taken to perform a simulation combining SLS and WC-Co. The simulation will then be validated using experimental results.

8.1 Software Setup

Abaqus/CAE 2017 was selected as the numerical software to perform the analysis. It is a finite element analysis software application used for both modeling, analysis and visualisation of mechanical components, assemblies and structures. Abaqus/CAE 2017 has a wide range of multiphysics modeling capabilities such as full structural loads, dynamic vibration, multibody systems, impact crash, nonlinear static, thermal coupling, etc. Abaqus/CAE 2017 is used in applications for the automotive, aerospace and industrial product industries. (Dassault Systems, 2016)

The decision to use this software package was based on the following reasons:

1. An Abaqus/CAE 2017 licence was freely available to the researcher through the university with the activation of the subroutine package being the only additional expense.

2. Software support was available to the student in the form of skilled researchers based at the university, as well as external support from a software support and retail company (FEAS), located approximately 50 km from the university.

3. It was found to be the second most widely used software application used to simulate the SLS/SLM process (Olivier *et al.*, 2017), as shown in Figure 6.5.

8.2 Numerical Model

The SLS process was simulated using an implicit uncoupled thermal heat transfer analysis.

8.2.1 Physical Model Setup

In order to reduce the required computational power required to solve the developed thermal fields, the model geometry was limited to a simple rectangular solid. The rectangle consisted out of two sections, namely the powder layer and the base substrate (). The base substrate material varied from that of the powder layer. In this case two materials were selected, namely tool steel and a titanium alloy (Ti-6Al-4V), primarily to test the rigidity of the simulation experiment but also due to the potential for future coating applications. Although the powder layer can be varied, however it was fixed for this study according to the specifics given by the CRPM research facility. The dimensions of the base substrate was specifically selected in order to reduce the computational time, while still allowing the thermal fields to fully develop during processing. In this study the base substrate size was chosen to be 500 x 600 x1000 µm (h x w x l). A sketch of the numerical model geometry is shown in Figure 8.1.

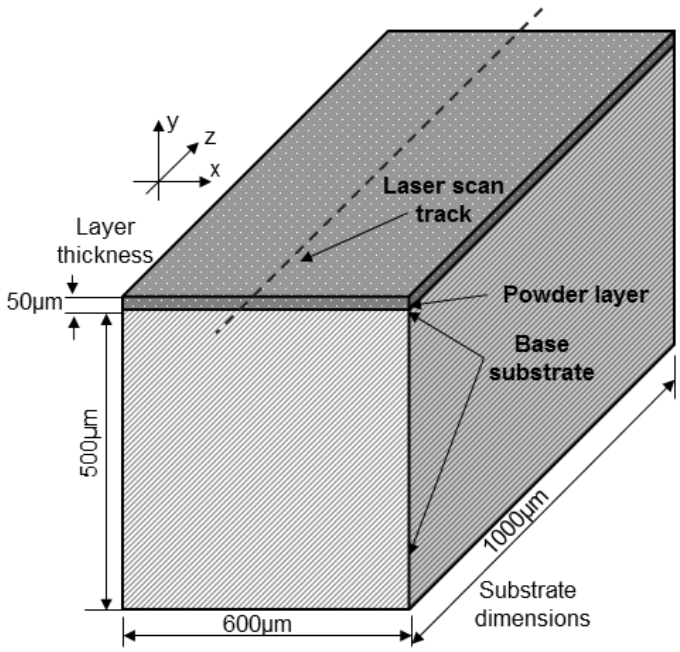

Figure 8.1: The geometry and material allocation used for the numerical model (Olivier, 2018).

8.2.2 Material Properties

The material properties are critically important to the accuracy of the results. The main aspect contributing to the thermal fields is the unique material properties of the powdered material. During the material assignment step in the Abaqus software both the powder layer and base substrate were assigned with material properties, which vary with changes in temperature. Such material properties are known as temperature dependent material properties. The temperature dependent properties taken into consideration in this study included the thermal conductivity, *k*, and specific heat capacity, c_p. The temperature dependent material properties of the WC-Co powder layer were calculated using the formulations as specified by Xiong *et al.*, (2009) and are shown in Equations 8.1 and 8.2. The temperature dependent property data provided by Xiong *et al.*, (2009) in literature is shown in the adapted graphs in Figure 8.2 and Figure 8.3.

WC-Co powder layer

The thermal conductivity (k) adjustment equation for the WC-12Co binder content.

$$\boldsymbol{k}_{WC-Co} = g_{WC}\boldsymbol{k}_{WC} + g_{Co}\boldsymbol{k}_{Co} \qquad \left[\frac{W}{m\,K}\right] \tag{8.1}$$

The specific heat (c) adjustment equation for the WC-12Co content.

$$\boldsymbol{c}_{WC-Co} = f_{WC}\boldsymbol{c}_{WC} + f_{Co}\boldsymbol{c}_{Co} \qquad \left[\frac{J}{kg\,K}\right] \tag{8.2}$$

Where g_i and f_i are the weight percentages of the powder constituents.

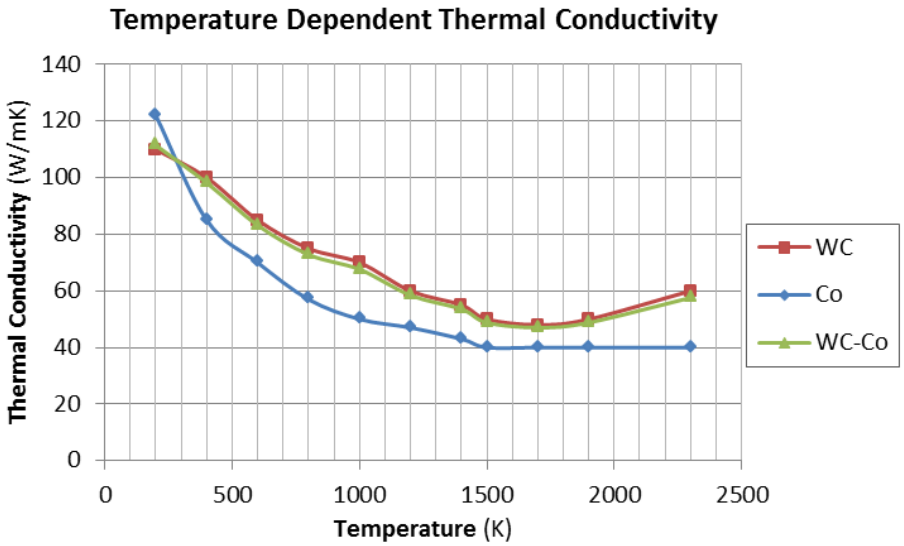

Figure 8.2: Temperature dependent thermal conductivity of WC-12Co, adapted from Xiong et al. (2009)

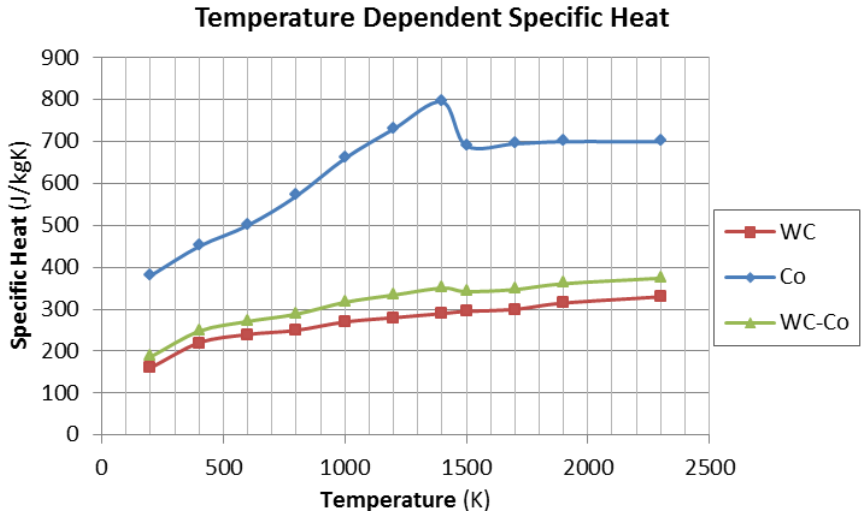

Figure 8.3: Temperature dependent specific heat of WC-12Co, adapted from Xiong et al. (2009)

Another important consideration in the material assignment step was the powder to solid transformation during processing. Laser sintering actually involves three phases during processing, namely the powder phase, liquid phase and the solid phase. However, the liquid phase was assumed to be too rapid to be considered for heat transfer in the model. Hence in this study only two phases, namely the powder and solid phase, were considered for heat transfer. Owing to presence of trapped air between the powder particles, the thermal conductivity, *k*, of the powdered material is about 1% to that of the solid material (Foroozmehr *et al.*, 2016). As shown in the following equation.

$$k_{powder} = \begin{cases} 0.01\ k_{solid,} & T < T_m \\ k_{solid,} & T \geq T_m \end{cases} \tag{8.3}$$

Whereas the heat capacity of metal powder is almost equal to the heat capacity of the solid phase (Foroozmehr *et al.*, 2016). The adjusted values of the thermal conductivity for each phase is shown in Appendix D.

Tool steel

A tool steel known as maraging steel DIN1.2709 was selected as a base substrate. It is used in a variety of industry applications such as injection moulding, die casting, and punching and extrusions of light metal alloys. This type of tool steel is characterised by having good mechanical properties and being easily heat-treatable using thermal age hardening processes to obtain excellent strength and hardness features. The temperature dependent thermal properties, which were included numerical model, are listed in Table 8.1.

Table 8.1: Temperature dependent thermal properties of tool steel. (Mondal, Biswas & Bag, 2015)

Temperature [°C]	Thermal conductivity [W / m K]	Specific heat [J / kg K]
100	51.1	499.2
300	46.1	565.5
450	41.1	630.5
550	37.5	705.5
600	35.6	773.3
720	30.6	1080.4
800	26.0	931.0
1450	29.5	437.9

Ti-6Al-4V base plate

As the base substrate is made from a solid Ti-6Al-4V, phase change is not considered. However, temperature dependent material properties are still needed for the solid phase. The temperature dependent properties of Ti-6Al-4V is shown in the graph below as specified in literature (Cheng & Chou, 2015). Tabulated values corresponding to specific temperature values can be found in Appendix D.

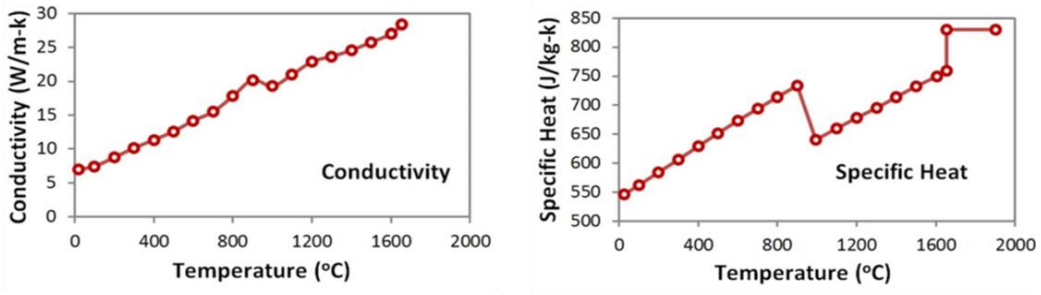

Figure 8.4: Temperature dependent properties of the Ti-6Al-4V base substrate. Temperature dependent thermal conductivity and (b) temperature dependent specific heat capacity (Cheng & Chou, 2015).

8.2.3 Meshing

The mesh type used for the uncoupled thermal analysis is linear hexahedral DC3D8 (8-node brick element) with one degree of freedom at each node.

An efficient meshing strategy, requiring less computational power was used in the model. Meshing was performed using an iterative process in order to ensure the final mesh configuration would save on computational time, whilst still providing accurate results. Initially, a very coarse mesh was constructed, and, although it did not yield very accurate results, it was useful to the researcher to easily test the loading conditions. Once the analysis converged, the meshing could be refined.

The regions closest to the laser scan path were more finely meshed than the regions further away from the laser tracks. The 600 µm geometry was divided/partitioned into three sections, each with a width of 200 µm with the scan track located on top of the centre partition. The 50 µm powder layer required the finest mesh and was therefore meshed with 10x10x10 µm elements. The choice of this mesh was also motivated by the average particle size of 28 µm in diameter. The underlining substrate in the centre partition was divided into eight sections, each 50 µm thick directly beneath the powder layer. These 50µm partitions were subsequently divided into 10 µm elements. The regions further away were assigned a coarser mesh structure. The meshing strategy is shown in Figure 8.5 and Figure 8.6.

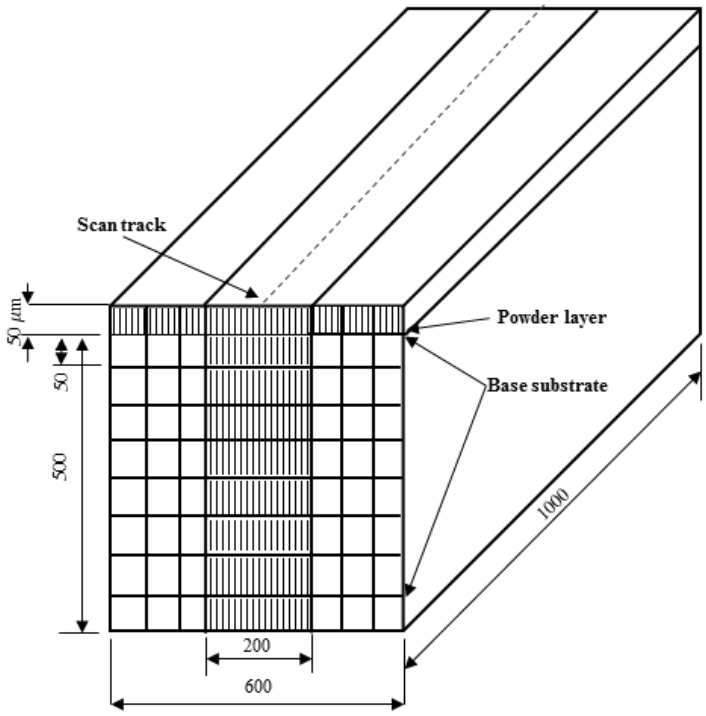

Figure 8.5: Schematic of the model meshing strategy (Olivier, 2018).

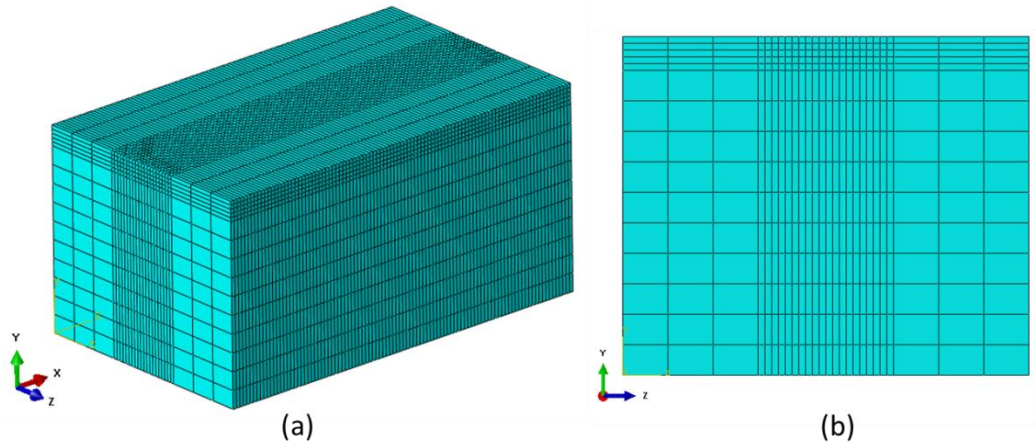

Figure 8.6: Meshing strategy in the (a) isometric and (b) front view (Olivier, 2018).

8.2.4 Loads and Boundary Conditions

Heating

The only input loading condition in the SLS thermal analysis was the heat flux caused by the scanning laser beam. It is important to specify the proper heat distribution since the accuracy of the simulation outcome is largely affected by the load condition. A user defined surface heat flux was specified on the top surface of the powder layer. The user defined heat flux was written in a separate subroutine with all information on the scan vectors, which is discussed in Section 8.2.6. The laser beam's surface heat flux was specified according to Goldak's double ellipsoidal intensity distribution, as per Equation 8.4 as discussed in Section 5.1.3. The values of the constant factors are listed in Table 8.2. These constants were selected based on the shape of the ellipsoidal melt pools reviewed in past literature (Foroozmehr *et al.*, 2016).

$$\dot{q}_{laser}(x,y,z,t) = \frac{6\sqrt{3}\eta P f_{f,r}}{abc\pi\sqrt{\pi}} exp\left(-\frac{3(x+v\cdot t)^2}{a_{f,r}} - \frac{3y^2}{b^2} - \frac{3z^2}{c^2}\right) \qquad \left[\frac{W}{m^3}\right] \tag{8.4}$$

The values for the factors describing the double ellipsoidal characteristics shown in Figure 8.7 is listed in Table 8.2.

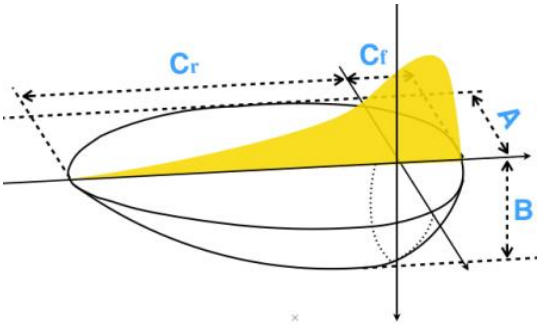

Figure 8.7: Goldak's double ellipsoidal volumetric energy distribution, adapted from (Esfahani, 2016).

Table 8.2: The constant values used for the factors in the double ellipsoidal equation.

Dimension	Corresponding axis	Value
a_f	X-axis (front)	0.00004
a_r	X-axis (rear)	0.0002
b	Y-axis	0.00004
c	Z-axis	0.0002
f_f	Factor (fraction of 2)	0.10
f_r	Factor (fraction of 2)	1.90

Cooling

Cooling was accounted for in terms of the boundary conditions applied to the model. Heat is transferred through top surface convection and radiation to the build chamber atmosphere and conduction through the powder layer to the base plate (Dong *et al.*, 2016). The simulation assumed that thermal conditions at the initial starting location of the scanning laser have stabilised, therefore no other heat sources affected the scan track. The environment in the build chamber was not pre-heated, therefore the initial temperature of the powder bed and base plate and the atmospheric heat sink will be at room temperature, which was selected to be 25℃. Constants used for the cooling boundary conditions are shown in Table 8.3. These values were fixed based the advice from experts at CUT.

Table 8.3: Constant values used for the boundary conditions.

Parameter	Value	Unit	Note
Initial build chamber temperature	25	℃	Value fixed by CUT
Heat transfer coefficient	25	W / m^2 K	As specified by Wang *et al.*, (2002)
Emissivity	0.8	-	As specified by Wang *et al.*, (2002)
Stefan-Boltzmann constant	5.67×10^{-8}	W / m^2 K^4	Radiation constant (Cengel & Ghajar, 2015)

8.2.5 Processing Parameters

Fixed parameters

The ability of SLS processing to change its processing parameters allows it to process a variety of materials. However, adjusting all available parameters for a new material can consume precious development time. Hence, some parameters were fixed from the start to limit the scope of the investigation. For this study most of the parameters, as listed in
Table 8.**4**, were fixed by the research institute, which provided the SLS technology. These parameters are also consistent with a parametric study performed by Yadroitsev, Bertrand and Smurov (2007).

Table 8.4: Fixed parameter values.

Parameter	Value	Unit	Note
Initial build chamber temperature	25	℃	Residual stress not a consideration for single track processing
Layer thickness	50	µm	Value fixed by CUT
Spot size (Dia.)	80	µm	Value fixed by CUT
Absorption coefficient	0.52		As specified by Wang *et al.*, (2002)

Variable parameters

Various parameters influence the final quality of SLS/SLM parts. The SLM280HL machine, for example, contains more than 150 parameter settings that can be changed. The most important process parameters that affect quality relate to the laser exposure to the powder, also known as the in-process parameters. These include laser power, P [W], scanning speed *v* [mm/s], layer thickness, *t* [µm], hatch spacing, *h* [µm] and scan strategy (Vrancken, 2016). These parameters can be used to formulate an equation to quantify the laser or energy density, E, which hits the surface of the powder bed (Kruth, Kumar & Van Vaerenbergh, 2005).

$$E = \frac{P}{v \cdot h \cdot t} \qquad \left[\frac{J}{mm^3}\right] \tag{8.5}$$

Laser power and scanning speed were selected as variable parameters in this study, as they are regarded as two of the most important parameters when it comes to porosity optimisation. The specific energy density can be used to quantify the energy density if the hatch spacing is not varied (Savalani, Hao & Harris, 2006). Hence, when the hatch spacing remains constant equation 8.5 can be simplified to:

$$E = \frac{P}{v \cdot t} \qquad \left[\frac{J}{mm^2}\right] \tag{8.6}$$

The experimental parameter screening process is seen as one of the most time- and cost inefficient processes of the SLM/SLS R&D process. One of the many advantages of numerical simulation is the ability to produce reasonably accurate results without much computational effort. The parameter screening was performed by systematically disqualifying areas, which were deemed improbable for laser sintering of WC-Co. If the maximum model temperature value lies below the melting temperature of the Co (1496 ℃) binder, continuous scan tracks will be impossible theoretically. On the other hand, if the model maximum temperature results in temperatures above evaporation temperature of the Co (2900 ℃) binder, the binder would boil away leading to irregular scan tracks. Hence, the ideal region would be parameters sets that yield temperature values between 1496 ℃ and 2900℃. This was described in an equation by Yadroitsev *et al.*, (2015) i.e.:

$$T_{melting} < T_{max} < T_{evaporation} \tag{8.7}$$

The simulated parameter screening that was performed in this project is shown in Figure 8.8. A low, medium, and high approach was used for the screening. The temperature responses at each of these values was then used to predict a response surface for all parameter set combinations between the set limits. The lower parameter set combinations were based on a study performed by Wang *et al.*, (2002), whereas the higher parameter set values were based on predictions from Panwisawas *et al.*, (2017). If no past literature is available, the physical machine limits are suggested, which can be found in Appendix L. The experimental parameter sets, shown in Figure 8.8, were entered into the numerical model in order to measure the predicted maximum temperature responses. The response at each parameter set sample is shown in Table 8.5.

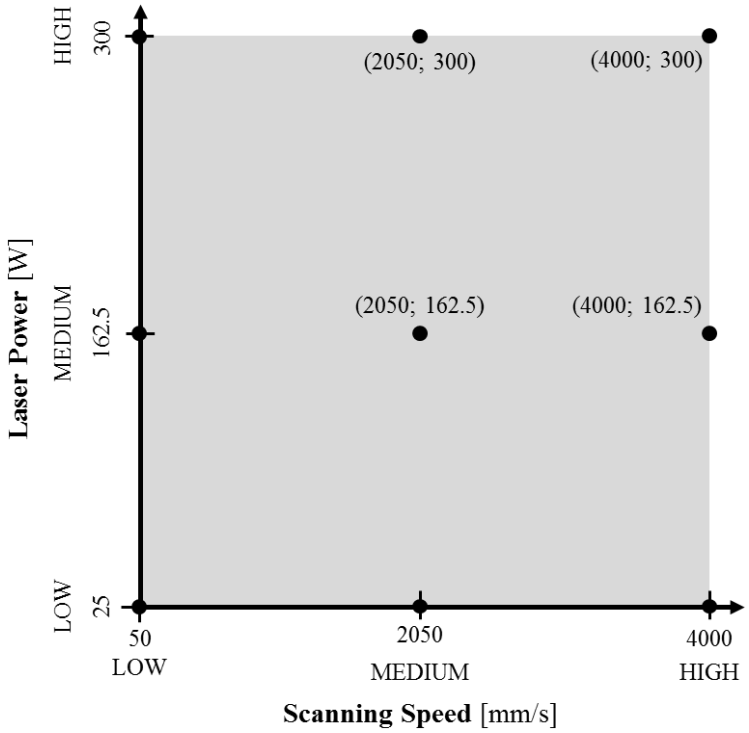

Figure 8.8: Simulated parameter screening procedure based on model maximum temperature results (Olivier, 2018).

The temperature responses were used to construct a response surface, which predicts the results from all parameter set possibilities within the set sample limits. The response surface was calculated using the Design Expert software. The results from this analysis is shown in Figure 8.9. It is clear from the 3D surface plot that there is a clear temperature slope angled such that the highest

temperature values are caused at the lowest scanning speed and highest laser power, whereas the highest scanning speed and lowest laser power results in the lowest maximum model temperature. The complete ANOVA analysis from this prediction is listed in Appendix B.

Table 8.5: Temperature responses from initial simulated parameter screening tests.

Region	Power	Scan Speed	Maximum Temp	Comments
LL*	25	50	1755	$T_{melt} < T_{max} < T_{evap}$
LM	25	2025	524.2	$T_{max} < T_{melt}$
LH	25	4000	370.6	$T_{max} < T_{melt}$
ML	162.5	50	6890	$T_{max} > T_{evap}$
MM	162.5	2025	1955	$T_{melt} < T_{max} < T_{evap}$
MH	162.5	4000	1586	$T_{melt} < T_{max} < T_{evap}$
HL	300	50	10830	$T_{max} > T_{evap}$
HM	300	2025	3171	$T_{max} > T_{evap}$
HH	300	4000	2387	$T_{melt} < T_{max} < T_{evap}$

*L=Low M=Medium H=High

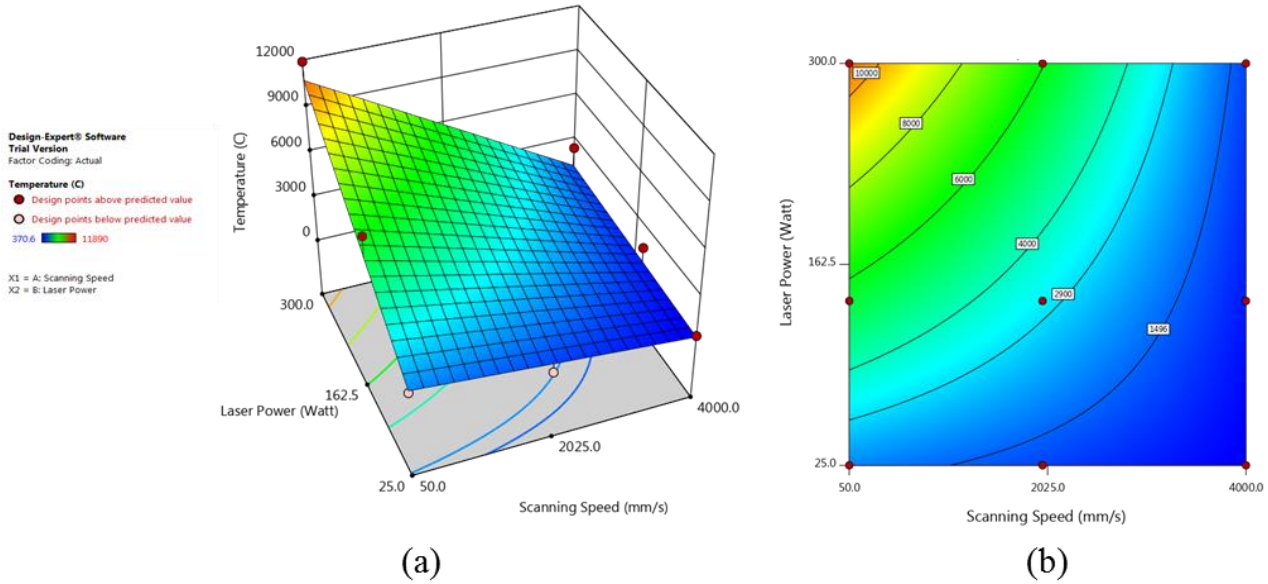

Figure 8.9: Surface response prediction represented by (a) a 3D and (b) a contour plot of the model maximum temperature values (Olivier, 2018).

Once the parameter screening was completed, the feasible region was examined and discussed. As it was difficult to test all values in the identified feasible region, it was decided to test the simulation against three main parameter sets. One at the lower end, one in the upper middle region at one at the higher limits. The parameter sets selected for this study was also advised by experts at the CRPM. However, some exceed the feasible region as seen in Figure 8.10. The details of the selected parameter sets are listed in Table 8.6. A validation of the feasible region can be based on a qualitative analysis of experimental results. Such an analysis is performed in Section 10.2.

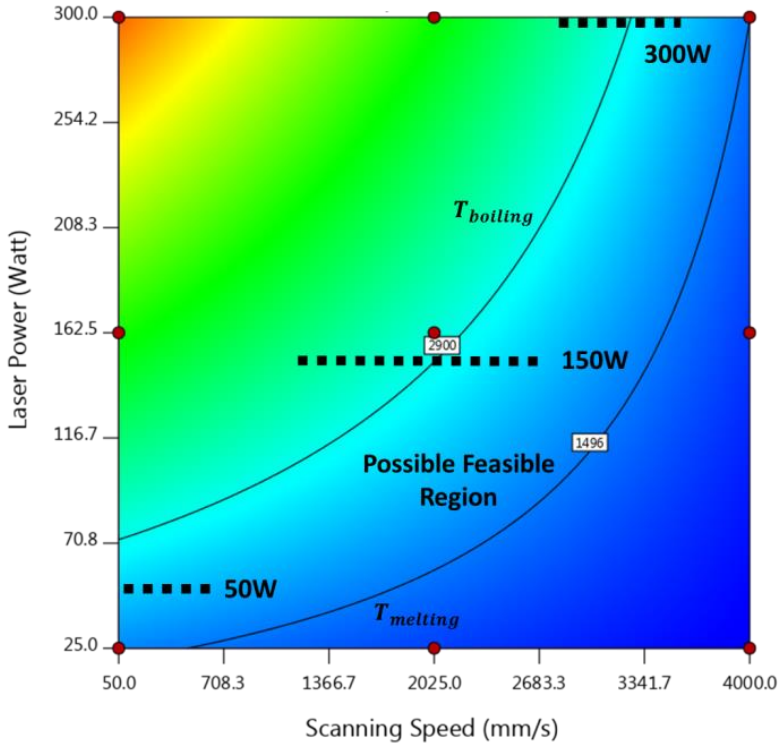

Figure 8.10: Variable parameter selection based on temperature response prediction and industry expert advice (Olivier, 2018).

Table 8.6: Variable parameters used in the numerical model.

Parameter Set	Laser Power [W]	Scanning Speed [mm/s]	Specific Energy Density* [J/mm²]
1	50	60	208.33
2	50	80	156.25
3	50	100	125.00
4	50	120	104.17
5	50	140	89.29
6	50	160	78.13
7	50	180	69.44
8	50	200	62.50
9	150	400	93.75
10	150	600	62.50
11	150	800	46.88
12	150	1000	37.50
13	150	1200	31.25
14	150	1400	26.79
15	150	1600	23.44
16	150	1800	20.83
17	300	1000	75.00
18	300	1200	62.50
19	300	1400	53.57
20	300	1600	46.88
21	300	1800	41.67
22	300	2000	37.50
23	300	2200	34.09
24	300	2400	31.25

*50μm layer thickness

8.2.6 Subroutine

The uncoupled thermal analysis calculates the heat transfer caused by the thermal loads of the moving laser beam. The DFLUX subroutine is a special user defined load condition for use with ABAQUS, which describes the energy distribution of the volumetric laser heat sources. The subroutine is written in the FORTRAN programming language and linked to the ABAQUS compiler. This unique code developed for specifically the simulation in this document can be found in Appendix E along with additional information on linking the DFLUX subroutine with ABAQUS.

8.2.7 Processing and Visualisation

The final model was submitted in the job step of the software. The analysis took approximately 65 minutes to produce a thermal field with one set of parameters. This was on a standard machine with 4 cores, running at 3.07 GHz with 12 GB of installed RAM. Increasing the processing power will significantly reduce the computational time of each simulation run.

Once the job had been completed, the results could be visualised. The thermal fields were displayed by selecting the field output to show the nodal temperature values, as shown in Figure 8.11. The animation tools allow the user to visualise the temperature field develop over time. Another powerful feature of the visualisation window is the ability to create sections in the model. An indication of the heat penetration depth can be obtained by sectioning the model in the z-plane. The scale bar displays the temperature values corresponding to each colour of the contour plot.

The contour options can be changed to change the colour of a contour range once it reaches a certain temperature limit. In this case the maximum temperature was set to the melting temperature of cobalt (1496 ℃). The melt pool characteristics can be displayed after changing this option.

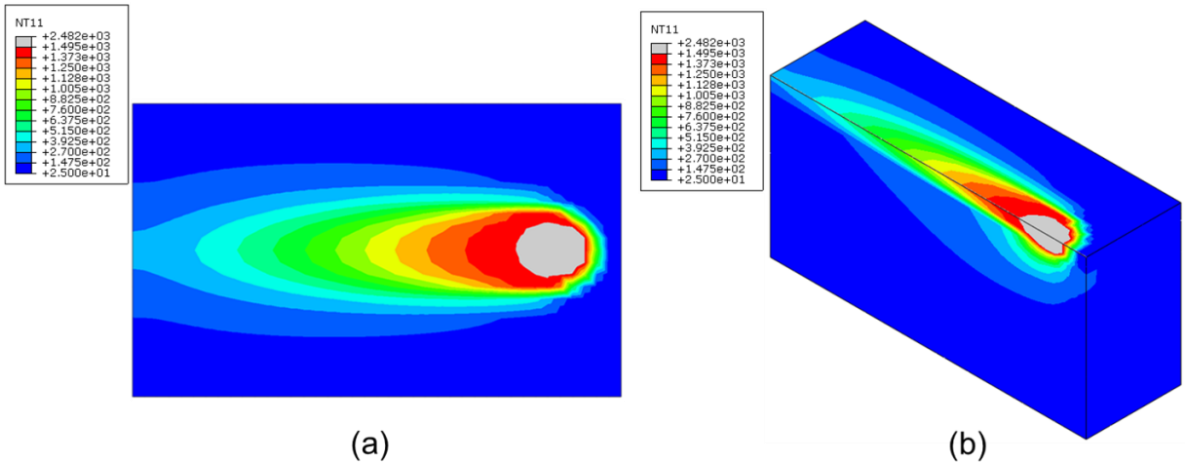

Figure 8.11: Model visualisation. (a) A top view and (b) a sectioned view of the developed thermal fields (Olivier, 2018).

8.2.8 Post Processing

If the model is free of any error messages and the thermal fields seem logical, the results can go through the post processing stage. In order to perform post processing, it is important to know what the original model objectives are. In this case, the processing parameters, which result in sintering, were of interest. Hence, a time-temperature plot would display whether the powder at an arbitrary point in the centre of the track has been sufficiently heated in order to ensure that the cobalt binder had melted, but not evaporated.

A central node was selected and its corresponding nodal temperature was measured over time in order to obtain a time-temperature plot, as shown Figure 8.12. The maximum temperature value was then recorded from the plot. The shape of the time-temperature plot was compared to that of similar plots from literature, as seen in the multi-pass scan from Foroozmehr *et al.*, (2016), shown in Figure 8.13. The node heats up almost instantaneously as the laser centre approaches the node. The unsymmetrical shape before and after the maximum peak temperature is due to the double ellipsoidal input heat flux. Once the laser moves away, the node gradually cools down.

The similarity in shape between the current model's temperature response curve and that of literature provides validation that the model's setup is correct. However, it is suggested that the simulated results be compared to any available experimental results from past literature using a similar material before any resources are invested in actual experimental scans.

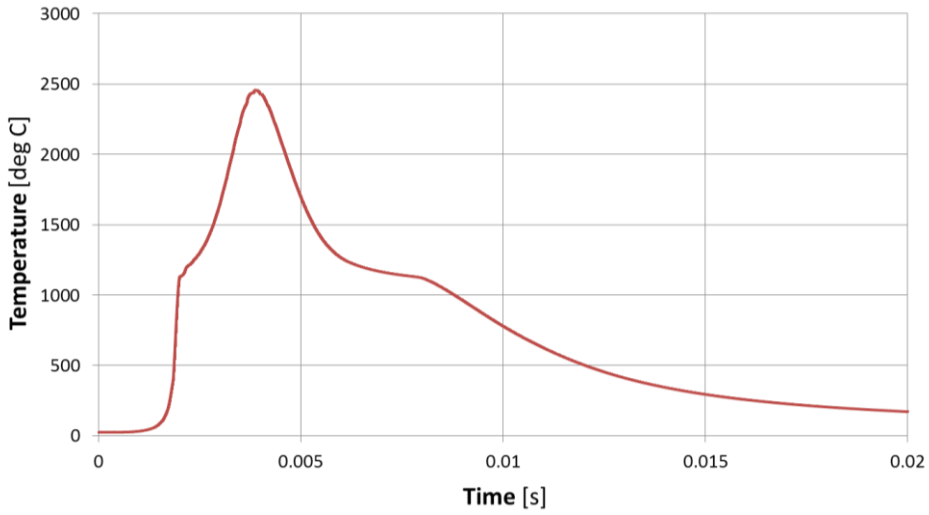

Figure 8.12: Nodal time-temperature plot for a central node (Olivier, 2018).

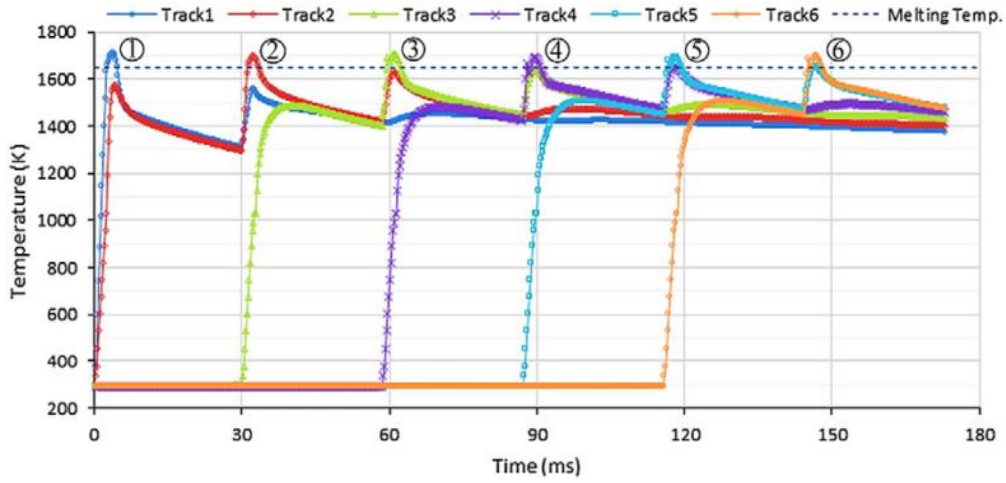

Figure 8.13: Nodal time-temperature plot for a multi-track simulation (Foroozmehr *et al.*, 2016).

8.3 Model Calibration

In order to ensure the model produces accurate results before proceeding to the final calibration stage, a model calibration test can be performed. During this test the model's accuracy is compared to experimental results from literature. A flow chart explaining the calibration process is shown in Figure 8.14.

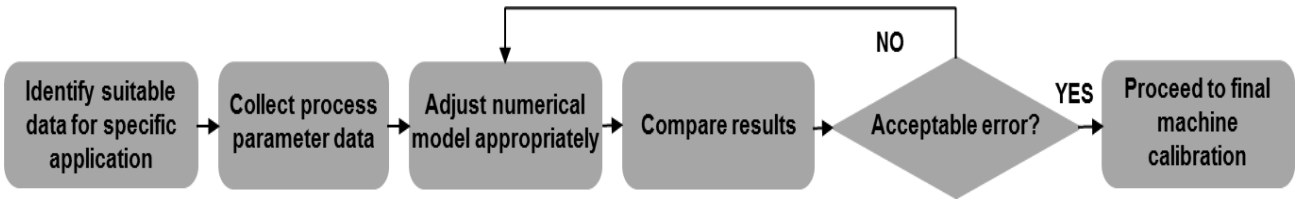

Figure 8.14: Process flow chart explaining the model calibration methodology (Olivier, 2018).

In this study three different publications were identified, which focused on developing WC-Co for SLS processing, as shown in Table 8.7. Their respective process parameters were recorded and listed in Table 8.7. These parameters were then implemented in the numerical model in order to establish whether the model's results were accurate.

Table 8.7: Past research identified for the simulation comparison

Institute	Powdered material	Abbreviation	Reference
Lyon University	MBN Nanomaterials S.P.A WC/Co12	UDL	(Domashenkov, Borbély & Smurov, 2017)
TU Clausthal ISAF and Bremer Institut für angewandte Strahltechnik	Praxair WC-Co 88/12	ISAF, BIAS	(ISAF & BIAS, 2012)
Moscow State Technological University, STANKIN	WC-Co 25% Co	STANKIN	(Khmyrov, Safronov & Gusarov, 2017)

The selected publications provided information regarding the scan track width (w). The exact melt-track width measurements were obtained using the scale bar provided in the micrographs, shown in Figure 8.15. Various experimental scans were produced in order to determine the correct parameters for processing the powdered material. These tracks were then recreated using the numerical model where after the melt tracks were measured and compared in order to determine the numerical models accuracy.

Table 8.8: Parameters used by each institute for experimental testing.

Parameters	ISAF, BIAS	UDL	STANKIN
Spot size, diameter [µm]	Assume 50	40	100
Powder layer thickness [µm]	200	70	100
Laser Power [W]	110 and 140	40	80
Scanning Speed [mm/s]	250	130	10 to 50

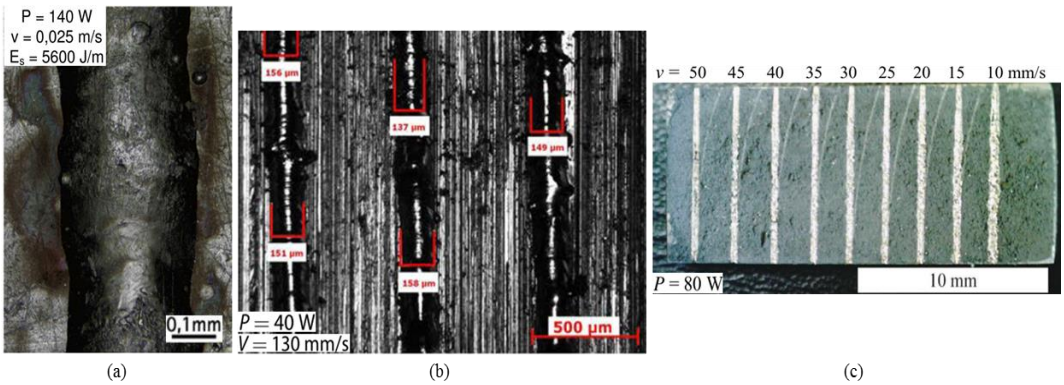

Figure 8.15: Single-track experimental results, produced by (a) ISAF, BIAS (ISAF & BIAS, 2012), (b) UDL (Domashenkov *et al.*, 2017) and (c) STANKIN (Khmyrov *et al.*, 2017).

A positive sign from the initial observation of the temperature results were that all of scans resulted in temperatures higher than the melting temperature of cobalt, which is required for liquid phase sintering. Also, none of the models exceeded the evaporation temperature of the binder. After accepting the results as being logical the melt pool width was measured in the visualisation window of the software. The differences between the experimental and simulated widths (Δw) are shown in Figure 8.16.

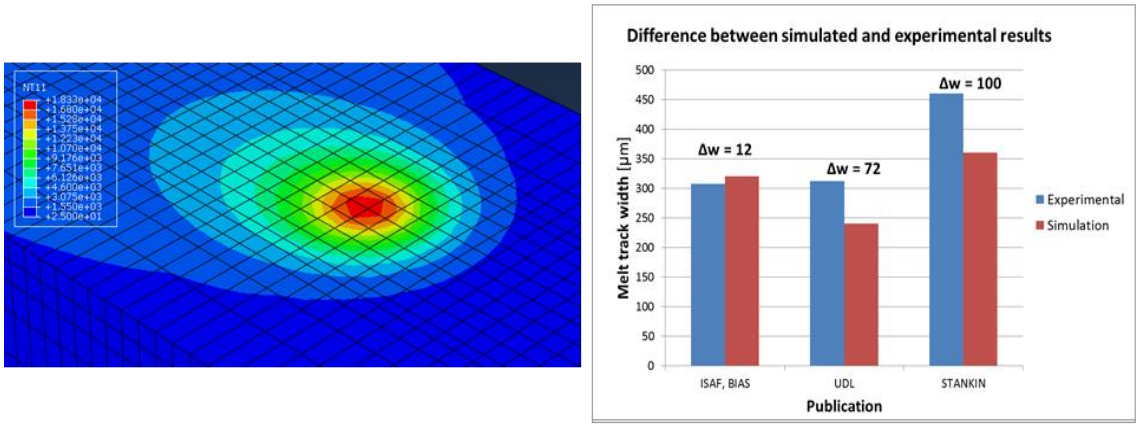

(a) (b)

Figure 8.16: Results of the comparison between the literature experimental and simulated scan tracks (Olivier, 2018).

The comparison revealed a set of mixed results. The ISAF, BIAS simulation predicted the scan-track width with excellent accuracy, with only a 4% (12 µm) error. However, the results of the UDL and STANKIN simulation proved to be less accurate with errors of 30% (72 µm) and 28% (100 µm), respectively. This inaccuracy may be due to a variety of factors, as SLS is a multi-physical process, which was only partially recreated in this numerical model.

Chapter 9: Experimental Validation Preparations

Overview

In order to determine whether the numerical model was able to provide an accurate approximation to the laser processing, the simulation results will need to be validated using experimental samples. The exact inputs used for setting up the numerical model will be incorporated in the experimental test in order to compare the accuracy. In this chapter, the experimental process is explained in detail in order to ensure the results can be universally replicated. The experimental samples are compared to the numerical model in the following chapters.

9.1 Powder Analysis

The first step of the experimental part of the project was to procure the raw powder. It is known that powder characteristics significantly affect quality aspects such as part density, surface roughness and mechanical properties. Particles should not have defects such as satellites or internal pores (Ardila *et al.*, 2014). Spherical powder particles are preferred to irregularly shaped particles, due to a denser packing and more even heat absorption (Kovaleva, Kovalev & Smurov, 2014).

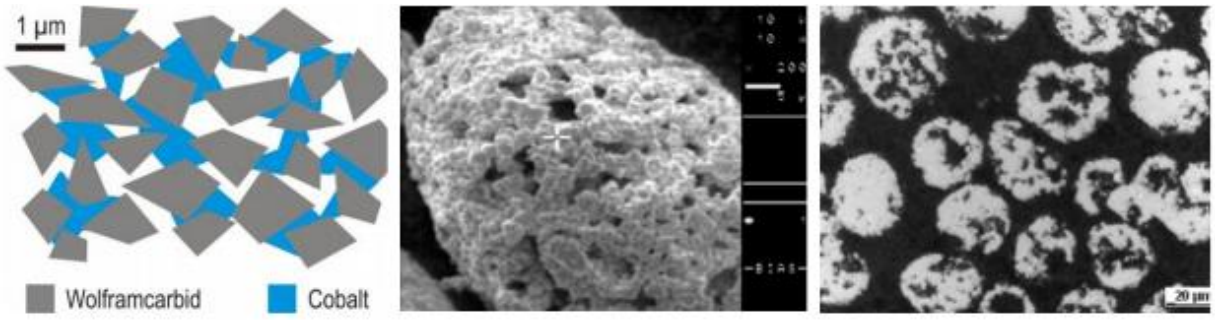

Figure 9.1: Schematic representation and SEM imaging of WC-Co 12 powder used in literature, adapted from ISAF & BIAS (2012).

Two types of WC-Co powders were obtained and considered for the experimental section. These are:

1. Mitsubishi Materials Corporation (MMC) UTI 20 tungsten carbide cobalt powder mixture
2. Praxair WC-12Co Agglomerated & Sintered powder

After obtaining the powders, a scanning electron microscope (SEM) analysis was performed at the Central Analytical Facilities (CAF) - Stellenbosch University. The results from the SEM analysis are shown Figure 9.2 and Figure 9.3, respectively.

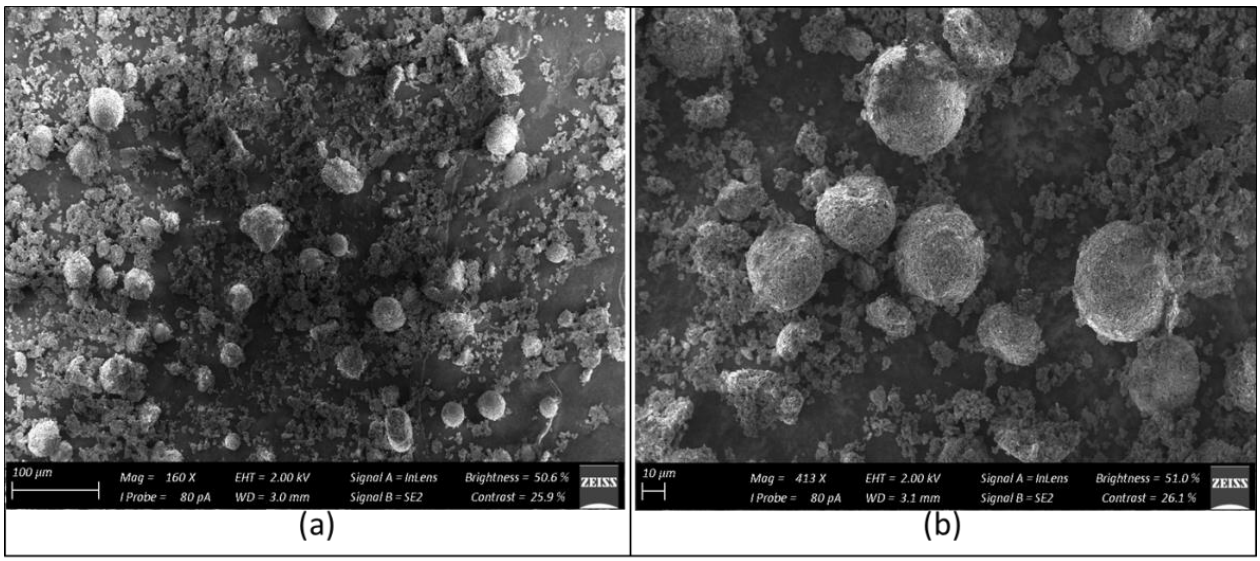

Figure 9.2: MMC UTI 20 WC-Co powder observed using a SEM at (a) low magnification and (b) high magnification.

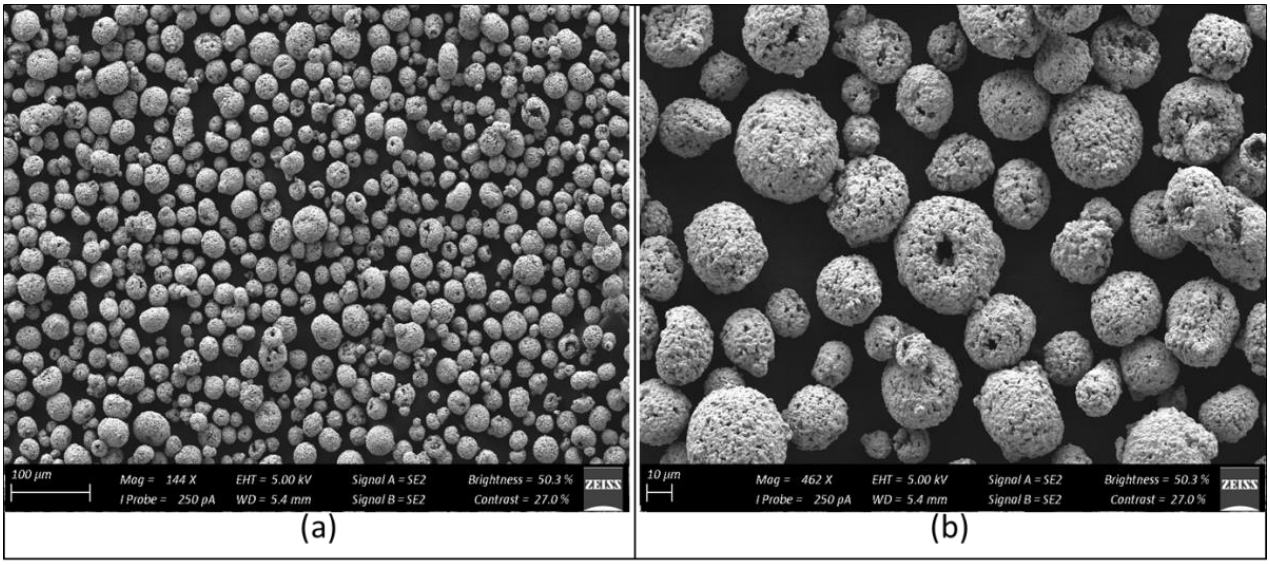

Figure 9.3: Praxair WC-12Co agglomerated & sintered powder observed using a SEM at (a) low magnification and (b) high magnification.

A full analysis of the particle size distribution was performed using the open software program ImageJ. The results of this analysis can be found in Appendix C. The MMC powder size ranges from 16.7 µm to 60.7 µm with an average particle size of 29 µm and standard deviation of 12.4. Although the powder was close to perfectly spherical, it also contained loose flaky satellites. The Praxair powder size ranged from 2.6 µm to 56.2 µm with an average particle size of 25.4 µm and standard deviation of 12.0. It had smaller variations in particle size, with most particles close to the average. One major concern was the presence of internal pores in some of the particles. This could worsen scan track porosity.

An energy-dispersive x-ray spectroscopy (EDX) analysis was performed on a particle of each of the powders to determine their respective compositions. The MMC particle contained a surprisingly high concentration of trace elements niobium (Nb) and titanium (Ti).

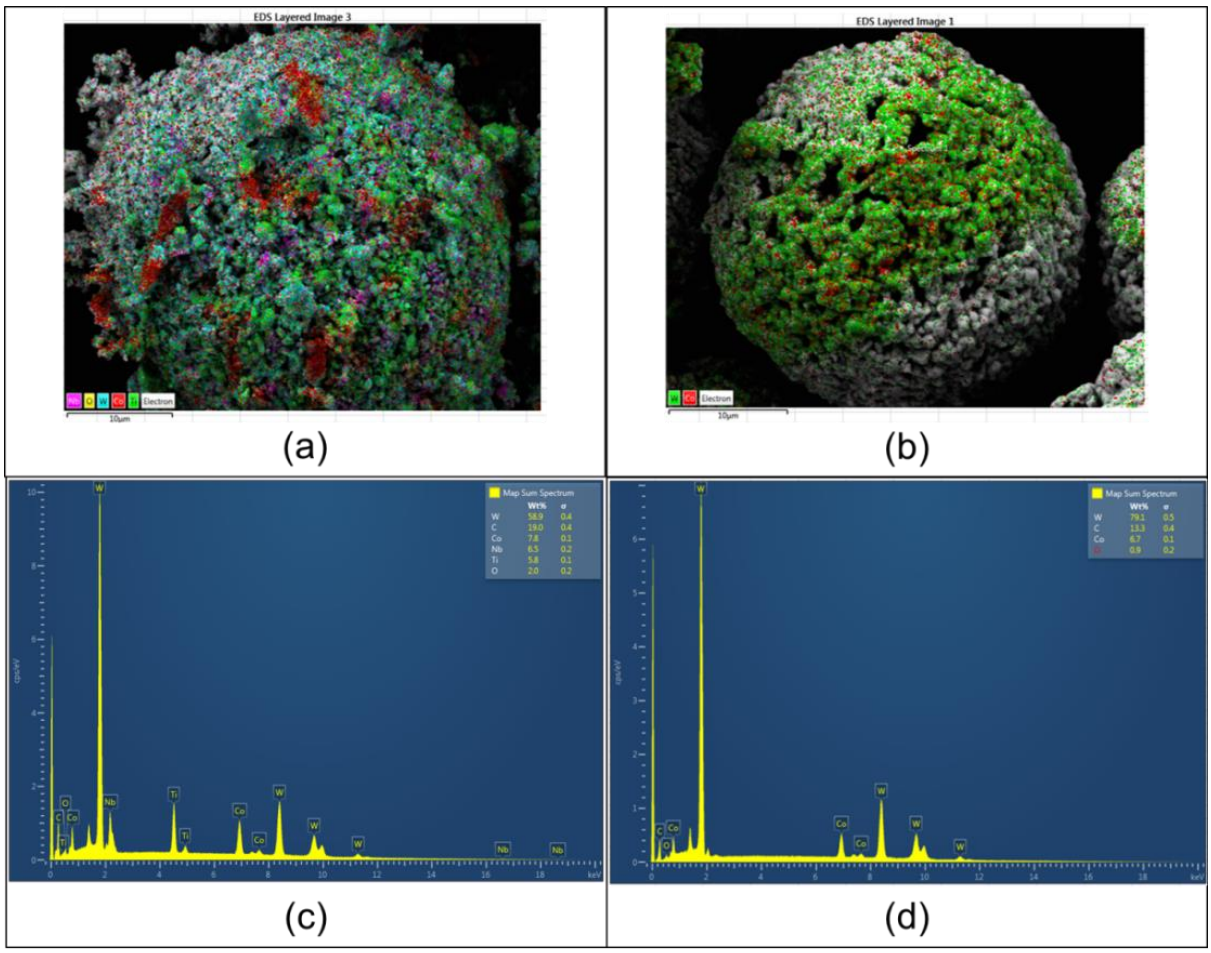

Figure 9.4: EDX powder analysis. An EDX analysis provides information on the constituent elements in the MMC (a) (c) and Praxair (b) (d) powder, respectively.

After analysing the images of the particle morphology of each powder it was decided to use the Praxair WC-12Co powder for perform the experimental tests. This decision was based on the reasoning that the powder particles had a more spherical shape and did not contain high amounts of trace elements, which may influence the results.

9.2 Experimental Preparations

9.2.1 Base plate Material Acquisition and Manufacturing

The next step in the experimental process was to manufacture the base plates, which would support the single powder layer and scan tracks. The base plate acquisition and manufacturing step was an important consideration of the project, as it would add significantly to the total project cost.

Tool steel

The tool steel was recovered from a piece of scraped 250 x 250 x 10 mm Concept Laser base plate, which was used for past SLS/SLM operations by the US. Smaller sections were cut using a water jet cutter from the tool steel. The cut-outs were machined flat on a DMU 65 monblock 3-axis milling machine at the Stellenbosch Technology Centre (STC). A sand blasting operation followed the machining, which increased the surface roughness in order to reduce the laser refraction.

Ti-6Al-4V

The titanium base substrates were manufactured from a solid, Ti-6Al-4V, round bar (Ø = 75mm x 250mm) using various machining operations (including milling and cutting) at the Stellenbosch STC.

Detailed information regarding the composition and material characteristics of the base substrates can be found in Appendix G. The design specifics, as indicated by the CRPM for use in their EOSINT machine, can also be found in Appendix G.

The base plate specifics are an important aspect of the SLS experimental setup, as the SLS process requires thermomechanical support for processing the powder material. The base plate acts as an:

- Support surfaces for the scan tracks (impossible to scan in the air).
- Heat dissipation medium (conducts heat away from scan track).

As the build chamber of each SLS machine differs in size and shape, the base plate geometry is machine specific. A common feature used for R&D purposes is a volume reduction unit, as seen in Figure 9.8(a). This custom build unit limits the amount of stock powder required for experimental builds, which add to limit developmental costs.

It is essential that the base plate has a flat surface, as this will have a considerable influence on the laser spot size. The implications of an uneven base plate are illustrated in Figure 9.5. Internal algorithms calculate the distance from the mirror system to the top surface of the powder layer based on a fixed distance, say *L*, from a reference point to the top surface powder layer. This distance stays constant even when the laser scans between two points at time t_1 and t_2. However, if the base plate is uneven, the distance, *L*, will be different for the two positions at t_1 and t_2. This will result in a misalignment of the laser's focus point, causing the laser spot size to increase.

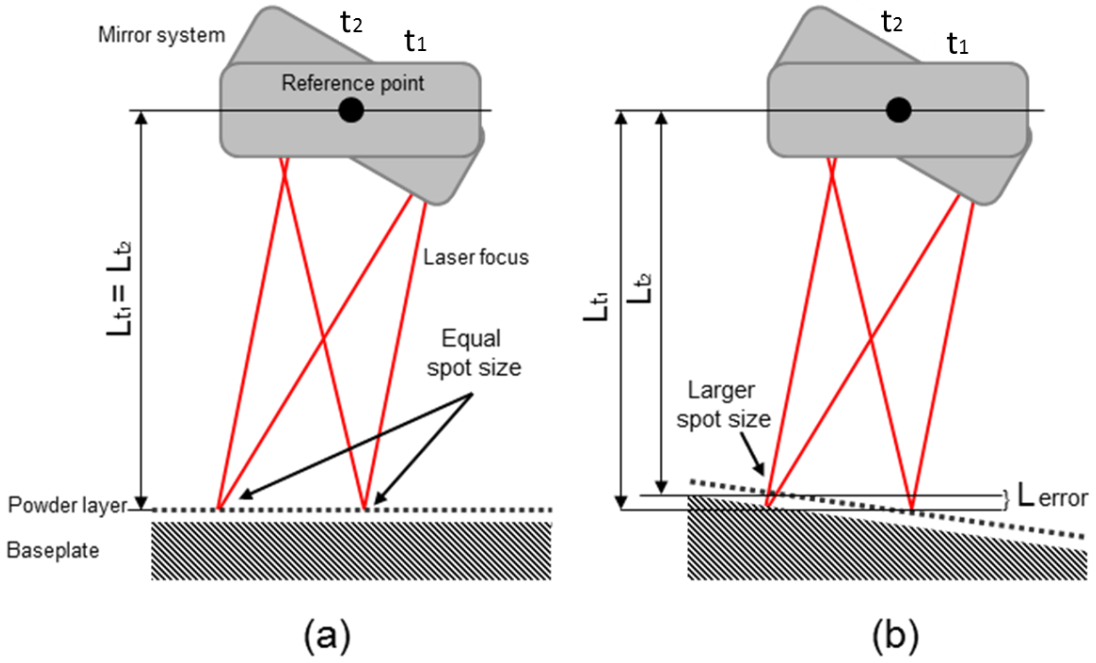

Figure 9.5: Implications of an uneven base plate surface. (a) Correct flat surface. (b) Incorrect uneven surface.

9.3 Design of Experiments

In total 48 single tracks were printed using parameters corresponding to those obtained with the numerical model. The spacing between each scan track was 2 mm, which was argued to be large enough that the heat affected zone of neighbouring tracks would not influence any results. Hence, any resintering was avoided. The 48 tracks were a result of a duplication of the 24 parameters sets. The reason behind the duplication was to ensure that the SLS machine was scanning correctly. The machine started scanning the first 24 tracks (parameter sets) from left to right, and the duplicated parameter sets by scanning from right to left. A schematic of the base plate is shown in Figure 9.6.

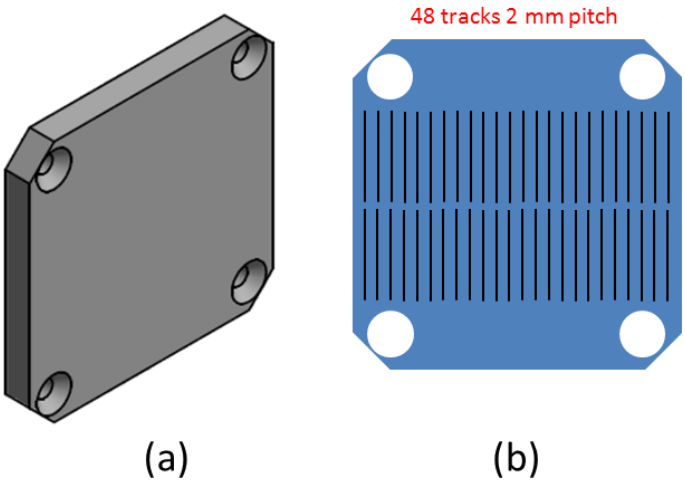

Figure 9.6: Base plate design for the volume reduction unit in the build chamber.

9.3.1 Parameter Checklist

A list, which specified the details of each of the 24 parameter sets were provided to CUT for the SLS single track processing. This ensured that the experimental tracks were identical to the simulated scan tracks. The laser spot size and layer thickness were set to 80 μm and 50 μm, respectively. The complete list of parameter sets is shown in Table 9.1.

Table 9.1: Checklist with each parameter set for the experimental scan tracks.

Track Number	Laser Power [W]	Scanning Speed [mm/s]	Specific Energy Density* [J/mm²]
1	50	60	27.8
2	50	80	20.8
3	50	100	16.7
4	50	120	13.9
5	50	140	11.9
6	50	160	10.4
7	50	180	9.3
8	50	200	8.33
9	150	400	12.5
10	150	600	8.33
11	150	800	6.25
12	150	1000	5.00
13	150	1200	4.17
14	150	1400	3.57
15	150	1600	3.13
16	150	1800	2.78
17	300	1000	10.0

18	300	1200	8.33
19	300	1400	7.14
20	300	1600	6.25
21	300	1800	5.56
22	300	2000	5.00
23	300	2200	4.55
24	300	2400	4.17

*50μm layer thickness

9.4 Experimental Setup

The experimental samples were processed at the Centre for Rapid Prototyping and Manufacturing (CRPM) at the Central University of Technology (CUT) in the Free State, South Africa. The facility utilises the EOSINT M280 machine for SLM/SLS research and development purposes. A full technical data sheet of the machine can be found in Appendix D. The build chamber was filled with nitrogen gas before operation with oxygen content kept below 0.1%. The experimental setup at CUT is shown in Figure 9.7 and Figure 9.8. It is advised that the correct personal protective equipment is worn when handling the powdered metal. This is due to the possibility of inhaling nanoparticles, which may lead to the possible medical complications, as mentioned in Section 4.5.

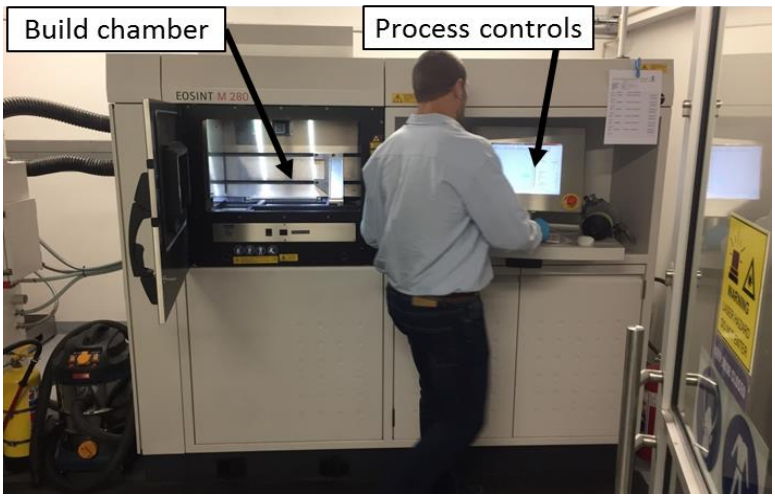

Figure 9.7: The EOSINT M280 machine being prepared for laser processing at CUT.

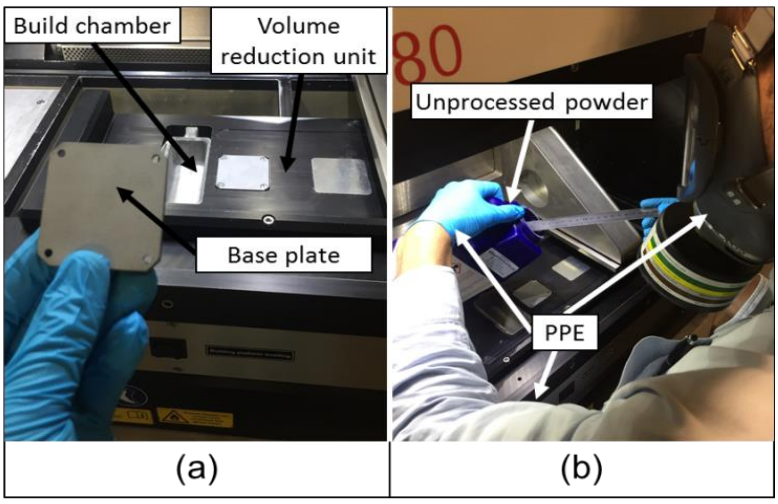

Figure 9.8: Inside the build chamber. (a) A custom-made volume reduction unit was fitted in the build chamber to save on research cost. (b) Care should be taken when handling the raw powder.

9.5 Final Processed Samples

The two final processed samples were essentially identical, with the only differences being the different base substrate materials. It is good practice to label the samples according to the parameters or parameter set numbers in order to avoid confusion when orientating the samples when performing the track measurements. The final processed experimental samples are shown in Figure 9.9. The 48 scan tracks were processed in an clockwise direction, starting with the lowest laser intensity setting (50W) at the top half of the base substrate and then moving down to the bottom half and ending with the highest laser power intensity (300W). The tracks were grouped in pairs of eight, as indicated by the red grid.

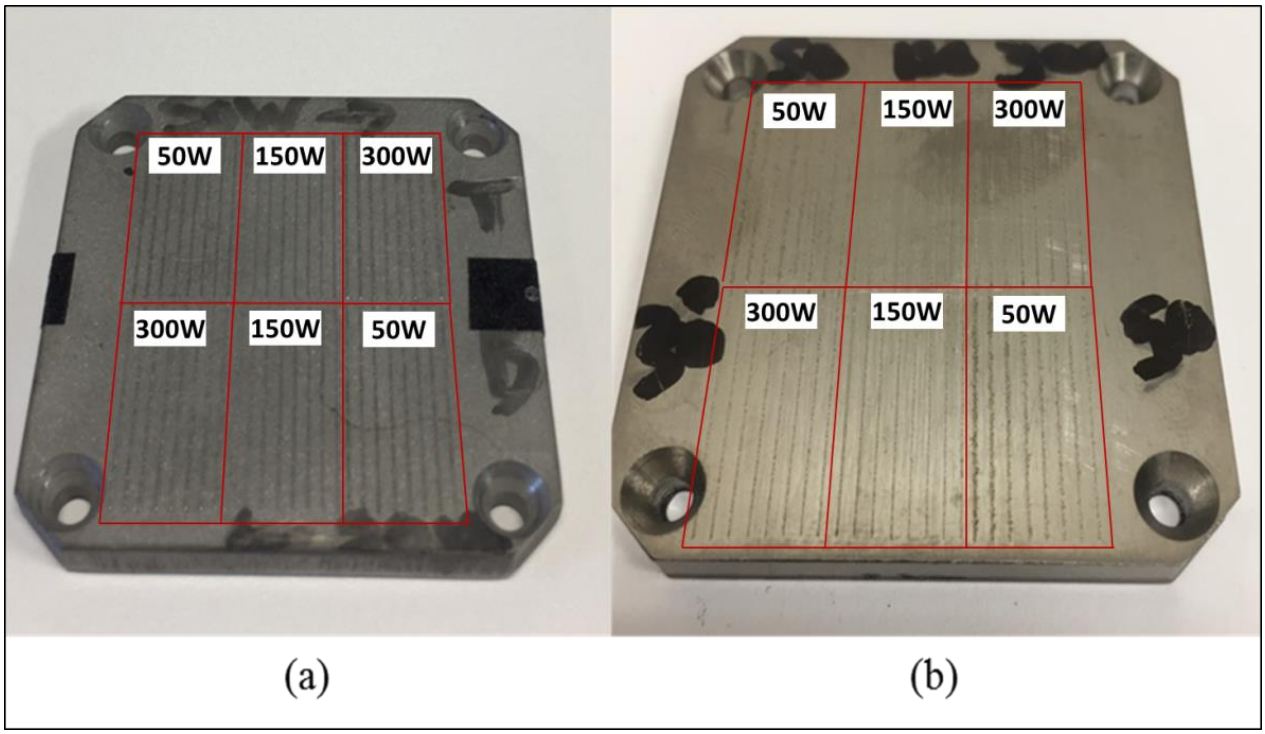

Figure 9.9: Experimental WC-Co single tracks scanned on a (a) tool steel and (b) Ti-6Al-4V base plate. The grid indicates the different laser power intensity groupings.

After receiving the samples, they were prepared for experimental analysis, which included compositional scans and optical and SEM imaging of both the top surface and sectioned views of each sample. The following section explains the sample analysis process and discusses the results from each of the scan track measurements.

Chapter 10: Results and Validation Discussion

Overview

This chapter discusses the methods used to study the geometrical features of the developed melt pool using the numerical thermal model and experimental scan tracks. The chapter briefly explains the process of collecting the data from each method before moving on to representing the results in various charts. Finally, the results obtained from each method are compared and presented in a visual format. An overall conclusion can be formulated using the results presented in this chapter.

10.1 Simulation Results

The first results to be collected were the melt pool geometry measurements from the numerical thermal model. The thermal contours can be set to display all temperature values up to a certain user defined maximum allowable value (Visualisation→Contour Plot Options→Limits→Specify Max) in the visualisation toolbar of the Abaqus user interface. This value was assumed to be the general sintering temperature (1496℃) of WC-Co in industry, see Section 4.4. The contour limit forced all temperature values exceeding the maximum allowable temperature to be displayed in a grey shading, as seen in Figure 10.1. This was then used to estimate the geometrical features of the melt pool.

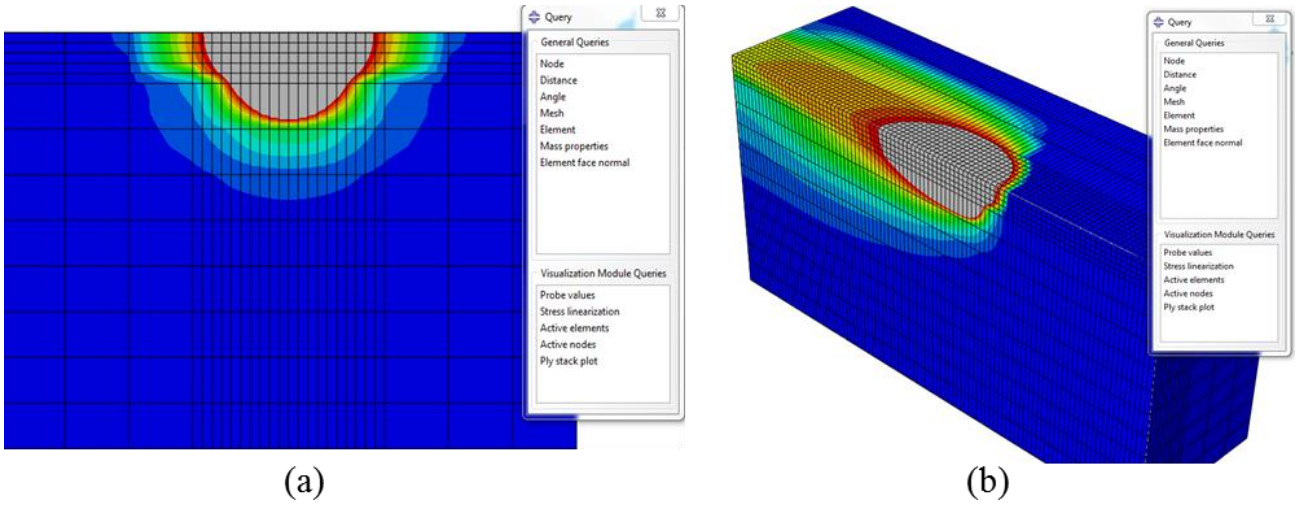

Figure 10.1: Simulated section views. The (a) lateral and (b) longitudinal sectioned views of the simulated melt pool were used for measuring the scan track width and penetration depth.

An advantage of numerical simulations is the ease with which results can be analysed. This became clear when sectioning the model in order to assess the extent of the melt pool thermal effects. The model could easily be sectioned at any distance and on any axes using a view cut feature (Visualisation→View Cut Manager→Select Plane). The scan track width and penetration depth was measured using the measuring tool in the Abaqus user interface (Tools→Query→Distance). Another advantage of numerical simulations is repeatability. Hence, it was only required to perform a simulation run once for each of the 24 parameter sets. This is a great benefit when considering the total process efficiency.

10.1.1 Simulated Track Width

The measured simulated track width data was recorded in an MS Excel spread sheet. Initially, the recorded data appeared to be organised randomly, however once represented graphically, clear trends became visible between the three selected laser power intensity settings and the scanning

speed. Scanning speed was selected as the independent factor as it was found to have a greater effect on the response than specific energy density. The results for both base plate materials are shown on a log scale in Figures 10.2 and 10.3, respectively. Identical parameter sets were applied to both experimental samples. Although the graphical representation of the Ti-6Al-4V scan track width measurements appear similar to that of the tool steel base plate there are some slight differences. The tabulated results from the experimental measurements along with a sample image of each simulated parameter set for each of the base plate materials can be found in Appendix F.

The following is visible from the simulated track width measurement charts:

1. There is a clear negative correlation between the scanning speed and the measured scan track width. As the scanning speed increases, the scan track width decreases.
2. The decreasing scan track width measurements follow a linear trend line.
3. The trend lines of the three laser power intensity groupings reveal that the scan track width measurements slope is the steepest for the lowest laser power intensity grouping followed by the middle and highest grouping in both of the base materials.
4. The width measurements of the Ti-6Al-4V plate are notably wider at the lowest power intensity range, however it is only marginally wider at the middle and highest power intensity ranges. This may be due to titanium's increase in thermal conductivity at elevated temperatures.

Tool steel base plate

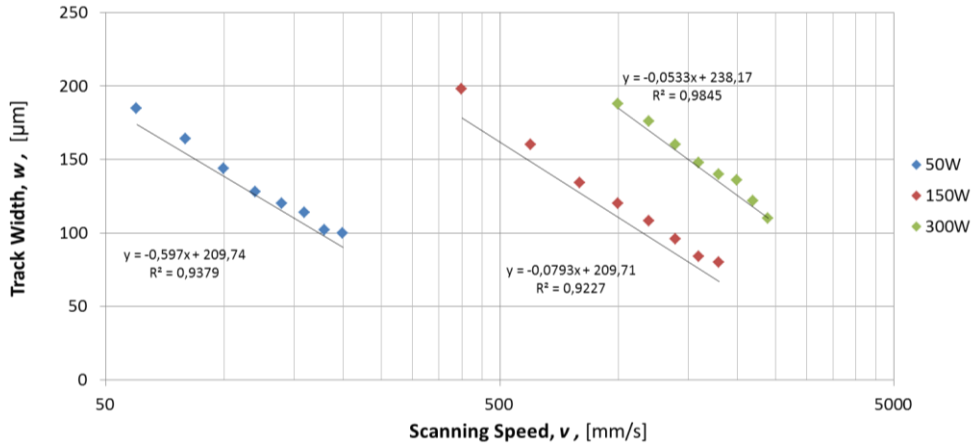

Figure 10.2: Chart displaying the recorded simulated scan track width measurements for each WC-12Co scan track on the tool steel base plate.

Ti-6Al-4V base plate

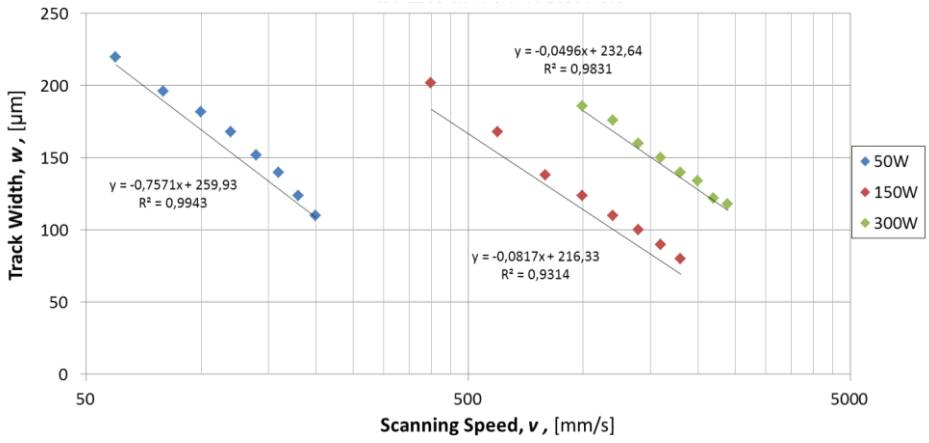

Figure 10.3: Chart displaying the recorded simulated scan track width measurements for each WC-12Co scan track on the Ti-6Al-4V base plate.

10.1.2 Simulated Penetration Depth

The simulated penetration depth was measured similarly to the scan track width measurements. The data was recorded and presented in the same format as the scan track width measurements. The charts for the simulated penetration depth on the tool steel and Ti-6Al-4V base plates are shown in the log charts in Figures 10.4 and 10.5, respectively.

The following is visible from the simulated penetration depth measurement charts:

1. There is also a clear negative correlation between penetration depth measurements and the scanning speed. As the scanning speed increases the penetration depth decreases correspondingly.
2. The trend lines of the three laser power intensity groupings reveal that the penetration depth measurement slope is the steepest for the lowest laser power intensity grouping followed by the middle and highest grouping in both of the base materials.
3. Linear trend lines are also a good fit for the penetration depth measurements, however the R^2 values are lower than those of the width measurements.
4. The penetration depth at the lowest scanning speed for the 50W and 150W intensity settings deviate from the linear trend line. This is especially notable on the titanium base plate.
5. Penetration is on average 8.4 μm deeper in the Ti-6Al-4V base plate.

Tool steel base plate

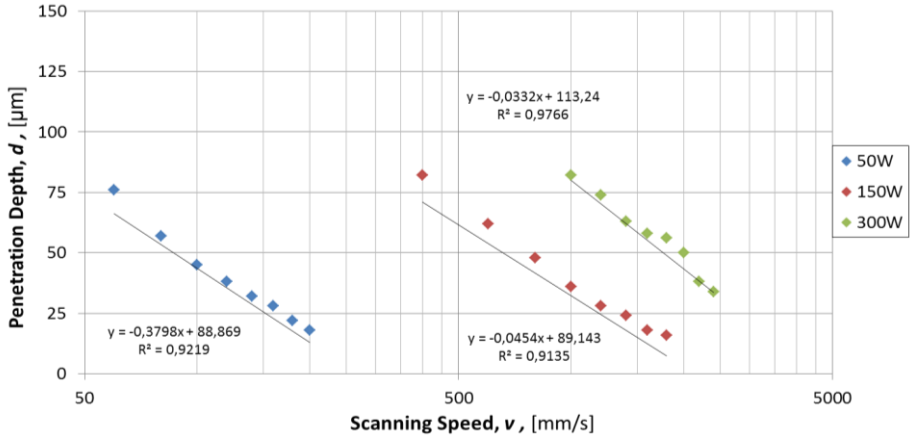

Figure 10.4: Chart displaying the recorded simulated penetration depth measurements for each WC-12Co scan track on the tool steel base plate.

Ti-6Al-4V base plate

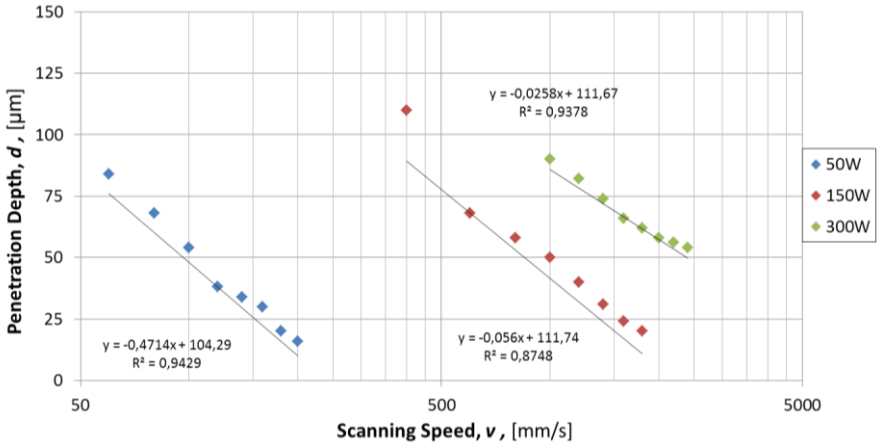

Figure 10.5: Chart displaying the recorded simulated penetration depth measurements for each WC-12Co scan track on the Ti-6Al-4V base plate.

10.2 Experimental Results

The experimental section can be divided into two parts, namely: WC-12Co on a tool steel base plate and WC-12Co on a Ti-6Al-4V base plate. The reason for the material difference is to test the rigidity and transferability of the numerical model for different materials.

Image montage

A SEM image montage provided an overview of all the scan tracks on the surface of the base plate simultaneously. Small, individual images were taken of every track on the base plate and then stitched together to form a single collective image containing all the scanned tracks. The SEM image montage is useful as it provides a clear qualitative perspective of the individual scan tracks on a single image. The montage shown in Figure 10.6 displays the two distinct regions, that is the top and bottom sections. The track numbering were added after the images were processed in order to avoid confusion over the parameter set order in future. A qualitative analysis of the individual scan tracks can be used as validation for the variable parameter screening performed in Section 8.2.

The SEM image montage of the tool steel base plate revealed that there were some noticeable differences in the appearance of the scan tracks.

1. Size: There are visible differences in the scan track widths with a change in parameter set combinations. This was confirmed when the track widths were measured in the optical microscope images. The size differences is due to the transient nature of heat conduction through the powder bed and underlying base plate. The specific energy density describes the amount of energy that a unit of area experiences for one second. Hence, it is expected that a higher energy density will result in more heat conduction, a larger heat affected zone and, ultimately, wider scan tracks. The opposite is true for lower energy densities.

2. Balling / Splatter: Balling occurs when there is a lack of wetting and penetration of the melt pool into the underlying base layer or base plate. The surface tension of the melt pool becomes too low, which allows several small spheres (balls) to be ejected from the melt pool. The phenomenon of balling can be reduced by increasing both the scanning speed and laser power (Gebhardt *et al.*, 2014). Balling was especially evident in the experimental scan tracks produced in the 50W parameter set ranges (tracks 1 to 8).

3. Melt droplets / Melt inconsistency: Melt droplets are considered to be created at rapid heating conditions, without allowing the binder to form sufficient necks between the structural powder particles. Hence, the strength of these necks are insufficient to resist the surface tension of the melt causing incontinuity and inconsistency in the scan track. (Antony, Arivazhagan & Senthilkumaran, 2014). This was also proven to be the case with droplet formation in the high power, 300W parameter set ranges (tracks 17-24).

4. Micro-cracks: A large degree of shrinkage occurs during the liquid-solid transformation, which tends to lead to considerable stresses, ultimately resulting in micro-cracks in scan tracks (Gu, *et al.*, 2016). Micro-cracks were present in most of the experimental scan tracks, with the cracks running almost perpendicular to the scanning direction. This may be due to large temperature differences between the centre and the edges of the melt pool causing residual thermal stresses in the solidified tracks.

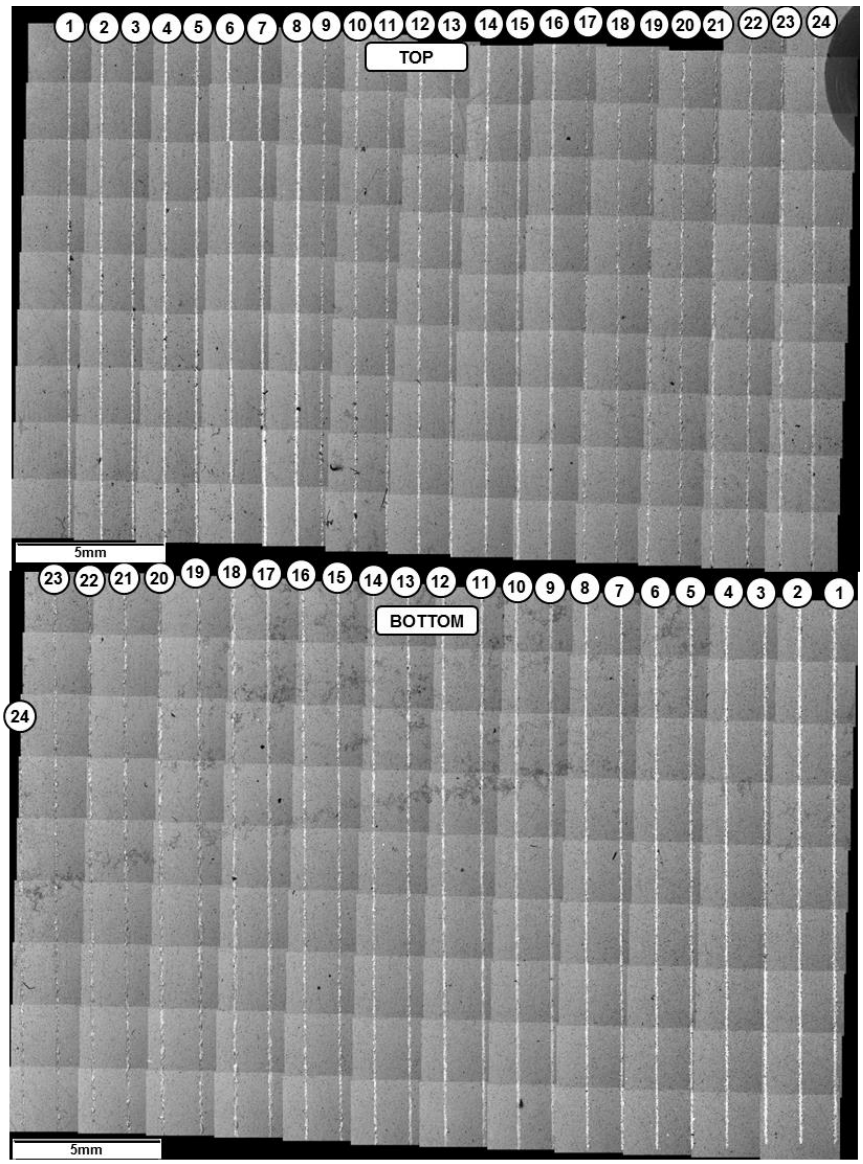

Figure 10.6: SEM image montage of all scan tracks on the surface of the tool steel base plate.

The transient thermal behaviour of the SLS process is controlled considerably by the processing parameters. This behaviour results in complex and, often, unwanted thermal phenomenon such as balling, porosity, droplets and micro-cracks which is difficult to control. Advances in numerical modeling may lead to future operations where such phenomena can be predicted before actual experimental results are produced.

Single scan track composition

A higher magnification of the scan tracks provides information on the melt pool, which developed during processing. An energy dispersive x-ray spectroscopy analysis (EDS) of the individual scan tracks revealed the composition of each track after melting. This is important to know whether the binder had in fact been melted at each of the parameter set, otherwise the scan track may be very weakly bonded to the base plate.

The scan track composition analysis of the tool steel base plate revealed that there was significant melting of the base plate itself, which is evident in the high iron (Fe) content as seen in the composition analysis in Figure 10.7. This may be due to the similar melting point of the maraging steel, 1413℃ (Raabe, 2014), vs that of the cobalt binder in the powder mixture 1496 ℃ (see Section

4.4.1). Another possibility may be due to Co / Fe peak overlap on the EDS. Unfortunately, the final cause for the high FE content could not be clarified in this study.

Hence, the scan track composition analysis indicates a strong inter-layer bonding between the base plate and the initial scan track. A sectioned view of the scan track will reveal the melt penetration depth within the base plate. Naturally, a deeper penetration depth will result in better first layer bonding.

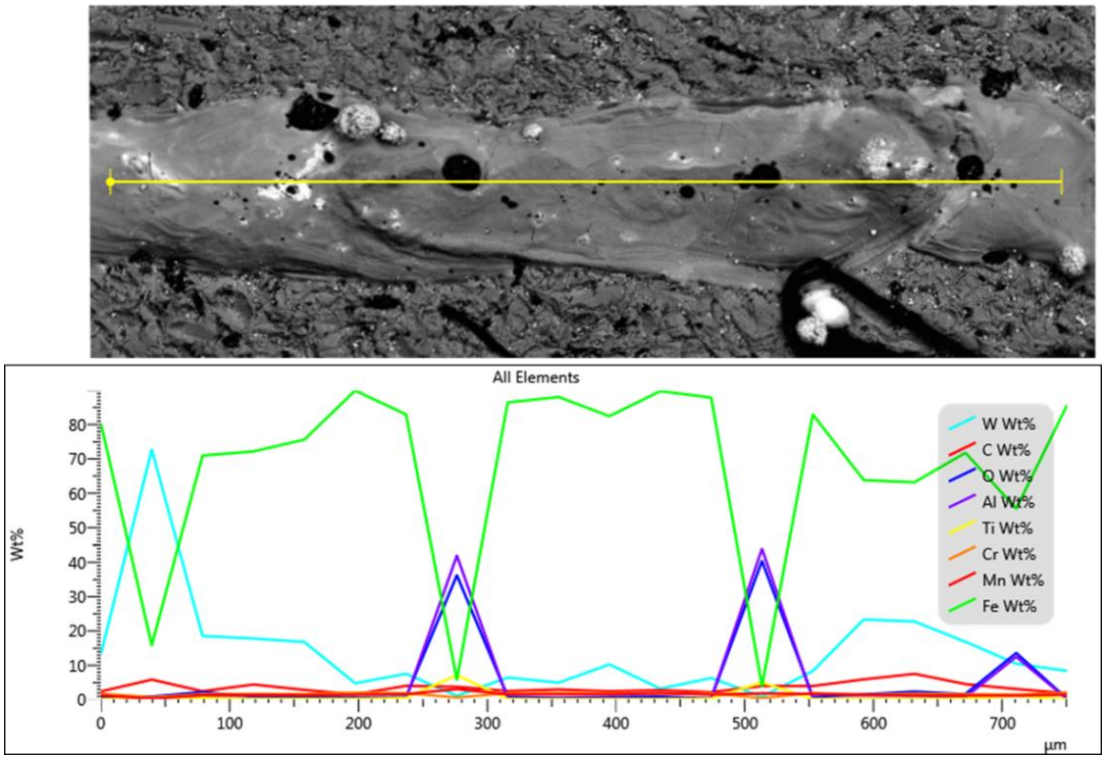

Figure 10.7: Scan track element composition analysis. Each colour represents a different element.

10.2.1 Experimental Scan Track Width Measurements

The width measurements were made using the Olympus GX51 optical microscope. The base plate was placed on the microscope with the tracks facing the magnification eyepiece. The microscope images were captured using the Olympus Stream Analysis software. This software package was also used to make the width measurements directly on the images. In total, six measurements were made of each parameter set, three at the top track and three at the bottom track. The measurements were saved to a MS Excel spread sheet along with the process parameter details of the corresponding scan track. Finally, the spread sheet data was converted to a graphical format, which made it easier to recognise trends and discuss results. A schematic of the top view of the base plate and scan tracks is shown in Figure 10.8. All 288 scan track width measurements can be found in Appendices H and J. It should be noted that there is a colour difference between the tool steel and Ti-6Al-4V base plates. It was challenging to set the contrast between the WC-Co scan track and tool steel base plate due to the similarities in colour, as shown in Figure 10.9.

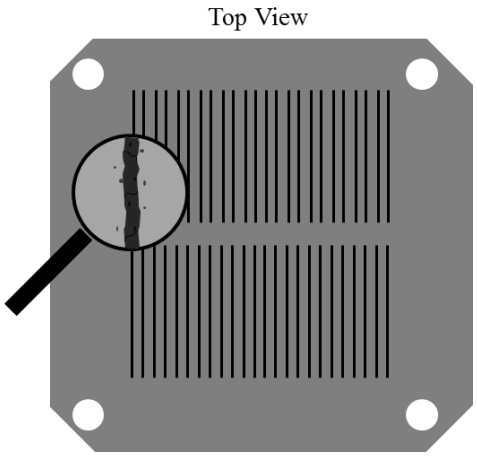

Figure 10.8: Schematic of the top view analysis of a single scan track on the base plate.

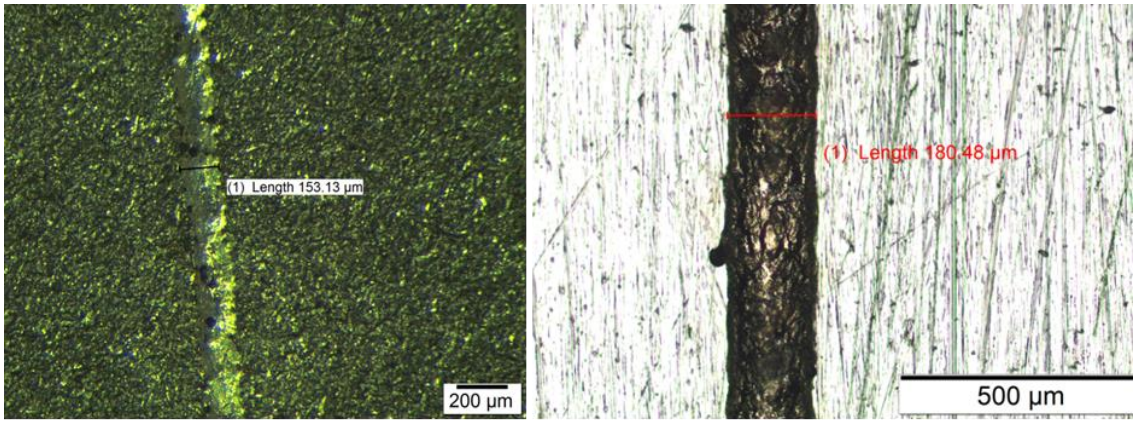

Figure 10.9: Optical microscope images of WC-12Co SLS scan tracks produced at 150 W, 400 mm/s on a (a) tool steel and (b) Ti-6Al-4V base plates, respectively.

The scan track width measurements are displayed using two representations. Firstly, the graph plots the data against the scanning speed at the three power intensity settings and secondly it compares the same measurements to the specific energy density. Due to the wide range of speeds used for this study, the scanning speed comparison graph is represented on a logarithmic scale. Error bars representing the standard deviation of each average measurement was also included in each of the plots. This is repeated for the width measurements on both the tool steel and Ti-6Al-4V base plates. The two tool steel scan track width charts are shown in Figures 10.10 and 10.11, respectively.

The following observations were made from the experimental width measurement graphs:

1. There is a negative correlation between scanning speed and track width. As the scanning speed increases, the scan track width decreases.
2. The lowest laser power value has the slowest (smallest slope), followed by the middle and highest laser power parameter sets.
3. On both base plates, the 150 W, 400 mm/s parameter set resulted in the widest scan track.
4. Similar specific energy densities do not necessarily result in similar scan track widths. However, this seems to be true for the higher laser intensity settings.
5. Scan tracks displayed similar trends on both base plate materials.
6. On average, scan tracks were wider on the Ti-6Al-4V base plate than on the tool steel base plate

Tool steel base plate

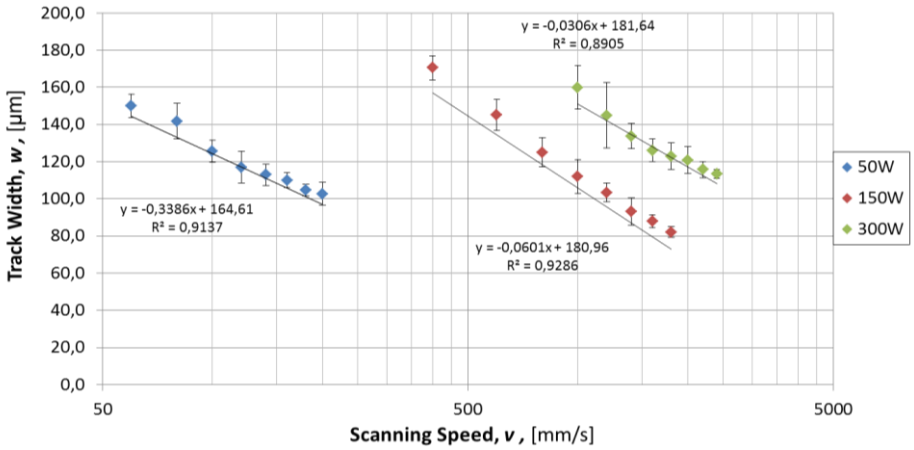

Figure 10.10: Chart displaying the recorded experimental scan track width measurements against scanning speed for each WC-12Co scan track on the tool steel base plate.

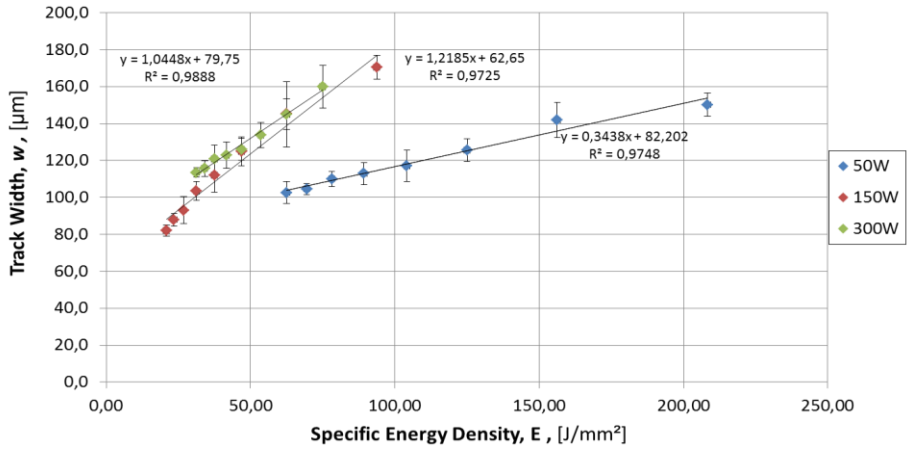

Figure 10.11: Chart displaying the recorded experimental scan track width measurements against specific energy density for each WC-12Co scan track on the tool steel base plate.

The two Ti-6Al-4V scan track width charts are shown in Figures 10.12 and 10.13, respectively. The experimental and simulated scan track width measurements are compared further in the chapter.

Ti-6Al-4V base plate

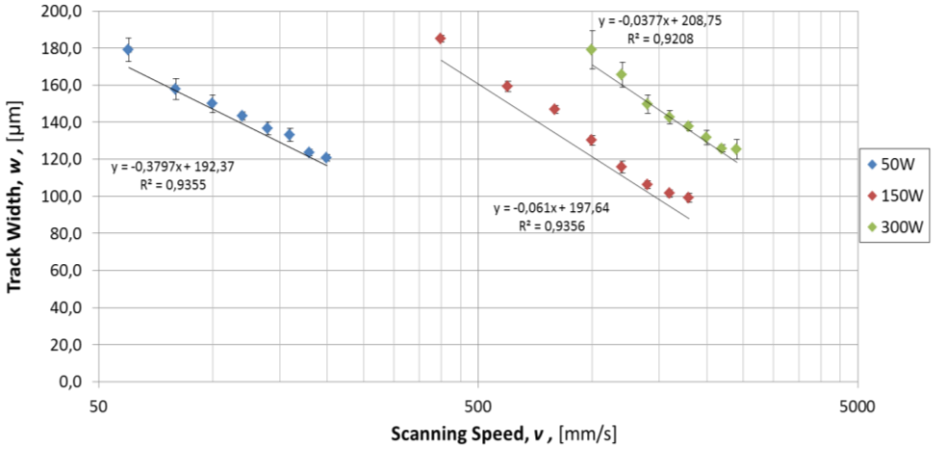

Figure 10.12: Chart displaying the recorded experimental scan track width measurements against scanning speed for each WC-12Co scan track on the Ti-6Al-4V base plate.

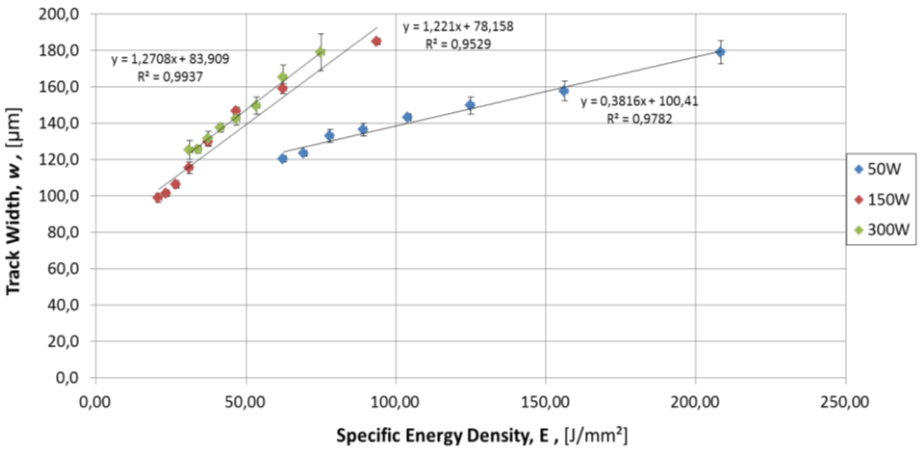

Figure 10.13: Chart displaying the recorded experimental scan track width measurements against specific energy density for each WC-12Co scan track on the Ti-6Al-4V base plate.

10.2.2 Scan Track Penetration Depth Measurements

In order to determine the scan track penetration depth, the base plates needed to be sectioned perpendicular to the scanning direction. Moreover, accuracy was increased by measuring the penetration depth at more than one location along the scan track. This was accomplished by sectioning the base plates at four locations across the tracks. In order to avoid influencing the heat affected zone (HAZ) with the cutting procedure, a low speed cutter was used to make the section cuts. The diamond tipped blade was well lubricated throughout the entire cutting process. An image of the sectioned tool steel base plate is shown in Figure 10.14.

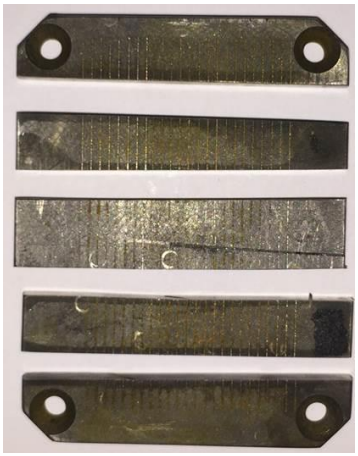

Figure 10.14: Image showing the sections made in order to study the penetration depth of the scan track at different locations in the experimental sample.

Initially, it was difficult to determine the melt pool penetration profile of the raw sectioned samples using the optical microscope. However, this problem was solved using different etching solutions for each base plate material in order to enhance the contrast of the HAZ against the base plates. A list of the etchants used in the study is provided in Table 10.1. In total, five depth measurements were made of each parameter set, three at the top track (top top, top middle, and top bottom) and two at the bottom track (bottom top and bottom bottom). A schematic of the sectioned view of the base plate and scan tracks is shown in Figure 10.15. All 240 (2 x 5 x 24) images and scan track depth measurements can be found in Appendices I and K

Table 10.1: Etchants used for each of the different base plate material.

Etchant name	Concentration / Ratio	Use
Nital (Nitric acid + alcohol)	1: 10 mL HNO3 **or** 9: 90 mL methanol (95%)	Iron, iron alloys and steels
Oxalic acid	$COOHCOOH.2H_2O$	Titanium alloys
Kroll's reagent	92 mL H_2O 6 mL HNO_3 2 mL HF	Titanium alloys

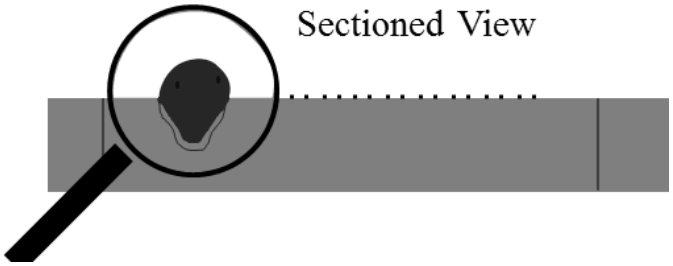

Figure 10.15: Schematic of the section view analysis of a single scan track on the base plate.

Similarly, to the width measurement plots, the scan track penetration depth can also be represented using two plots. One graph comparing the penetration depth against laser scanning speed and the other plotting it against the specific energy density. The two tool steel penetration depth charts are shown in Figures 10.16 and 10.17, respectively.

The following observations were made from the experimental penetration measurement graphs:

1. There is a negative correlation between scanning speed and penetration depth.
2. The lowest laser power value has the slowest (smallest slope), followed by the middle and highest laser power parameter sets.
3. On both base plates, the 150 W, 400 mm/s parameter set resulted in the deepest penetration depth. This value was particularly high in the tool steel base plate.
4. Similar specific energy densities do not necessarily result in similar penetration depth mesurements. However, this seems to be true for the higher laser intensity settings.
5. Scan tracks displayed similar trends on both base plate materials.
6. On average, scan tracks at the higher laser power intensities were deeper on the Ti-6Al-4V base plate; however, the lowest power intensity resulted in very shallow penetration for this material.

Tool steel base plate

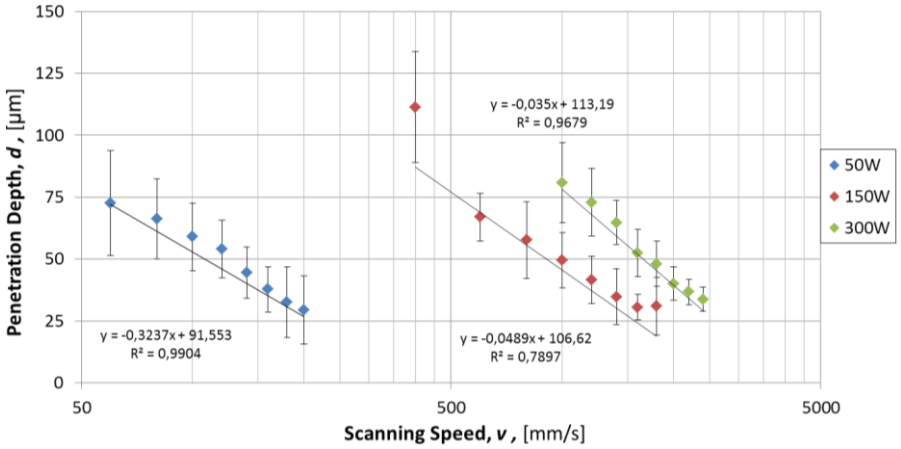

Figure 10.16: Chart displaying the recorded experimental penetration depth measurements against scanning speed for each WC-12Co scan track on the tool steel base plate.

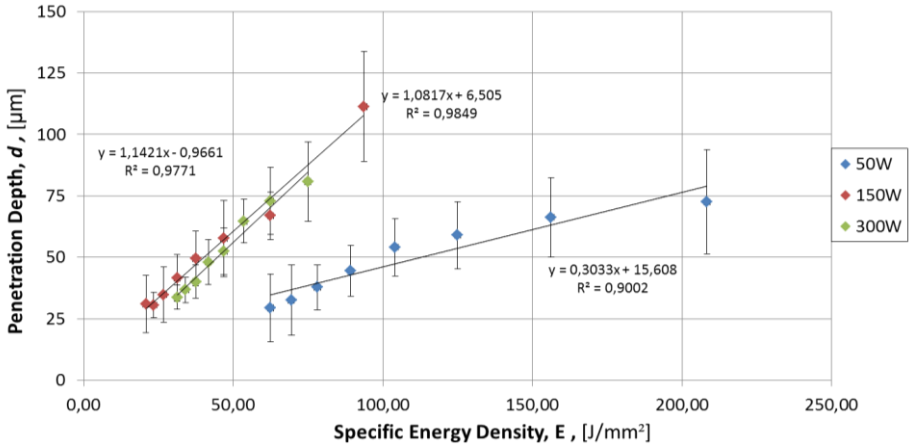

Figure 10.17: Chart displaying the recorded experimental penetration depth measurements against specific energy density for each WC-12Co scan track on the tool steel base plate.

Ti-6Al-4V base plate

The two Ti-6Al-4V penetration depth charts are shown in Figures 10.18 and 10.19, respectively. The experimental and simulated scan track width measurements are compared further in the chapter.

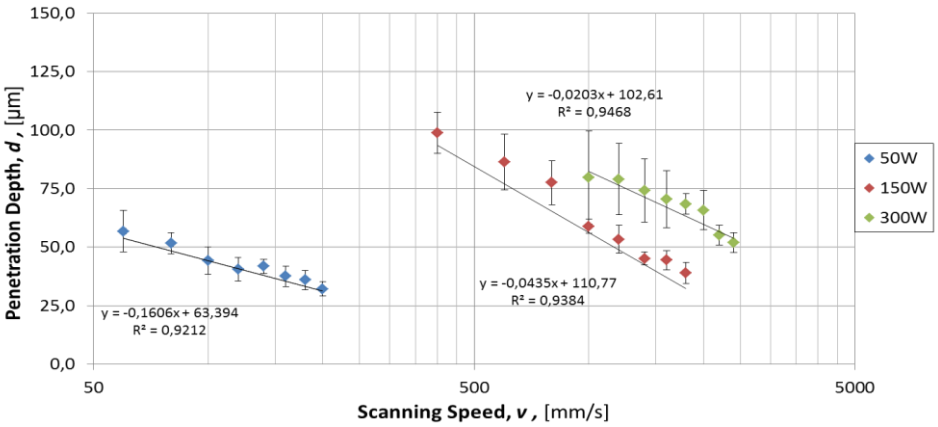

Figure 10.18: Chart displaying the recorded experimental penetration depth measurements against scanning speed for each WC-12Co scan track on the Ti-6Al-4V base plate.

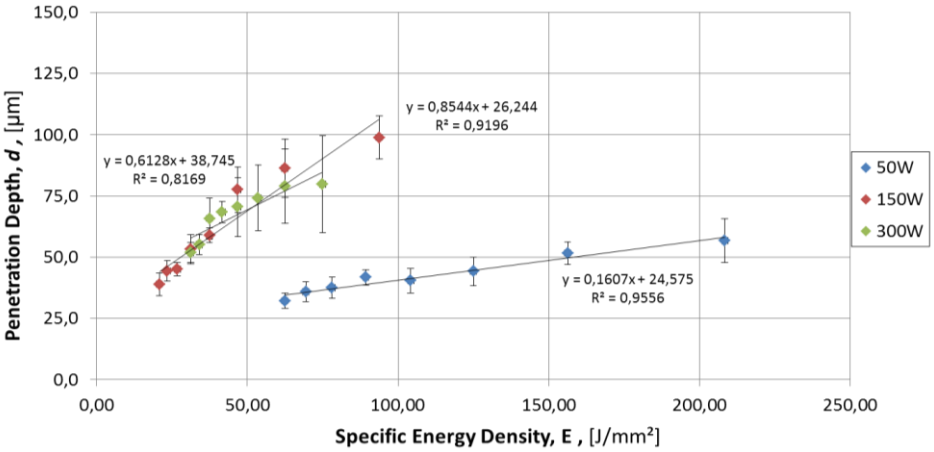

Figure 10.19: Chart displaying the recorded experimental penetration depth measurements against specific energy density for each WC-12Co scan track on the Ti-6Al-4V base plate.

Keyholeing

The reason behind the anomaly at 150W and 400 mm/s is due to a phenomenon known as keyholeing. It is caused by cavitation driving evaporating material deeper into the base layers (Meier *et al*., 2017). Keyholes are common at high energy densities and causes gasses (pores) to be trapped in the solidified melt pool. Keyholes are unwanted defects as they are one of the main sources of part porosity (Gong *et al*., 2014). The keyhole observed in the experimental result is shown in Figure 10.20 along with a description of the phenomena from literature.

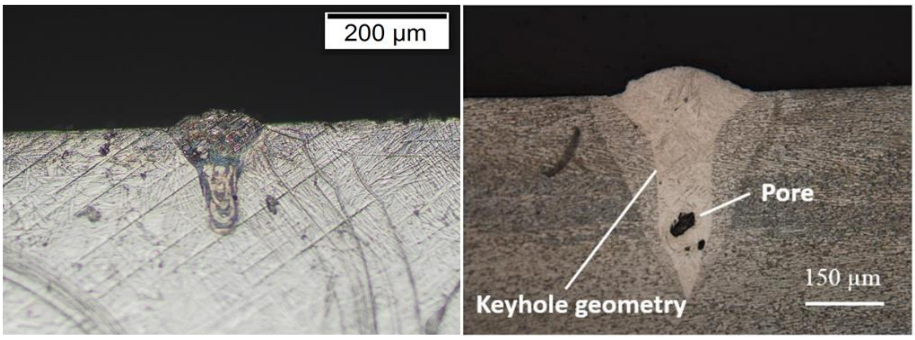

(a) (b)

Figure 10.20: Keyholeing observed in (a) experimental results at 150W, 400mm/s compared to (b) literature observations (Gong *et al.*, 2014).

Single track penetration composition

Although it is possible to determine the penetration depth solely from the optical microscope measurements, additional information about the HAZ can be provided by a SEM analysis of the sectioned base plate. The SEM analysis provides a clear indication of the HAZ without the need for chemical etching. The SEM image of the sectioned Ti-6Al4V base plate can be seen in Figure 10.21.

Another method of determining the scan track penetration depth is by performing an EDX analysis of the sectioned sample. It provides information on the chemical composition of the section and reveals whether the HAZ has penetrated deeper than what can be observed. The penetration depth EDX analysis is shown in Figure 10.22. It is evident from the analysis that weight percentage (wt%) of the scan track decreases with increasing distance through the Ti-6Al-4V base plate. Diffusion at the scan track – base plate interface appears to have taken place, as both of these materials compositions are present at the interface. It is significant to see that diffusion has exceeded what can be observed on the SEM images. In the SEM image in the top half of Figure 10.22, the observed scan track penetrated only 55 μm into the base plate, however the EDX analysis reveals that diffusion of the powdered material has exceeded 65 μm. Although this technique reveals more about the penetration depth than optical microscopy, it was decided to keep to the methods used by past researchers, hence this data was not fully utilised in this study. However, it serves as a reminder for possible simulation inaccuracy.

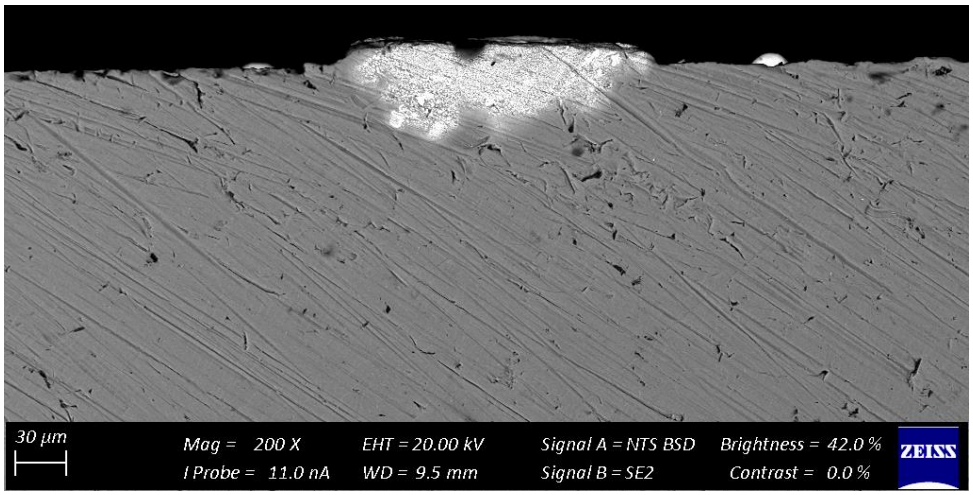

Figure 10.21: SEM image of the sectioned scan track at 50W, 60 mm/s on the Ti-6Al-4V base plate.

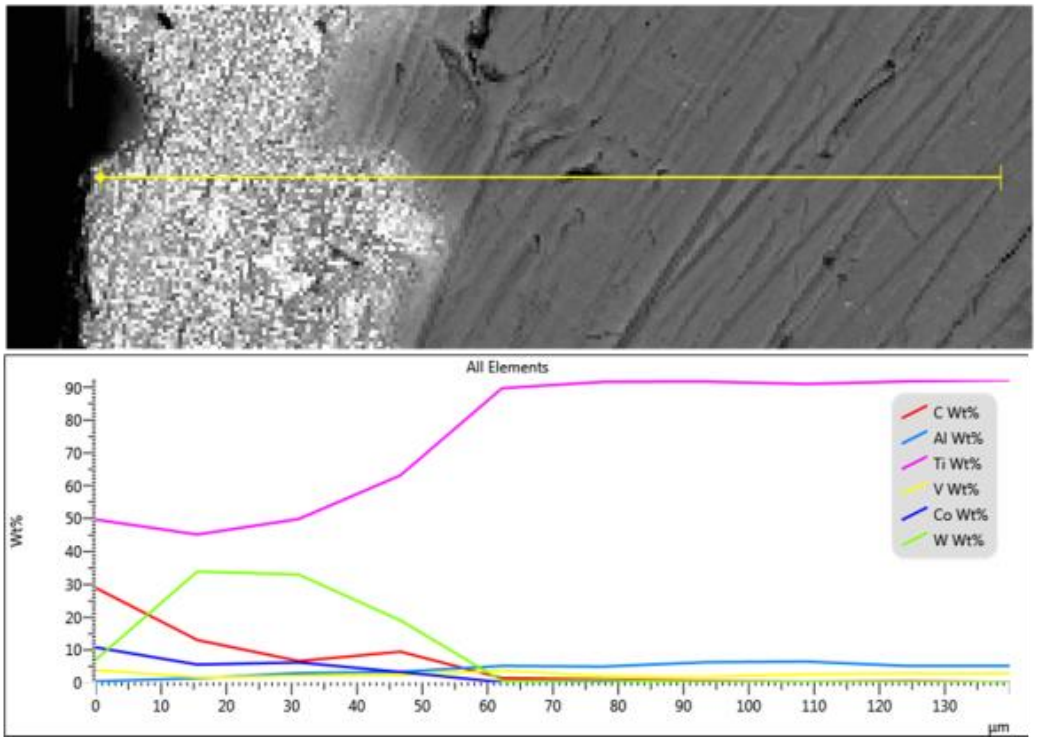

Figure 10.22: Melt pool penetration analysis. EDX analysis of the HAZ composition through the Ti-6Al-4V base plate. Each colour represents a different element.

10.3 Simulation vs Experimental Comparison

The final task in the result analysis section is to compare the simulated results to the experimental results and to determine the deviation or error between the measurements. The error is calculated by determining the absolute value of the percentage difference in the simulated measurement from the actual experimental value. Once again, the comparisons are made for all width and depth measurements for both materials. The comparisons are grouped in their respective laser power intensity settings against the increasing scanning speeds.

10.3.1 Track Width Comparison

Tool steel base plate

The track width comparison and deviation graphs for the tool steel base plate are displayed in Figure 10.23 and Figure 10.24, respectively.

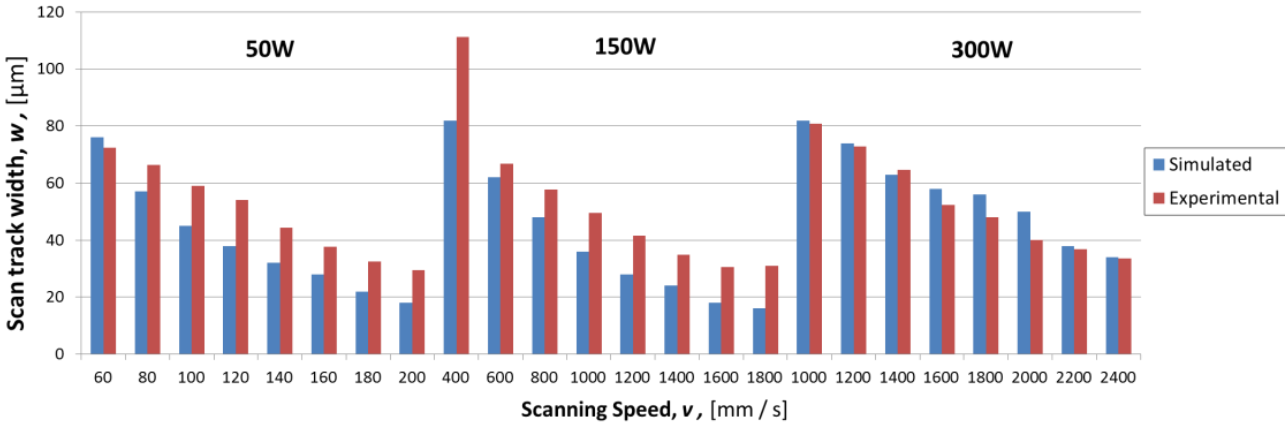

Figure 10.23: Chart displaying the track width comparison for the tool steel base plate.

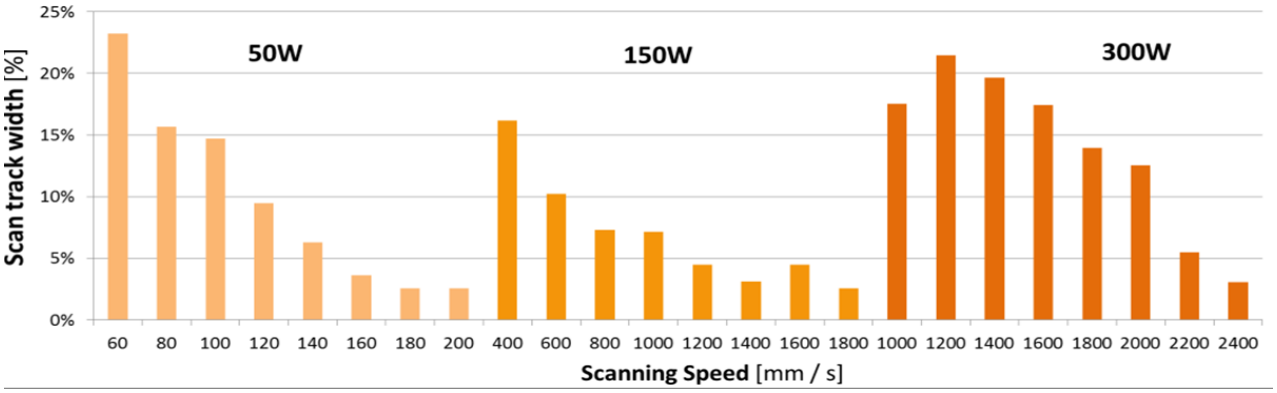

Figure 10.24: Chart displaying the track width deviation for the tool steel base plate.

Ti-6Al-4V base plate

The track width comparison and deviation graphs for the Ti-6Al-4V base plate are displayed in Figure 10.25 and Figure 10.26, respectively.

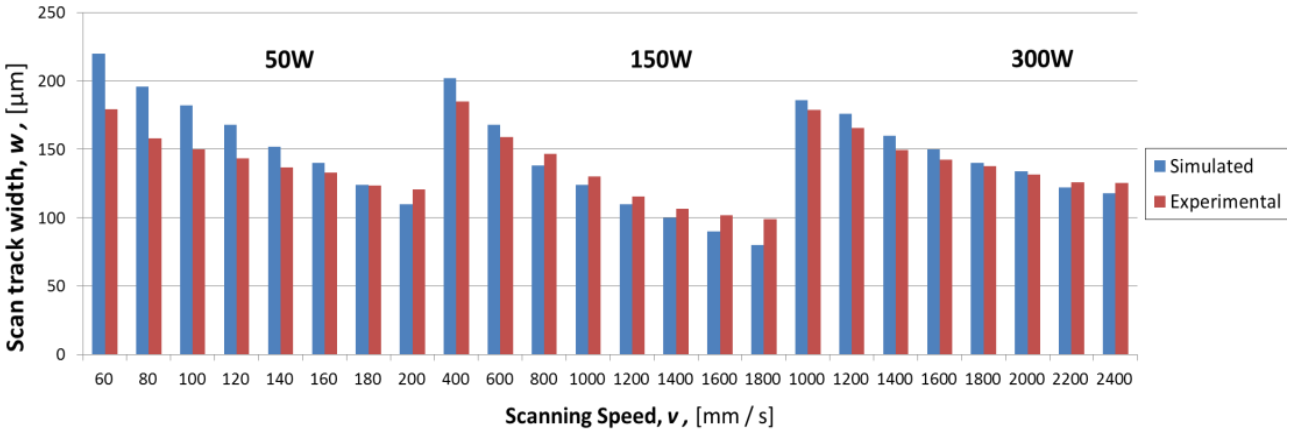

Figure 10.25: Chart displaying the track width comparison for the Ti-6Al-4V base plate.

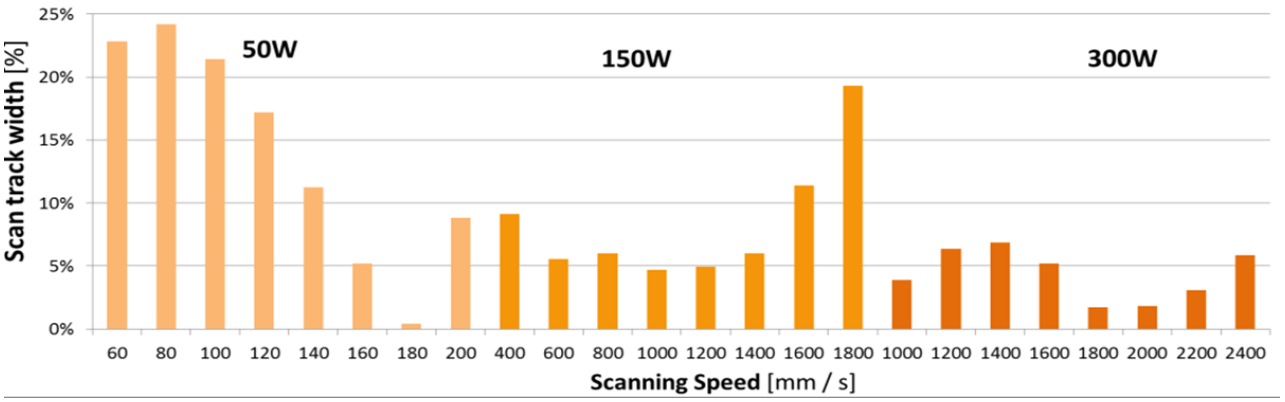

Figure 10.26: Chart displaying the track width deviation for the Ti-6Al-4V base plate.

The following observations were made from the track width comparison graphs:

1. In both of the comparison graphs, the simulation follows the same declining trend as the experimental measurements.
2. The simulation displays a faster decline than the experimental results.

3. There seems to be a constant error trend for all power intensity settings in the width measurements. Initially the deviation is large at the lower scanning speeds, but then slowly decreases until an inflection point is reached where after it increases again.
4. The lower power intensity setting yielded the highest error values for both base plate materials. However, the error value is below 25%, which may be argued as acceptable for an initial estimation.
5. The average width measurement deviation for the tool steel and Ti-6Al-4V base plate is 10.2% and 8.9%, respectively, which is an indication good of the rigidity of the simulation.

10.3.2 Penetration Depth Comparison

Tool steel base plate

The penetration depth comparison and deviation graphs for the tool steel are displayed in Figure 10.27 and Figure 10.28, respectively.

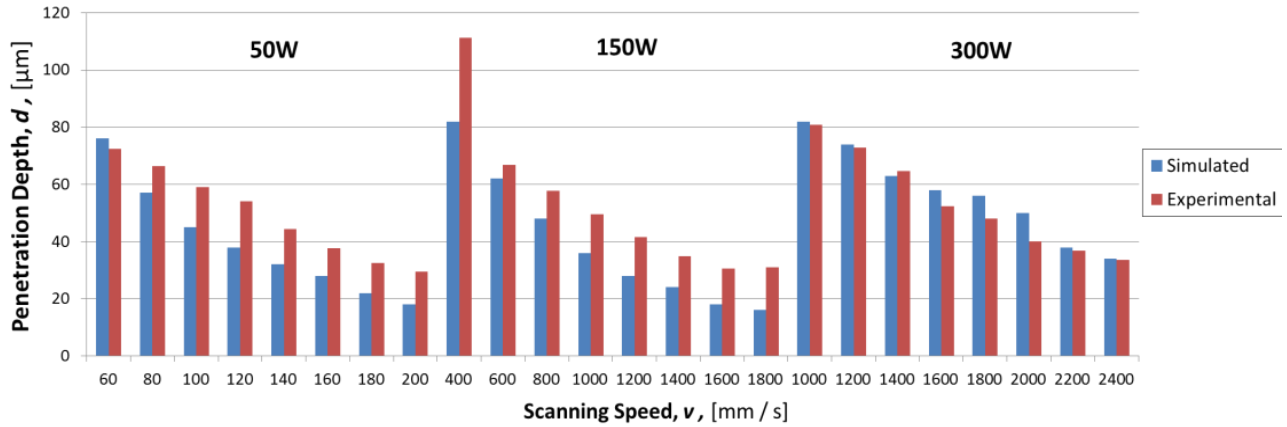

Figure 10.27: Chart displaying the penetration depth comparison for the tool steel base plate.

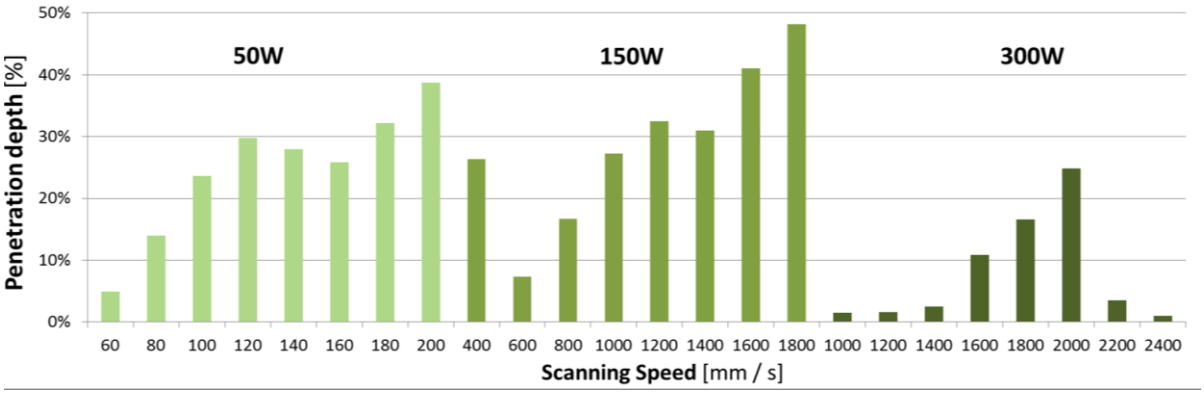

Figure 10.28: Chart displaying the penetration depth deviation for the tool steel base plate.

Ti-6Al-4V base plate

The penetration depth comparison and deviation graphs for the Ti-6Al-4V base plate are displayed in Figure 10.29 and Figure 10.30, respectively.

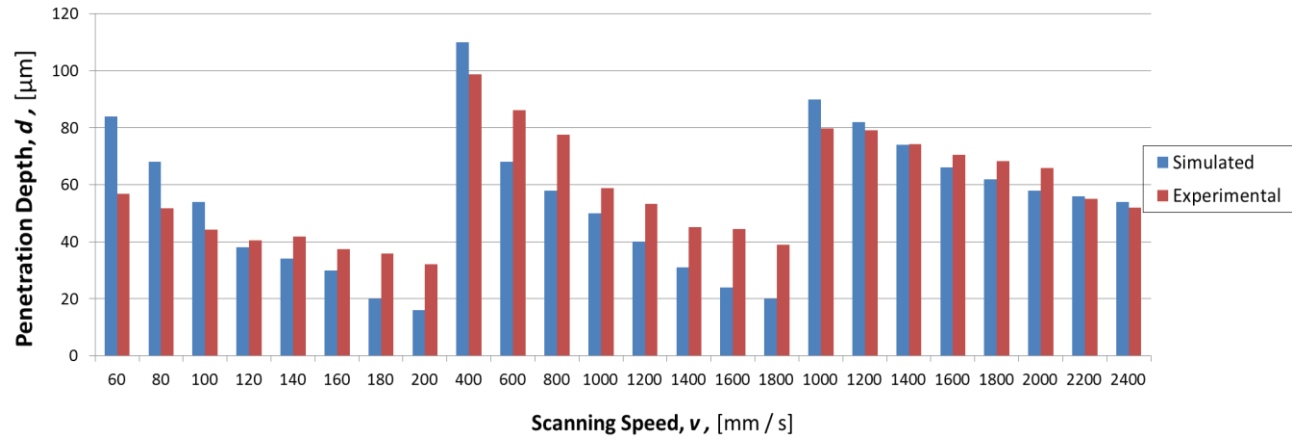

Figure 10.29: Chart displaying the penetration depth comparison for the Ti-6Al-4V base plate.

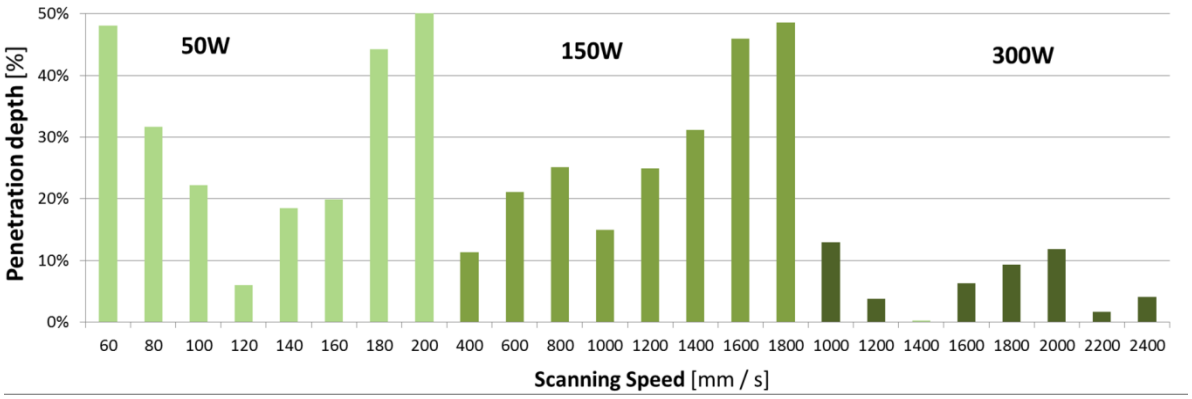

Figure 10.30: Chart displaying the penetration depth deviation for the Ti-6Al-4V base plate.

The following observations were made from the penetration depth comparison graphs:

1. In both comparisons graphs the simulation follows the same declining trend as the experimental measurements.
2. The simulation displays a faster decline than the experimental results.
3. The error trend observed for the width measurements is still present in the penetration depth comparison although it is not so clearly visible in the tool steel base plate deviation results.
4. There is a much larger deviation in the penetration depth comparison than in the scan track width comparison. Although, in both cases, the 300W grouping displayed a very good approximation to the actual results as all error lie below 25%.
5. The lower and medium power intensity settings both yielded the highest error values (above 30%) in both base plate materials.
6. The average penetration depth deviation for the tool steel and Ti-6Al-4V base plate is 20.4% and 21.4%, respectively, which is once again very similar and an indication of good model rigidity.

10.3.3 Reasons for Model Deviation

As mentioned previously in the study, the laser powder bed fusion process is a highly complex phenomena, which makes it extremely difficult to describe analytically. There could be multiple reasons why the simulated model deviates from the experimentally observed results.

1. Powder continuum approach. Erroneous assumptions are one of the main contributors to simulation errors. Although the thermal model in this study included measures, which took into

account the voids between neighbouring powder particles, this was a global assumption based on a mean and not a distribution (Meier *et al.*, 2017).

2. Over simplification. The input heat distribution may be oversimplified. Vaporization can carry away a substantial amount of laser energy affecting the powder's absorptivity (Khairallah *et al.*, 2016). However, this study did not aim to develop a new numerical thermal model, it rather employed well researched models from past literature, although the author acknowledges that it may have effects on the outcome.

3. Experimental setup may be incorrect. An uncalibrated machine, which does not produce the actual process parameters as selected by the operator may lead to experimental inaccuracies (Loh *et al.*, 2015).

10.3.4 Cost Comparison

A cost comparison between the simulation and experimental parameter analysis was performed using the actual expenses of this study. A full summary of each expense is provided in Appendix A. The experimental section was based on expenses related to the Ti-6Al-4V base plate only as this was the most expensive material used during the calibration tests. The results of the cost comparison between the single track simulation processing parameter predictions and experimental tests are shown in the graph in Figure 10.31.

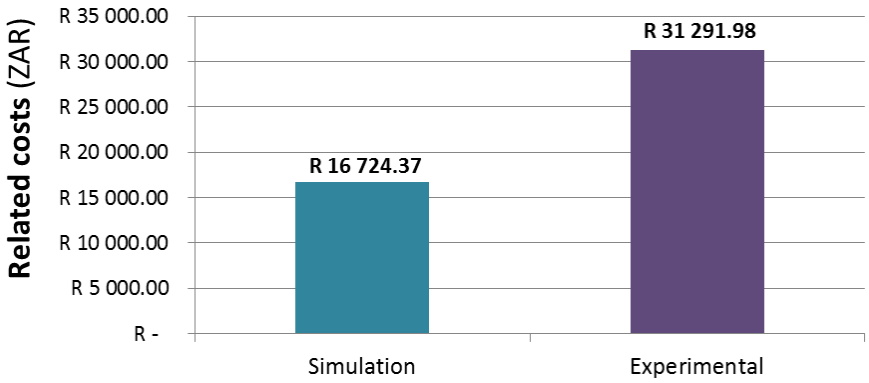

Figure 10.31: Cost comparison between the two material calibration methods discussed in this study.

It is clear from the graph that the experimental calibration method was nearly double the costs of the simulated calibration method. This further adds to the motivation that numerical methods should be considered to aid in the R&D calibration process. Although the expenses of the material calibration phase seem disconcerting, it is still greatly lower than that of externally developed material calibration tests. A quote from EOS, which provides the full set of parameters for the Laser processing of maraging steel MS1 was set at €23 080.00 or R371 818.80 (at €1 = R16.11). Clearly, the financial motivation exists to perform processing parameter calibration tests in-house rather than from external suppliers, however without the correct methods and past knowledge these tests could prove to be unsuccessful and equally expensive.

Chapter 11: Conclusion

Overview

This concluding chapter summarises the findings of the study and discusses future work, which may lead to possible improvements on the current results. It aims to answer the questions about the initial research problem and project objectives. Finally, the chapter highlights the benefits of this study for the research and industry fields alike.

11.1 Conclusion

The aim of this study was to address a specific problem identified in the current SLS process chain. The researcher identified a shortcoming in the efficiency of the current research and development process chain of the SLS industry. The researcher aimed to improve the way manufacturers currently perform material calibration tests when introducing new materials to their existing SLS manufacturing setup. This has been identified as a problem area as the material specific processing parameters, which are required to produce high quality components, are often unavailable or need to be purchased separately from the SLS/SLM OEM's.

Processing parameters for the more established SLS materials such as stainless steel (304L) or titanium (Ti-6Al-4V) are readily available to manufacturers, however parameters for lesser-known SLS materials such as tungsten carbide (WC) are more difficult to find. Hence, manufacturers are forced to undergo rigorous machine calibration tests, which are time-consuming and resource intensive. This is a highly inefficient approach, especially for SMEs who aim to compete in an ever evolving and highly competitive global industry. A good business strategy is to incorporate novel tools, which may minimise or eliminate current inefficiency in a process chain.

The aim of this study was to investigate whether numerical methods could be used to predict the developed melt pool in a single track SLS scan track whilst varying certain processing parameters. The processing parameters recommended from the developed thermal model were able to produce experimental WC-Co scan tracks of a sufficient quality. Measurements of the experimental scan track geometry proved that the numerical thermal model was able to predict the heat transfer in the powder bed and base plate successfully.

Past numerical models have been developed, which were able to describe the multi-physical behaviour of the laser sintering process, however these models require expertise of highly skilled persons. Hence, the focus in this study shifted towards a more basic thermal numerical model, which is inexpensive and easy to develop for moderately skilled manufacturers. The hope is that the results from even this simple thermal model will drastically improve the efficiency of the R&D SLS process chain.

11.1.1 Project Methodology

A basic thermal model was constructed in order to predict the thermal behaviour of WC-Co using specific software programs, material properties and numerical techniques identified through an extensive literature study. The parameter screening was reduced to laser power and scanning speed, as these have been proven in literature to have the most significant influence on the final part quality. A suitable parameter processing window was identified using the maximum temperature values from the developed thermal model. This allowed the researcher to reduce the parameter search area dramatically from the traditional calibration search window. However, the parameters identified in this window still needed to be validated experimentally in order to ensure the

numerical thermal model produced an accurate approximation. The validation was based on the geometry of the melt pool caused by the moving laser beam. The simulated scan track width and base plate penetration depth was then compared to experimental results in a graphical format in order to determine the error in the approximation. Additionally, two different base plate materials, namely tool steel and a titanium alloy, were used to prove model rigidity.

11.1.2 Project Findings

It was found that:

1. The numerical simulation was able to reproduce a melt pool, which followed a similar geometrical trend as the experimental validation single track scan. Both the scan track width and penetration depth decreased with increasing scanning speed, which is constant with literature. However, the width and penetration depth did not seem to be highly affected by increasing laser power. This was evident from the ANOVA statistical study.

2. The simulation was not able to match the same rate of decay of the geometrical features of the experimental scan tracks. Scanning speed became less significant at higher speeds in the experimental results; however, the numerical model could not track this change precisely. This resulted in a constant simulation error, whereby the simulated predictions were higher at slower scanning speeds and lower at faster scanning speeds.

3. The numerical model was successful at predicting the scan track width measurements. The average error between the simulated and experimental results for the tool steel and Ti-6Al-4V was 10.2% and 8.9%, respectively, with the highest deviation below 25% for both materials.

4. The numerical model was less accurate at predicting the scan track penetration depth measurements. The average error between the simulated and experimental results for the tool steel and Ti-6Al-4V was 20.4% and 21.4%, respectively, with the highest deviation below 50% for both materials.

5. The model rigidity seemed reasonable with a good correlation between the simulation and experimental results for both the tool steel and Ti-6Al-4V base plates.

6. The cost comparison revealed that the simulation was 46.5% cheaper than experimental calibration method. The simulation and experimental methods remained more affordable than purchasing the pre-developed parameter sets.

11.2 Benefit to Industry

Although the numerical thermal model could not precisely track the variation in each scan track's geometrical features with changes in the parameter sets, it was still able to provide a reasonable estimation of the influences of the varying parameters. From the quantitative literature review, it was observed that very few numerical models were able to simulate a multi-track, multi-layer laser process and even these complex models have inherent inaccuracies.

Hence, the message to industry is that numerical simulation may not be able to completely replace the physical material calibration, but may be used in order to reduce the scope of the parameter screening analysis and predict the extent of the HAZ. It was shown in the project that a basic single-track thermal model was able to predict the scan track width within 25% and penetration depth within 50% of actual results, which may be argued as a good initial estimation of possible processing parameters for novel or unconventional SLS materials. The decision lies with

manufacturers whether to spend more time to improve the simulation in order to reduce the error, or to accept the simulated results and make decisions regarding other input parameters such as hatch spacing and layer thickness based on these results.

On the financial side, it was proven that the simulation calibration method was 47% cheaper than the experimental screening. This is a substantial decrease in costs for a dramatically reduced calibration window.

11.3 Recommendations

Owing to some general assumptions made in this study, some recommendations can be made in order to improve on the findings of this project.

1. An assumption made during this project, which most definitely affected the deviation from reality was the assumption of phase transformation. In this project, it was assumed that the melt pool changed from the powder state directly to the solid state, ignoring the liquid state completely. However, this may become a challenging task, when considering the temperature dependent material properties of the liquid phase.

2. The influence of different heat input profiles should be investigated. During this study, only Goldaks's ellipsoidal distribution was investigated, however numerous profiles exists, as mentioned in this study. Perhaps there is a heat distribution approximation, which yields a better fit for the experimental results.

3. More parameter sets combinations should be included for the parameter screening. In this study, there was an adequate variation of scanning speed, but the laser power was only tested at three laser power intensity settings. Ideally, four or five power settings would give a better understanding of the material response.

4. In future studies, the selected base plate material should have a melting temperature substantially higher than that of the powder. The similar melting temperatures of the cobalt binder and tool steel base plate made it difficult to perform accurate observations and measurements of the scan tracks.

11.4 Future Work

Owing to time and resource constraints, some aspects of this study were left as future work. This may include:

1. The study only investigated a single-track scan track. Future work may investigate the temperature-history caused by multiple-track and multiple-layer scans.

2. The researcher was limited to a single software programme. However, from the quantitative systematic review, it was observed that multiple numerical modeling environments exists, which are equally capable of performing the uncoupled thermal analyses shown in this study.

3. Future researchers may expand the study to include different numerical techniques and even combinations of these techniques in order to reduce the simulation error.

4. The study may also be developed to include another powder material, other than WC-Co. This may add strength to the findings and theory of this report.

5. Future work may investigate whether WC-Co samples made from the SLS processing parameters identified in this study will have adequate mechanical properties for industry purposes.

Ideally, in future researchers and manufacturers would be able to simulate the SLS process including all of the multi-physics involved in this study on a multiple-scale, with a very high level of accuracy.

References

1. 3T RPD. 2016. *Material Specification*. [Online], Available: https://www.3trpd.co.uk/wp-content/uploads/2015/05/Maraging-Steel-1-2709.pdf [2018, August 27].
2. A. Cengel, Y. & J. Ghajar, A. 2015. *Heat and Mass Transfer, Fundamentals & Application, Fifth Edition in SI Units*. Vol. 5th. New York.
3. ACNA. 2014. *Pros and Cons of Additive Manufacturing*. [Online], Available: http://compositesmanufacturingmagazine.com/2014/10/pros-cons-additive-manufacturing/ [2017, April 21].
4. Almond, E.A. & Roebuck, B. 1988. Identification of Optimum Binder Phase Compositions for Improved WC Hard Metals. *Materials Science and Engineering*. 105(1):237–248.
5. Amatoa, K.N., Gaytana, S.M., Murra, L.E., Martineza, E., Shindoa, P.W., Hernandeza, J., Collinsc, S. & Medina, F. 2012. Microstructures and mechanical behavior of Inconel 718 fabricated by selective laser melting. *Acta Materialia*. 60(5):2229–2239.
6. Antony, K., Arivazhagan, N. & Senthilkumaran, K. 2014. Numerical and experimental investigations on laser melting of stainless steel 316L metal powders. *Journal of Manufacturing Processes*. 16(3):345–355.
7. Ardila, L.C., Garciandia, F., González-Díaz, J.B., Álvarez, P., Echeverria, A., Petite, M.M., Deffley, R. & Ochoa, J. 2014. Effect of IN718 recycled powder reuse on properties of parts manufactured by means of Selective Laser Melting. *Physics Procedia*. 56(56):99–107.
8. Ashley, S. 1991. Rapid Prototyping Systems. *Mechanical Engineering*. 113(4):34.
9. Bak, D. 2003. Rapid prototyping or rapid production? 3D printing processes move industry towards the latter. *Assembly Automation*. 23(4):340–345.
10. Basu, B. 2018. *The Technological Innovation and Shift in Business Practices*.
11. Basu, B. & Date, A.W. 1990. Numerical study of steady state and transient laser melting problems—I. Characteristics of flow field and heat transfer. *International Journal of Heat and Mass Transfer*. 33(6):1149–1163.
12. Beard, M.A., Ghita, O.R. & Evans, K.E. 2011. Monitoring the effects of selective laser sintering (SLS) build parameters on polyamide using near infrared spectroscopy. *Journal of Applied Polymer Science*. 121(6):3153–3158.
13. van Belle, L., Vansteenkiste, G. & Boyer, J.C. 2013. Investigation of Residual Stresses Induced during the Selective Laser Melting Process. *Key Engineering Materials*. 554–557:1828–1834.
14. Berman, B. 2012. 3-D printing: The new industrial revolution. *Business Horizons*. 55(2):155–162.
15. Berry, E., Brown-T, J.M., Connellf, M., Craven&, C.M., Effordll, N.D., Radjenovic, A. & Smith, M.A. 1997. Preliminary experience with medical applications of rapid prototyping by selective laser sintering Computer visualization techniques for rendering. *Med. Eng. Phys. Med. Eng. Phys*. 19(19):90–96.
16. Bhargav, A., Sanjairaj, V., Rosa, V., Feng, L. & Yh, J. 2017. Applications of additive manufacturing dentistry: A review. *Journal of Biomedical Materials Reserch*. 10(1):213.
17. Bhaskaran, R. & Collins, L. 2002. *Introduction to CFD basics*.
18. Brecher, C. & Ozdemir, D. 2016. *Integrative Production Technology: Theory and Applications*. Springer.
19. Brundtland, G.H. 1987.
20. BusinessDictionary. 2018. *What is efficiency?* [Online], Available: http://www.businessdictionary.com/definition/efficiency.html [2018, February 12].
21. Busse, M. 2016. *Additive manufacturing using laser sintering*. Bremen. [Online], Available: http://www.phenix-systems.com/en.
22. Campbell, R.I. & de Beer, D.J. 2005. Rapid prototyping in South Africa: past, present and future. *Rapid Prototyping Journal*. 11(4):260–265.
23. Campbell, I., Bourell, D. & Gibson, I. 2012. Additive Manufacturing: Rapid Prototyping comes

of age. *Rapid Prototyping Journal*. 18(4):255–258.
24. Capus, J.M. 2000. *Metal Powders: A Global Survey of production, Applications and Markets*.
25. Cheng, B. & Chou, K. 2015. Melt Pool Evolution Study in Selective Laser Melting. In Austin, Texas *26th International Solid Freeform Fabrication Symposium*. 1182–1194.
26. Cohen, M.A., Eliasberg, J. & Ho, T.-H. 1996. New Product Development: The Performance and Time-to-Market Tradeoff. *Management Science*. 42(2):173–186.
27. Cook, R.D., Malkus, D.S., Plesha, M.E. & Witt, R.J. 2002. *Concepts and Applications of Finite Element Analysis*. 4th ed. Hoboken: John Wiley & Sons.
28. Dai, D. & Gu, D. 2014. Thermal behavior and densification mechanism during selective laser melting of copper matrix composites: Simulation and experiments. *Materials and Design*. 55:482–491.
29. Dantzig, J.A. & Rappaz, M. 2016. *Solidification*. 2nd ed. EPFL Press.
30. Das, S., McWilliams, B., Wu, B. & Beaman, J.J. 1991. Design of a High Tem perature Workstation for the Selective Laser Sintering Process. In Austin, TX: Department of Mechanical Engineering. The University if Texas at Austin. *Proceedings of the 2nd Solid Freeform Symposium*. 164–170.
31. Dassault Systems. 2016. *ABAQUS/Standard User's Manual, Version 6.14*. Providence, RI: Simulia.
32. Deckard, C.R. 1990. *Patent No. US5017753 A*. United States of America.
33. Desai, A. 2015. *Why innovation and enterprise are a driving force for social impact | World Economic Forum*.
34. Diegel, O., Singamneni, S., Reay, S. & Withell, A. 2010. Tools for Sustainable Product Design: Additive Manufacturing. *Journal of Sustainable Development*. 3(3):68–75.
35. Domashenkov, A., Borbély, A. & Smurov, I. 2017. Structural modifications of WC/Co nanophased and conventional powders processed by selective laser melting. *Materials and Manufacturing Processes*. 32(1):93–100.
36. Dong, L., Barth, N., Correia, J.P.M., Ahzi, S. & Cnrs, U.D.S. 2016. Modeling and Numerical Simulation of Selective Laser Sintering. In *Thermal, Mechanical and Multi-Physics Simulation and Experiments in Microelectronics and Microsystems (EuroSimE), 2016 17th International Conference*. 2–5.
37. Dunbar, A.J., Denlinger, E.R., Gouge, M.F. & Michaleris, P. 2016. Experimental validation of finite element modeling for laser powder bed fusion deformation. *Additive Manufacturing*. 12(1):108–120.
38. Duzevik, D. 2017. *Advantages and Disadvantages of Simulation - Concentric*. [Online], Available: https://concentricmarket.com/blog/advantages-and-disadvantages-of-simulation/ [2018, April 23].
39. EDinformatics. 1999. *The Carbon Atom*. [Online], Available: http://www.edinformatics.com/math_science/c_atom.htm [2018, January 09].
40. Emsley, J. 2001. *Nature's Building Blocks: An A-Z Guide to the Elements*.
41. Esfahani, M.M. 2016. Welding simulation of steels welded with low transformation temperature (LTT) filler materials. Chalmers University of Technology.
42. Fang, Z.Z. 2004. Correlation of transverse rupture strength of WC–Co with hardness. *Refractory Metals & Hard Materials*. 23(2):119–127.
43. Fernandes, C.M. & Senos, A.M.R. 2011. Cemented carbide phase diagrams: A review. *International Journal of Refractory Metals and Hard Materials*. 29(4):405–418.
44. Fernandes, C.M., Senos, A.M.R., Vieira, M.T. & Antunes, J.M. 2008. Mechanical characterization of composites prepared from WC powders coated with Ni rich binders. *International Journal of Refractory Metals & Hard Materials*. 26(5):491–498.
45. Fisher, U.K.R., Hartzell, E.T. & Akerman, J.G.H. 1988.
46. Foroozmehr, A., Badrossamay, M., Foroozmehr, E. & Golabi, S. 2016. Finite Element Simulation of Selective Laser Melting process considering Optical Penetration Depth of laser in powder bed. *Materials and Design*. 89:255–263.

47. Fu, C.H. & Guo, Y.B. 2014. 3-Dimensional Finite Element Modeling of Selective Laser Melting Ti-6Al-4V Alloy. *Solid Freeform Fabrication Symposium*. 1129–1144.
48. Fujibayashi, S., Neo, M., Kim, H.-M., Kokubo, T. & Nakamura, T. 2004. Osteoinduction of porous bioactive titanium metal. *Biomaterials*. 25(1):443–450.
49. Fysikopoulos, A., Pastras, G., Alexopoulos, T. & Chryssolouris, G. 2014. On a generalized approach to manufacturing energy efficiency. *International Journal of Advanced Manufacturing Technology*. 73(9):1437–1452.
50. Gebhardt, A., Fateri, M., Hotter, J.-S., Knothe, M., Schmidt, F.M. & Rieper, H. 2014. Numerical and Experimental Investigation of Selective Laser Melting of Silver. In *Fraunhofer Direct Digital Manufacturing Conference, (DDMC)*.
51. Georgakopoulos, D., Hornick, M. & Sheth, A. 1995. An Overview of Workflow Management: From Process Modeling to Workflow Automation Infrastructure. 3:119–153.
52. German, R.M. 2005. *Powder Metallurgy and Particulate Materials Processing*.
53. German, R. Suri, P. & Park, J. S. 2009. Review: Liquid Phase Sintering. *Journal of Material Science*. 44(1):1-39.
54. Gershenfeld, N. 2012. How to Make Almost Anything: The Digital Fabrication Revolution. *Foreign Affairs*. 91(6):43–57.
55. Goldak, J., Chakravarti, A. & Bibby, M. 1984. A new finite element model for welding heat sources. *Metallurgical Transactions B*. 15(2):299–305.
56. Gong, H., Gu, H., Zeng, K., Dilip, J.J.S., Pal, D., Stucker, B., Christiansen, D., Beuth, J., et al. n.d. Melt Pool Characterization for Selective Laser Melting of Ti-6Al-4V Pre-alloyed Powder.
57. Govender, N., Wilke, D.N., Pizette, P. & Rajamani, R.K. 2017. Industrial Scale Particle Simulations on the GPU Using the Blaze-DEM Code. In Springer *Proceedings of the 7th International Conference on Discrete Element Methods*. 1379–1388.
58. Group, F. 2018. *Environmental Impact of Metal Additive Manufacturing | Farinia Group*. [Online], Available: http://www.farinia.com/additive-manufacturing/3d-technique/environmental-impact-metal-additive-manufacturing [2018, February 23].
59. Gu, D. & He, B. 2016. Finite element simulation and experimental investigation of residual stresses in selective laser melted Ti – Ni shape memory alloy. *Computational Materials Science*. 117:221–232.
60. Gu, D., Dai, D., Chen, W. & Chen, H. 2016. Selective Laser Melting Additive Manufacturing of Hard-to-Process Tungsten-Based Alloy Parts With Novel Crystalline Growth Morphology and Enhanced Performance. *Journal of Manufacturing Science and Engineering*. 138(8):1003–1011.
61. Gu, D.D., Meiners, W., Wissenbach, K. & Poprawe, R. 2012. Laser additive manufacturing of metallic components: materials, processes and mechanisms. *International Materials Reviews*. 57(3):133–164.
62. Gürtler, F.-J., Karg, M., Leitz, K.-H. & Schmidt, M. 2013. Simulation of Laser Beam Melting of Steel Powders using the Three-Dimensional Volume of Fluid Method. *Physics Procedia*. 41:881–886.
63. Gürtler, F. j., Karg, M., Dobler, M., Kohl, S., Tzivilsky3, I. & Schmidt, M. 2014. Influence of powder distribution on process stability in laser beam melting: Analysis of melt pool dynamics by numerical simulations. *Solid freeform symposium, Texas*. 1099–1117.
64. Gusarov, A. V. & Kruth, J.-P.P. 2005. Modelling of radiation transfer in metallic powders at laser treatment. *International Journal of Heat and Mass Transfer*. 48(16):3423–3434.
65. Gustafson, P. 1987. A thermodynamic evaluation of the C−Fe−W system. *Metallurgical Transactions A*. 18(2):175–188.
66. Hagedorn-Hansen, D. 2017. The Effects of Developed Selective Laser Melting Strategies on Titanium Hybrid Parts by.
67. Hauser, C., Chillds, T. & Dalgarno, K.W. 1999. Selective Laser Sintering of Stainless Steel 314S HC processed using room temperature powder beds. In *Proceedings of the SFF Symposium*. 273–280.

68. Heilala, J., Paju, M., Montonen, J., Hentula, M. & Heikkila, A. 2010. Modelling and Simulation for Lean and Sustainable Manufacturing System Development. In *Advance in Production Management Systems (APMS)*. 22.
69. Heinze, C. Schwenk, C. Rethmeier, M. 2012. Effect of heat source configuration on the results of quality of numerical calculation of welding induced distortion. *Simulation Modelling Practice and Theory*. 112-123.
70. House, C.H. & Price, R.L. 1991. *The Return Map: Tracking Product Teams*.
71. Huang, S.H., Liu, P., Mokasdar, A. & Hou, L. 2013. Additive manufacturing and its societal impact: A literature review. *International Journal of Advanced Manufacturing Technology*. 67(5–8):1191–1203.
72. Huang, Y., Yang, L.J., Du, X.Z. & Yang, Y.P. 2016. Finite element analysis of thermal behavior of metal powder during selective laser melting. *International Journal of Thermal Sciences*. 104:146–157.
73. Hussein, A., Hao, L., Yan, C. & Everson, R. 2013. Finite element simulation of the temperature and stress fields in single layers built without-support in selective laser melting. *Materials and Design*. 52(1):638–647.
74. International Trade Administration. 2010. *How Does Commerce Define Sustainable Manufacturing?*
75. ISAF & BIAS. 2012. *Generieren und Fügen von SLM-Bauteilen aus Hartmetall*.
76. Jones, J.L.S. & Linderman, K. 2014. Process management, innovation and efficiency performance. The moderating effect of competitive intesity. *Business Process Management Journal*. 20(2):335–358.
77. Kearney, A.T. 2015. *3D Printing : a Manufacturing Revolution*. Korea.
78. Kempen, K., Thijs, L., Vrancken, B., Buls, S., Humbeeck, J. Van & Kruth, J.-P. 2013. Producing Crack-Free, High Density M2 HSS Parts by Selective Laser Melting: Pre-Heating the Base plate. *Solid FreeformFabrication Symposium Proceedings*. 131–139.
79. Khairallah, S.A., Anderson, A.T., Rubenchik, A. & King, W.E. 2016. Laser powder-bed fusion additive manufacturing: Physics of complex melt flow and formation mechanisms of pores, spatter, and denudation zones. *Acta Materialia*. 108:36–45.
80. Khmyrov, R.S., Safronov, V.A. & Gusarov, A. V. 2017. Synthesis of Nanostructured WC-Co Hardmetal by Selective Laser Melting. *Procedia IUTAM*. 23:114–119.
81. Kim, H.-C., Shon, I.-J., Yoon, J.-K., Doh, J.-M. & Munir, Z.. 2006. Rapid sintering of ultrafine WC-Ni cermets. *International Journal of Refractory Metals & Hard Materials*. 24(6):427–431.
82. Kovaleva, I., Kovalev, O. & Smurov, I. 2014. Model of heat and mass transfer in random packing layer of powder particles in selective laser melting. *Physics Procedia*. 56(C):400–410.
83. Król, M., Dobrzański, L.A., Reimann, Ł., Czaja, I. & Reimann, I. 2013. Surface quality in selective laser melting of metal powders. *Archives of Materials Science*. 60(2):87–92.
84. Kruth, J.P. 1991. Material Incress Manufacturing by Rapid Prototyping Techniques. *CIRP Annals - Manufacturing Technology*. 40(2):603–614.
85. Kruth, J.-P., Mercelis, P. & Van Vaerenbergh, J. 2005. Binding mechanisms in selective laser sintering and selective laser melting. *Rapid Prototyping Journal*. 11(1):26–36.
86. Kruth, J.-P., Mercelis, P., Van, J., Froyen, V.L., Rombouts, M., Vaerenbergh, J. Van & Froyen, L. 2005. Binding mechanisms in selective laser sintering and selective laser melting. *Rapid Prototyping Journal Rapid Prototyping Journal Iss Rapid Prototyping Journal*. 11(5):314–326.
87. Kruth, J.-P., Vandenbroucke, B., Van Vaerenbergh, J. & Naert, I. 2005. Digital manufacturing of biocompatible metal frameworks for complex dental prostheses by means of SLS/SLM. In *Proceedings of the VRAP*. 139–145.
88. Kruth, J.P., Kumar, S. & Van Vaerenbergh, J. 2005. Study of laser sinterability of ferro based powders. *Rapid Prototyping Journal*. 11(5):287–292.
89. Kumar, S. 2003. Selective Laser Sintering: A Qualitative and Objective Approach. *Journal of Manufacturing*. 55(10):43–47.
90. Kumar, S. 2009. Manufacturing of WC-Co moulds using SLS machines. *Journal of Material*

Processing Technology. 209(8):3840–3848.
91. Kundakcioglu, E., Lazoglu, I. & Rawal, S. 2016. Transient thermal modeling of laser-based additive manufacturing for 3D freeform structures. *The International Journal of Advanced Manufacturing Technology*. 85(4):493–501.
92. Kuznetsov, A.P., Koriath, H.-J. & Kalyashina, A.V. 2017. Comparative Integrated Manufacturing Efficiency in Production Engineering. In *The 50th CIRP Conference on Manufacturing Systems*. 527–532.
93. Lange, J.-P. 2002. Sustainable development: efficiency and recycling in chemicals manufacturingElectronic supplementary information (ESI) available: appendix A: calculation of carbon and inorganic waste production; appendix B: production of carbon and inorganic wastes from . *Green Chemistry*. 4(6):546–550.
94. Lassner, E. & Schubert, W.-D. 2005. The History of Tungsten. *International Tungsten Industry Association*. (December 2005):7–8.
95. Lee, Y.S. & Zhang, W. 2015. Mesoscopic Simulation of Heat Transfer and Fluid Flow in Laser Powder Bed Additive Manufacturing. *International Solid Free Form Fabrication Symposium, Austin*. 1154–1165.
96. Leitz, K.H., Singer, P., Plankensteiner, A., Tabernig, B., Kestler, H. & Sigl, L.S. 2016. Multi-physical simulation of selective laser melting. *Metal Powder Report*. 00(00).
97. Leuders, S., Thöne, M., Riemer, A., Niendorf, T., Tröster, T., Richard, H.A. & Maier, H.J. 2013. On the mechanical behaviour of titanium alloy TiAl6V4 manufactured by selective laser melting: Fatigue resistance and crack growth performance. *International Journal of Fatigue*. 48(1):300–307.
98. Levy, G.N., Schindel, R. & Kruth, J.P. 2003. Rapid Manufacturing and Rapid Tooling with Layer Manufacturing (LM) Technologies State of the Art and Future Perspectives. *CIRP Annals - Manufacturing Technology*. 52(2):589–602.
99. Li, Y. & Gu, D. 2014. Thermal behavior during selective laser melting of commercially pure titanium powder: Numerical simulation and experimental study. *Additive Manufacturing*. 1:99–109.
100. Li, C., Liu, J.F. & Guo, Y.B. 2016. Prediction of Residual Stress and Part Distortion in Selective Laser Melting. *Procedia CIRP*. 45:171–174.
101. Li, C., Fu, C.H., Guo, Y.B. & Fang, F.Z. 2016. A multiscale modeling approach for fast prediction of part distortion in selective laser melting. *Journal of Materials Processing Technology*. 229(1):703–712.
102. Li, J., Wu, B. & Myant, C. 2016. *The Current Landscape for Additive Manufacturing Research: A review to map the UK's research activities in AM internationally and nationally*. London.
103. Liu, C. 2014. Alternative binder phases for WC cemented carbides.
104. Loeber, A.L., Biamino, S., Ackelid, U., Sabbadini, S., Epicoco, P., Fino, P. & Eckert, J. 2011. Comparison of Selective Laser and Electron Beam Melted Titanium. In *Proceedings of the Solid Freeform Fabrication Symposium*. 547–556.
105. Loh, L.-E., Chua, C.-K., Yeong, W.-Y., Song, J., Mapar, M., Sing, S.-L., Liu, Z.-H. & Zhang, D.-Q. 2015. Numerical investigation and an effective modelling on the Selective Laser Melting (SLM) process with aluminium alloy 6061. *International Journal of Heat and Mass Transfer*. 80(2):288–300.
106. Lopez-Botello, O., Martinez-Hernandez, U., Ramírez, J., Pinna, C. & Mumtaz, K. 2017. Two-dimensional simulation of grain structure growth within selective laser melted AA-2024. *Materials and Design*. 113:369–376.
107. Luding, S., Lätzel, M. & Herrmann, H.J. 2001. From discrete element simulations towards a continuum description of particulate solids. *Handbook of Powder Technology*. 10:39–44.
108. Luo, Z. & Zhao, Y.F. 2017. Numerical simulation of temperature fields in powder bed fusion process by using hybrid heat source model. In *Proceedings of the 28th Annual Solid Freeform Fabrication Symposium*. 1141–1158.

109. Maidana, C.O. 2014. *Thermo-Magnetic Systems for Space Nuclear Reactors*. 1st ed. Springer International Publishing.
110. Maszybrocka, J., Stwora, A., Gapinski, B., Skrabalak, G. & Karolus, M. 2017. Morphology and surface topography of Ti6Al4V lattice structure fabricated by selective laser sintering. *Bulletin of the Polish Academy of Sciences: Technical Sciences*. 65(1):85–92.
111. Meier, C., Penny, R.W., Zou, Y., Gibbs, J.S. & Hart, A.J. 2017. Thermophysical Phenomena in Metal Additive Manufacturing by Selective Laser Melting: Fundamentals, Modeling, Simulation and Experimentation.
112. Mierzejewska, Ż.A. 2015. Process Optimization Variables for Direct Metal Laser Sintering. *Advances in Materials Science*. 15(4):38–51.
113. Miller, D., Morris, E. & Colvin, G. 2016. Metals Additive Manufacturing. *Defense AT&L*. 45(6):38–43.
114. Moletsane, M.G., Krakhmalev, P., Kazantseva, N., Du Plessis, A., Yadroitsava, I. & Yadroitsev, I. 2016. Tensile Properties and Microstructure of Direct Metal and Laser-Sintered Ti 6Al4V (ELI) Alloy. *South African Journal of Industrial Engineering*. 27(3):110–121.
115. Mondal, A.K., Biswas, P. & Bag, S. 2015. Influence of tacking sequence on residual stress and distortion of single sided fillet submerged arc welded joint. *Journal of Marine Science and Application*. 14(3):250–260.
116. Moukalled, F., Mangani, L. & Darwish, M. 2015. *The Finite Volume Method in Computational Fluid Dynamics*. Vol. 113. Springer.
117. Murr, L.E., Gaytan, S.M., Ramirez, D.A., Martinez, E., Hernandez, J., Amato, K.N., Shindo, P.W., Medina, F.R., et al. 2012. Metal Fabrication by Additive Manufacturing Using Laser and Electron Beam Melting Technologies. *Journal of Materials Science & Technology*. 28(281):1–14.
118. Ndolo, P.S. 2014. The Relationship Between Operational Efficiency and Financial Performance of Firms Listed Nairobi Securities. University of Nairobi.
119. Neikov, O.D., Naboychenko, S.S., Murashova, I. V, Gopienko, V.G., Frishberg, I. V & Lotsko, D. V. 2009. *Handbook of Non-Ferrous Metal Powders*.
120. Nemery, B. & Abraham, J.L. 2007. Hard Metal Lung Disease Still Hard to Understand. *AMERICAN JOURNAL OF RESPIRATORY AND CRITICAL CARE MEDICINE*. 176.
121. Olakanmi, E.O., Cochrane, R.F. & Dalgarno, K.W. 2015. A review on selective laser/sintering of aluminium alloy powders: processing, microstructure and properties. *Progress in Materials Science*. 74(1):401–477.
122. Olivier, C.M., Du Toit, D., van Coller, M.C., Oosthuizen, G.A. & Sacks, N. 2017. Review of Simulation Techniques Developed for the Analysis of the Selective Laser Melting Process. In *Rapdasa 2017 Conference Additive Manufacturing*. 226–242.
123. Panwisawas, C., Qiu, C., Anderson, M.J., Sovani, Y., Turner, R.P., Attallah, M.M., Brooks, J.W. & Basoalto, H.C. 2017a. Mesoscale modelling of selective laser melting: Thermal fluid dynamics and microstructural evolution. *Computational Materials Science*. 126(1):479–490.
124. Panwisawas, C., Qiu, C., Anderson, M.J., Sovani, Y., Turner, R.P., Attallah, M.M., Brooks, J.W. & Basoalto, H.C. 2017b. Mesoscale modelling of selective laser melting: Thermal fluid dynamics and microstructural evolution. *Computational Materials Science*. 126:479–490.
125. Peng, T., Kellens, K., Tang, R., Chen, C. & Chen, G. 2018. Sustainability of additive manufacturing: An overview on its energy demand and environmental impact. *Additive Manufacturing*. 21(June 2017):694–704.
126. Pierson, H.O. 1996. *Processing of Refractory Carbides and Nitrides (Coatings)-15*.
127. Pil, F.K. & Rothenberg, S. 2003. Environmental Performance as a Driver of Superior Quality. *Production and Operations Management*. 12(3):404–408.
128. Pyka, G., Kerckhofs, G., Papantoniou, I., Speirs, M., Schrooten, J. & Wevers, M. 2013. Surface roughness and morphology customization of additive manufactured open porous Ti6Al4V structures. *Materials*. 6(10):4737–4757.
129. Raabe, D. 2014. *Maraging Steels and Maraging TRIP Steels*. [Online], Available:

http://www.dierk-raabe.com/martensite-alloys-and-transformations/maraging-trip-steels/ [2018, July 23].
130. Ramirez-Cedillo, E., Sandoval-Robles, J.A., Ruiz-Huerta, L., Caballero-Ruiz, A., Rodriguez, C.A. & Siller, H.R. 2018. Process planning guidelines in selective laser melting for the manufacturing of stainless steel parts. *Procedia Manufacturing*. 26(1):973–982.
131. Riedlbauer, D., Drexler, M., Drummer, D., Steinmann, P. & Mergheim, J. 2014. Modelling, simulation and experimental validation of heat transfer in selective laser melting of the polymeric material PA12. *Computational Materials Science*. 93:239–248.
132. Robinson, I.C. & Belowt, M.A. Von. 1990. The role of the domestic market in promoting the beneficiation of raw materials in South Africa. *Journal of the South African Institute of Mining and Metallurgy*. 90(4):91–98.
133. Rodriguez, M.A., Ricart, J.E. & Sanchez, P. 2002. Sustainable development and the sustainability of competitive advantage: A dynamic and sustainable view of the firm. *Creativity and Innovation Management*. 11(3):135–146.
134. Romano, J., Ladani, L. & Sadowski, M. 2016. Laser Additive Melting and Solidification of Inconel 718 : Finite Element Simulation and Experiment. *Journal of Metals*. 68(3):967–977.
135. Rosochowski, A. & Matuszak, A. 2000. Rapid tooling: the state of the art. *Journal of Materials Processing Technology*. 106(1–3):191–198.
136. Ruan, J., Sparks, T.E., Fan, Z., Stroble, J.K., Panackal, A. & Liou, F. 2006. A Review of Layer Based Manufacturing Processes for Metals. In Austin, Texas *Solid Freeform Fabrication Symposium*. 233–245.
137. Safdar, A., He, H.Z., Wei, L., Snis, A., Chavez De Paz, L.E. & Wei, L.-Y. 2012. Rapid Prototyping Journal Effect of process parameters settings and thickness on surface roughness of EBM produced Ti-6Al-4V Effect of process parameters settings and thickness on surface roughness of EBM produced Ti-6Al-4V. *Rapid Prototyping Journal Rapid Prototyping Journal Iss Rapid Prototyping Journal*. 18(5):401–408.
138. Sames, W.J., List, F.A., Pannala, S., Dehoff, R.R. & Babu, S.S. 2016. The metallurgy and processing science of metal additive manufacturing. *International Materials Reviews*. 1–46.
139. Sandvik Coramant. 2016. *Coated cemented carbide*. [Online], Available: https://www.sandvik.coromant.com/en-gb/knowledge/materials/cutting_tool_materials/coated_cemented_carbide/pages/default.aspx [2018, January 10].
140. Savalani, M. M., Hao, L., Harris., R. A. 2006. Evaluation of CO2 and Nd: YAG lasers for the selective laser sintering of HAPEX. *Proceedings of the Institution of Mechanical Engineers, Part B: Journal of Engineering Manufacture*. 220(2): 171-128.
141. Seabra, M., Azevedo, J., Araújo, A., Reis, L., Pinto, E., Alves, N., Santos, R. & Pedro Mortágua, J. 2016. Selective laser melting (SLM) and topology optimization for lighter aerospace componentes. *Procedia Structural Integrity*. 1(1):289–296.
142. Seneci, C.A., Shang, J., Darzi, A. & Yang, G.Z. 2015. Rapid manufacturing with selective laser melting for robotic surgical tools: Design and process considerations. In Vol. 1. Hamburg, Germany *IEEE International Conference on Intelligent Robots and Systems*. 824–830.
143. Serres, N., Tidu, D., Sankare, S. & Hlawka, F. 2011.) Environmental comparison of MESO-CLAD process and conventional machining. *Journal of Cleaner Production*. 19(1):1117–1124.
144. Seyda, V., Kaufmann, N. & Emmelmann, C. 2012. Investigation of Aging Processes of Ti-6Al-4 v Powder Material in Laser Melting. *Physics Procedia*. 39(1):425–431.
145. Shao, Z., Pu, B. & Fan, X. 2010.
146. Shellabear, M. & Nyrhilä, O. 2004. DMLS – DEVELOPMENT HISTORY AND STATE OF THE ART. In Erlangen, Germany *Proceedings of the 4th LANE*. 21–24.
147. Silberberg, M. S. 2013. *Principles of General Chemistry*. 3de ed. New York: McGraw-Hill. 325-340.
148. Singh, A. 2016. 3D Printing Technology : Its principles and processes. *International Journal of Research in Advanced Engineering and Technology*. 2(4):53–65.

149. Siwak, P. & Garbiec, D. 2016. Microstructure and mechanical properties of WC−Co, WC−Co−Cr 3 C 2 and WC−Co−TaC cermets fabricated by spark plasma sintering. *Transactions of Nonferrous Metals Society of China*. 26(1):2641–2646.
150. Song, Y.-A. & Koenig, W. 1997. Experimental Study of the Basic Process Mechanism for Direct Selective Laser Sintering of Low-Melting Metallic Powder. *CIRP Annals*. 46(1):127–130.
151. Sreenivasan, R., Goel, A. & Bourell, D.L. 2010. Sustainability issues in laser-based additive manufacturing. *Physics Procedia*. 5(A):81–90.
152. Staden, A.C. Van. 2015. A Fundamental Analysis on Additive Manufacturing.
153. Van Staden, A.C., Hagedorn-Hansen, D., Oosthuizen, G.A. & Sacks, N. 2016. Characteristics of single layer Selective Laser Melted tool grade cemented tungsten carbide. In *International Conference on Competitive Manufacturing, COMA '16*. 141–146.
154. Stam, E. & Wennberg, K. 2009. The Roles of R&D in New Firm Growth. *Small Business Economics*. 33(1):77–89.
155. Sun, S., Zheng, L., Liu, Y., Liu, J. & Zhang, H. 2015. Selective laser melting of Al-Fe-V-Si heat-resistant aluminum alloy powder: modeling and experiments. *The International Journal of Advanced Manufacturing Technology*. 80(9–12):1787–1797.
156. Szost, B.A., Terzi, S., Martina, F., Boisselier, D., Prytuliak, A., Pirling, T., Hofmann, M. & Jarvis, D.J. 2016. A comparative study of additive manufacturing techniques: Residual stress and microstructural analysis of CLAD and WAAM printed Ti-6Al-4V components. *Materials and Design*. 89:559–567.
157. Teece, D.J. 1986. Profiting from technological innovation: Implications for integration, collaboration, licensing and public policy. *Research Policy*. 15(6):285–305.
158. Teng, C. Pal, D. Gong, H. & Tucker, . 2014. A Two Dimensional Analytical Evolution of Temperature in Selective Laser Sintering. *Solid Freeform Fabrication Symposium.*
159. Terui, H., Konno, S., Kaga, K., Matsuno, Y., Hatanaka, K.C., Kanno, H., Moriyama, H., Uo, M., et al. 2015. Two cases of hard metal lung disease showing gradual improvement in pulmonary function after avoiding dust exposure. *Journal of Occupational Medicine and Toxicology*. 10(1):29.
160. Thomas, D. 2009. The Development of Design Rules for Selective Laser Melting. University of Wales Institute, Cardiff.
161. Townsend, A., Senin, N., Blunt, L., Leach, R.K. & Taylor, J.S. 2016. Surface texture metrology for metal additive manufacturing: a review. *Precision Engineering*. 46(1):34–47.
162. Tracey, V.A. 1992. Nickel in Hardmetals. *Refractory Metals & Hard Materials*. 11(3):137–149.
163. Traini, T., Mangano, C., Sammons, R.L., Mangano, F., Macchi, A. & Piattelli, A. 2008. Direct laser metal sintering as a new approach to fabrication of an isoelastic functionally graded material for manufacture of porous titanium dental implants. *Dental Materials*. 24(1):1525–1533.
164. Uhlmann, E., Bergmann, A. & Gridin, W. 2015. Investigation on Additive Manufacturing of Tungsten Carbide-cobalt by Selective Laser Melting. *Procedia CIRP*. 35:8–15.
165. Uhrenius, B., Pastor, H. & Pauty, E. 1997. On the Composition of Fe-Ni-Co-WC-Based Cemented Carbides. *Journal of Refractory Metals and Hardmaterials*. 15(1):139–147.
166. Upadhyaya, G.S. 1998. *Cemented Tungsten Carbides - Production, Properties, and Testing*. 1st ed. Norwich: William Andrew Publishing.
167. Vijay, S. & Rao, S. 2013. Simulated optimum temperature distribution of selective laser melting process using design of experiments. *Manufacturing Technology Today*. 1(1):5–12.
168. Viswanadham, R.K., Lindquist, P.G. & Peck, J.A. 1983. *Science of Hard Materials*.
169. Vrancken, B. 2016. Study of Residual Stresses in Selective Laser Melting. KU Leuven.
170. Wang, D., Wu, S., Bai, Y., Lin, H., Yang, Y. & Song, C. 2017. Characteristics of typical geometrical features shaped by selective laser melting. *Journal of Laser Applications*. 29(2):022007.

171. Wang, X.C., Laoui, T., Bonse, J., Kruth, J.P., Lauwers, B. & Froyen, L. 2002a. Direct Selective Laser Sintering of Hard Metal Powders: Experimental Study and Simulation. *Int J Adv Manuf Technol*. 19:351–357.
172. Wang, X.C., Laoui, T., Bonse, J., Kruth, J.P., Lauwers, B. & Froyen, L. 2002b. Direct Selective Laser Sintering of Hard Metal Powders: Experimental Study and Simulation. *Int J Adv Manuf Technol*. 19(1):351–357.
173. Wiria, F.E., Leong, K.F. & Chua, C.K. 2010. Modeling of powder particle heat transfer process in selective laser sintering for fabricating tissue engineering scaffolds. *Rapid Prototyping Journal*. 16(6):400–410.
174. Wong, K. V. & Hernandez, A. 2012. A Review of Additive Manufacturing. *ISRN Mechanical Engineering*. 2012(1):1–10.
175. Xiao, B. & Zhang, Y. 2008. Numerical Simulation of Direct Metal Laser Sintering of Single-Component Powder on Top of Sintered Layers. *Journal of Manufacturing Science and Engineering*. 130(4):041002.
176. Xiong, Y., Hofmeister, W.H., Cheng, Z., Smugeresky, J.E., Lavernia, E.J. & Schoenung, J.M. 2009. In situ thermal imaging and three-dimensional finite element modeling of tungsten carbide–cobalt during laser deposition. *Acta Materialia*. 57:5419–5429.
177. Yadroitsava, I., Els, J., Booysen, G. & Yadroitsev, I. 2015. Peculiarities of Single Track Formation from Ti6Al4V Alloy at Different Laser Power Densities by Selective Laser Melting. *South African Journal of Industrial Engineering*. 26(November 2015):86–95.
178. Yadroitsev, I., Bertrand, P. & Smurov, I. 2007. Parametric analysis of the selective laser melting process.
179. Yadroitsev, I., Krakhmalev, P. & Yadroitsava, I. 2015. Hierarchical design principles of selective laser melting for high quality metallic objects. *Additive Manufacturing*. 7:45–56.
180. Yang, L., Wu, Y., Lassell, A. & Zhou, B. 2016. Electropolishing of Ti6Al4V Parts Fabricated by Electron Beam Melting. In *Solid Freeform Fabrication Proceedings*. 1333–1344.
181. Yap, C.Y., Chua, C.K., Dong, Z.L., Liu, Z.H., Zhang, D.Q., Loh, L.E. & Sing, S.L. 2015. Review of selective laser melting: Materials and applications. *Applied Physics Reviews*. 2(4).
182. Yasa, E. & Kruth, J.P. 2011. Microstructural investigation of selective laser melting 316L stainless steel parts exposed to laser re-melting. *Procedia Engineering*. 19(1):389–395.
183. Zeng, K., Teng, C., Xu, S., Sublette, T., Patil, N., Pala, D. & Stucker, B. 2014. A Comparison of the Computational Speed of 3DSIM versus ANSYS Finite Element Analyses for Simulation of Thermal History in Metal Laser Sintering. In *International Solid Freeform Fabrication Symposium*. 1205–1212.
184. Zhang, J., Liou, F., Seufzer, W., Newkirk, J. & Fan, Z. 2013. Probabilistic Simulation of Solidification Microstructure Evolution During Laser-Based Metal Deposition. *Utwired.Engr.Utexas.Edu*. 739–748.
185. Zinoviev, A., Zinovieva, O., Ploshikhin, V., Romanova, V. & Balokhonov, R. 2016. Evolution of grain structure during laser additive manufacturing. Simulation by a cellular automata method. *Materials and Design*. 106:321–329.

Appendices

Appendix A: The Research Project Financials

A cost comparison between the simulation and experimental parameter analysis is provided in Table A1. The cost are based on quotes and actual expenses realised in this study. Only the costs surrounding the experimental procedures of Ti-6Al-4V are listed in the experimental column, and not those of the tool steel. It should be noted that labour costs were not included in the cost comparison as both the simulation and experimental procedures were performed by students at the university, which makes it difficult to quantify.

Table A1: Financial summary of the expenses relating to a simulation and experimental calibration method.

Simulation			Experimental		
Item	**Supplier**	**Cost**	**Item**	**Supplier**	**Cost**
Abaqus software license	FEAS	R13 988.37	Raw powder acquisition	Weartech	R6296.98
Software training	FEAS	R2736.00	Powder property analysis	Ceratizit	R250.00
			SEM analysis	Central Analytical Facilities	R4550.00
			Tool steel acquisition	STC	R6000.00
			Tool steel base plate machining	Leading Edge, STC	R1420.00
			Ti6Al4V acquisition	Tifab	R1515.00
			Tool steel base plate machining	STC	R7550.00
			SLS scanning	CRPM	R3420.00
			Shipping cost	DHL	R290.00
Total Amount		**R16 724.37**	Total Amount		**R31 291.98**

Appendix B: Variable Parameter ANOVA Study of the Simulated Processing Parameters

The analysis of variance (ANOVA) test was performed on the processing parameters in order to determine the level of significance of each processing parameter and understanding their interaction on the resulting maximum model temperature (response). A response prediction can be constructed using the results of the ANOVA study. Design-Expert was the software used to perform the analysis. Figures B1 display the fit summary for the model evaluated by the software to describe the temperature response resulting from the scanning speed and laser power.

It is evident in the tables in Figure B2 that the software suggests either a linear or two factor interaction (2FI) model for the temperature response, yet the 2FI has a higher predicted R^2, which is gives an indication of the goodness of fit. The agreement between the adjusted and predicted R^2 values is said to be good if it falls between 0.2 of each other. However, the R^2 values for both these predictions are low, which may lead to variance between the predicted and actual values, as can be seen in Figure B3.

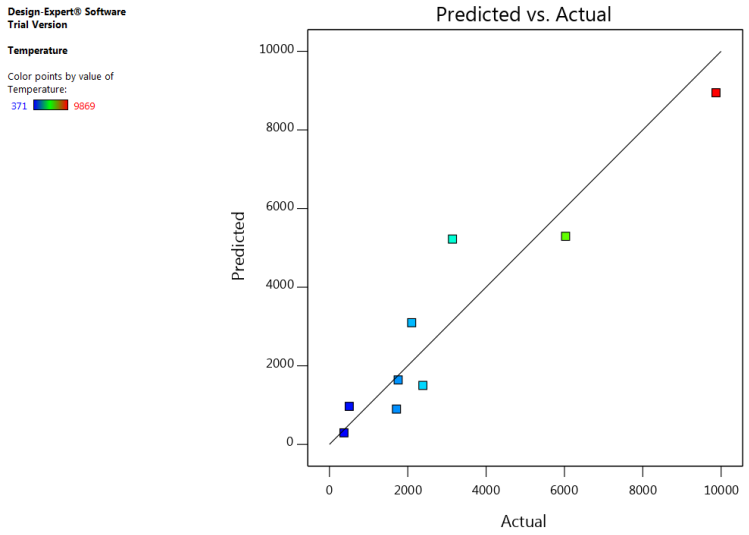

Figure B1: The fit summary of the ANOVA study with the given design points.

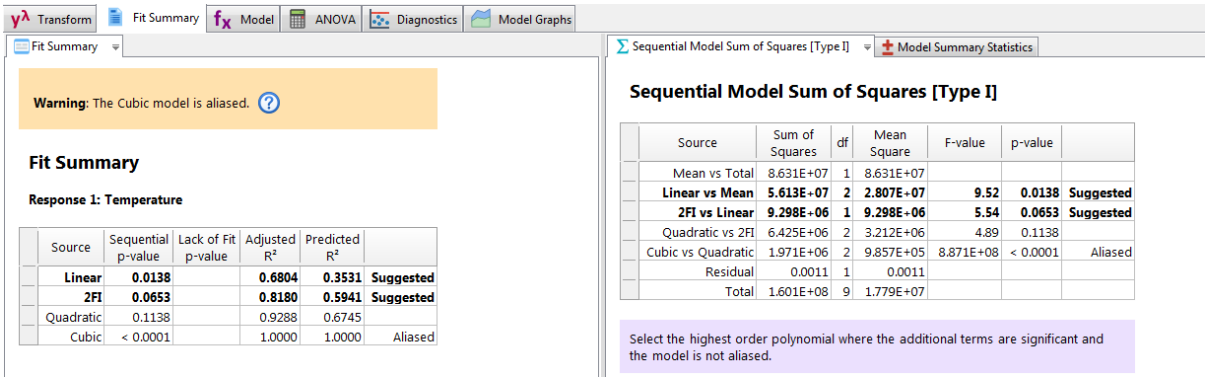

Figure B2: Results of the fit summary.

The ANOVA study for the 2FI in Figure B4 determined which factors needed to be included in the model due to their significance. By analysing the F- and p- values it can be determined whether a parameter is significant or not. Both the scanning speed (parameter A) and laser power (B) displays F-values above the critical value and p-values less than 0.05, which indicates that they are significant to the model. The F-values are similar for the two parameters indicating that they have an equal influence on the temperature response.

Transform | Fit Summary | Model | ANOVA | Diagnostics | Model Graphs

Analysis of Variance

ANOVA for 2FI model

Response 1: Temperature

Source	Sum of Squares	df	Mean Square	F-value	p-value	
Model	6.543E+07	3	2.181E+07	12.99	0.0085	significant
A-Scanning Speed	2.898E+07	1	2.898E+07	17.26	0.0089	
B-Laser Power	2.716E+07	1	2.716E+07	16.17	0.0101	
AB	9.298E+06	1	9.298E+06	5.54	0.0653	
Residual	8.396E+06	5	1.679E+06			
Cor Total	7.383E+07	8				

Factor coding is **Coded**.
Sum of squares is **Type III - Partial**

The **Model F-value** of 12.99 implies the model is significant. There is only a 0.85% chance that an F-value this large could occur due to noise.

P-values less than 0.0500 indicate model terms are significant. In this case A, B are significant model terms. Values greater than 0.1000 indicate the model terms are not significant. If there are many insignificant model terms (not counting those required to support hierarchy), model reduction may improve your model.

Fit Statistics | Model Comparison Statistics

Fit Statistics

Std. Dev.	1295.85	**R^2**	0.8863
Mean	3096.78	**Adjusted R^2**	0.8180
C.V. %	41.85	**Predicted R^2**	0.5941
		Adeq Precision	10.0129

The **Predicted R^2** of 0.5941 is not as close to the **Adjusted R^2** of 0.8180 as one might normally expect; i.e. the difference is more than 0.2. This may indicate a large block effect or a possible problem with your model and/or data. Things to consider are model reduction, response transformation, outliers, etc. All empirical models should be tested by doing confirmation runs.

Coefficients | Coded Equation | Actual Equation

Coefficients in Terms of Coded Factors

Factor	Coefficient Estimate	df	Standard Error	95% CI Low	95% CI High	VIF
Intercept	3096.78	1	431.95	1986.42	4207.14	
A-Scanning Speed	-2197.57	1	529.03	-3557.48	-837.66	1.0000
B-Laser Power	2127.50	1	529.03	767.59	3487.41	1.0000
AB	-1524.65	1	647.92	-3190.19	140.89	1.0000

The coefficient estimate represents the expected change in response per unit change in factor value when all remaining factors are held constant. The intercept in an orthogonal design is the overall average response of all the runs. The coefficients are adjustments around that average based on the factor settings. When the factors are orthogonal the VIFs are 1; VIFs greater than 1 indicate multi-colinearity, the higher the VIF the more severe the correlation of factors. As a rough rule, VIFs less than 10 are tolerable.

Figure B3: Results from the ANOVA study.

The interaction plot predicts the temperature response at different scanning speeds for two laser power values, maximum (red) and minimum (black). As the scanning speed increases the temperature values decreases for both power values until they become almost equal. This indicates that scanning speed is more significant at lower speeds than at higher scanning speeds.

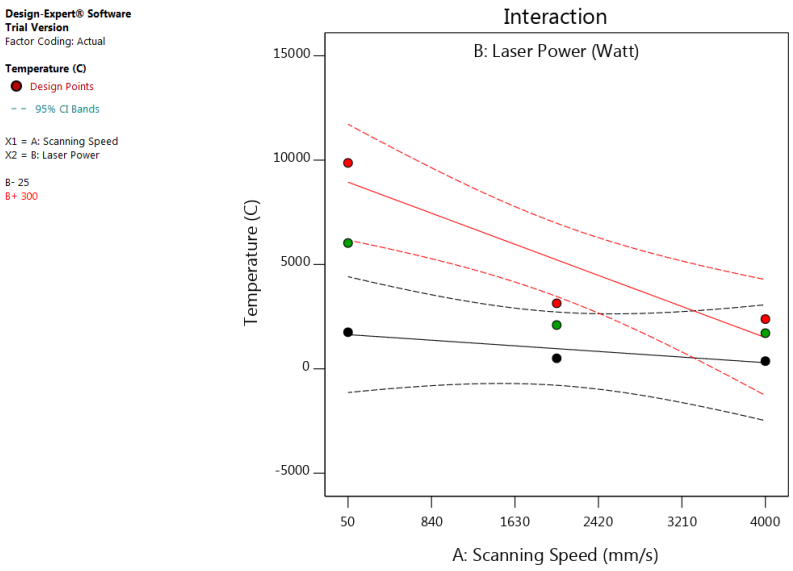

Figure B4: Interaction plot between the two factors (scanning speed and laser power).

Appendix C: Particle Size Distribution of the WC-Co Powder used in the Study

The powdered WC-Co was analysed using scanning electron microscope (SEM) at the Central Analytical Facilities (CAF) at the University of Stellenbosch (US). The SEM revealed the variations in the particle sizes. It was decided to use a software program known as ImageJ in order to quantify the particle distribution as accurately as possible. ImageJ performed image analyses using the pixels of the computer's display screen. It was calibrated by specifying the length of pixels in the scale bar on the uploaded image. The image was then passed through a threshold operation, which increased the contrast between the particles and background. Finally, ImageJ added the number of pixels per particle and calculated the area of each particle. It provided a results folder containing the analysed data. The analysis process is shown in Figure C1.

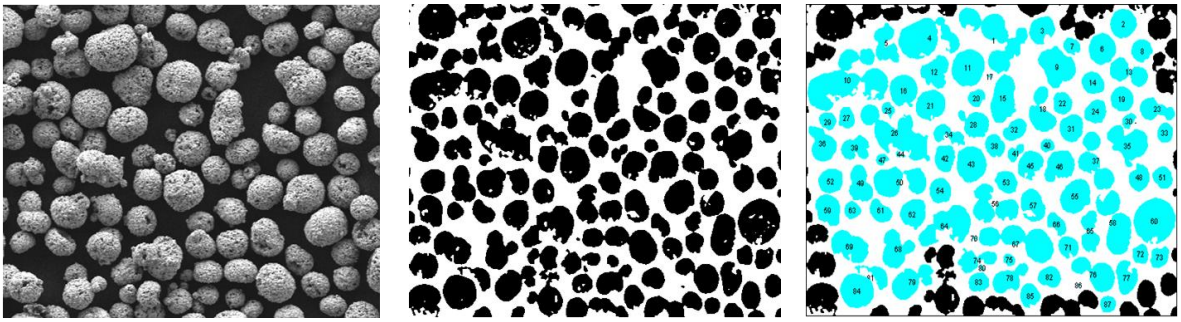

(a) (b) (c)

Figure C1: Particle analysis performed using ImageJ. (a) The original SEM image. (b) Increasing the image contrast. (c) Calculating the area of each particle.

However, the results were not yet useful as the original objective was to find the particle size distribution and not the particle's area. The size distribution is based on the particle diameter. If it is assumed that the particles are round then the effective diameter can be found using the following procedures.

$$A = \pi r^2 \tag{1}$$

$$r = \sqrt{\frac{A}{\pi}} \tag{2}$$

Then finally,

$$d = 2r \tag{3}$$

The results after calculating the effective diameter for each particle are shown in Table C1. A histogram of the results are presented in Figure C2

Table C1: Number of samples required of each machining process.

Particle size distribution analysis		
Sample size	-	87
Average particle size	[μm]	25.4
Maximum particle size	[μm]	56.2
Minimum particle size	[μm]	2.9

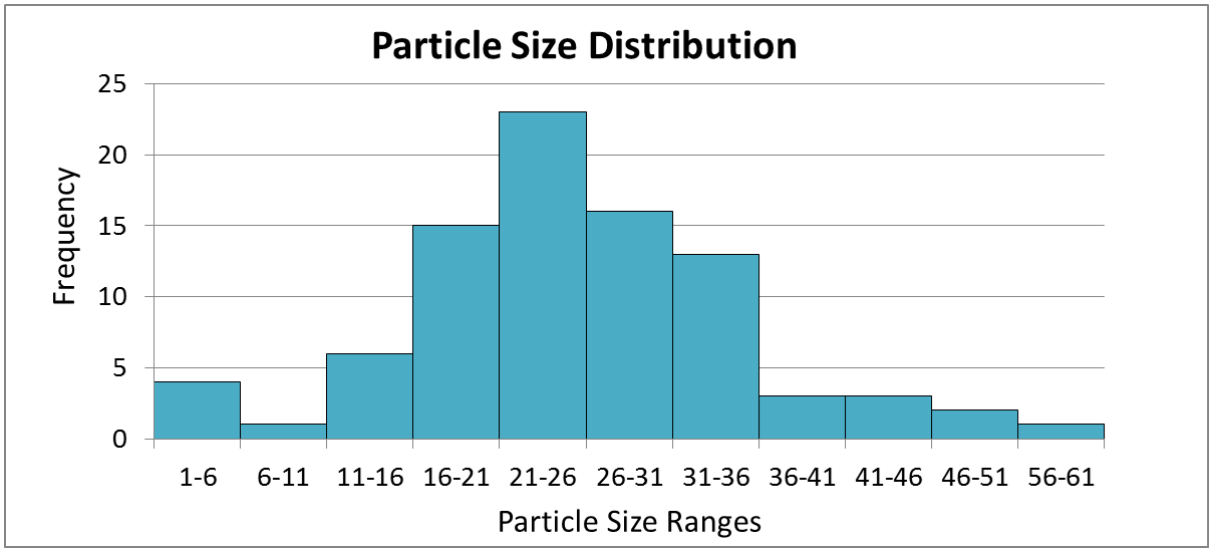

Figure C2: Particle size distribution.

Appendix D: Temperature Dependant Properties of the Powder and Base Plates

The values of the temperature dependant material properties of the powder and base plates are listed in the tables of this Appendix. These are the exact values used in the material assignment section of the simulation.

WC-Co

The thermal properties for the powder are calculated using composition ratio equations from literature.

$$k_{WC-Co} = g_{WC}k_{WC} + g_{Co}k_{Co} \qquad \left[\frac{W}{m\,K}\right] \qquad (4)$$

$$C_{WC-Co} = f_{WC}C_{WC} + f_{Co}C_{Co} \qquad \left[\frac{J}{kg\,K}\right] \qquad (5)$$

Powder: WC-Co

Table D1: Temperature dependent properties used in the simulation for the WC-Co powder.

Temperature [°C]	**Thermal Conductivity** (k) [W / m K]			**Specific Heat** (c_p) [J / kg K]		
	WC	**Co**	**WC-Co**	**WC**	**Co**	**WC-Co**
-27	110	122	111.4	160	380	186.4
127	100	85	98.2	220	450	247.6
327	85	70	83.2	240	500	271.2
527	75	57	72.8	250	570	288.4
727	70	50	67.6	270	660	316.8
927	60	47	58.4	280	730	334.0
1127	55	43	53.6	290	795	350.6
1227	50	40	48.8	295	690	342.4
1427	48	40	47.0	300	695	347.4
1727	50	40	48.8	315	700	361.2
2027	60	40	57.6	330	700	374.4

Base Plate 1: Tool Steel

Table D2: Temperature dependent properties used in the simulation for the tool steel base plate.

Temperature [°C]	**Thermal Conductivity** (k) [W / m K]	**Specific Heat** (c_p) [J / kg K]
100	51.1	499.2
300	46.1	565.5
450	41.1	630.5
550	37.5	705.5
600	35.6	773.3
720	30.6	1080.4
800	26.0	931.0
1450	29.5	437.9

Base Plate 2: Ti-6Al-4V

Table D3: Temperature dependent properties used in the simulation for the Ti-6Al-4V base plate.

Temperature [°C]	**Thermal Conductivity** (k) [W / m K]	**Specific Heat** (c_p) [J / kg K]
0	6	545
100	7	560
200	9	580
300	11	610
400	12	635
500	13	650
600	14	670
700	16	690
800	18	715
900	20	740
1000	19	640
1100	21	660
1200	23	680
1300	24	700
1400	25	720
1500	26	740
1600	27	760
1700	28	770
1800	28	830

Appendix E: DFLUX Subroutine Code written for ABAQUS

DFLUX is the FORTRAN code, which describes the moving volumetric heat flux. The code is written as a separate subroutine and complied by Visual Studio which is the compiler linked to ABAQUS. The code was specifically written to include the characteristics of the WC-Co powder.

```
      SUBROUTINE DFLUX(FLUX,SOL,JSTEP,JINC,TIME,NOEL,NPT,COORDS,JLTYP,
     1                 TEMP,PRESS,SNAME)
C
      INCLUDE 'ABA_PARAM.INC'

          ! Declaration of the standard DFLUX parameters
C     parameter(one=1.d0)
      DIMENSION COORDS(3),FLUX(2),TIME(2)
      CHARACTER*80 SNAME

          !Values of the semi-axes of the Gaussian heat flux distribution in an ellipsoid
          !Equation from Goldack, Chakravarti and Bibby (1984)

          ff = 0.1 ! fractions must equal 2. Front
          fr = 1.9 ! rear

          PI=3.1415 !Pi value
          s=1.866324 ! = 6*sqrt(3)/(PI*sqrt(PI))
          P=50 !Laser input power
          asorp = 0.52 !Powder absportion

          v=0.06                !Scanning speed
          d=v*TIME(1)           !Scanning distance

          !Assigning the coordinate system to the correct array
          x=COORDS(1)
          y=COORDS(2)
          z=COORDS(3)

          !Defining the initial starting point
          x0=0.00005
          y0=0.0005
          z0=0.0003
c
           !Volumetric shape function
          af=0.00004 !x axis front
          ar=0.0002  !x axis rear
          b=0.00004 !y axis
          c=0.0002 !z axis

          cpos = x-d-x0 !Current position

          if(cpos.GT.0) then

          F1=(P*asorp*s)/(a*b*cf)
```

```
        Gshape1= exp((-3*(((x-x0-d)**2)/(af**2)))+(-3*(((y-y0)**2)/(b**2)))+(-3*(((z-
z0)**2)/(c**2))))

        FLUX(1)=F1*ff*Gshape1
        else
        F2=(P*asorp*s)/(a*b*cr)
        Gshape2= exp((-3*(((x-x0-d)**2)/(ar**2)))+(-3*(((y-y0)**2)/(b**2)))+(-3*(((z-
z0)**2)/(c**2))))
        FLUX(1)=F2*fr*Gshape2
        end if

    JLTYP=1

    RETURN
    END
```

Appendix F: Scan Track Measurements - Simulation

This appendix includes a summary of the data collected from the simulated melt pool geometrical features. The image displayed below in Figure F1, and in the tables in this chapter show the section view of the simulated melt pool. The melt pool width and penetration depth measurements were made using the query tool in the Abaqus visualisation window.

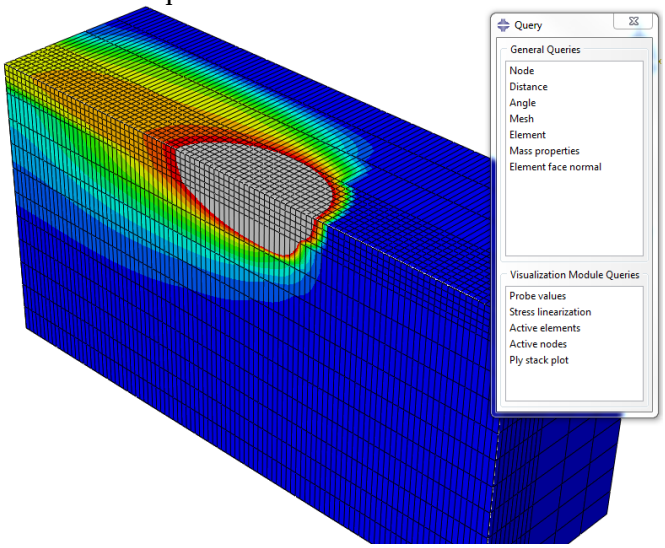

Figure F1: Example of the measuring technique used to measure the geometry of the simulated melt pool.

WC- 12Co on Tool Steel Base Plate

Table F1: Geometry data collected from the WC-12Co and tool steel base plate simulation.

Track 1	Track 2	Track 3	Track 4
width: 185µm depth: 76µm max temp: 2210°C	width: 164µm depth: 57µm max temp: 2109°C	width: 144µm depth: 45µm max temp: 2040°C	width: 128µm depth: 38µm max temp: 1971°C
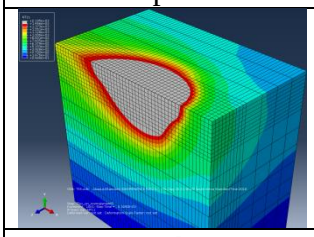	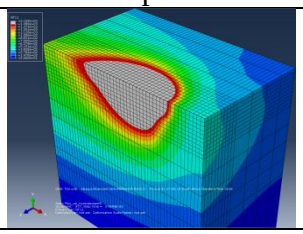	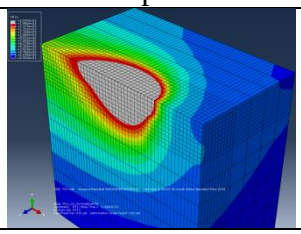	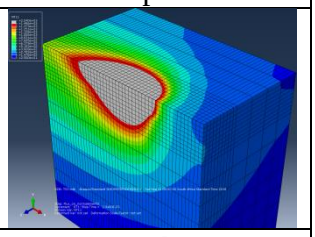
Track 5	Track 6	Track 7	Track 8
width: 120µm depth: 32µm max temp: 1951°C	width: 114µm depth: 28µm max temp: 1931°C	width: 102µm depth: 22µm max temp: 1886°C	width: 100µm depth: 18µm max temp: 1873°C
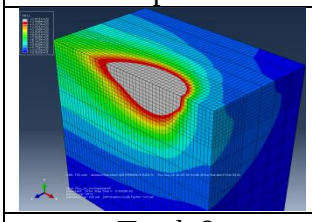	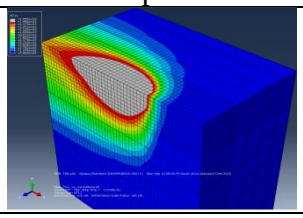	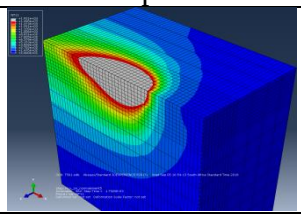	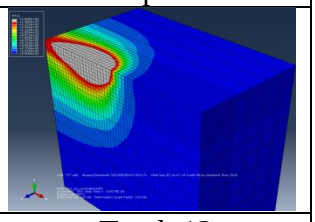
Track 9	Track 10	Track 11	Track 12
width: 198µm depth: 82µm max temp: 3173°C	width: 160µm depth: 62µm max temp: 2817°C	width: 134µm depth: 48µm max temp: 2593°C	width: 120µm depth: 36µm max temp: 2445°C

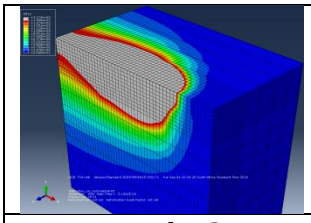	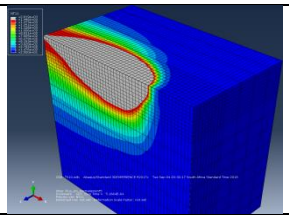	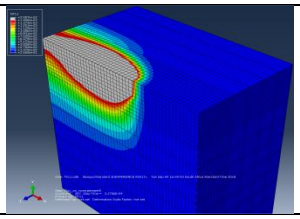	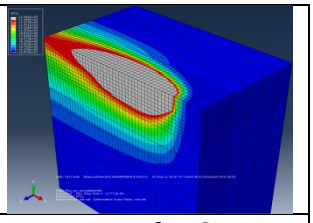
Track 13	Track 14	Track 15	Track 16
width: 108µm depth: 28µm max temp: 2325°C	width: 96µm depth: 24µm max temp: 2228°C	width: 84µm depth: 18µm max temp: 2151°C	width: 80µm depth: 16µm max temp: 2082°C
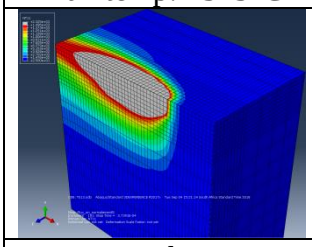	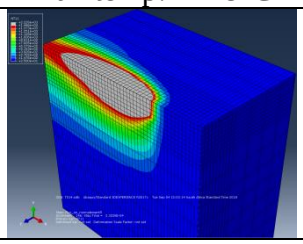	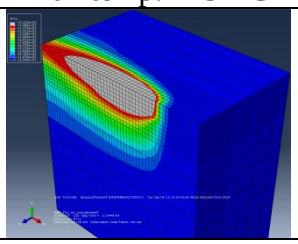	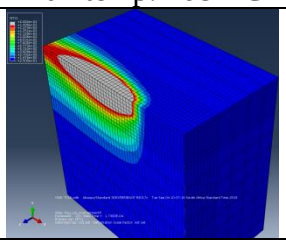
Track 17	Track 18	Track 19	Track 20
width: 100µm depth: 82µm max temp: 4160°C	width: 100µm depth: 74µm max temp: 3873°C	width: 100µm depth: 63µm max temp: 3642°C	width: 100µm depth: 58µm max temp: 3451°C
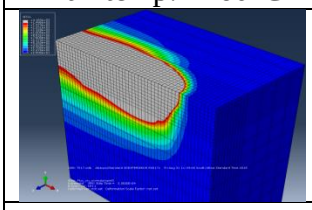	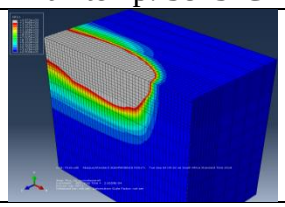	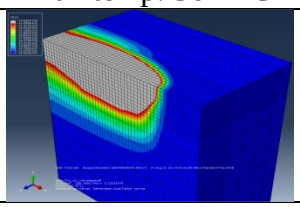	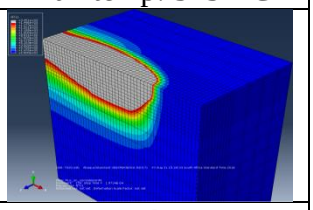
Track 21	Track 22	Track 23	Track 24
width: 100µm depth: 56µm max temp: 3286°C	width: 100µm depth: 50µm max temp: 3157°C	width: 100µm depth: 38µm max temp: 3036°C	width: 100µm depth: 34µm max temp: 2925°C
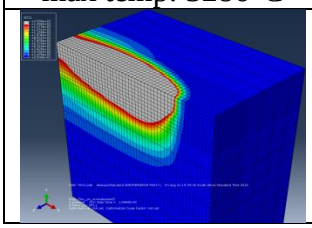	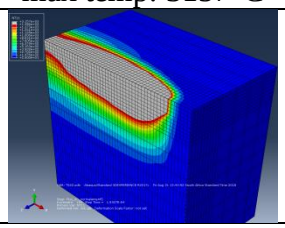	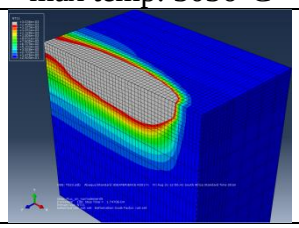	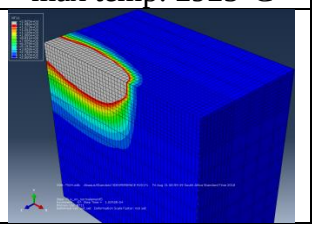

WC- 12Co on Ti-6Al-4V Plate

Table F2: Geometry data collected from the WC-12Co and tool steel base plate simulation.

Track 1	Track 2	Track 3	Track 4
width: 220µm depth: 84µm max temp: 3051°C	width: 196µm depth: 68µm max temp: 2240°C	width: 182µm depth: 54µm max temp: 2167°C	width: 168µm depth: 38µm max temp: 2108°C
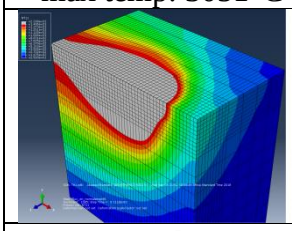	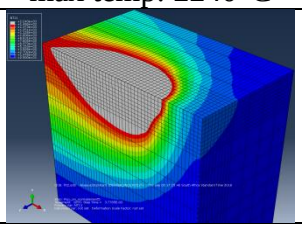	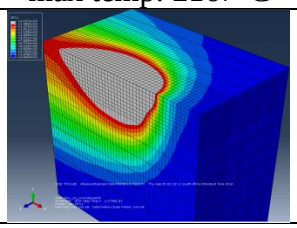	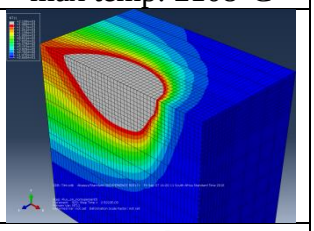
Track 5	Track 6	Track 7	Track 8
width: 152µm depth: 34µm	width: 140µm depth: 30µm	width: 124µm depth: 20µm	width: 110µm depth: 16µm

max temp: 2060°C	max temp: 2015°C	max temp: 1985°C	max temp: 1956°C
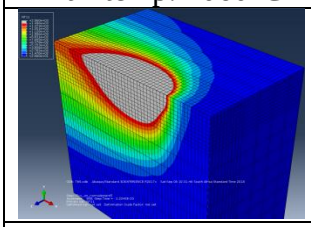	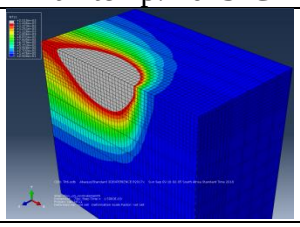	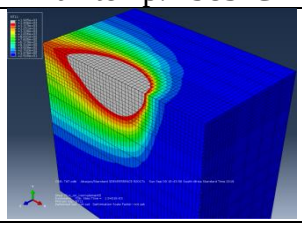	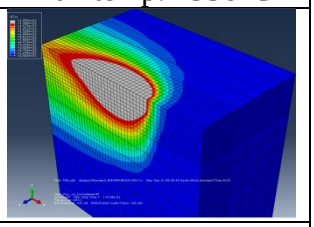
Track 9	Track 10	Track 11	Track 12
width: 202µm depth: 110µm max temp: 3193°C	width: 168µm depth: 68µm max temp: 2830°C	width: 108µm depth: 58µm max temp: 2620°C	width: 124µm depth: 50µm max temp: 2489°C
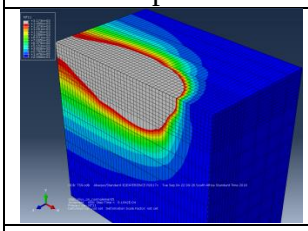	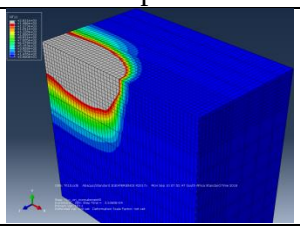	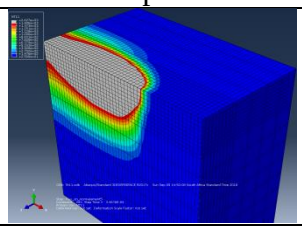	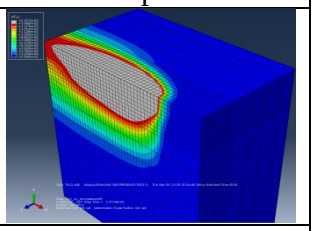
Track 13	Track 14	Track 15	Track 16
width: 110µm depth: 40µm max temp: 2350°C	width: 100µm depth: 31µm max temp: 2250°C	width: 90µm depth: 24µm max temp: 2165°C	width: 80µm depth: 20µm max temp: 2094°C
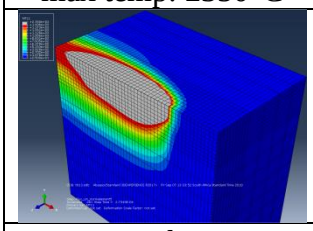	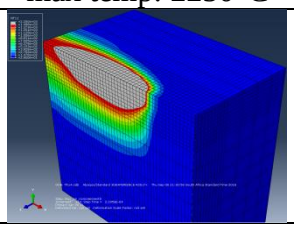	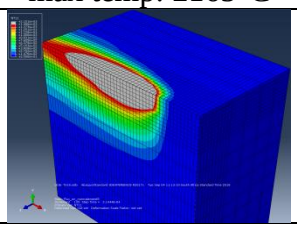	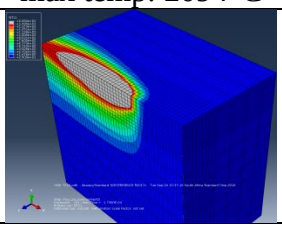
Track 17	Track 18	Track 19	Track 20
width: 186µm depth: 90µm max temp: 4105°C	width: 176µm depth: 82µm max temp: 3837°C	width: 160µm depth: 74µm max temp: 3623°C	width: 150µm depth: 66µm max temp: 3443°C
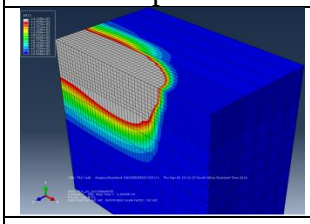	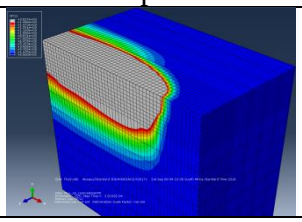	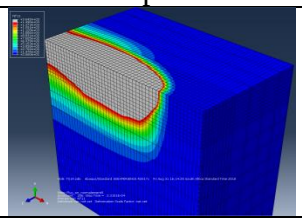	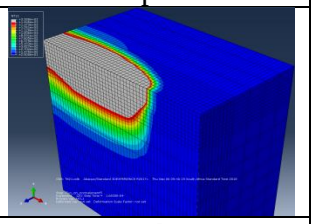
Track 21	Track 22	Track 23	Track 24
width: 140µm depth: 62µm max temp: 3346°C	width: 134µm depth: 58µm max temp: 3161°C	width: 122µm depth: 56µm max temp: 3046°C	width: 118µm depth: 54µm max temp: 2939°C
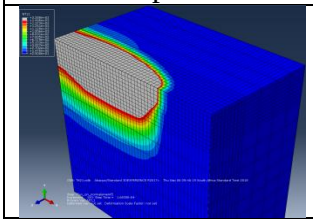	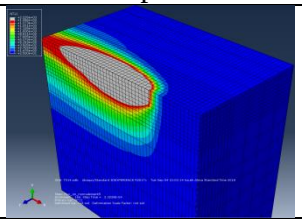	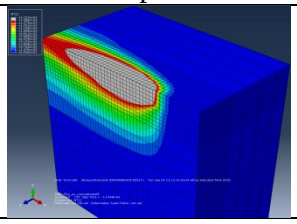	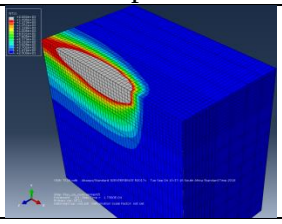

Appendix G: Base Plate Specifics for the Volume Reduction Unit

The appendix elaborates on the manufacturing techniques used to produce the base plates from the various materials.

Tool Steel

Twelve smaller sections were cut from a pre-existing 250 x 250 x 10 mm Concept Laser using a water jet cutter, as depicted in Figure G1. The cut-outs were machined flat on a DMU 65 monoblock 3-axis milling machine at the STC. A sand blasting operation followed the machining in order to increase the surface roughness and to reduce the laser refraction.

(a) (b)

Figure G1: Raw titanium billet used to manufacture the base plates.

The chemical composition and mechanical characteristics of the maraging tool steel used for this study is listed in Tables G1 and G2, respectively.

Table G1: Chemical composition of maraging tool steel (3T RPD, 2016).

Element	Fe	Ni	Co	Mo	Ti	Al	Cr, Cu	Mn, Si	C	P, S
% Content	Balance	18	9.5	5.2	0.8	0.15	Each ≤ 0.5%	≤ 0.1%	Each ≤ 0.03%	Each ≤ 0.01%

Table G2: Mechanical characteristics of maraging tool steel (3T RPD, 2016).

Mechanical Characteristics				
Relative density (kg/m^3)	Tensile Strength (MPa)	Yield Strength (MPa)	Elongation (%)	Hardness (HRC)
8100	2050	1990	4	50-56

Ti-6Al-4V

The titanium base substrates were manufactured from a solid, Ti-6Al-4V, round bar (Ø = 75mm x 250mm) using various machining operations at the Stellenbosch Technology Centre (STC). An image of the raw billet is shown below in Figure G2. The chemical composition and mechanical characteristics as stated by the data sheets are listed in Tables G3 and G4, respectively.

Figure G2: Raw titanium billet used to manufacture the base plates.

Table G3: Chemical composition of the titanium billet.

Element	Ti	Al	V	C	Fe	N	O	H	Others
% Content	89.069	6.0	4.1	0.02	0.14	0.01	0.16	0.001	0.5

Table G4: Mechanical characteristics of Ti-6Al-4V.

Mechanical Characteristics				
Treatment Condition	Tensile Strength (MPa)	Yield Strength (MPa)	Elongation (%)	Area reduction (%)
Annealed	969	847	13	28

The drawing used to produce the base plates is shown in the drawing in Figure G3. It is based on the dimensions of the volume reduction chamber fitted in the EOS laser machine at the Central University of Technology.

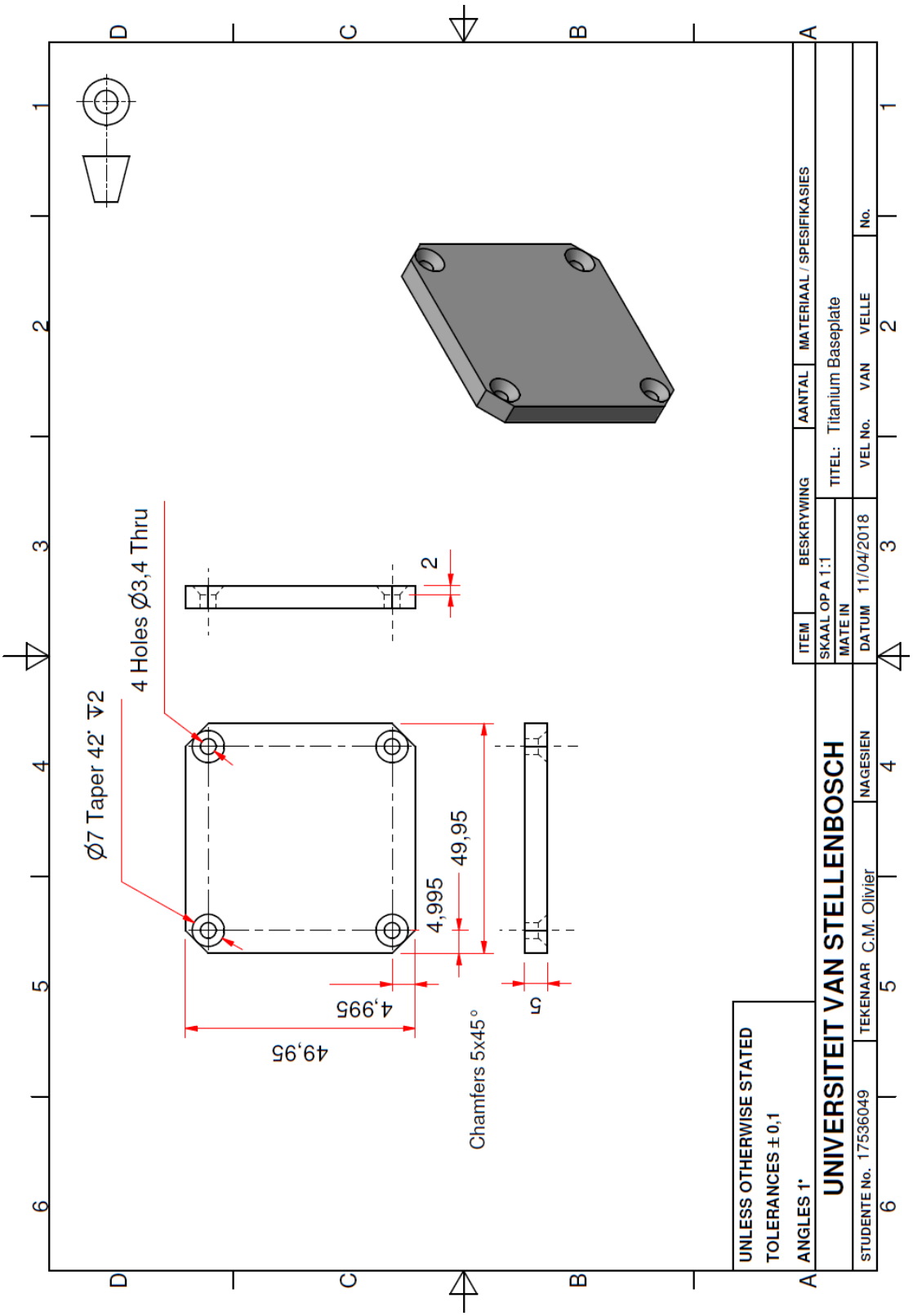

Figure G3: Base substrate drawing based on the dimensions of a volume reduction chamber.

Appendix H: Scan Track Width Measurements - Tool Steel Base Plate

Table H1: Experimental scan track width measurements of the WC-12Co on the tool steel base plate.

Parameter set/ scan track number	Power [W]	Scanning speed [mm/s]	Energy density [J / mm^2]	Width measurements [µm] 1	2	3	4	5	6	Average width [µm]
1	50	60	208.3	141.17	160.84	151.81	146.98	150.42	149.23	**150.08**
2	50	80	156.3	142.50	149.38	134.95	128.76	140.10	155.01	**141.78**
3	50	100	125.0	125.59	124.35	115.31	133.81	126.64	127.55	**125.54**
4	50	120	104.2	105.17	107.21	121.54	124.45	123.42	119.78	**116.93**
5	50	140	89.3	107.01	105.87	118.47	120.00	114.72	111.32	**112.90**
6	50	160	78.1	115.20	105.04	107.01	109.10	109.03	114.88	**110.04**
7	50	180	69.4	103.58	99.22	107.59	105.47	104.92	107.21	**104.67**
8	50	200	62.5	113.59	99.63	97.06	101.62	105.32	98.50	**102.62**
9	150	400	93.8	181.19	163.84	166.81	165.10	172.99	172.99	**170.49**
10	150	600	62.5	149.91	139.76	157.12	150.02	137.23	137.12	**145.19**
11	150	800	46.9	134.64	126.25	124.68	125.59	127.61	110.63	**124.90**
12	150	1000	37.5	96.93	104.72	120.74	117.49	116.45	115.56	**111.98**
13	150	1200	31.3	101.03	101.08	112.82	105.32	102.07	98.07	**103.40**
14	150	1400	26.8	91.00	99.48	97.36	81.30	89.09	100.36	**93.10**
15	150	1600	23.4	86.25	83.12	87.47	88.47	88.71	93.51	**87.92**
16	150	1800	20.8	85.29	80.45	86.67	79.30	80.45	80.35	**82.09**
17	300	1000	75.0	181.52	158.54	155.01	150.47	150.75	163.51	**159.97**
18	300	1200	62.5	168.93	158.68	150.75	133.34	120.83	137.02	**144.93**
19	300	1400	53.6	135.88	140.90	139.40	135.20	123.82	127.23	**133.74**
20	300	1600	46.9	118.47	128.92	125.40	120.00	134.64	128.92	**126.06**
21	300	1800	41.7	133.70	126.84	115.43	118.85	116.45	125.82	**122.85**
22	300	2000	37.5	120.56	130.93	110.53	122.91	114.95	125.32	**120.87**
23	300	2200	34.1	117.12	115.02	123.21	114.88	110.75	113.15	**115.69**
24	300	2400	31.3	115.56	117.31	112.73	111.39	111.45	112.50	**113.49**

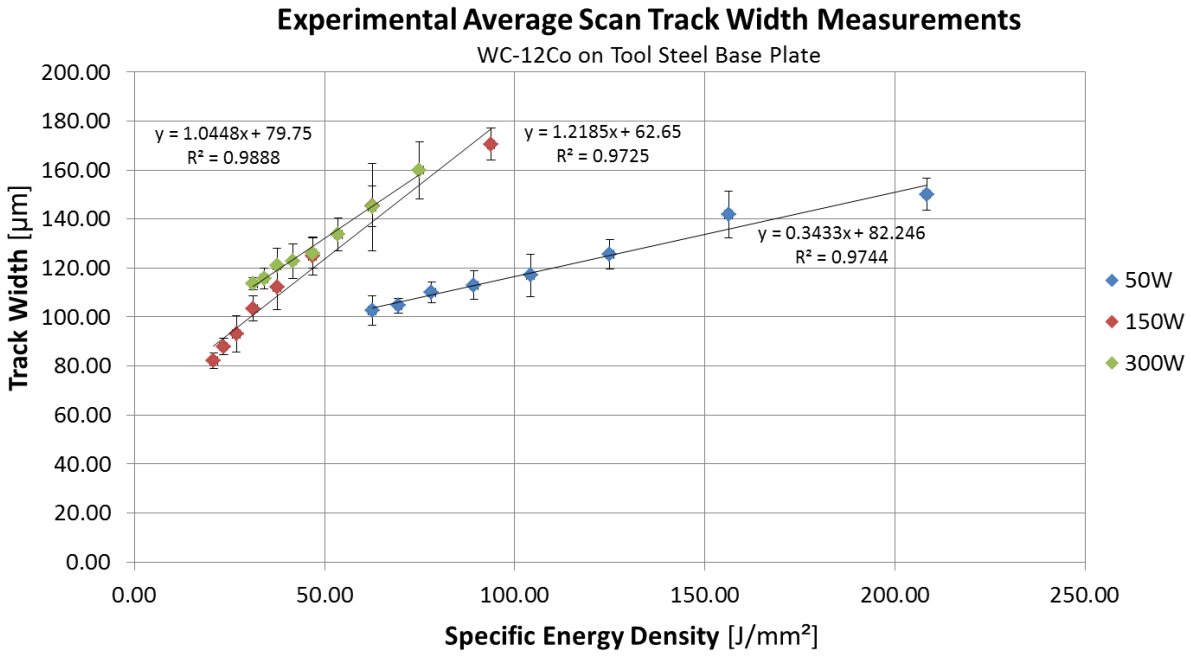

Figure H1: The average width of 24 scan tracks on the tool steel base plate measured at different specific energy density values.

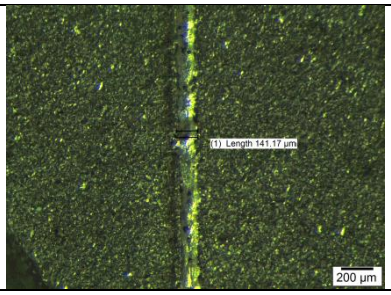	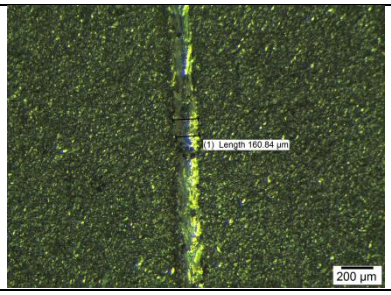	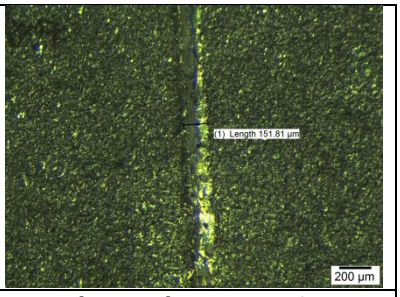
Track 1 - top top - 141.17µm	Track 1 - top middle - 160.84µm	Track 1 - top bottom - 151.81µm
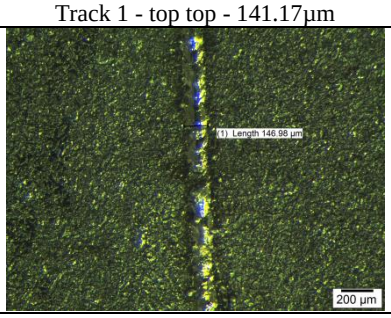	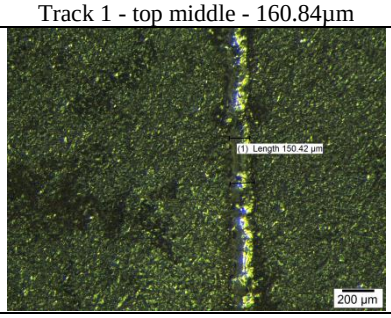	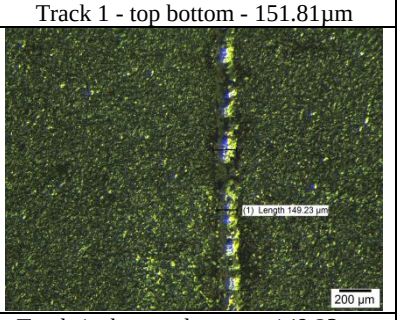
Track 1 - bottom top - 146.98µm	Track 1 - bottom middle - 150.42µm	Track 1 - bottom bottom - 149.23µm
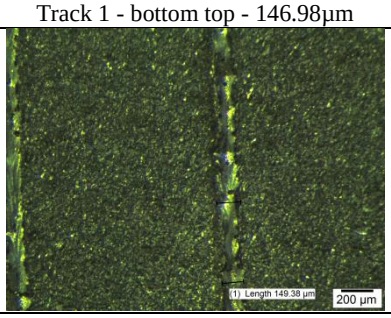	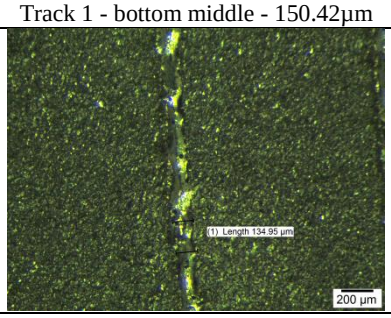	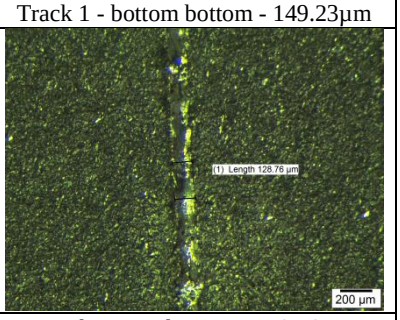
Track 2 - top top - 149.38µm	Track 2 - top middle - 134.95µm	Track 2 - top bottom - 128.76µm
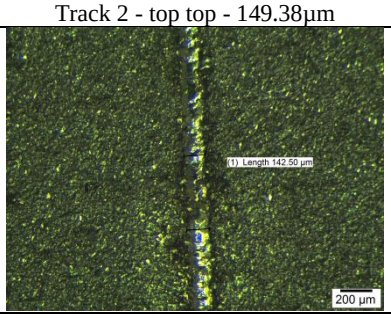	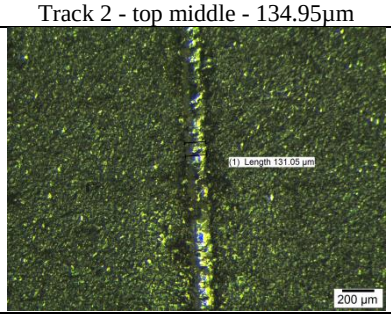	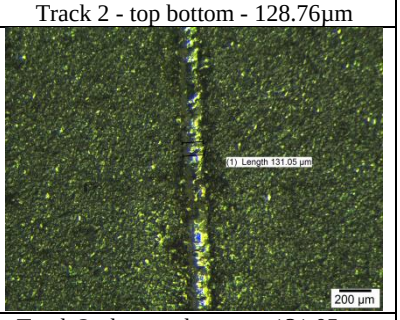
Track 2 - bottom top - 142.50µm	Track 2 - bottom middle -131.05µm	Track 2 - bottom bottom - 131.05µm
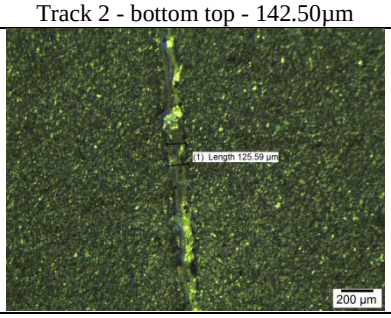	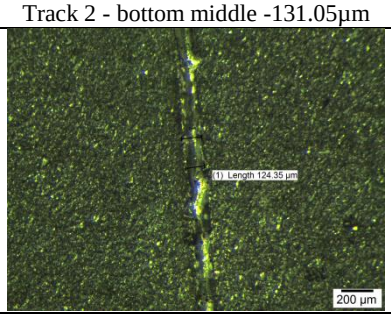	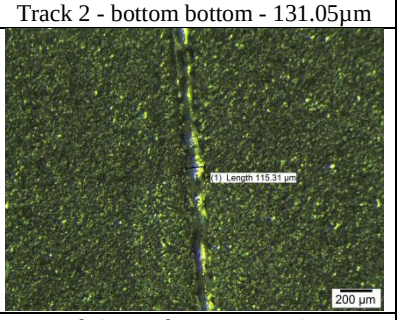
Track 3 - top top - 125.59µm	Track 3 - top middle - 124.35µm	Track 3 - top bottom - 115.31µm
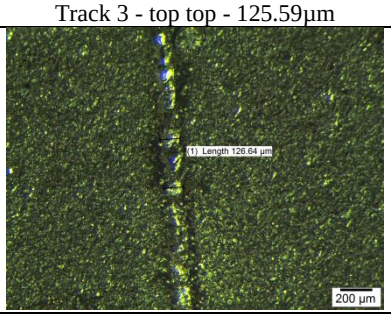	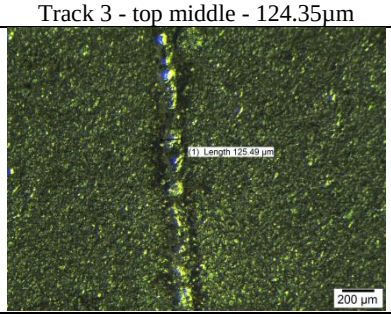	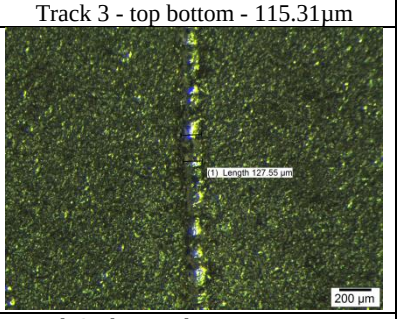
Track 3 - bottom top - 126.64µm	Track 3 - bottom middle - 125.49µm	Track 3 - bottom bottom - 127.55µm

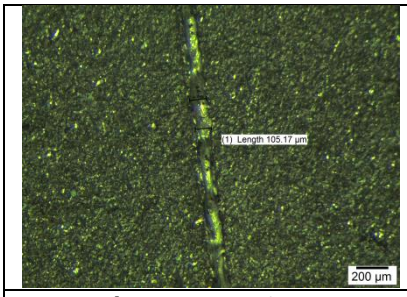	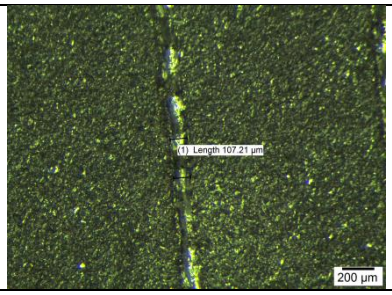	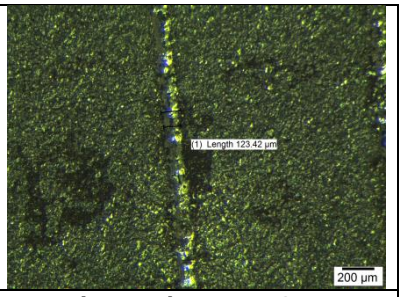
Track 4 - top top - 105.17µm	Track 4 - top middle - 107.21µm	Track 4 - top bottom - 123.42µm
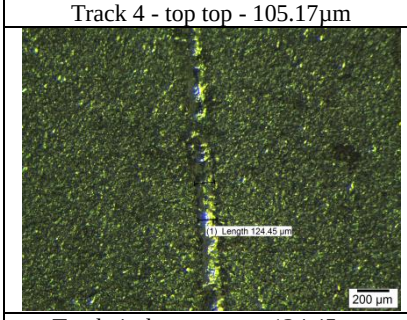	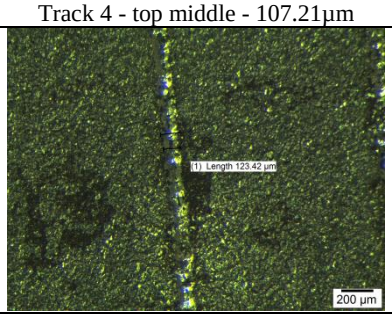	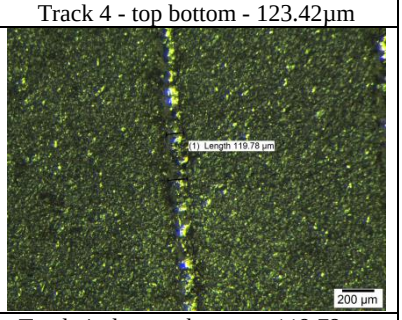
Track 4 - bottom top - 124.45µm	Track 4 - bottom middle - 123.42µm	Track 4 - bottom bottom - 119.78µm
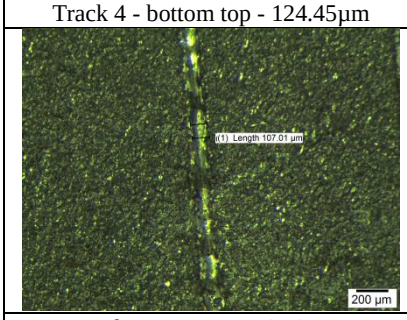	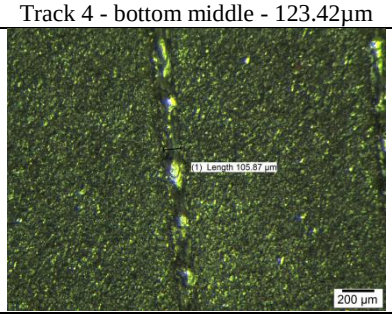	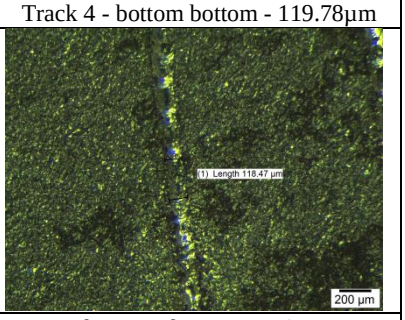
Track 5 - top top - 107.01µm	Track 5 - top middle - 105.87µm	Track 5 - top bottom - 118.47µm
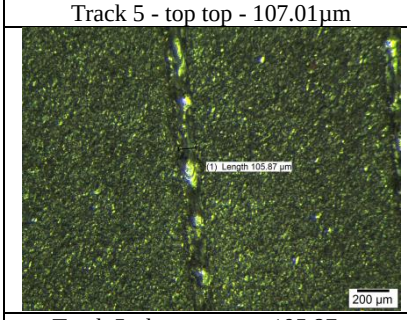	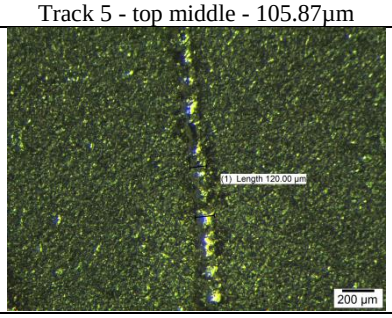	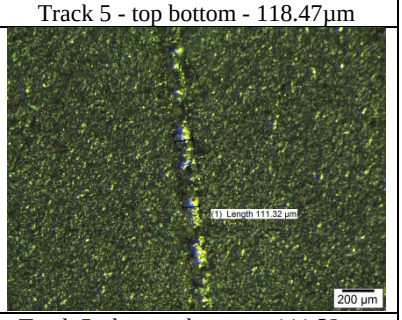
Track 5 - bottom top - 105.87µm	Track 5 - bottom middle - 120.00µm	Track 5 - bottom bottom - 111.32µm
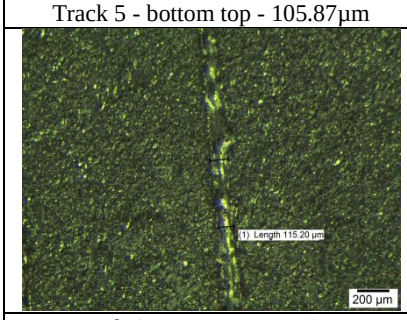	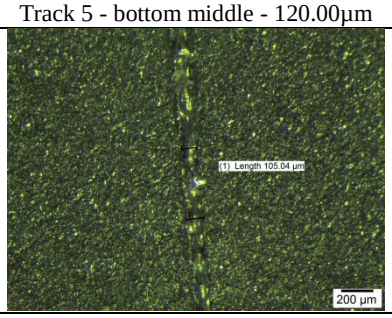	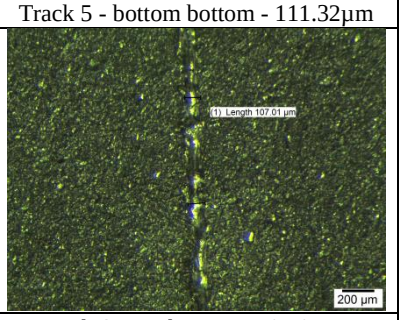
Track 6 - top top - 115.20µm	Track 6 - top middle - 105.04µm	Track 6 - top bottom - 107.01µm
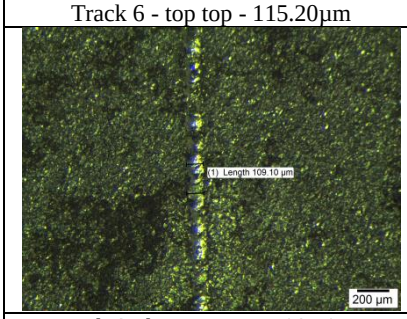	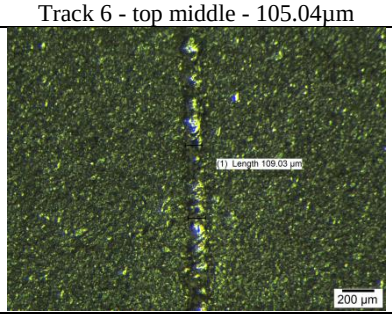	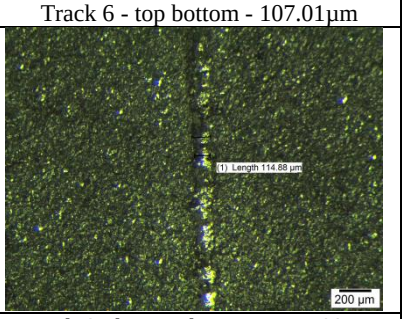
Track 6 - bottom top - 109.10µm	Track 6 - bottom middle - 109.03µm	Track 6 - bottom bottom - 114.88µm

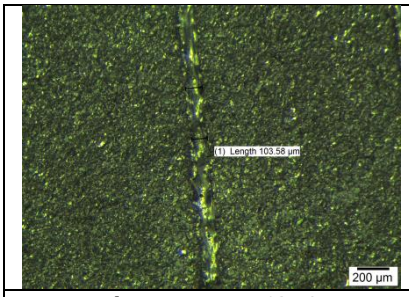

Track 7 - top top - 103.58µm

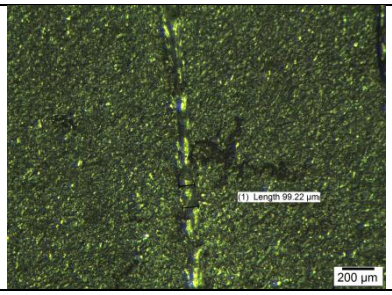

Track 7 - top middle - 99.22µm

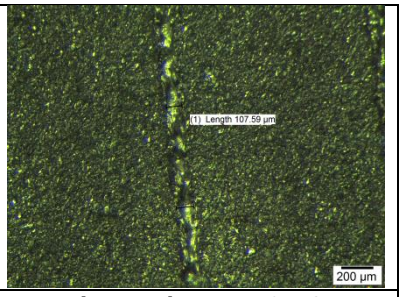

Track 7 - top bottom - 107.59µm

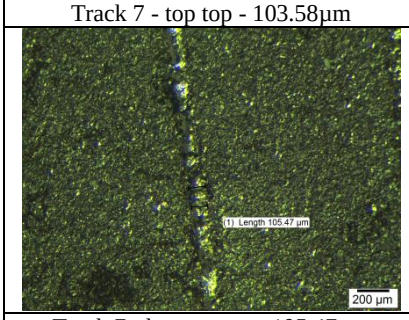

Track 7 - bottom top - 105.47µm

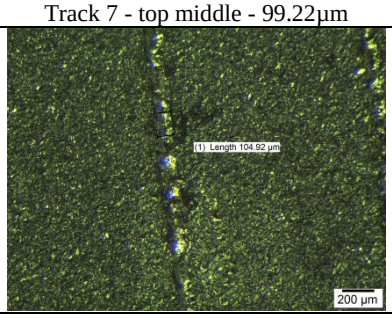

Track 7 - bottom middle - 104.92µm

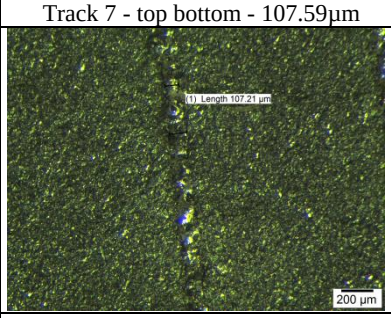

Track 7 - bottom bottom - 107.21µm

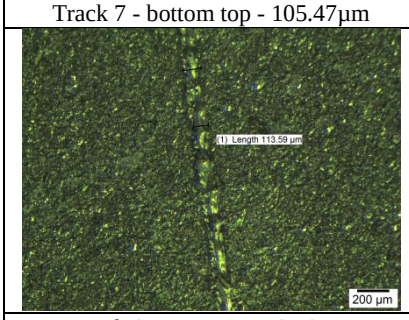

Track 8 - top top - 113.59µm

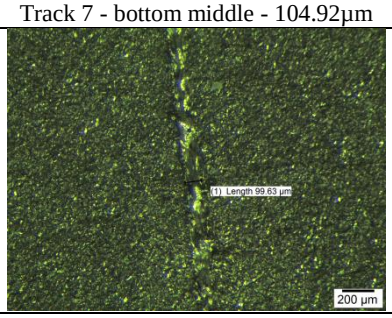

Track 8 - top middle - 99.63µm

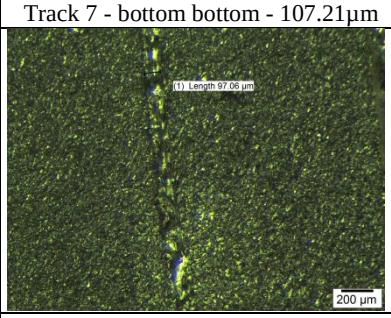

Track 8 - top bottom - 97.06µm

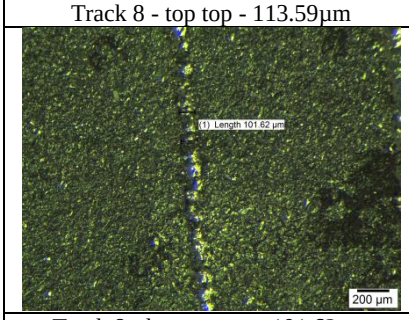

Track 8 - bottom top - 101.62µm

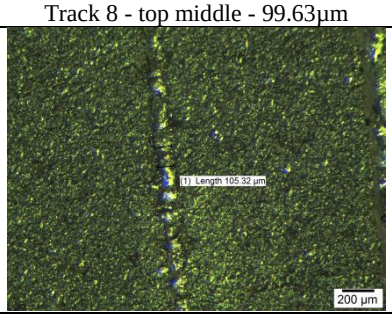

Track 8 - bottom middle - 105.32µm

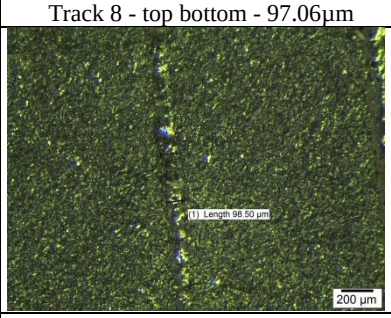

Track 8 - bottom bottom - 98.50µm

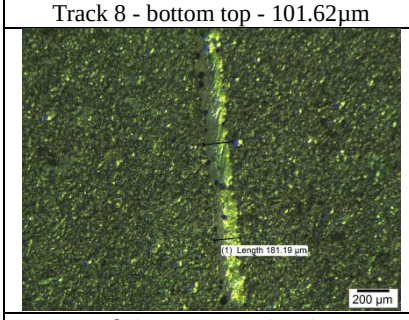

Track 9 - top top - 181.19µm

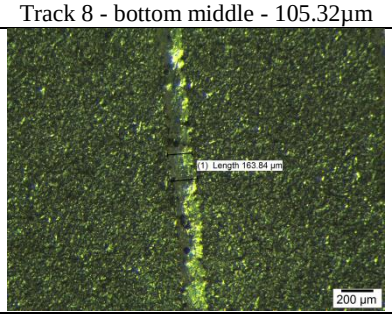

Track 9 - top middle - 163.84µm

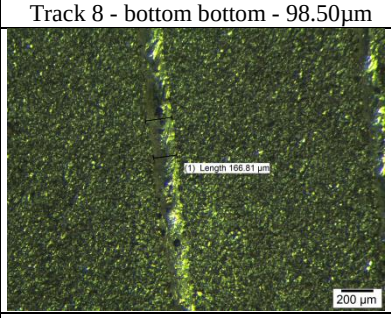

Track 9 - top bottom - 166.81µm

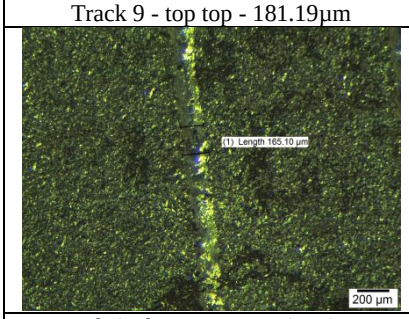

Track 9 - bottom top - 165.10µm

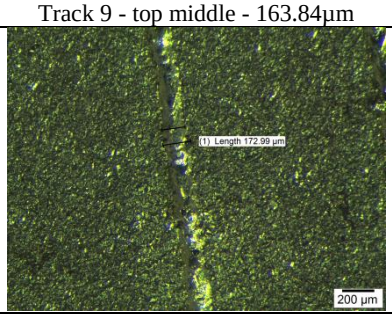

Track 9 - bottom middle - 172.99µm

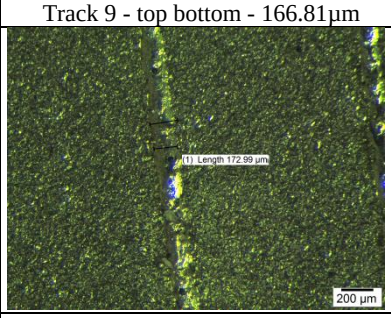

Track 9 - bottom bottom - 172.99µm

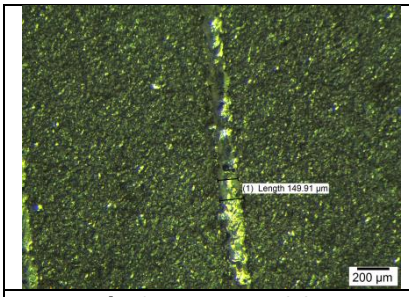

Track 10 - top top - 149.91µm

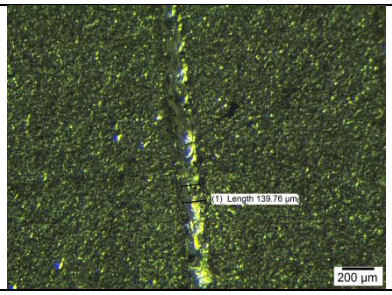

Track 10 - top middle - 139.76µm

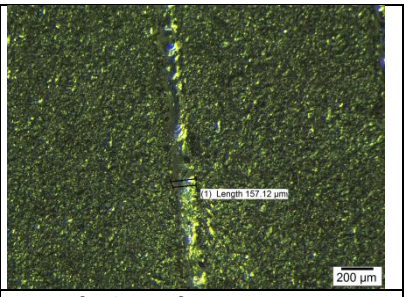

Track 10 - top bottom - 157.12µm

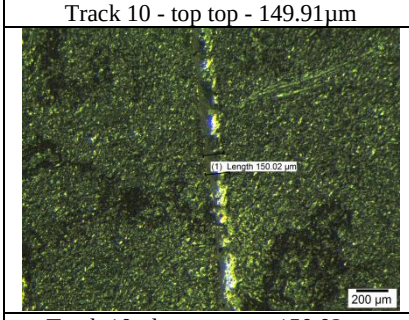

Track 10 - bottom top - 150.02µm

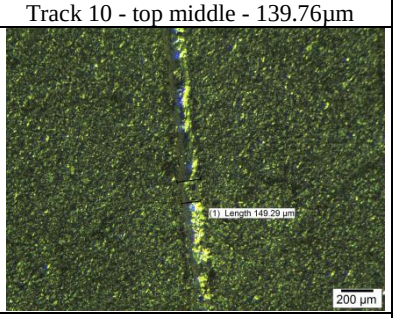

Track 10 - bottom middle - 149.29µm

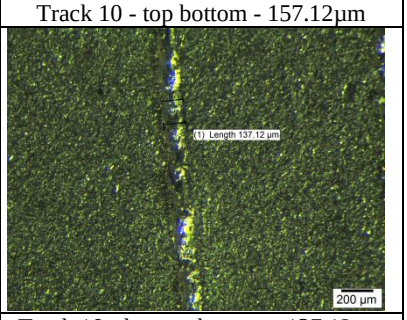

Track 10 - bottom bottom - 137.12µm

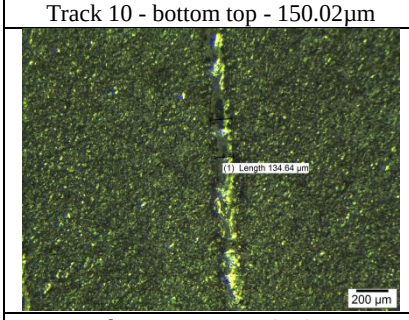

Track 11 - top top - 134.64µm

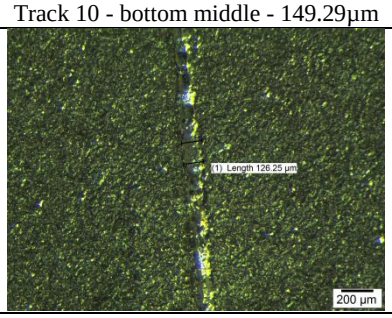

Track 11- top middle - 126.25µm

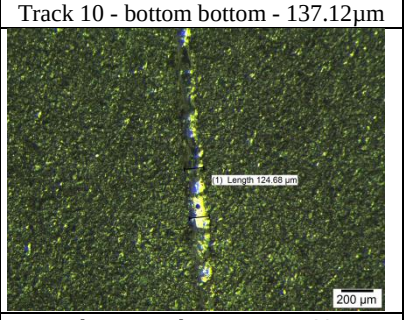

Track 11 - top bottom - 124.68µm

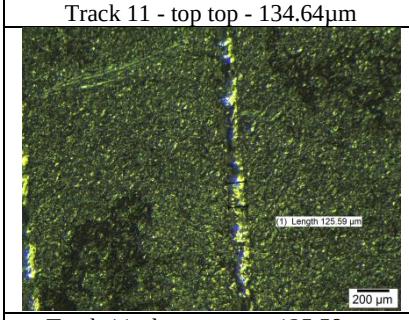

Track 11 - bottom top - 125.59µm

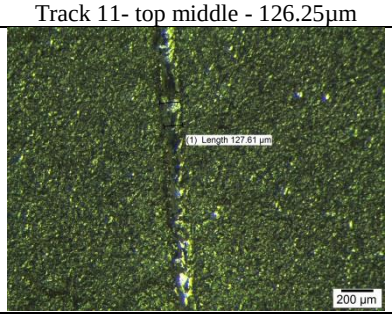

Track 11 - bottom middle - 127.61µm

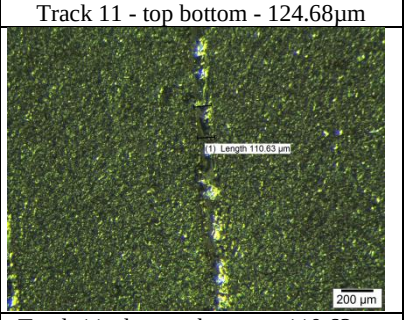

Track 11 - bottom bottom - 110.63µm

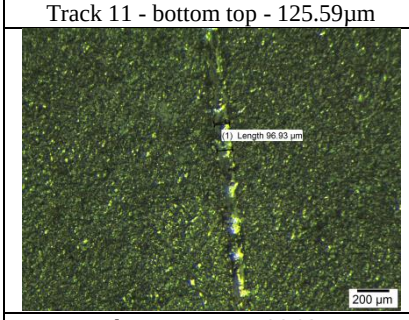

Track 12 - top top - 96.93µm

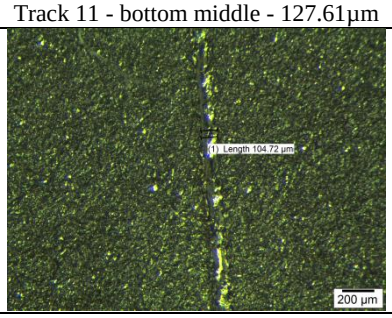

Track 12 - top middle - 104.72µm

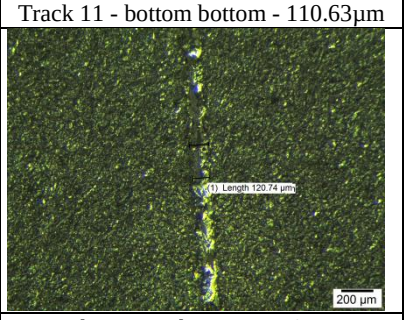

Track 12 - top bottom - 120.74µm

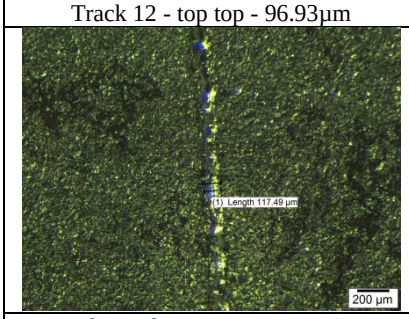

Track 12 - bottom top - 117.49µm

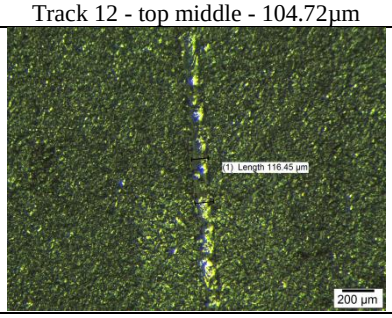

Track 12 - bottom middle - 116.45µm

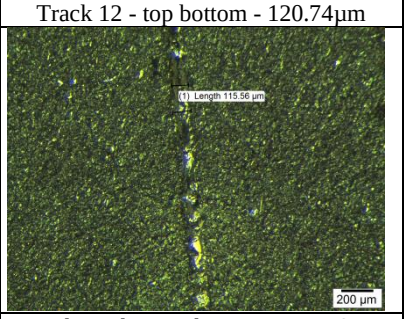

Track 12- bottom bottom - 115.56µm

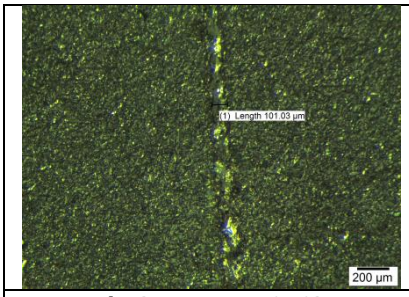	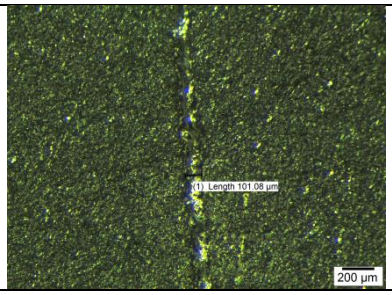	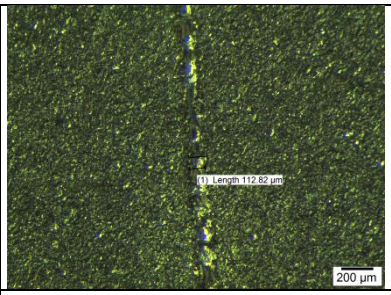
Track 13 - top top - 101.03µm	Track 13 - top middle - 101.08µm	Track 13 - top bottom - 112.82µm
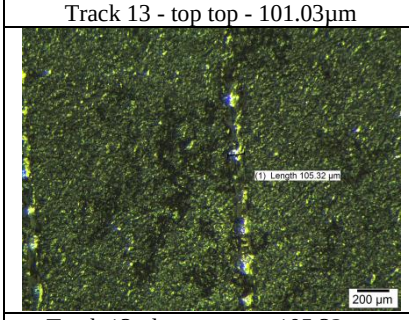	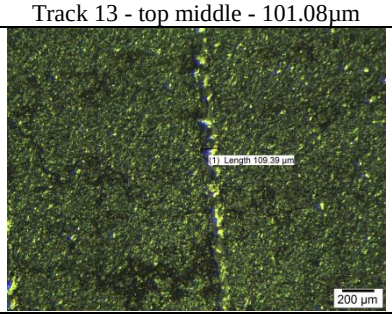	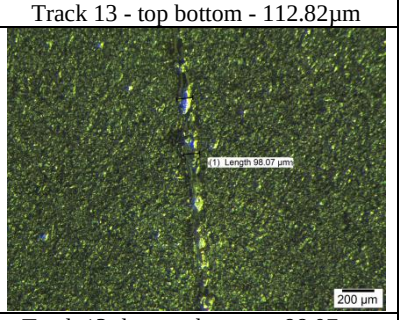
Track 13 - bottom top - 105.32µm	Track 13 - bottom middle - 109.39µm	Track 13- bottom bottom - 98.07µm
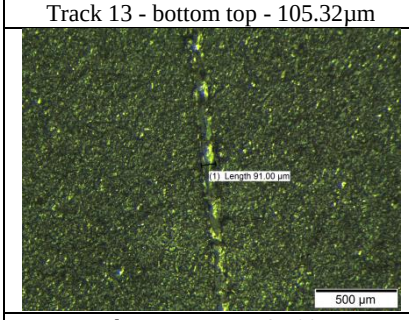	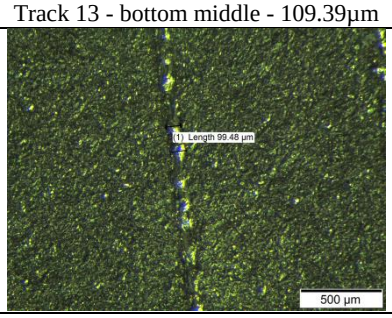	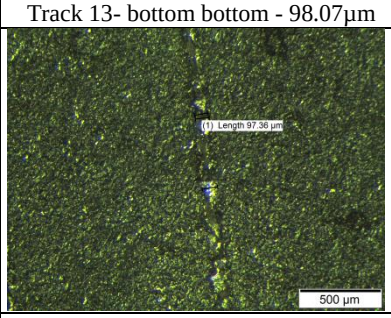
Track 14 - top top - 91.00µm	Track 14 - top middle - 99.48µm	Track 14 - top bottom - 97.36µm
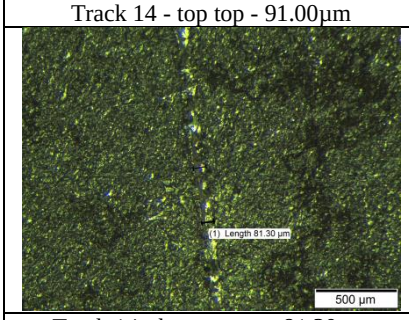	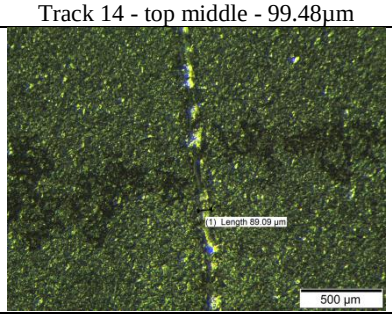	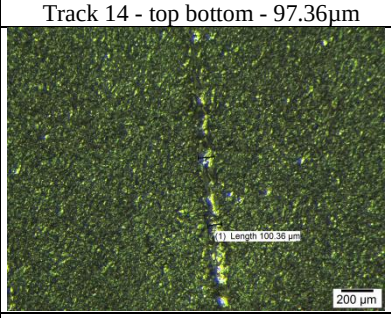
Track 14 - bottom top - 81.30µm	Track 14 - bottom middle - 89.09µm	Track 14 - bottom bottom - 100.36µm
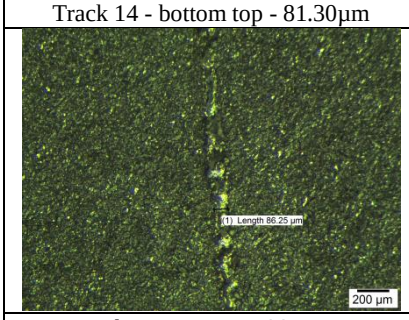	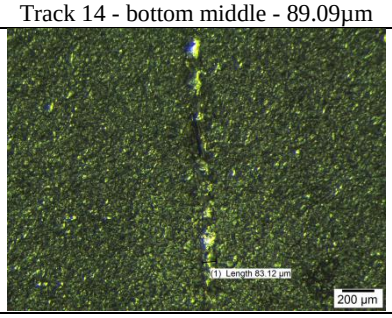	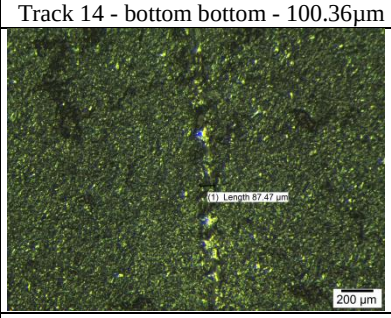
Track 15 - top top - 86.25µm	Track 15 - top middle - 83.12µm	Track 15 - top bottom - 87.47µm
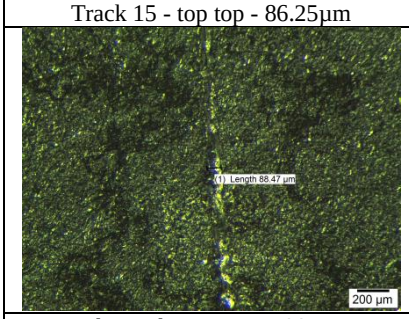	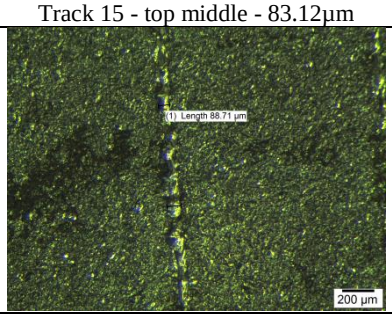	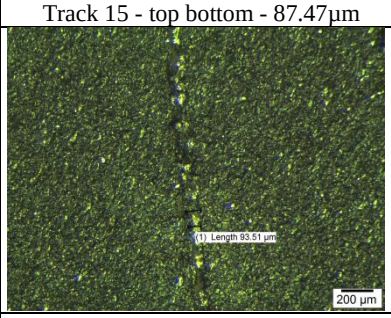
Track 15 - bottom top - 88.47µm	Track 15 - bottom middle - 88.71µm	Track 15 - bottom bottom - 93.51µm

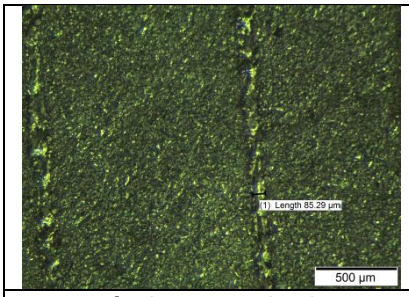	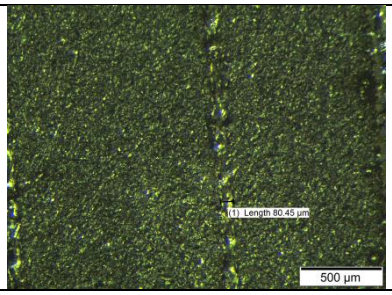	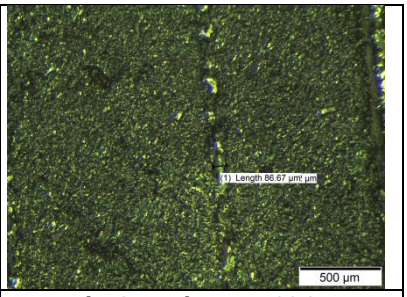
Track 16 - top top - 85.29µm	Track 16 - top middle - 80.45µm	Track 16 - top bottom - 86.67µm
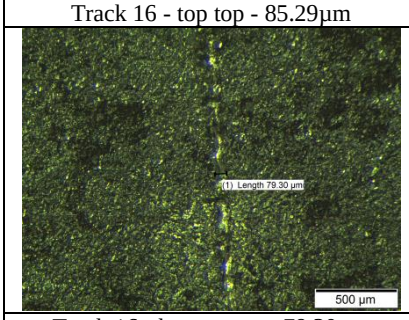	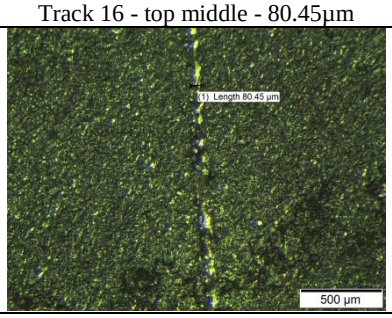	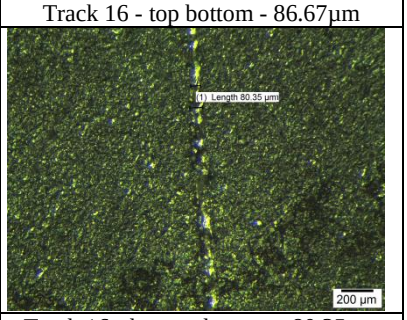
Track 16 - bottom top - 79.30µm	Track 16 - bottom middle - 80.45µm	Track 16 - bottom bottom - 80.35µm
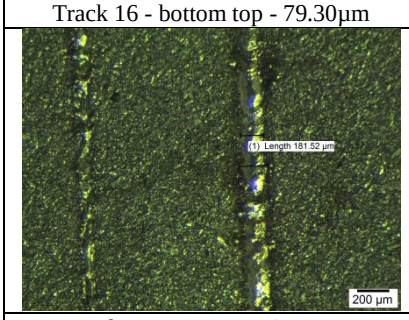	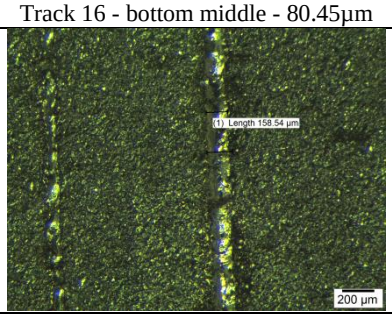	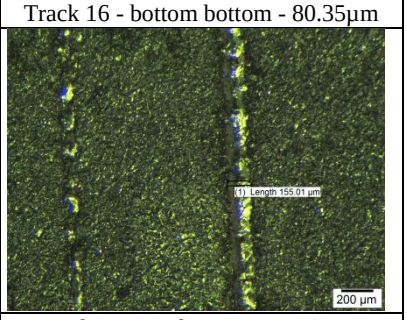
Track 17 - top top - 181.52µm	Track 17 - top middle - 158.54µm	Track 17 - top bottom - 155.01µm
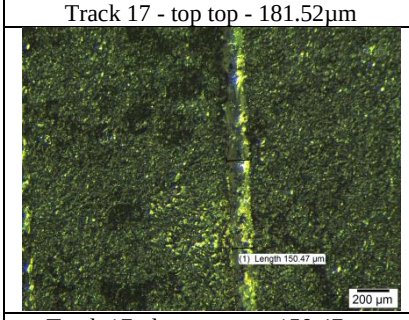	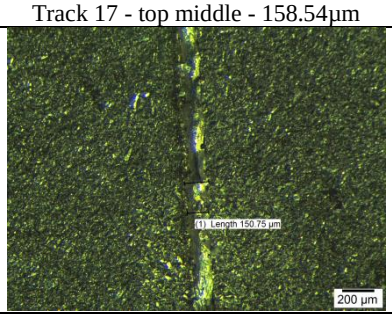	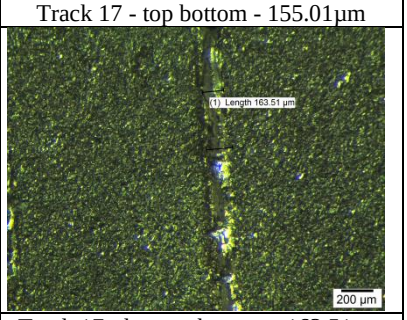
Track 17 - bottom top - 150.47µm	Track 17 - bottom middle - 150.75µm	Track 17 - bottom bottom - 163.51µm
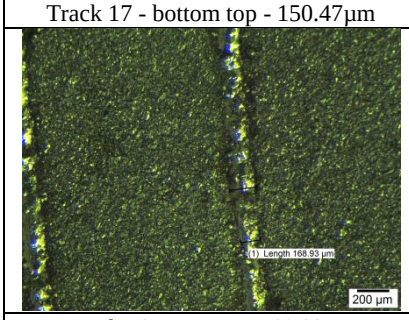	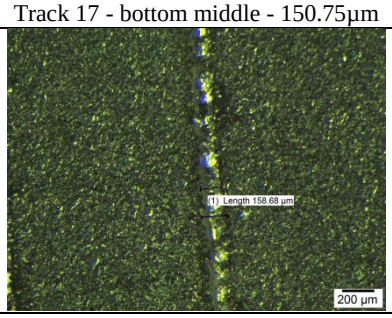	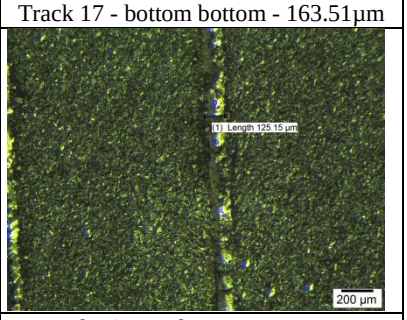
Track 18 - top top - 168.93µm	Track 18 - top middle - 158.68µm	Track 18 - top bottom - 125.15µm
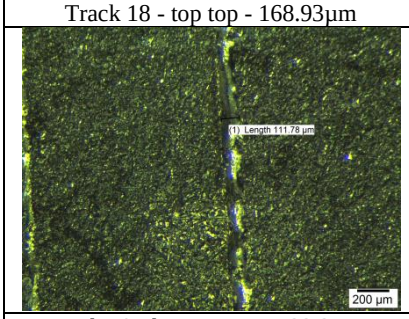	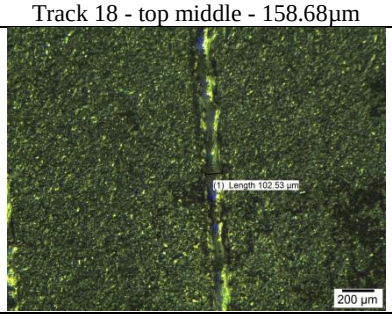	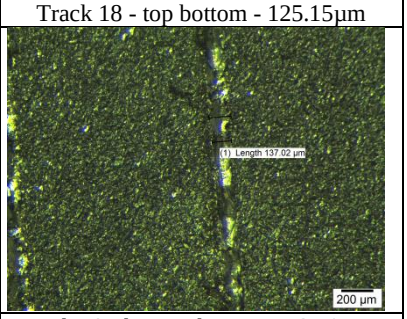
Track 18 - bottom top - 133.34µm	Track 18 - bottom middle - 120.83µm	Track 18 - bottom bottom - 137.02µm

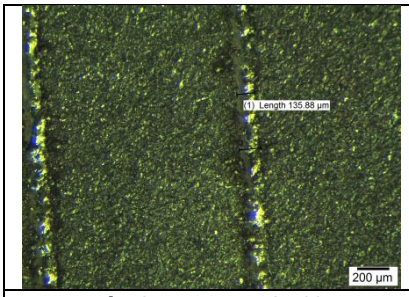

Track 19 - top top - 135.88µm

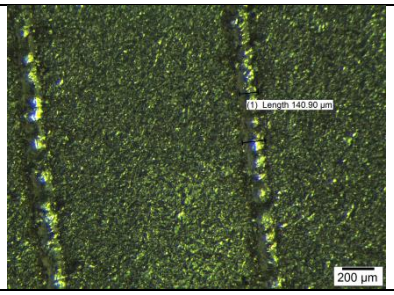

Track 19 - top middle - 140.90µm

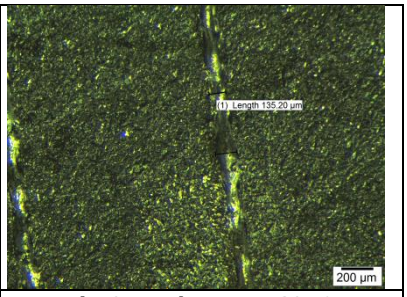

Track 19 - top bottom - 139.40µm

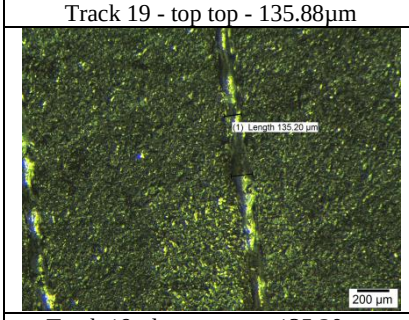

Track 19 - bottom top - 135.20µm

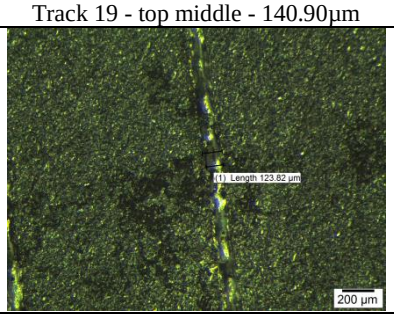

Track 19 - bottom middle - 123.82µm

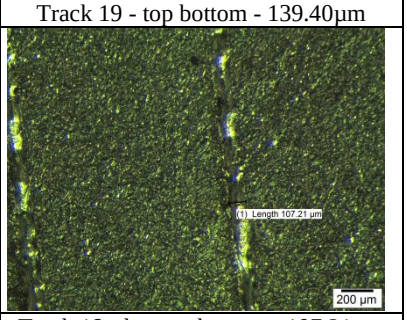

Track 19 - bottom bottom - 107.21µm

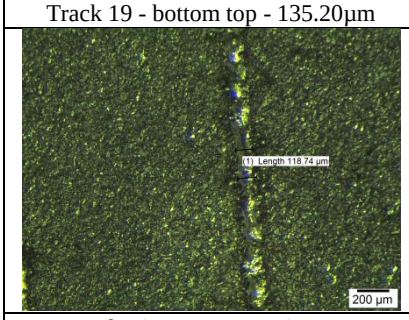

Track 20 - top top - 118.47µm

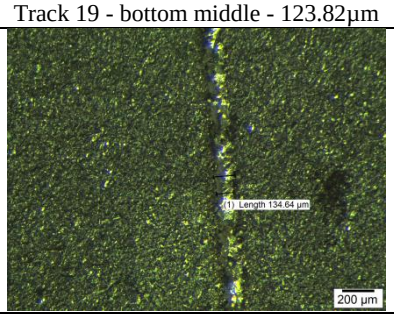

Track 20 - top middle - 134.64µm

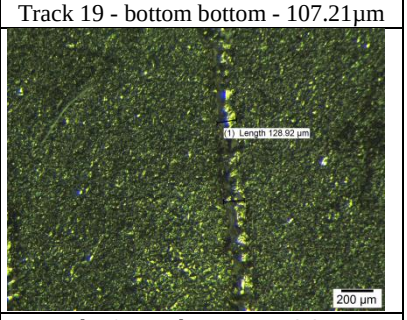

Track 20 - top bottom - 128.92µm

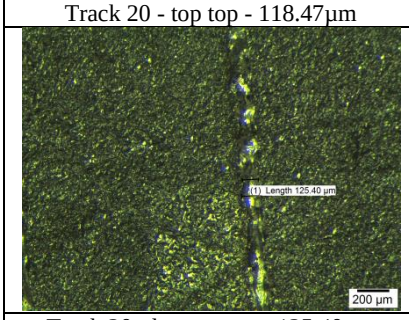

Track 20 - bottom top - 125.40µm

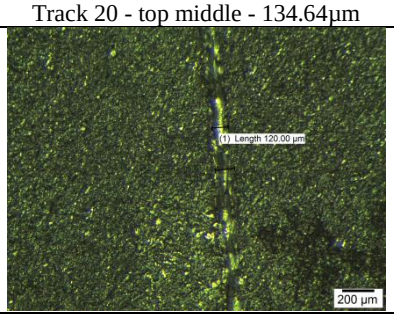

Track 20 - bottom middle - 120.00µm

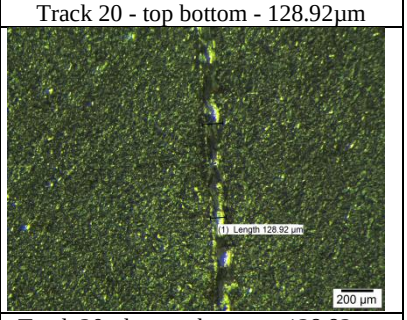

Track 20 - bottom bottom - 128.92µm

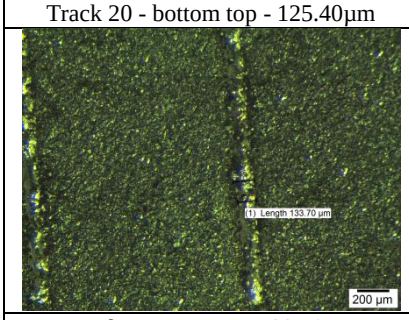

Track 21 - top top - 133.70µm

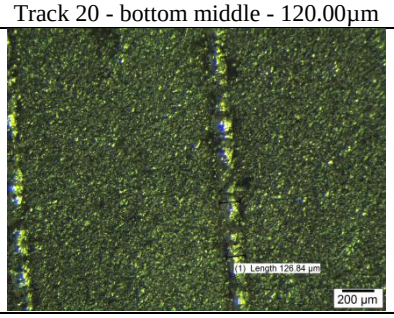

Track 21 - top middle - 126.84µm

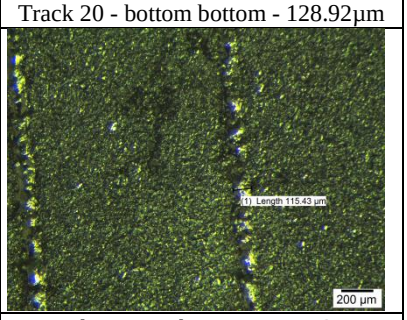

Track 21 - top bottom - 115.43µm

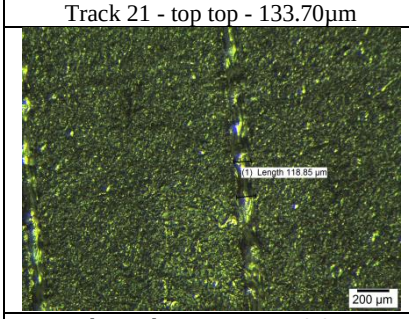

Track 21 - bottom top - 118.85µm

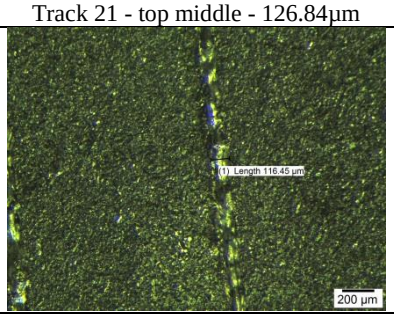

Track 21 - bottom middle - 116.45µm

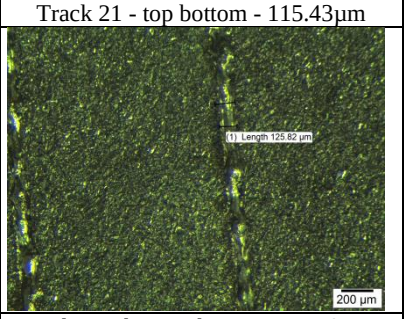

Track 21 - bottom bottom - 125.82µm

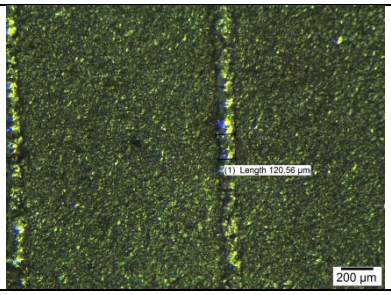	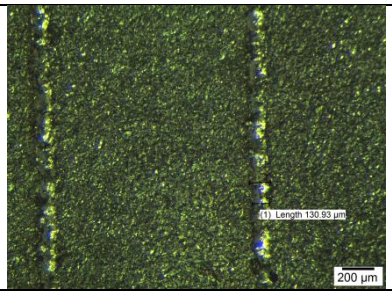	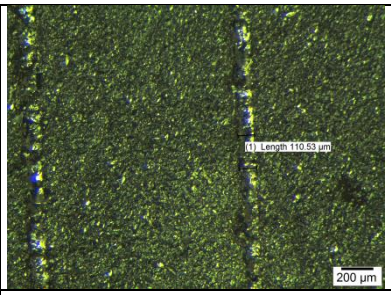
Track 22 - top top - 120.56µm	Track 22 - top middle - 130.93µm	Track 22 - top bottom - 110.53µm
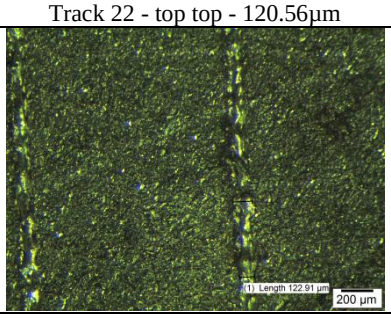	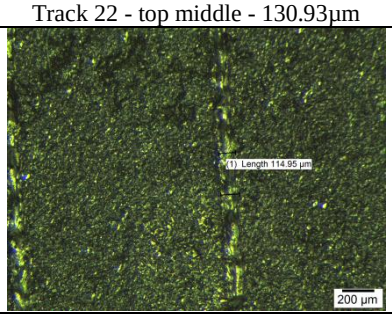	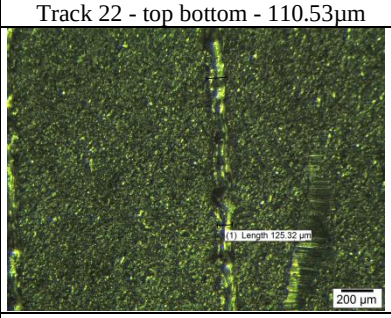
Track 22 - bottom top - 122.91µm	Track 22 - bottom middle - 114.95µm	Track 22 - bottom bottom - 125.32µm
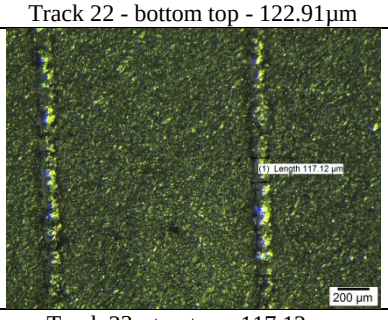	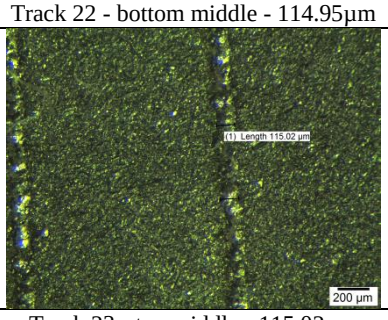	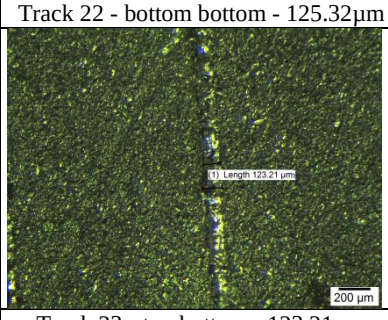
Track 23 - top top - 117.12µm	Track 23 - top middle - 115.02µm	Track 23 - top bottom - 123.21µm
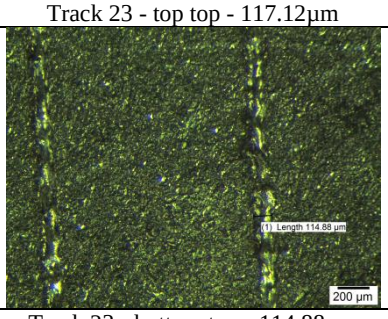	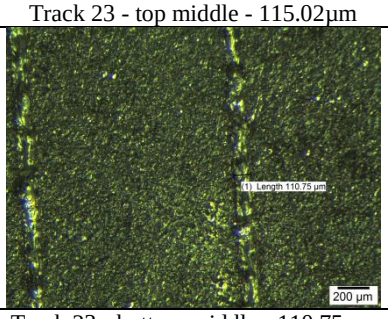	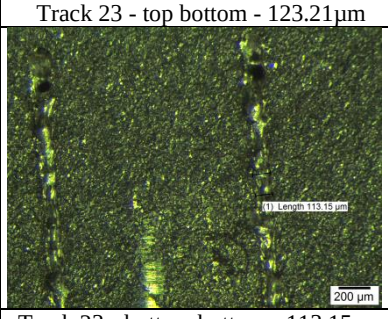
Track 23 - bottom top - 114.88µm	Track 23 - bottom middle - 110.75µm	Track 23 - bottom bottom - 113.15µm
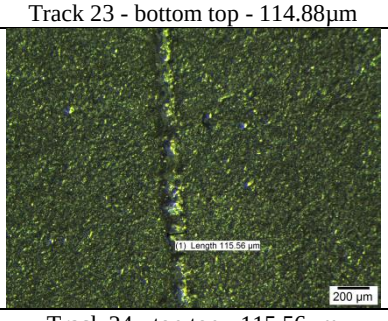	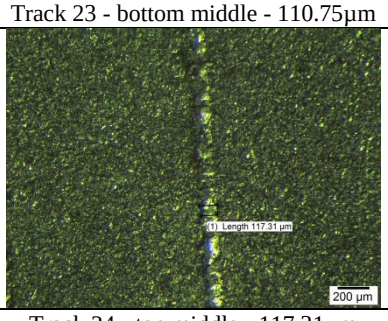	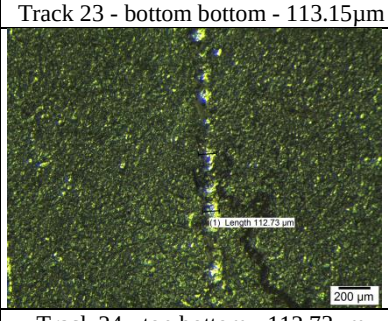
Track 24 - top top - 115.56µm	Track 24 - top middle - 117.31µm	Track 24 - top bottom - 112.73µm
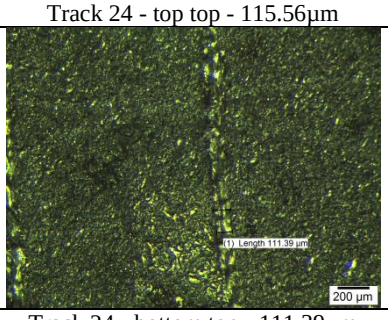	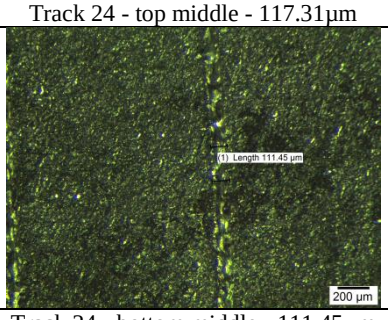	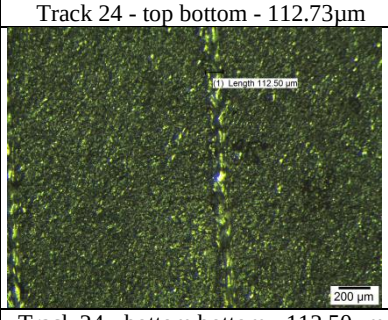
Track 24 - bottom top - 111.39µm	Track 24 - bottom middle - 111.45µm	Track 24 - bottom bottom - 112.50µm

Appendix I: Laser Penetration Depth Measurements - Tool Steel Base Plate

Table H1: Experimental scan track penetration depth of the WC-12Co on the tool steel base plate.

Parameter set/ scan track number	Power [W]	Scanning speed [mm/s]	Energy density [J / mm^2]	Depth measurements [µm] 1	2	3	4	5	Average width [µm]
1	50	60	208.33	71.89	108.41	68.25	57.41	56.36	72.46
2	50	80	156.25	69.54	91.81	64.70	52.52	52.76	66.27
3	50	100	125.00	62.20	81.43	52.92	49.21	48.95	58.94
4	50	120	104.17	55.87	73.64	46.91	48.21	45.77	54.08
5	50	140	89.29	36.53	60.13	48.87	41.21	35.38	44.42
6	50	160	78.13	35.15	49.48	41.69	37.61	24.79	37.74
7	50	180	69.44	26.23	45.41	39.36	41.02	10.24	32.45
8	50	200	62.50	17.51	41.00	40.81	35.86	11.77	29.39
9	150	400	93.75	72.40	115.67	129.50	122.16	116.61	111.27
10	150	600	62.50	59.00	74.33	76.82	69.51	54.75	66.88
11	150	800	46.88	41.99	68.37	69.23	69.16	39.44	57.64
12	150	1000	37.50	41.22	59.50	54.10	58.18	34.52	49.50
13	150	1200	31.25	39.72	52.54	38.00	48.79	28.28	41.47
14	150	1400	26.79	35.75	36.95	34.91	48.86	17.48	34.79
15	150	1600	23.44	30.97	35.33	30.55	33.79	21.98	30.52
16	150	1800	20.83	25.07	48.77	25.38	35.86	19.44	30.90
17	300	1000	75.00	66.70	65.23	78.90	104.23	88.82	80.78
18	300	1200	62.50	60.70	60.65	76.37	93.59	73.06	72.87
19	300	1400	53.57	52.65	60.00	73.29	73.28	63.88	64.62
20	300	1600	46.88	41.45	53.58	60.13	62.77	43.72	52.33
21	300	1800	41.67	39.45	53.17	51.67	58.36	37.45	48.02
22	300	2000	37.50	30.90	42.51	49.22	40.27	37.34	40.05
23	300	2200	34.09	29.05	42.37	38.96	38.60	34.58	36.71
24	300	2400	31.25	25.54	37.01	37.45	35.31	33.08	33.68

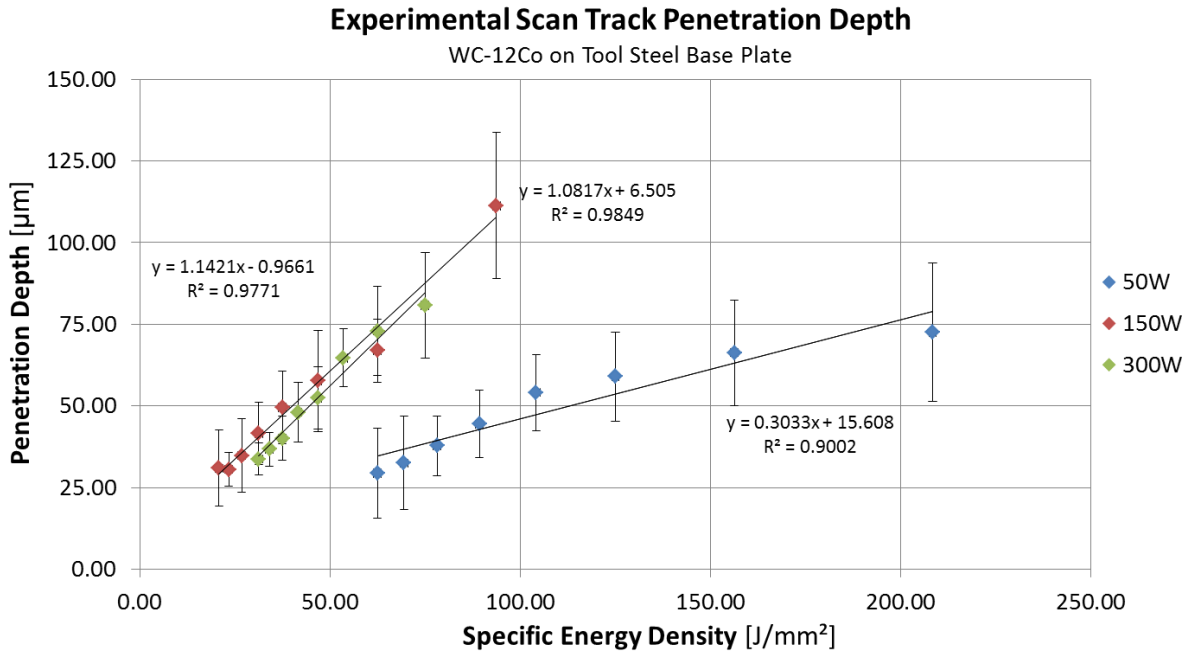

Figure H1: The average penetration depth of 24 scan tracks on the tool steel base plate measured at different specific energy density values.

Track 1 P = 50 W V = 60 mm/s	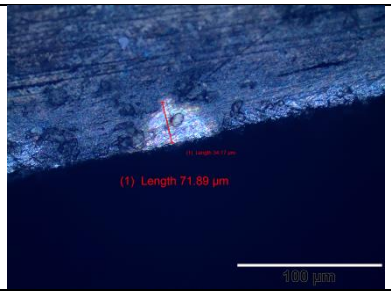	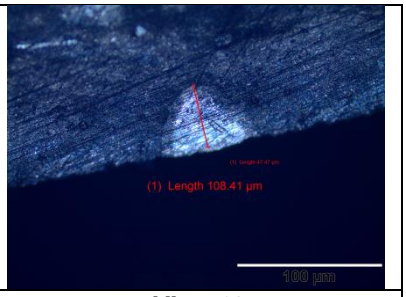
	top top - 71.89µm	top middle - 108.41µm
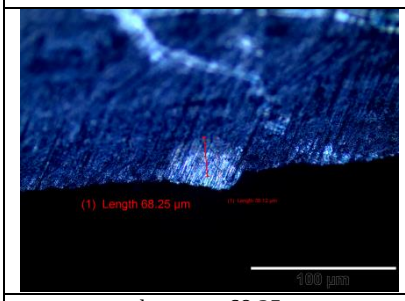	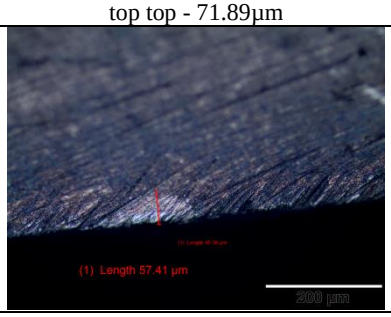	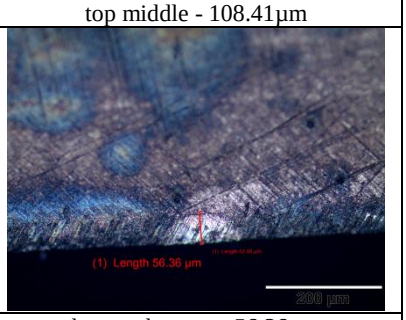
top bottom - 68.25µm	bottom top - 57.41µm	bottom bottom - 56.36µm
Track 2 P = 50 W V = 80 mm/s	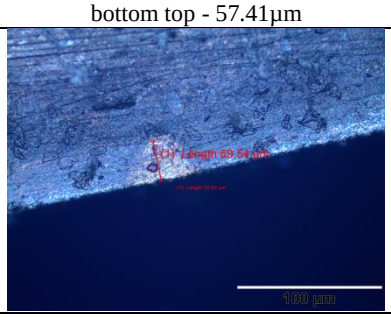	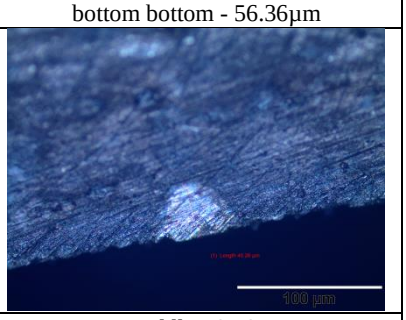
	top top - 69.54µm	top middle - 91.81µm
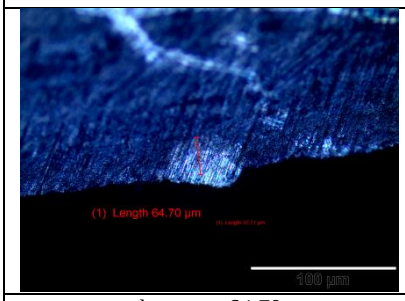	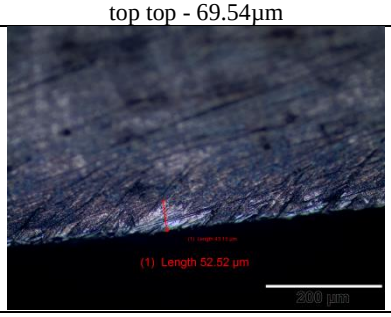	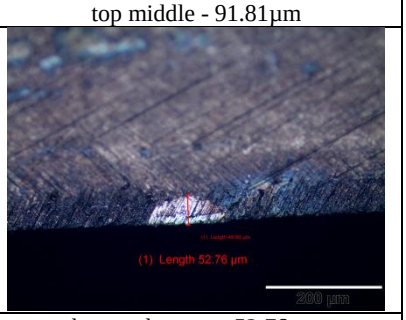
top bottom - 64.70µm	bottom top - 52.52µm	bottom bottom - 52.76µm
Track 3 P = 50 W V = 100 mm/s	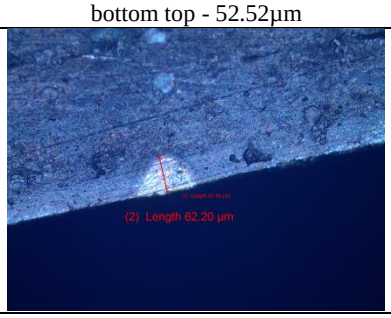	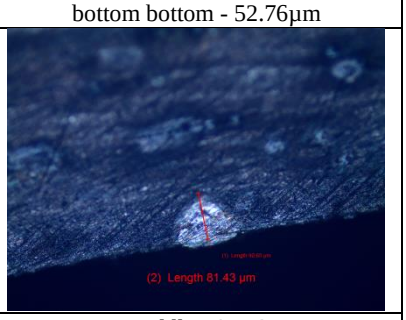
	top top - 62.20µm	top middle - 81.43µm
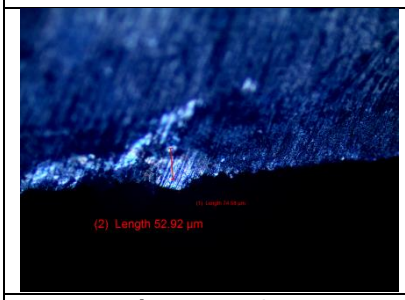	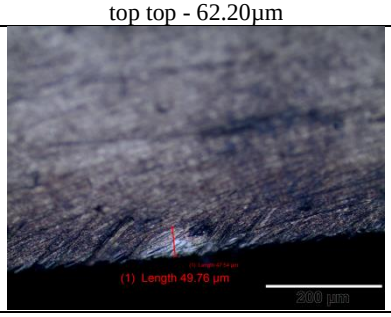	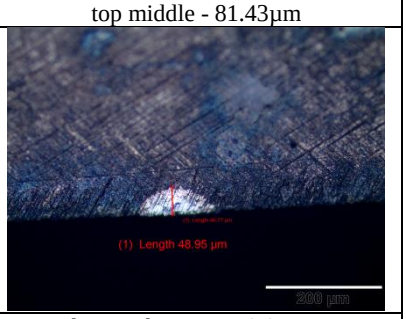
top bottom - 52.92µm	bottom top - 49.76µm	bottom bottom - 48.95µm

Track 4 P = 50 W V = 120 mm/s	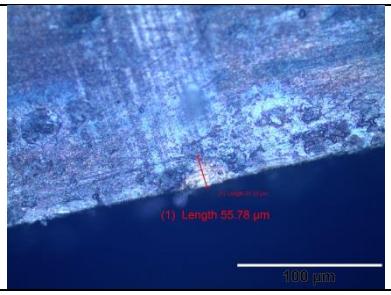	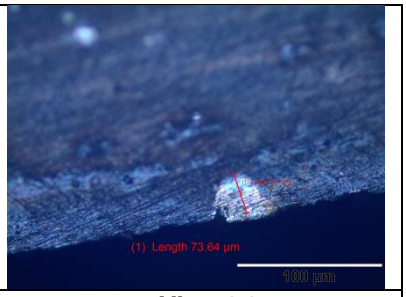
	top top - 55.78µm	top middle - 73.64µm
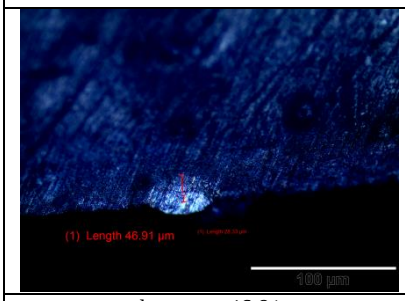	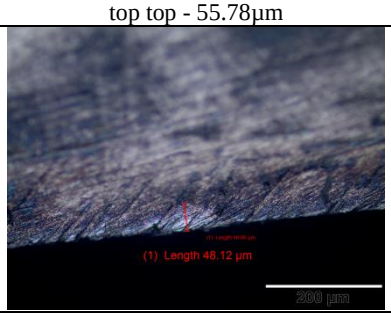	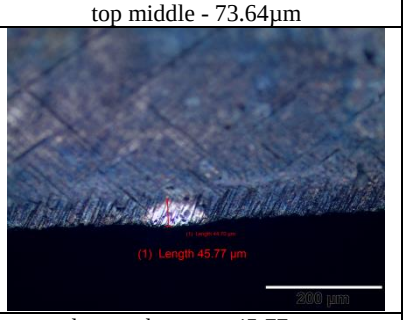
top bottom - 46.91µm	bottom top - 48.12µm	bottom bottom - 45.77µm
Track 5 P = 50 W V = 140 mm/s	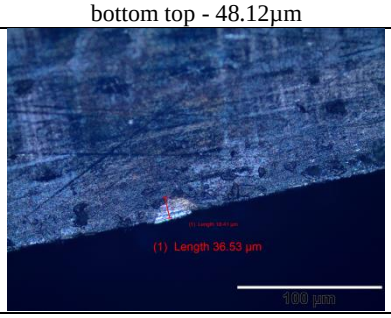	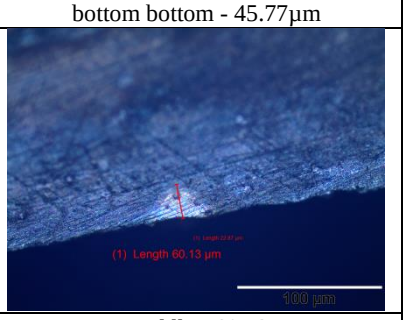
	top top - 36.53µm	top middle - 60.13µm
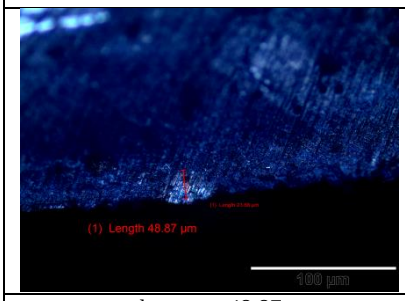	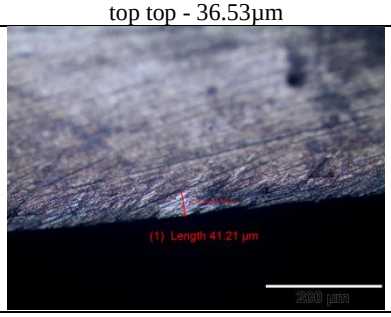	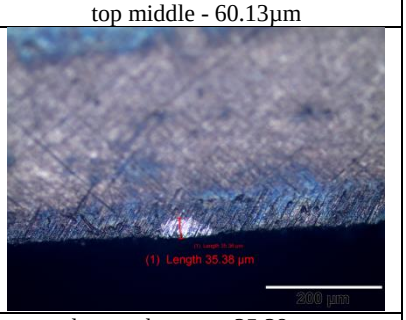
top bottom - 48.87µm	bottom top - 41.21µm	bottom bottom - 35.38µm
Track 6 P = 50 W V = 160 mm/s	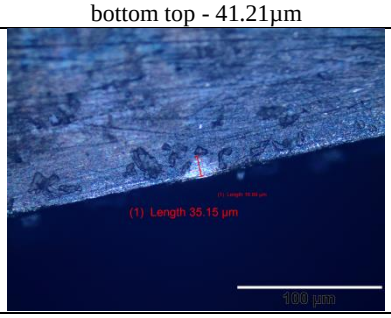	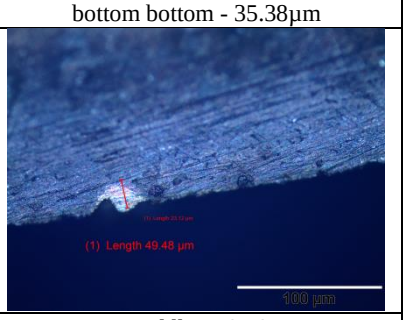
	top top - 35.15µm	top middle - 49.48µm
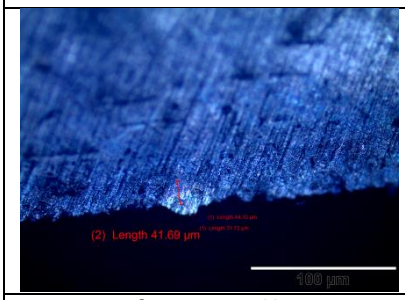	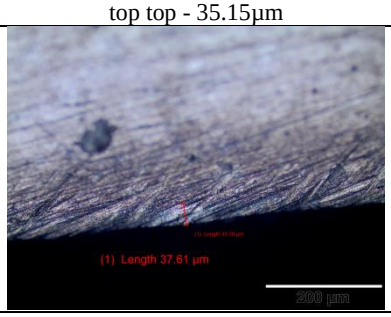	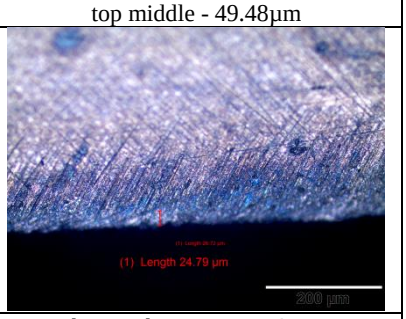
top bottom - 41.69µm	bottom top - 37.61µm	bottom bottom - 24.79µm

Track 7 P = 50 W V = 180 mm/s	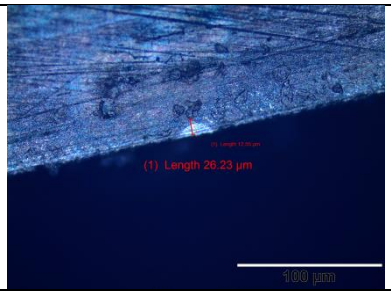	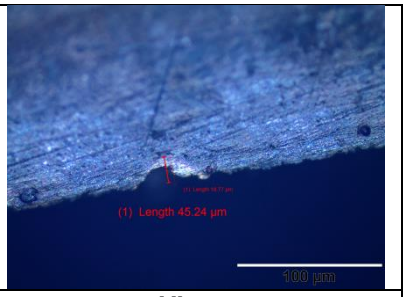
	top top - 26.23µm	top middle - 45.24µm
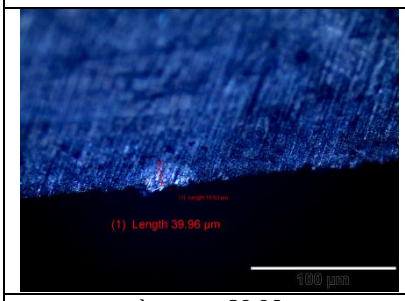	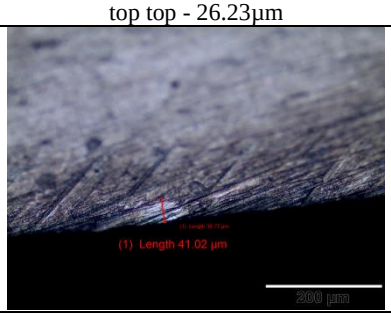	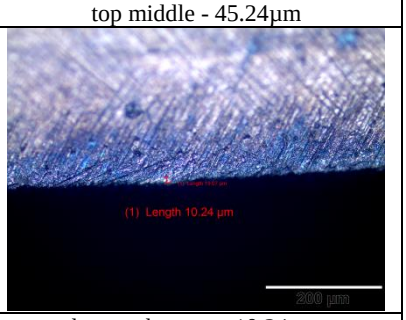
top bottom - 39.96µm	bottom top - 41.02µm	bottom bottom - 10.24µm
Track 8 P = 50 W V = 200 mm/s	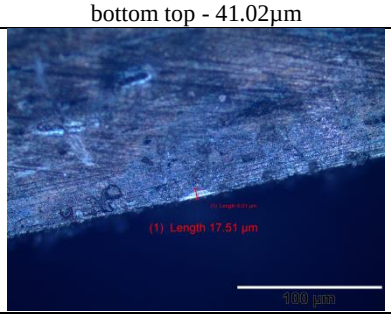	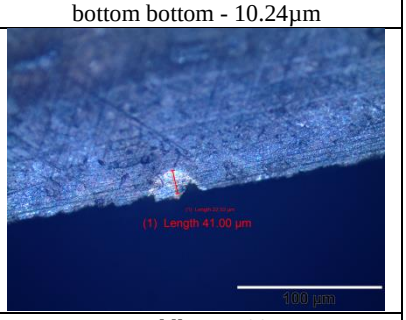
	top top - 17.51µm	top middle - 41.00µm
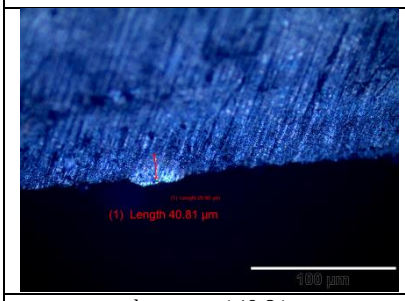	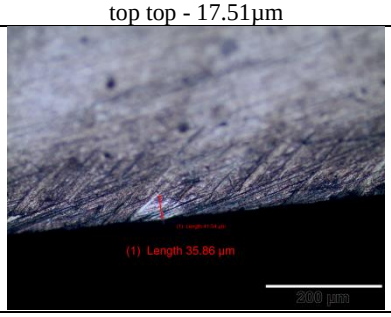	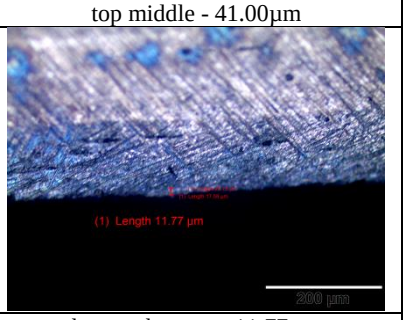
top bottom - 140.81µm	bottom top - 35.86µm	bottom bottom - 11.77µm
Track 9 P = 150 W V = 400 mm/s	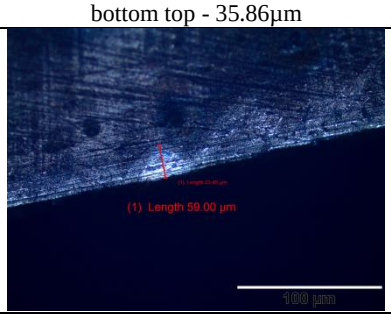	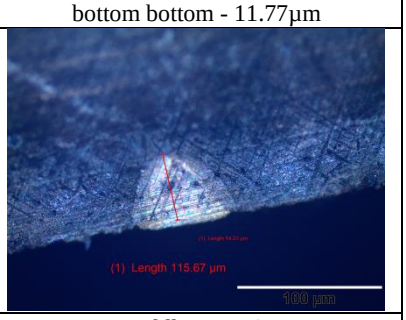
	top top - 59.00µm	top middle - 115.67µm
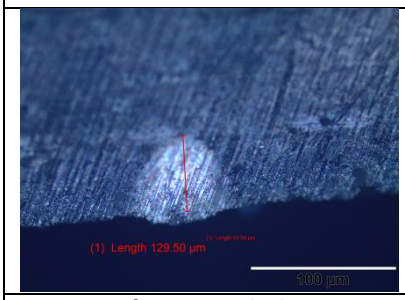	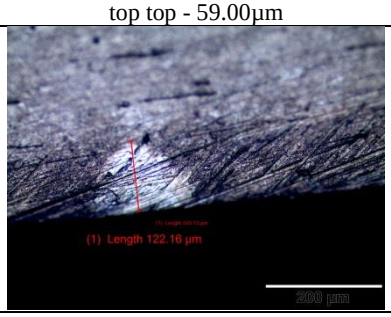	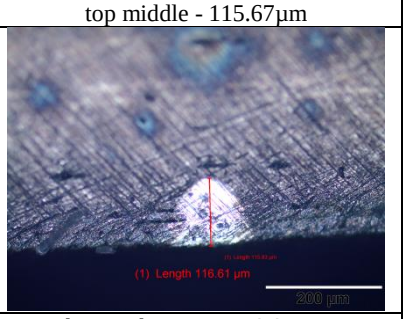
top bottom - 129.50µm	bottom top - 122.16µm	bottom bottom - 116.61µm

Track 10 P = 150 W V = 600 mm/s	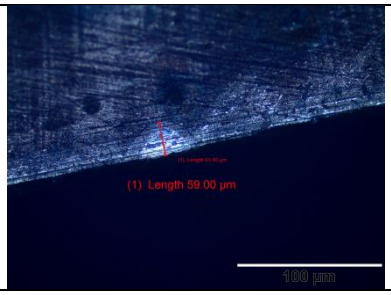	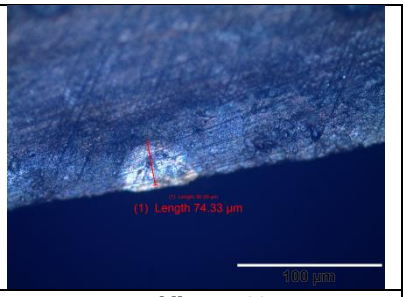
	top top - 59.00µm	top middle - 74.33µm
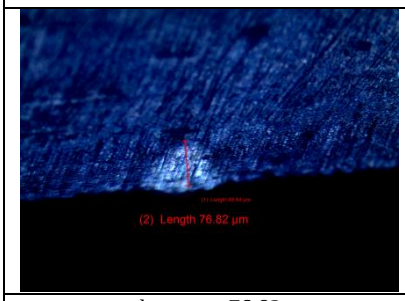	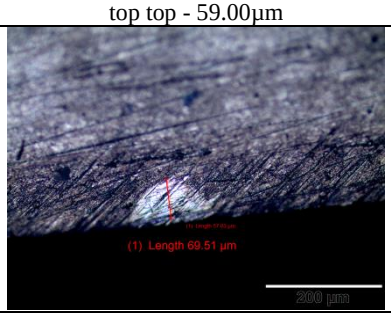	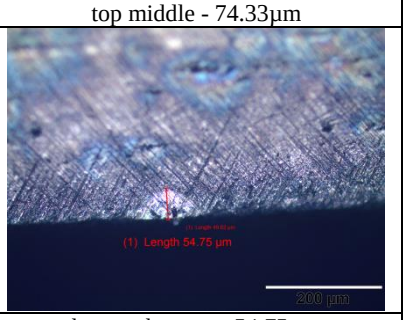
top bottom - 76.82µm	bottom top - 69.51µm	bottom bottom - 54.75µm
Track 11 P = 150 W V = 800 mm/s	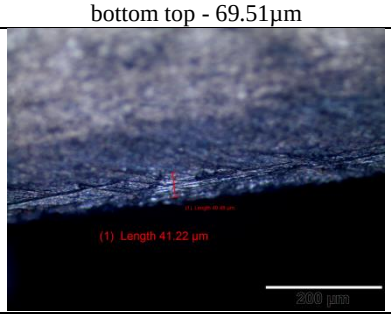	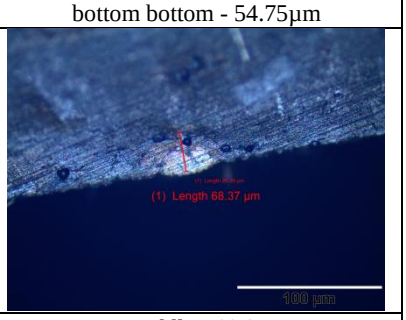
	top top - 41.22µm	top middle - 68.37µm
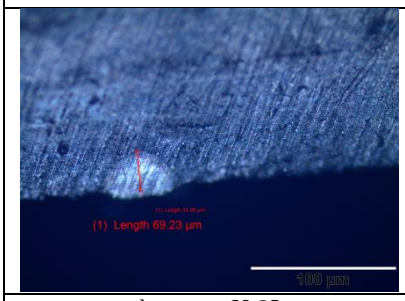	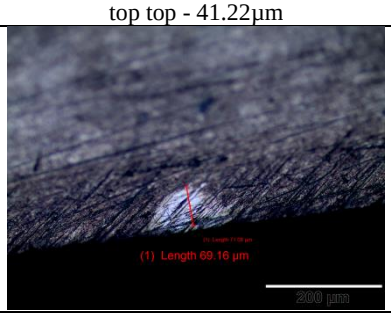	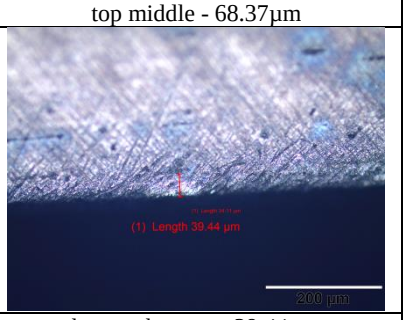
top bottom - 69.23µm	bottom top - 69.16µm	bottom bottom - 39.44µm
Track 12 P = 150 W V = 1000 mm/s	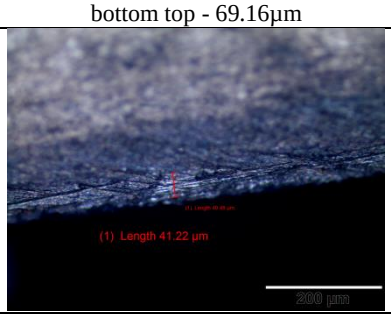	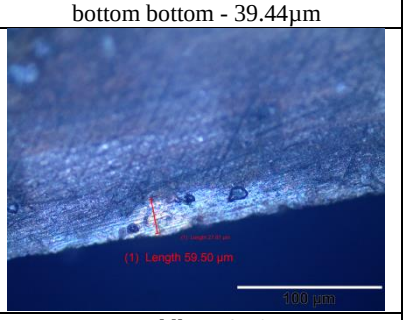
	top top - 41.22µm	top middle - 59.50µm
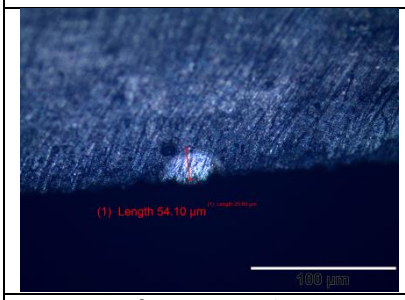	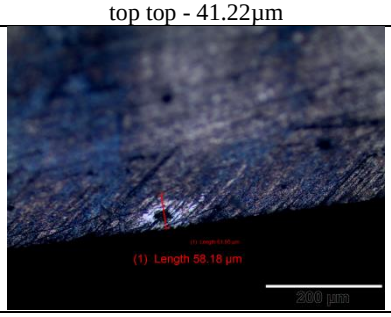	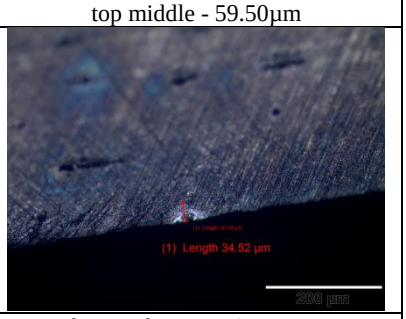
top bottom - 54.10µm	bottom top - 58.18µm	bottom bottom - 34.52µm

Track 13 P = 150 W V = 1200 mm/s	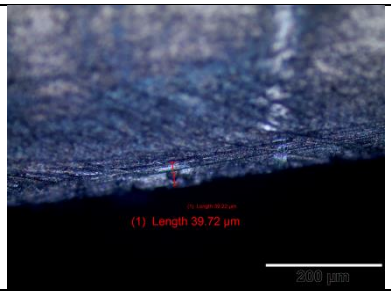	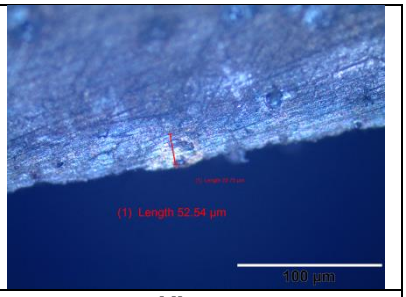
	top top - 39.72µm	top middle - 52.54µm
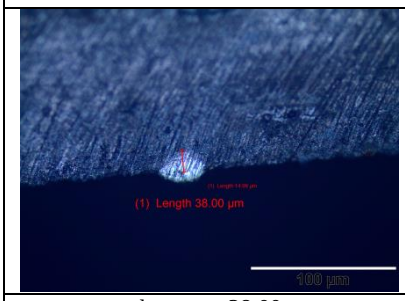	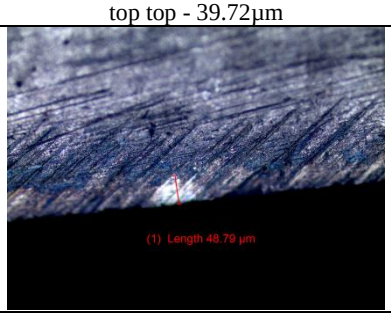	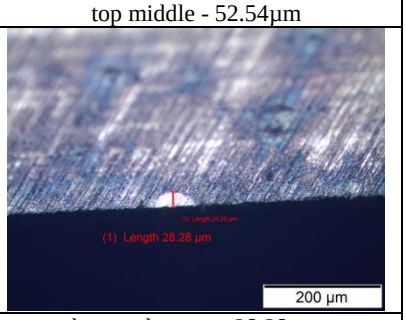
top bottom - 38.00µm	bottom top - 48.79µm	bottom bottom - 28.28µm
Track 14 P = 150 W V = 1400 mm/s	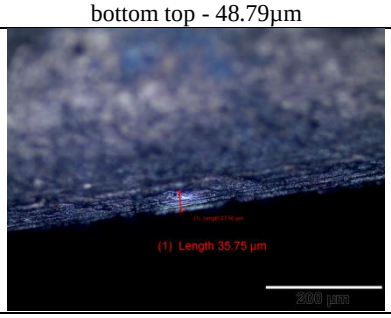	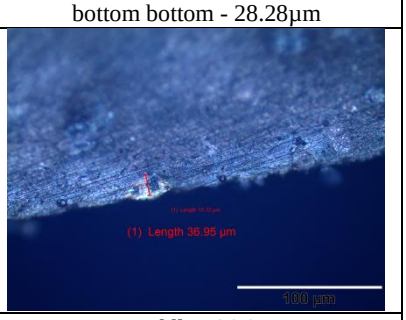
	top top - 35.75µm	top middle - 36.95µm
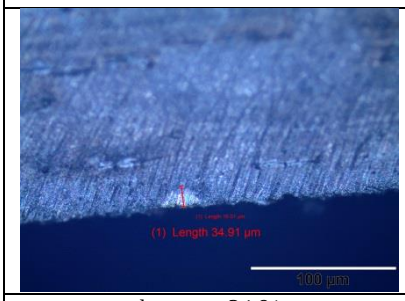	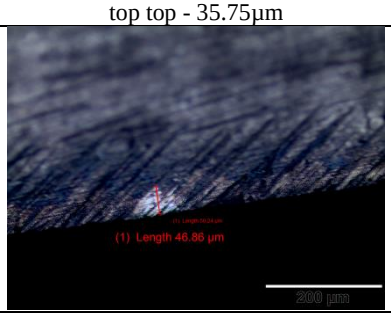	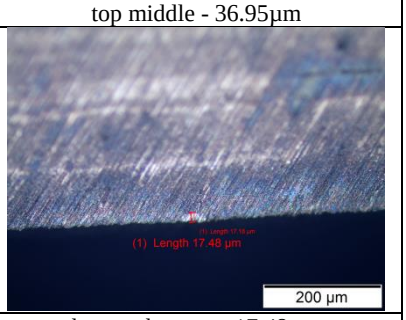
top bottom - 34.91µm	bottom top - 46.86µm	bottom bottom - 17.48µm
Track 15 P = 150 W V = 1600 mm/s	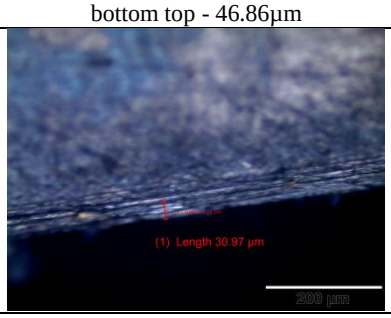	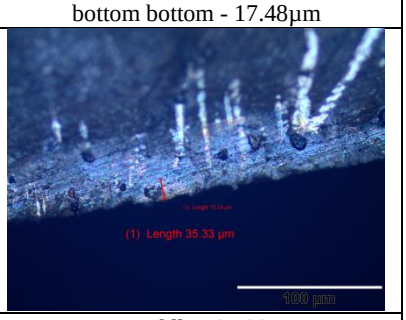
	top top - 30.97µm	top middle - 35.33µm
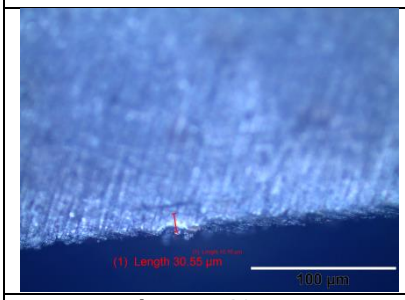	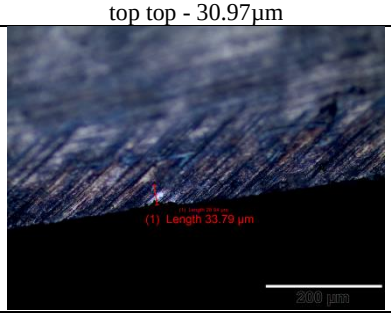	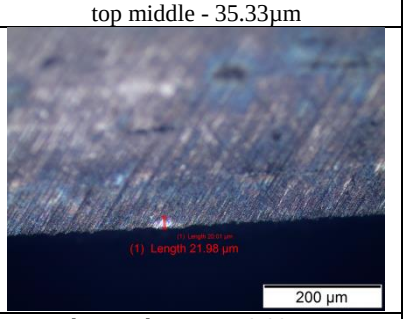
top bottom - 30.55µm	bottom top - 33.79µm	bottom bottom - 29.98µm

Track 16 P = 150 W V = 1800 mm/s	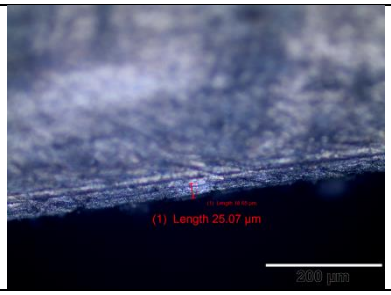	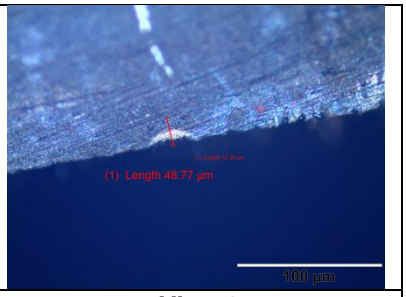
	top top - 25.07µm	top middle - 48.77µm
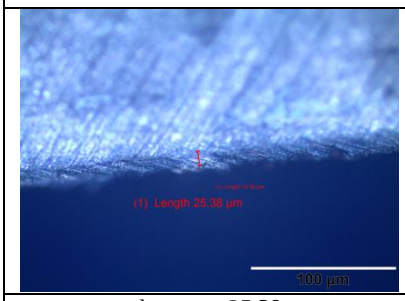	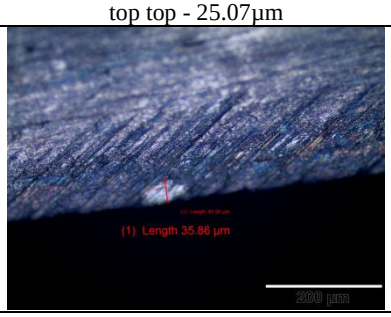	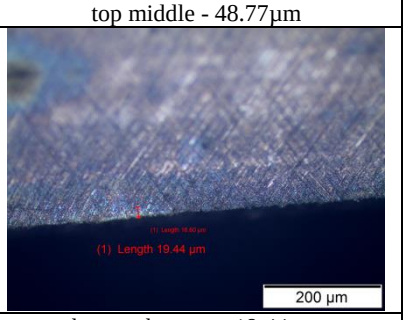
top bottom - 25.38µm	bottom top - 35.86µm	bottom bottom - 19.44µm
Track 17 P = 300 W V = 1000 mm/s	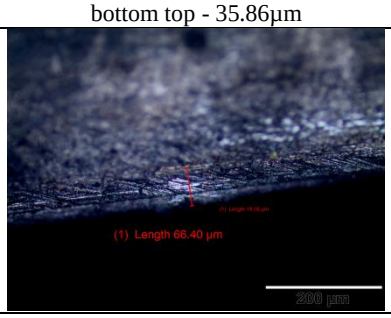	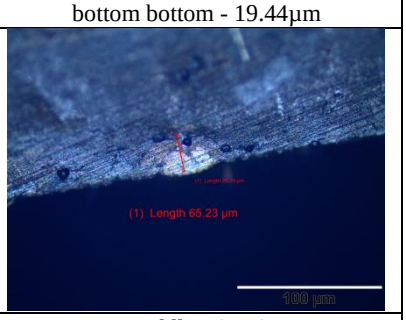
	top top - 66.40µm	top middle - 65.23µm
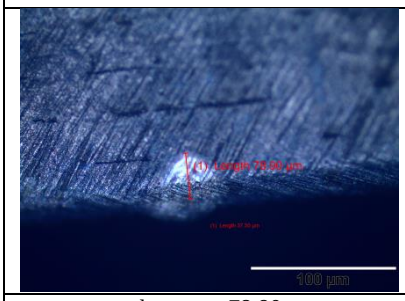	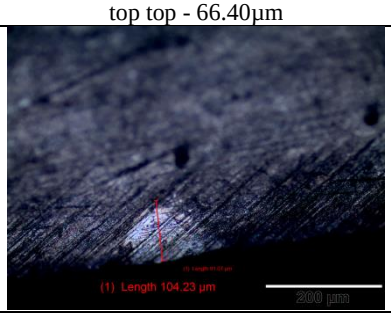	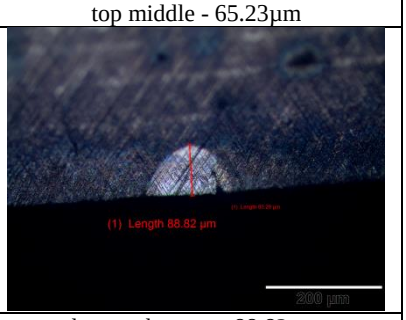
top bottom - 78.90µm	bottom top - 104.23µm	bottom bottom - 88.82µm
Track 18 P = 300 W V = 1200 mm/s	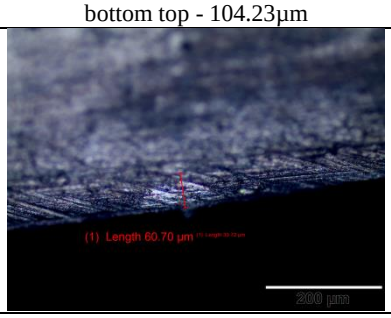	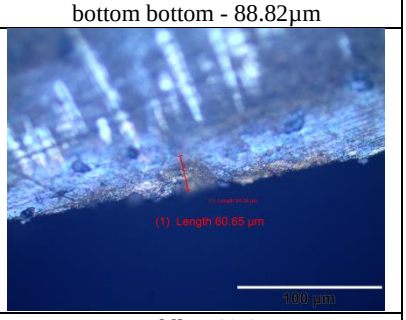
	top top - 60.70µm	top middle - 60.65µm
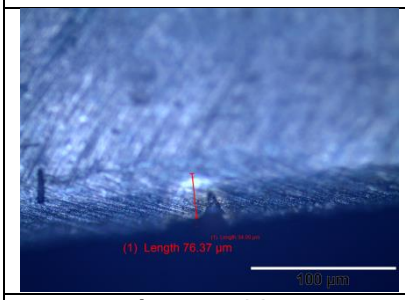	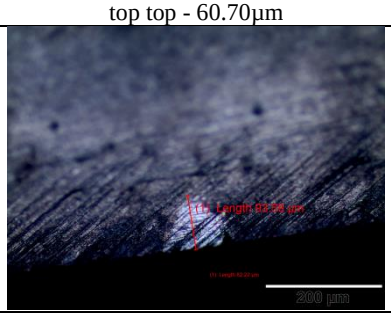	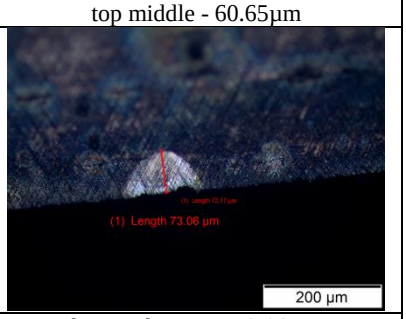
top bottom - 76.37µm	bottom top - 93.59µm	bottom bottom - 73.06µm

Track 19 P = 300 W V = 1400 mm/s	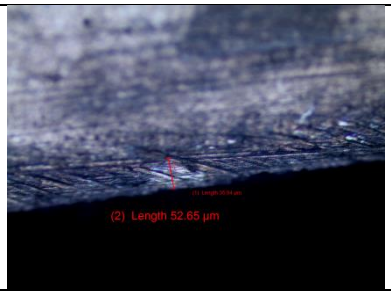	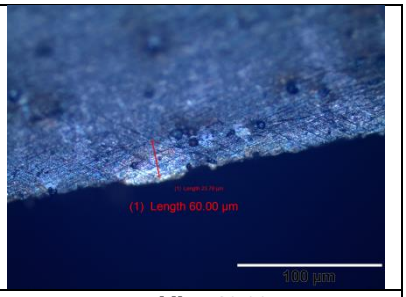
	top top - 52.65µm	top middle - 60.00µm
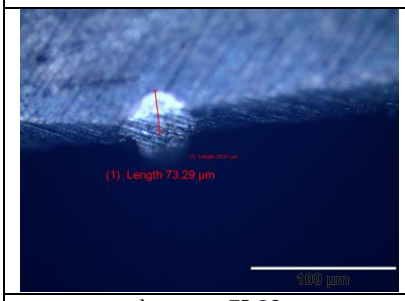	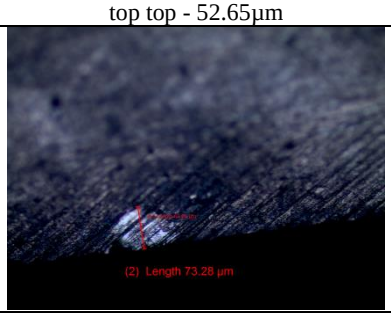	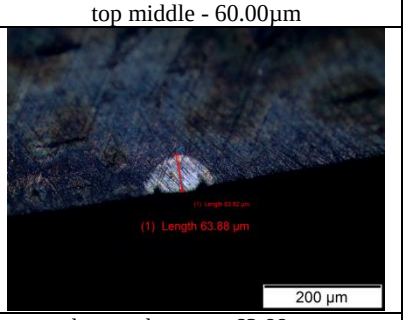
top bottom - 73.29µm	bottom top - 73.28µm	bottom bottom - 63.88µm
Track 20 P = 300 W V = 1600 mm/s	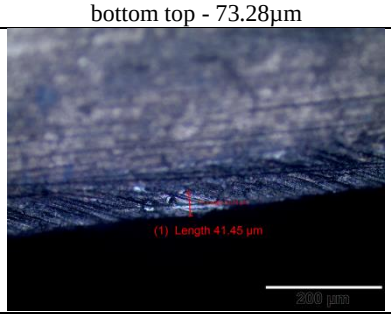	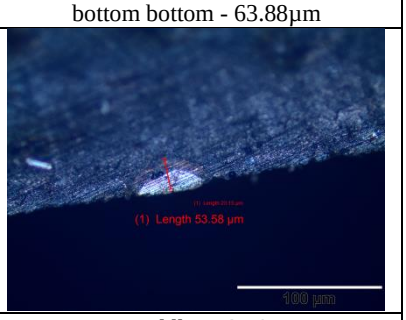
	top top - 41.45µm	top middle - 53.58µm
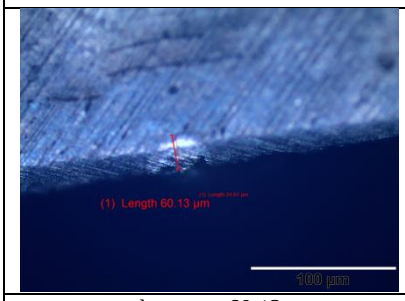	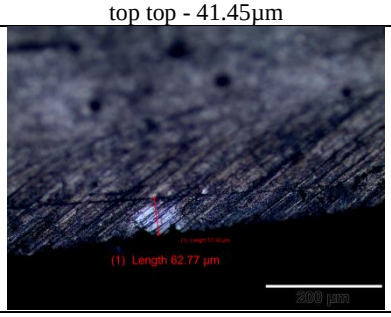	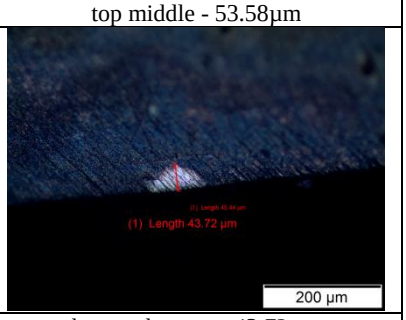
top bottom - 60.13µm	bottom top - 62.77µm	bottom bottom - 43.72µm
Track 21 P = 300 W V = 1800 mm/s	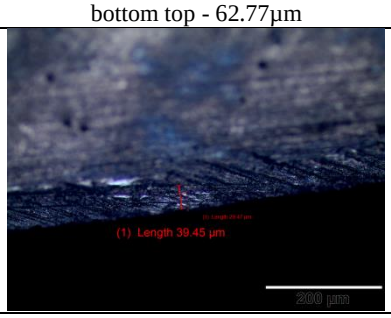	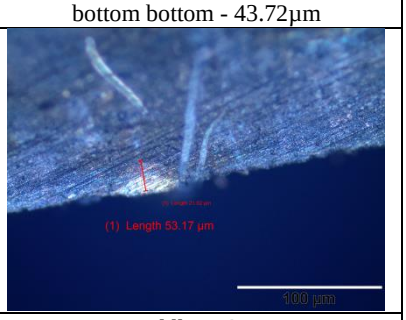
	top top - 39.45µm	top middle - 53.17µm
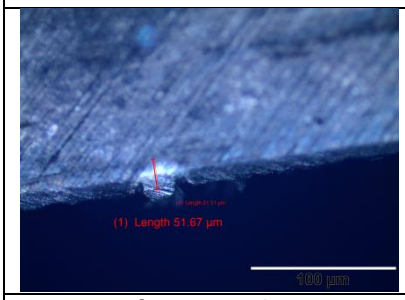	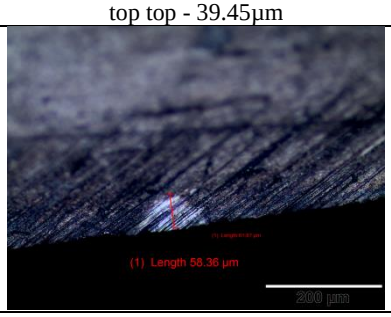	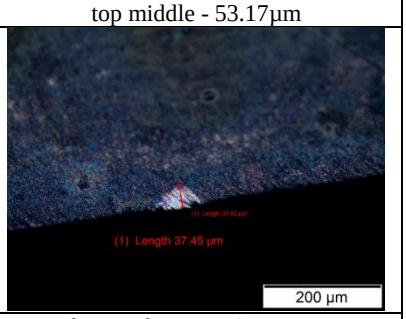
top bottom - 51.67µm	bottom top - 58.36µm	bottom bottom - 37.45µm

Track 22 P = 300 W V = 2000 mm/s	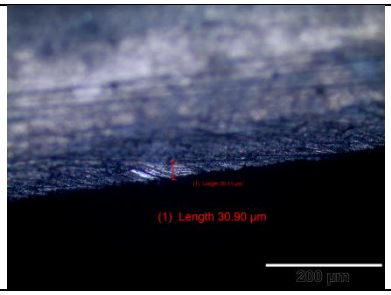	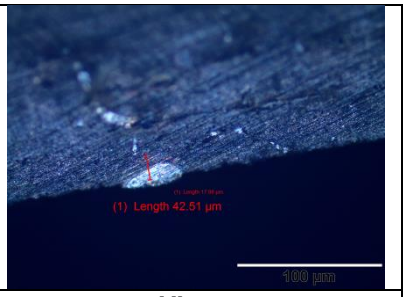
	top top - 30.90µm	top middle - 42.51µm
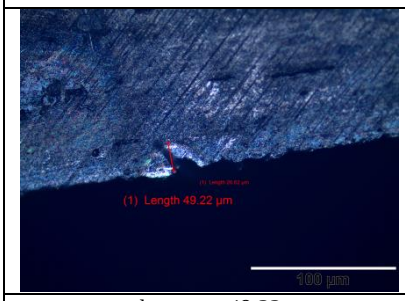	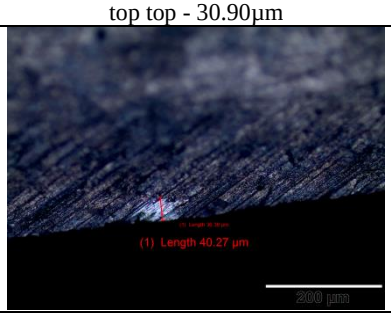	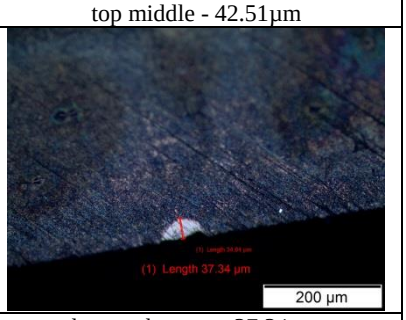
top bottom - 49.22µm	bottom top - 40.27µm	bottom bottom - 37.34µm
Track 23 P = 300 W V = 2200 mm/s	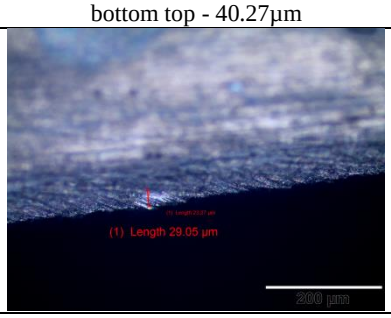	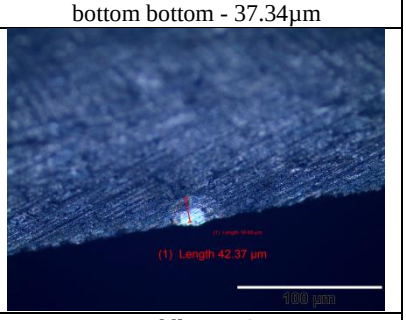
	top top - 29.05µm	top middle - 42.37µm
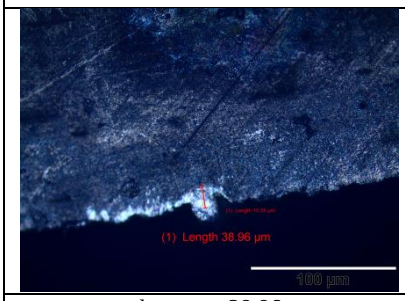	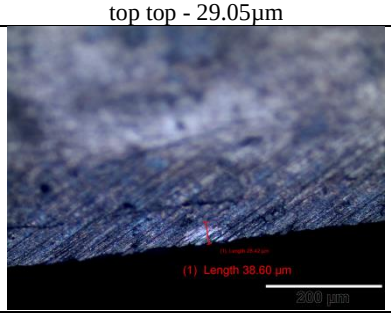	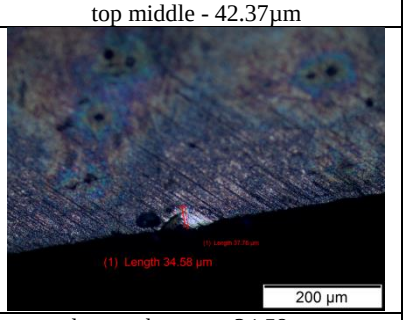
top bottom - 38.96µm	bottom top - 38.60µm	bottom bottom - 34.58µm
Track 24 P = 300 W V = 2400 mm/s	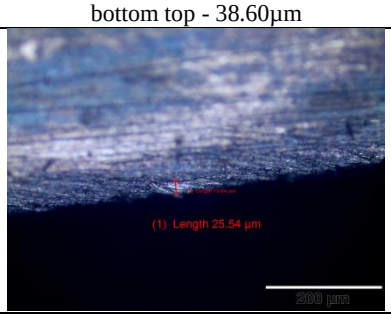	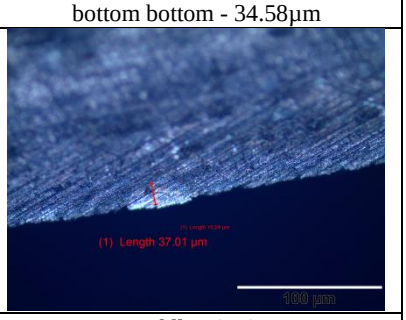
	top top - 25.54µm	top middle - 37.01µm
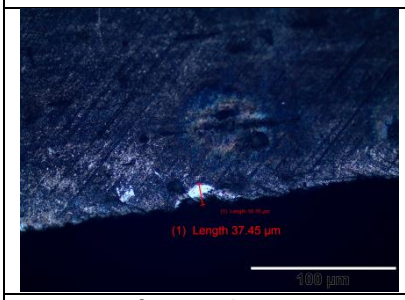	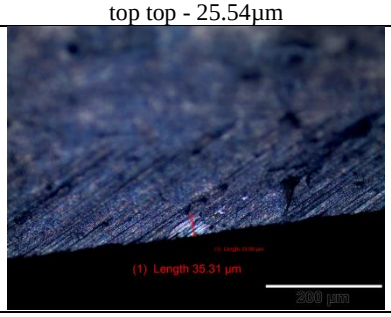	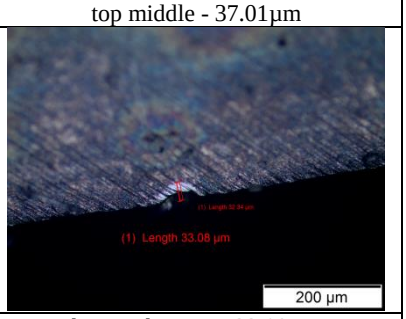
top bottom - 37.45µm	bottom top - 35.31µm	bottom bottom - 33.08µm

Appendix J: Scan Track Width Measurements - Ti-6Al-4V Base Plate

Table J1: Experimental scan track penetration depth of the WC-12Co on the titanium base plate.

Parameter set/ scan track number	Power [W]	Scanning speed [mm/s]	Energy density [J / mm^2]	Depth measurements [µm] 1	2	3	4	5	6	Average width [µm]
1	50	60	208.33	186.5	182.5	174.7	183.6	169.3	178.0	**179.1**
2	50	80	156.25	159.6	158.8	162.0	157.4	162.0	147.2	**157.8**
3	50	100	125.00	154.9	141.4	149.8	153.2	151.6	148.4	**149.9**
4	50	120	104.17	144.6	144.0	143.4	145.9	141.3	140.8	**143.3**
5	50	140	89.29	137.0	131.2	140.2	134.3	139.7	137.6	**136.7**
6	50	160	78.13	134.4	135.7	137.0	133.7	130.6	127.2	**133.1**
7	50	180	69.44	124.2	122.2	123.5	125.5	121.0	124.8	**123.5**
8	50	200	62.50	121.0	119.1	119.7	123.5	119.0	121.6	**120.6**
9	150	400	93.75	185.0	186.2	184.4	187.5	185.0	182.4	**185.1**
10	150	600	62.50	161.1	159.1	158.8	154.3	162.6	159.4	**159.2**
11	150	800	46.88	147.7	143.1	146.0	147.2	148.5	148.5	**146.8**
12	150	1000	37.50	129.1	125.8	129.7	133.1	131.2	131.9	**130.1**
13	150	1200	31.25	116.8	121.3	113.7	112.7	113.9	115.9	**115.7**
14	150	1400	26.79	107.9	105.9	107.7	102.4	106.9	107.5	**106.4**
15	150	1600	23.44	102.6	104.5	101.6	101.1	98.6	101.1	**101.6**
16	150	1800	20.83	100.1	102.1	100.1	97.3	95.4	99.8	**99.1**
17	300	1000	75.00	171.7	174.4	176.5	193.9	189.4	168.3	**179.1**
18	300	1200	62.50	160.7	162.1	161.4	172.8	175.4	160.6	**165.5**
19	300	1400	53.57	148.6	148.0	148.0	159.4	146.6	147.8	**149.7**
20	300	1600	46.88	142.8	139.7	140.2	147.9	145.9	139.0	**142.6**
21	300	1800	41.67	140.2	137.1	135.7	140.2	138.2	134.4	**137.6**
22	300	2000	37.50	130.2	131.3	134.5	131.2	125.5	137.0	**131.6**
23	300	2200	34.09	124.2	123.6	125.8	129.3	125.4	126.7	**125.8**
24	300	2400	31.25	120.3	120.3	122.4	133.8	128.7	126.7	**125.4**

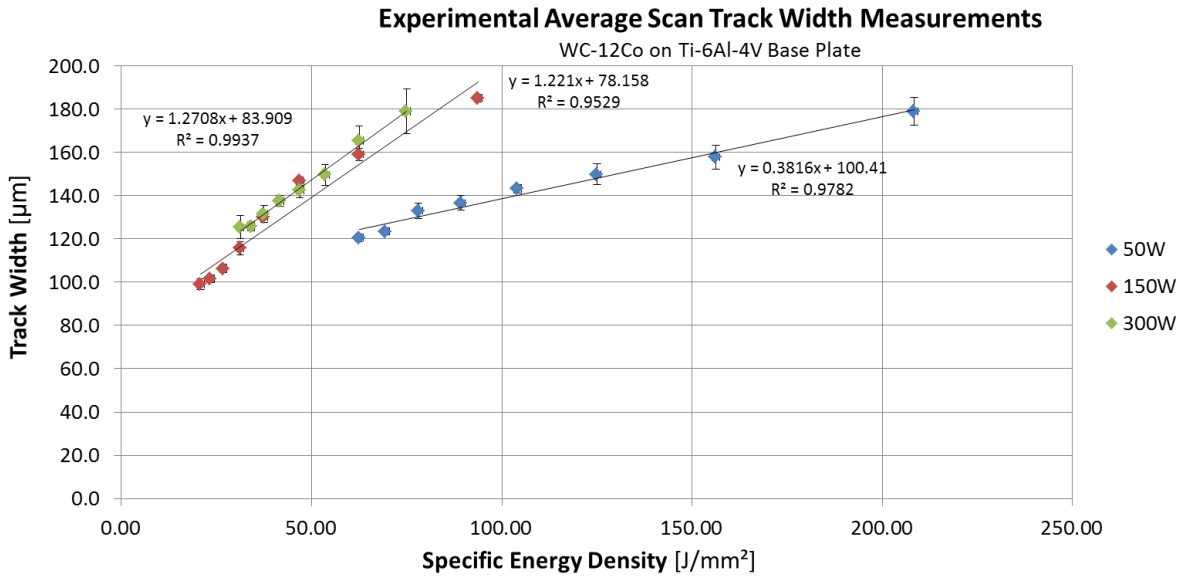

Figure J1: The average penetration depth of 24 scan tracks on the tool steel base plate measured at different specific energy density values.

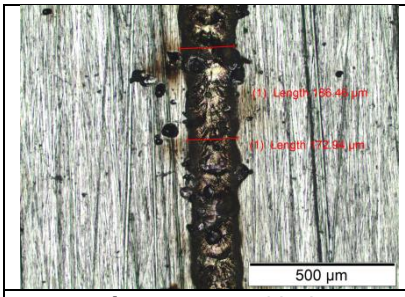

Track 1 - top top - 186.46µm

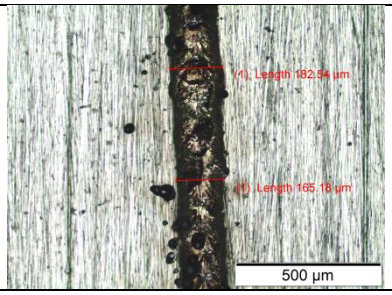

Track 1 - top middle - 182.54µm

Track 1 - top bottom - 174.74µm

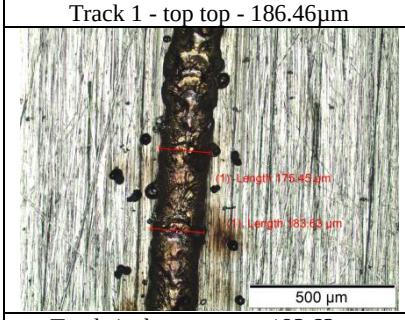

Track 1 - bottom top - 183.63µm

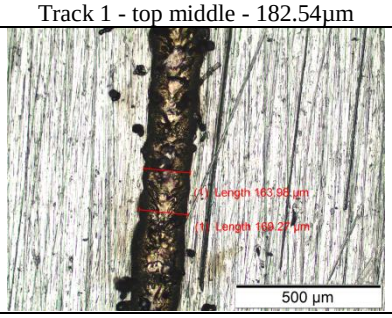

Track 1 - bottom middle - 169.27µm

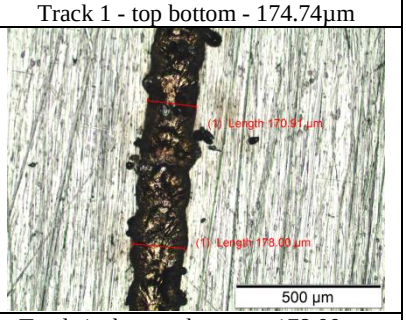

Track 1 - bottom bottom - 178.00µm

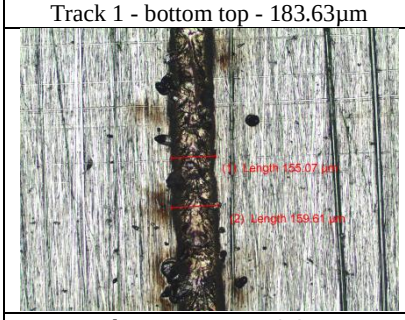

Track 2 - top top - 159.61µm

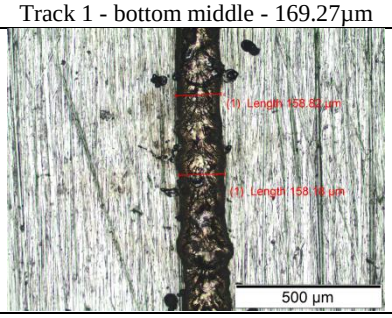

Track 2 - top middle - 158.82µm

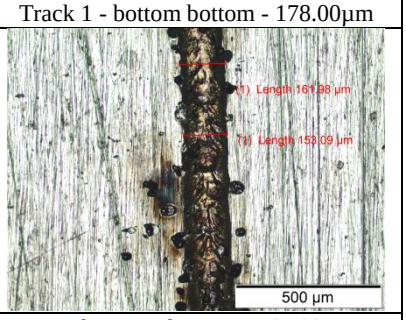

Track 2 - top bottom - 161.98µm

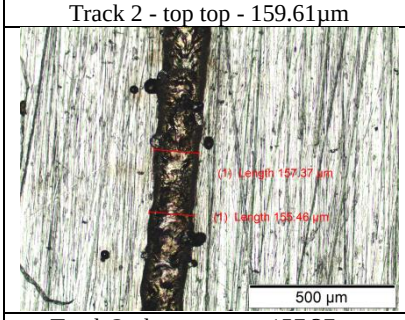

Track 2 - bottom top - 157.37µm

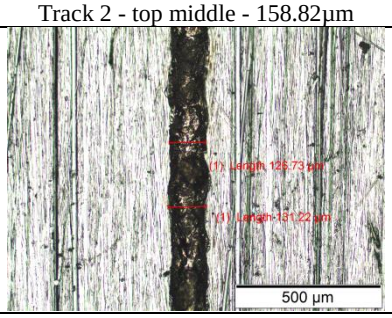

Track 2 - bottom middle - 131.22µm

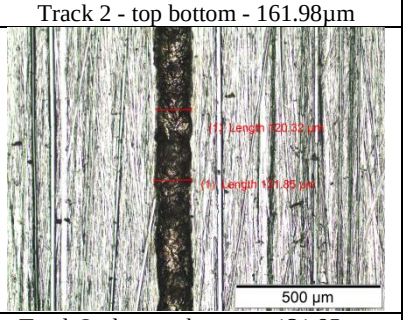

Track 2 - bottom bottom - 131.85µm

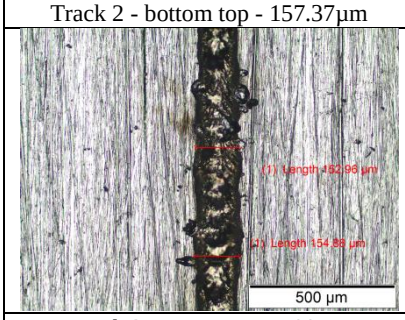

Track 3 - top top - 154.88µm

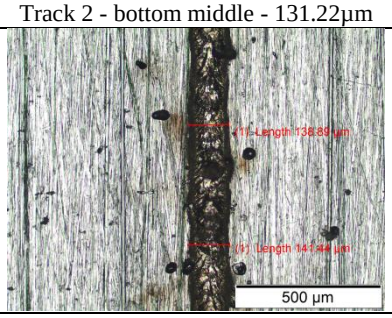

Track 3 - top middle - 141.44µm

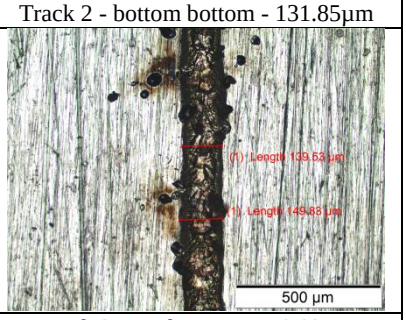

Track 3 - top bottom - 149.83µm

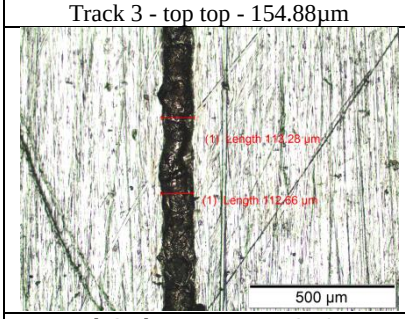

Track 3 - bottom top - 113.28µm

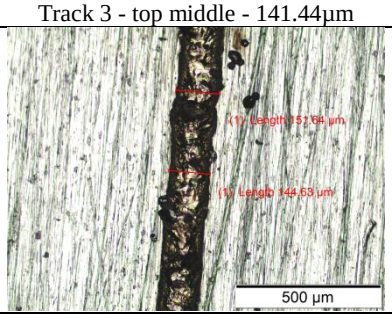

Track 3 - bottom middle - 151.64µm

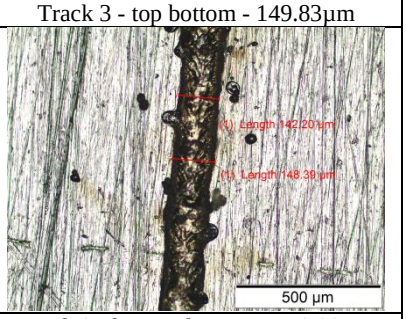

Track 3 - bottom bottom - 148.39µm

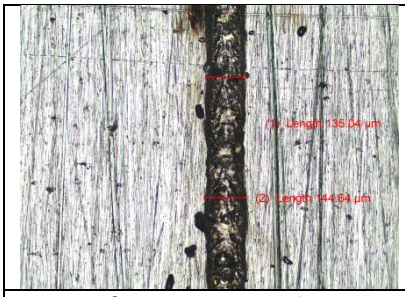

Track 4 - top top - 144.64µm

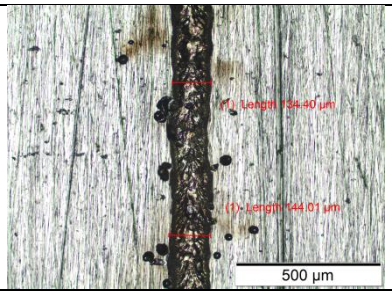

Track 4 - top middle - 144.01µm

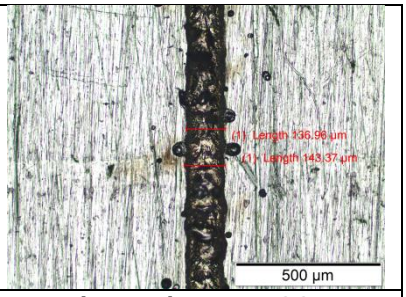

Track 4 - top bottom - 143.37µm

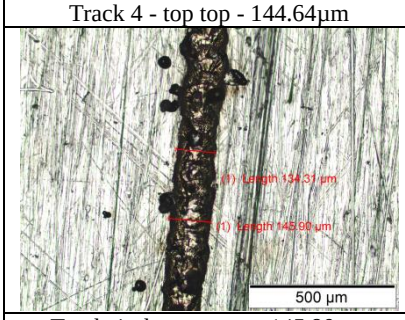

Track 4 - bottom top - 145.90µm

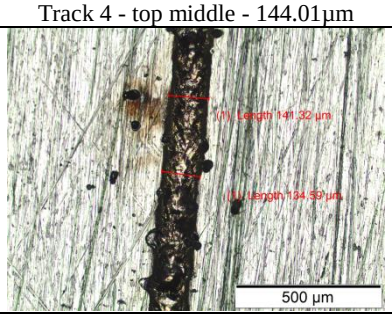

Track 4 - bottom middle - 141.32µm

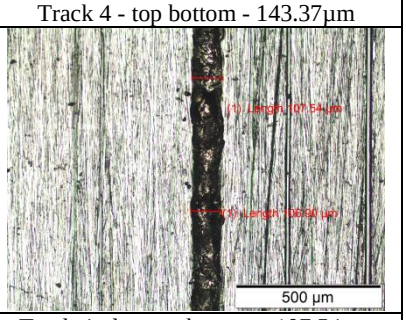

Track 4 - bottom bottom - 107.54µm

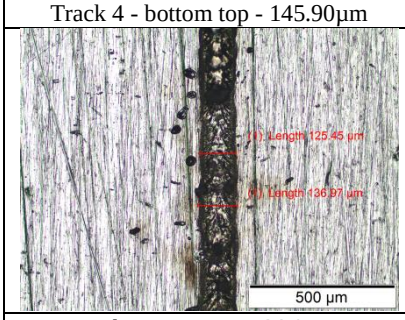

Track 5 - top top - 136.97µm

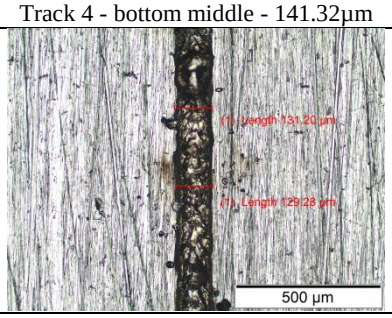

Track 5 - top middle - 131.20µm

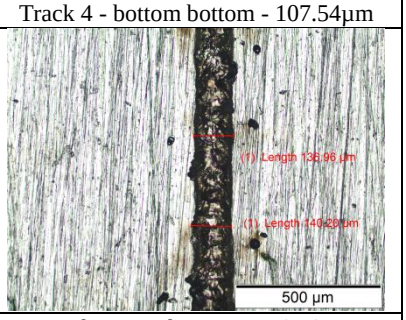

Track 5 - top bottom - 140.20µm

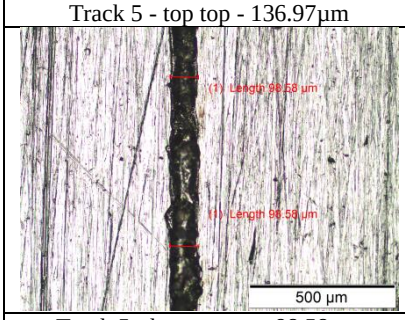

Track 5 - bottom top - 98.58µm

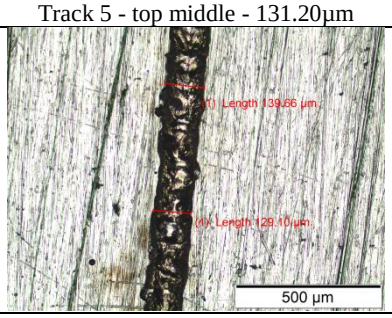

Track 5 - bottom middle - 129.10µm

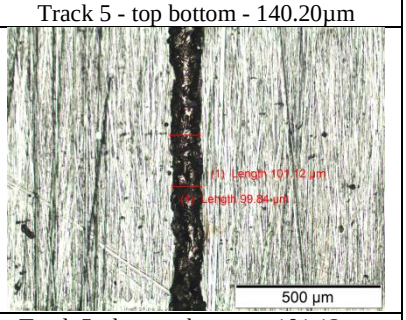

Track 5 - bottom bottom - 101.12µm

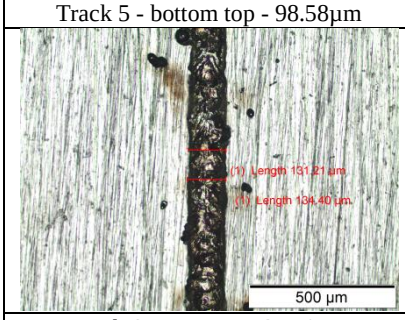

Track 6 - top top - 134.40µm

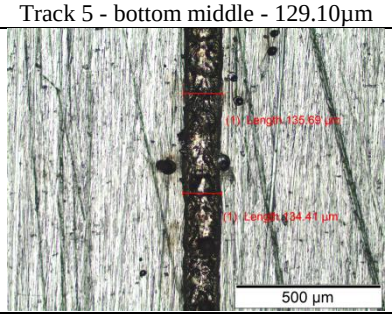

Track 6 - top middle - 135.69µm

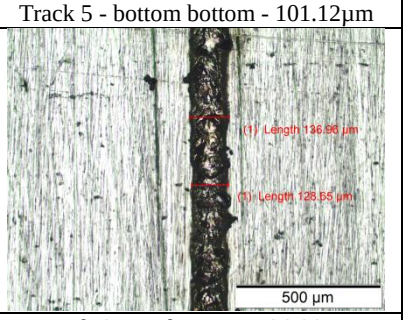

Track 6 - top bottom - 136.96µm

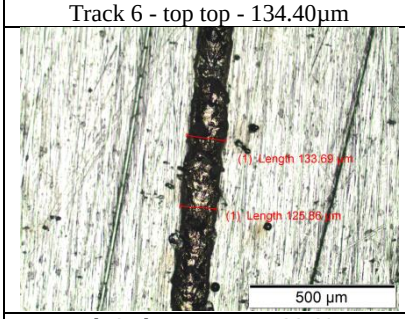

Track 6 - bottom top - 133.69µm

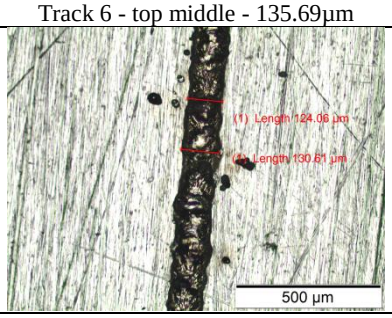

Track 6 - bottom middle - 130.61µm

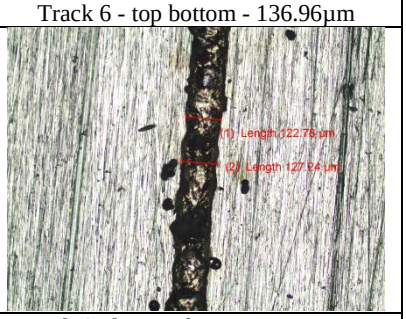

Track 6 - bottom bottom - 127.24µm

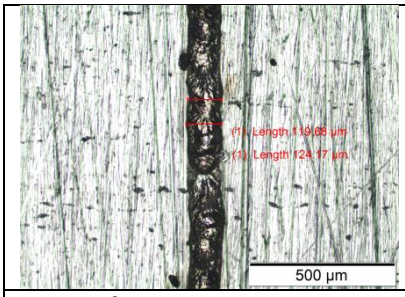	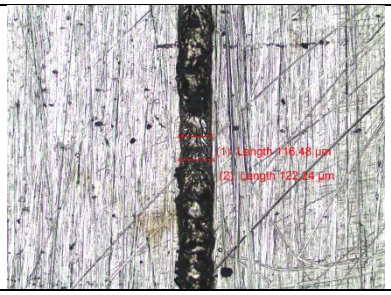	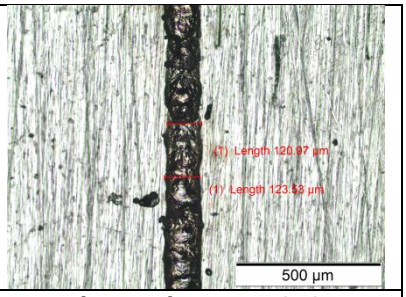
Track 7 - top top - 124.17µm	Track 7 - top middle - 122.24	Track 7 - top bottom - 123.53µm
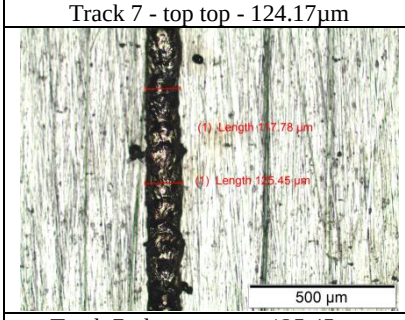	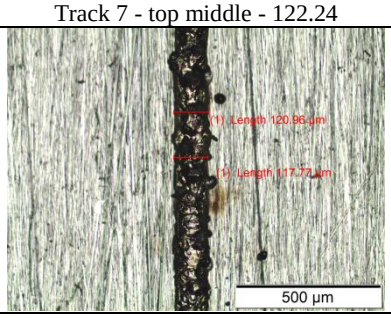	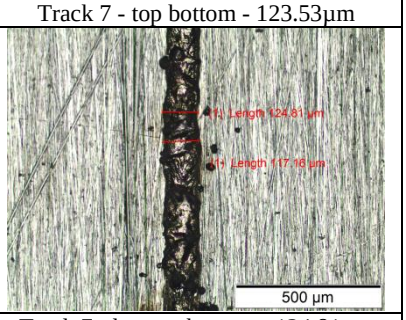
Track 7 - bottom top - 125.45µm	Track 7 - bottom middle - 120.96µm	Track 7 - bottom bottom - 124.81µm
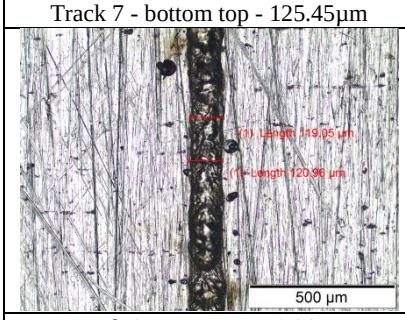	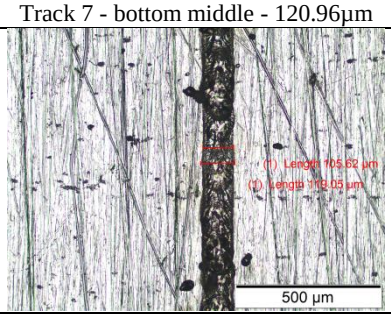	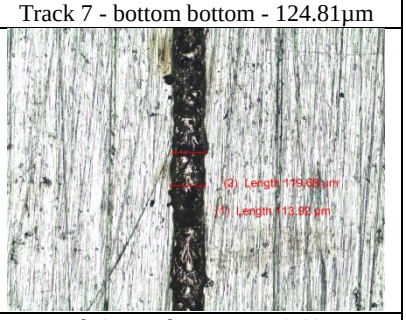
Track 8 - top top - 120.96µm	Track 8 - top middle - 119.05µm	Track 8 - top bottom - 119.68µm
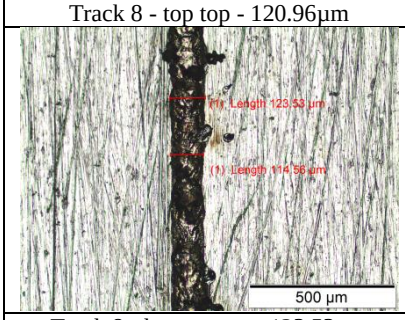	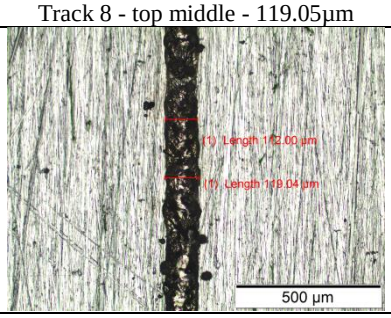	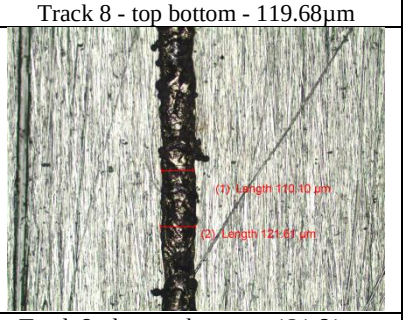
Track 8 - bottom top - 123.53µm	Track 8 - bottom middle - 119.04µm	Track 8 - bottom bottom - 121.61µm
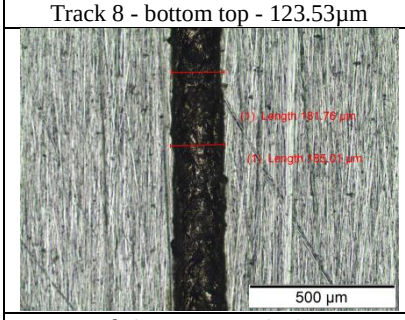	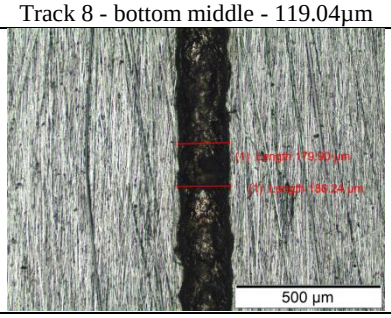	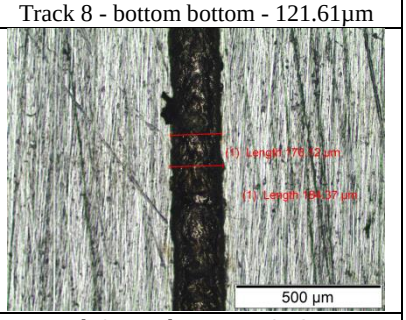
Track 9 - top top - 185.01µm	Track 9 - top middle - 186.24µm	Track 9 - top bottom - 184.37µm
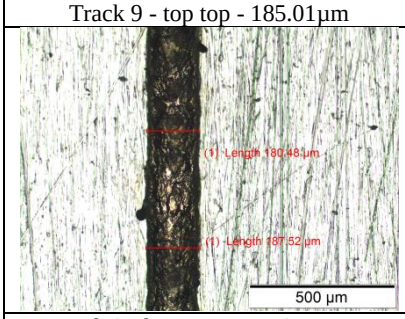	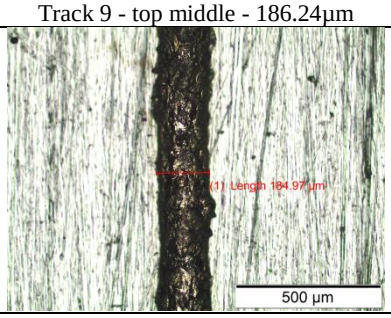	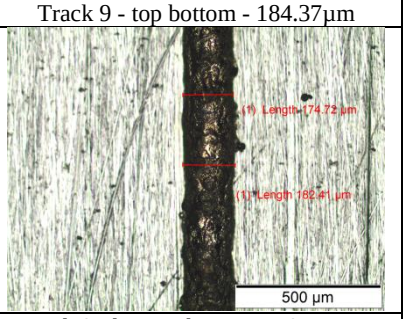
Track 9 - bottom top - 187.52µm	Track 9 - bottom middle - 184.97µm	Track 9 - bottom bottom - 182.41µm

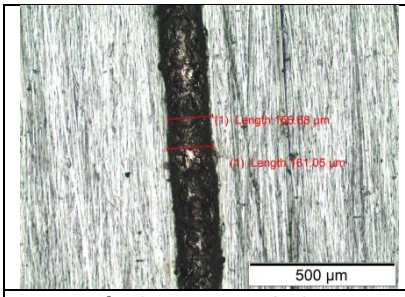

Track 10 - top top - 161.05µm

Track 10 - top middle - 159.05µm

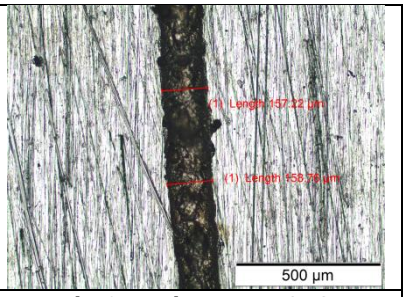

Track 10 - top bottom - 158.76µm

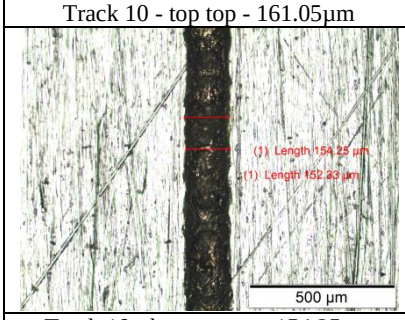

Track 10 - bottom top - 154.25µm

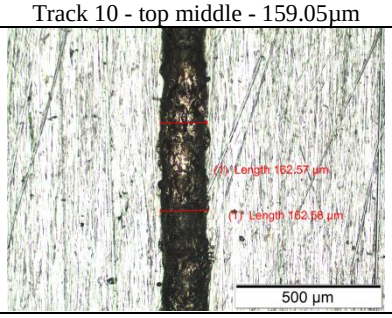

Track 10 - bottom middle - 162.58µm

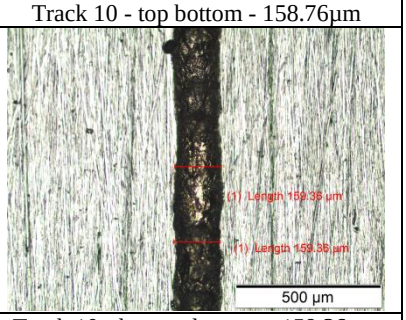

Track 10 - bottom bottom - 159.36µm

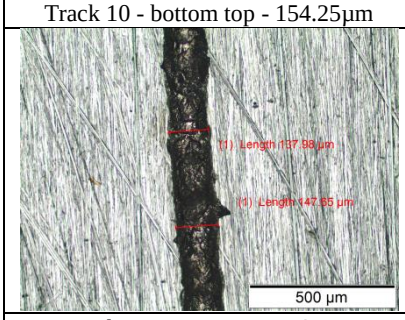

Track 11 - top top - 147.65µm

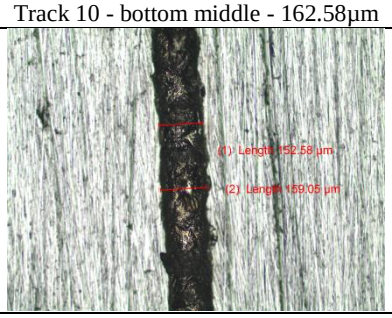

Track 11 - top middle - 159.05µm

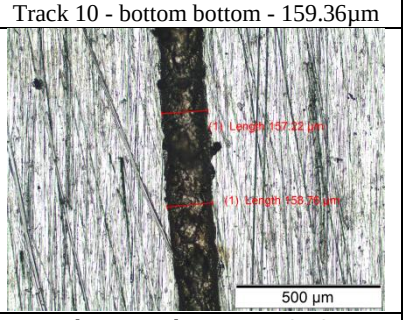

Track 11 - top bottom - 158.76µm

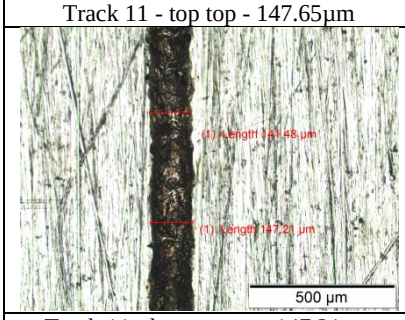

Track 11 - bottom top - 147.21µm

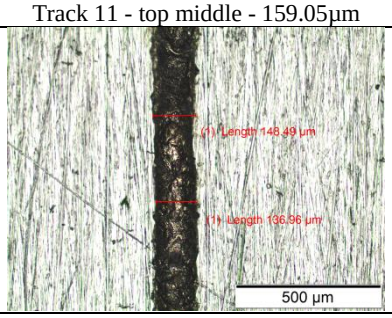

Track 11 - bottom middle - 148.49µm

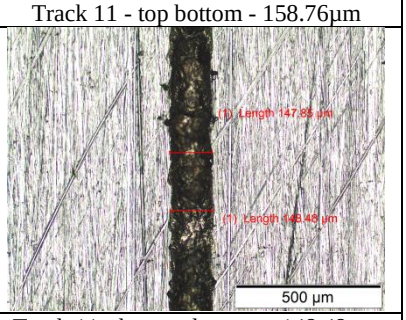

Track 11 - bottom bottom - 148.48µm

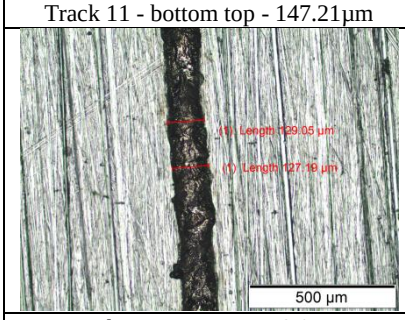

Track 12 - top top - 129.05µm

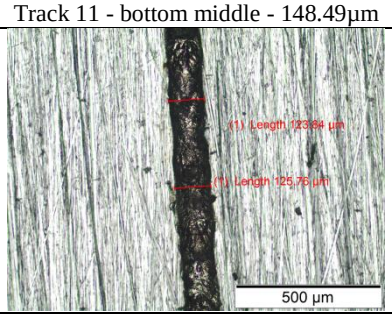

Track 12 - top middle - 125.76µm

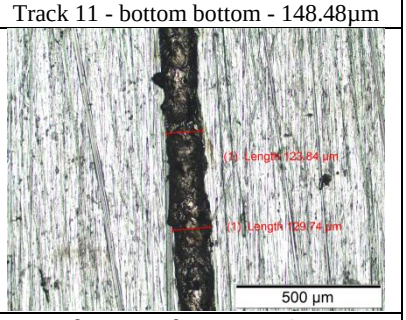

Track 12 - top bottom - 129.74µm

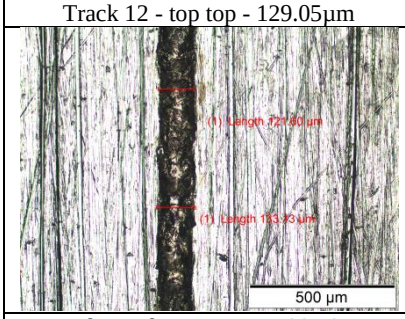

Track 12 - bottom top - 133.13µm

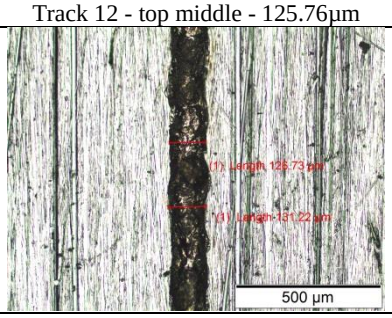

Track 12 - bottom middle - 131.22µm

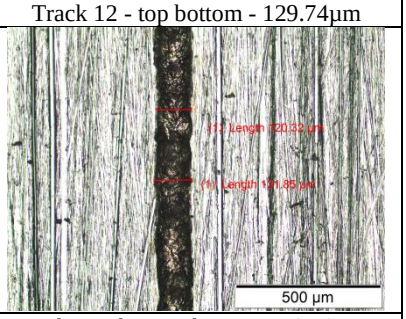

Track 12 - bottom bottom - 131.85µm

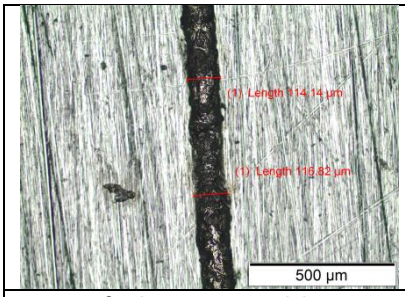

Track 13 - top top - 116.82µm

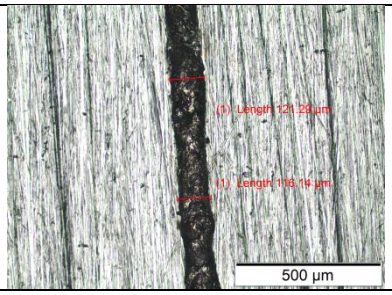

Track 13 - top middle - 121.29µm

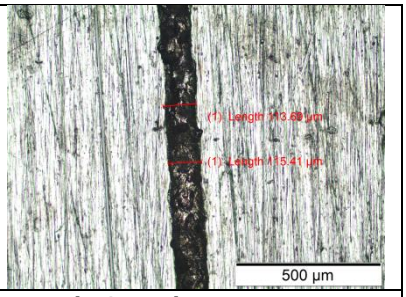

Track 13 - top bottom - 115.41µm

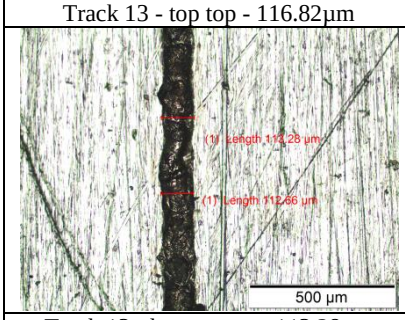

Track 13 - bottom top - 113.28µm

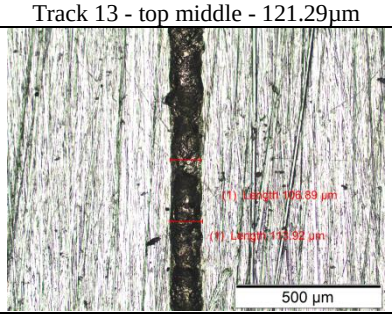

Track 13 - bottom middle - 113.92µm

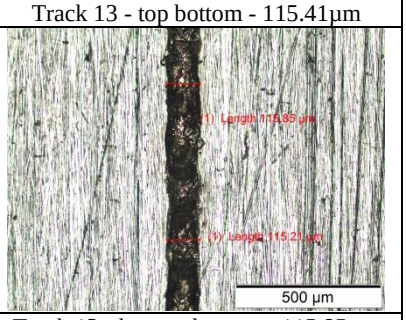

Track 13 - bottom bottom - 115.85µm

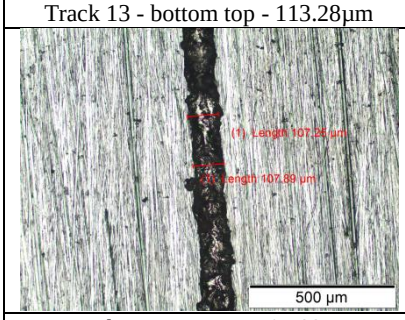

Track 14 - top top - 107.89µm

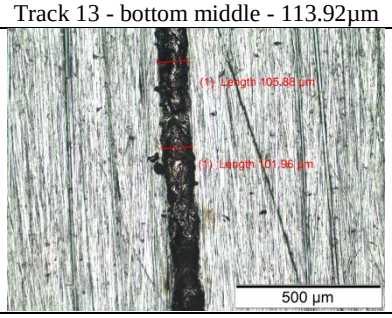

Track 14 - top middle - 105.88µm

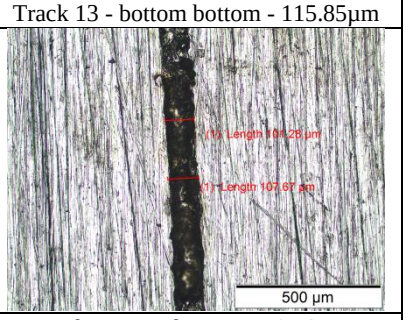

Track 14 - top bottom - 107.67µm

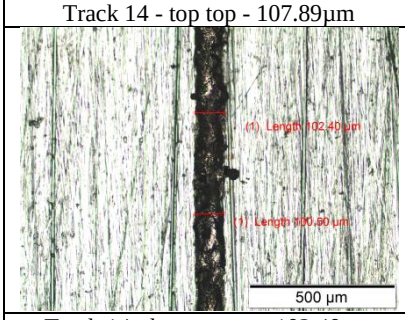

Track 14 - bottom top - 102.40µm

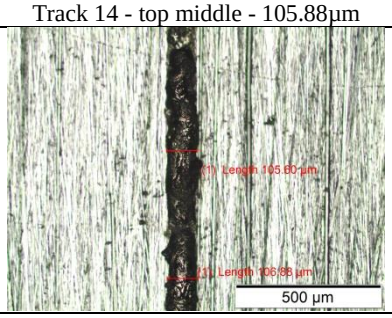

Track 14 - bottom middle - 106.88µm

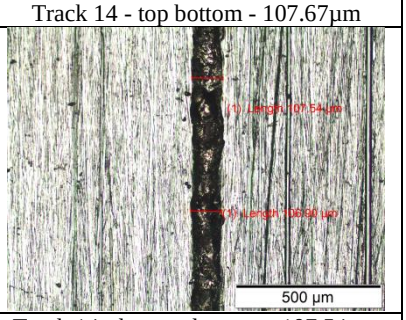

Track 14 - bottom bottom - 107.54µm

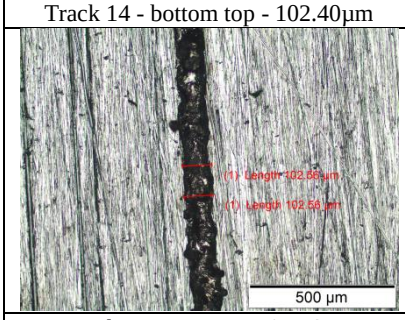

Track 15 - top top - 102.56µm

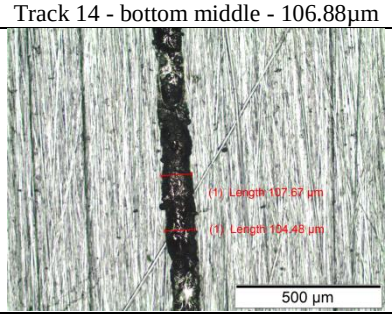

Track 15 - top middle - 107.67µm

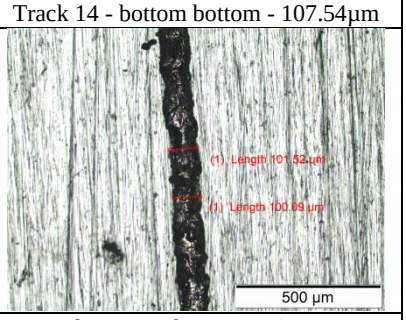

Track 15 - top bottom - 101.52µm

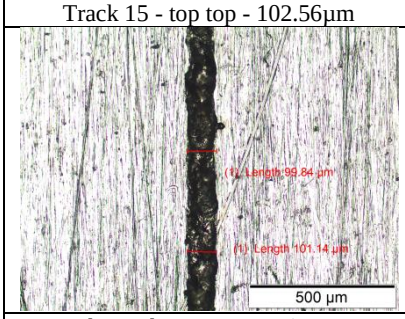

Track 15 - bottom top - 101.14µm

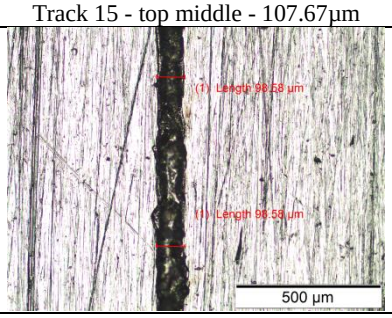

Track 15 - bottom middle - 98.58µm

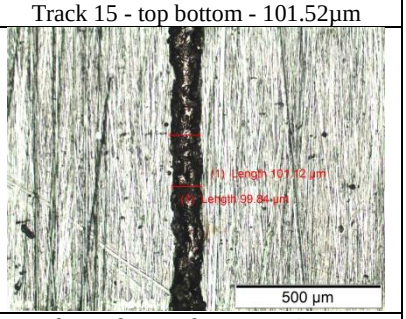

Track 15 - bottom bottom - 104.12µm

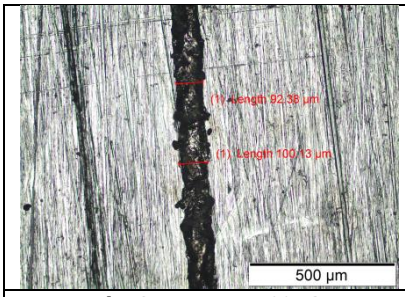

Track 16 - top top - 100.13µm

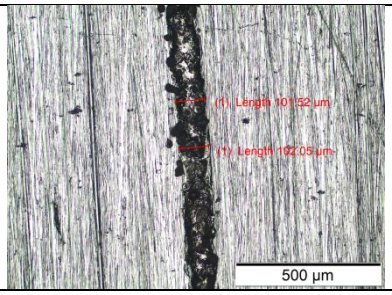

Track 16 - top middle - 102.05µm

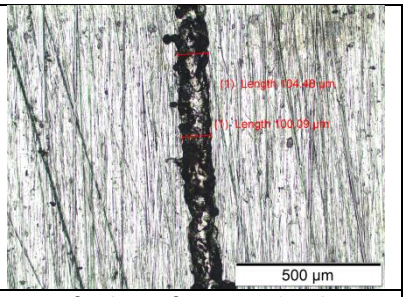

Track 16 - top bottom - 104.48µm

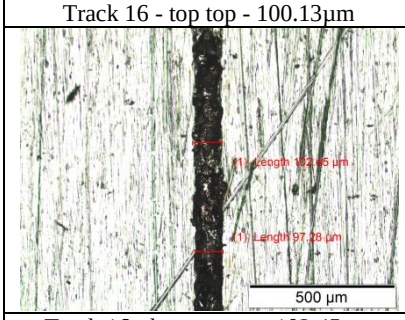

Track 16 - bottom top - 102.45µm

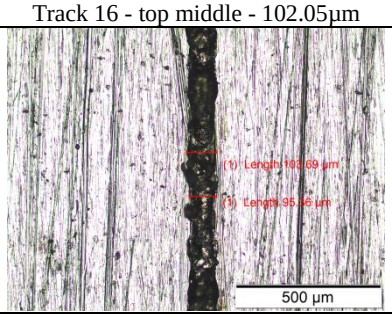

Track 16 - bottom middle - 103.69µm

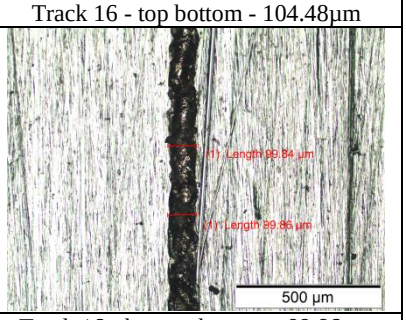

Track 16 - bottom bottom - 99.86µm

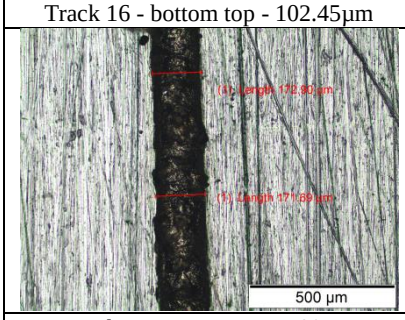

Track 17 - top top - 172.90µm

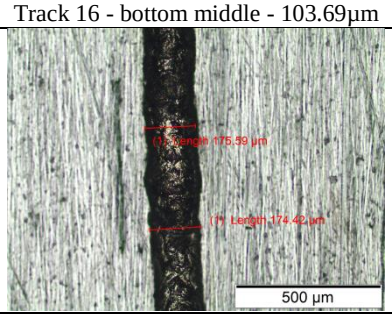

Track 17 - top middle - 175.59µm

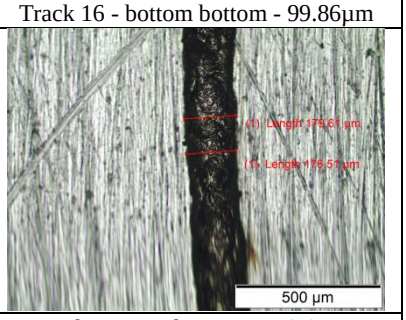

Track 17 - top bottom - 179.61µm

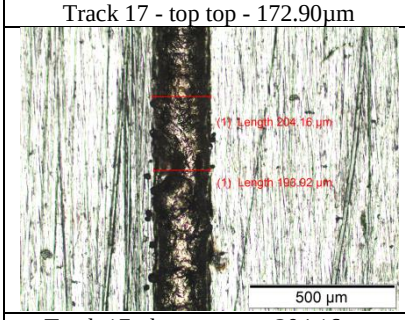

Track 17 - bottom top - 204.16µm

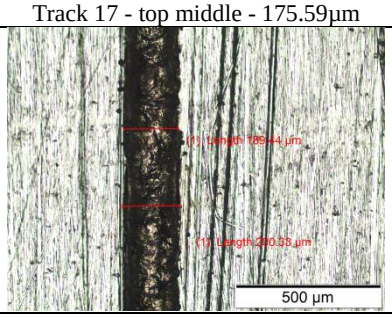

Track 17 - bottom middle - 200.33µm

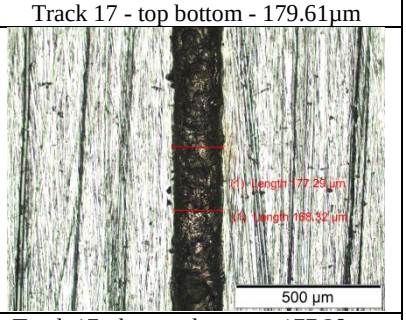

Track 17 - bottom bottom - 177.29µm

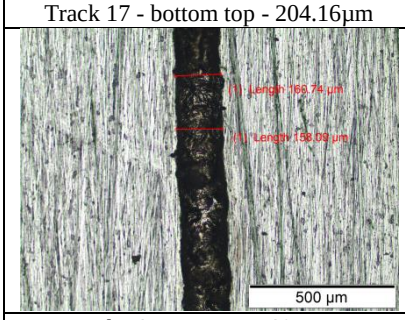

Track 18 - top top - 160.74µm

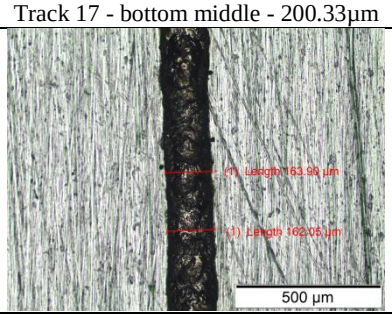

Track 18 - top middle - 163.90µm

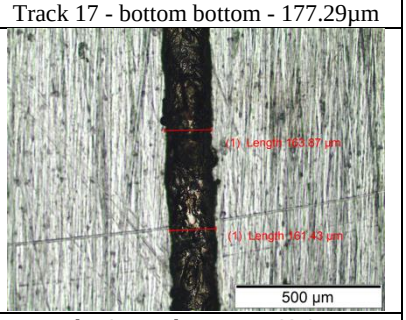

Track 18 - top bottom - 163.87µm

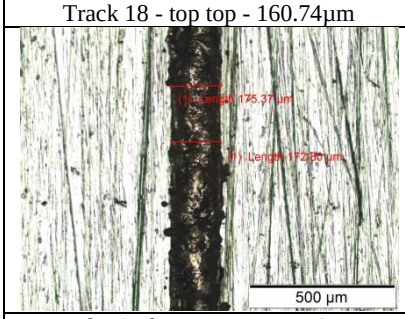

Track 18 - bottom top - 175.37µm

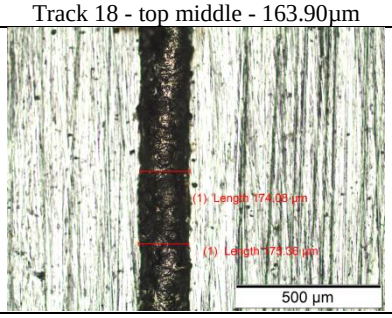

Track 18 - bottom middle - 175.36µm

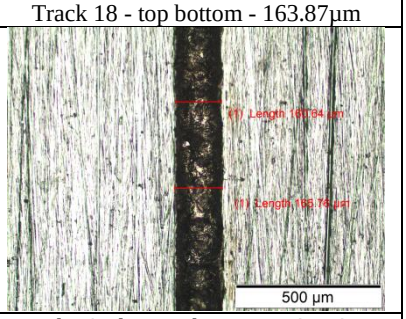

Track 18 - bottom bottom - 165.76µm

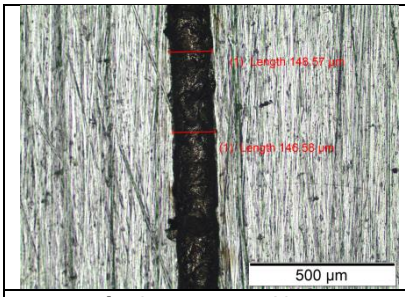

Track 19 - top top - 168.57µm

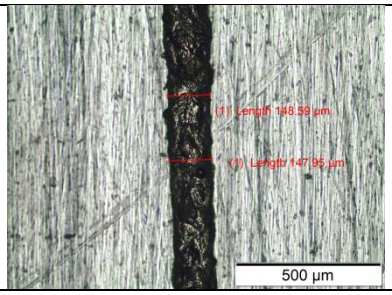

Track 19 - top middle - 148.59µm

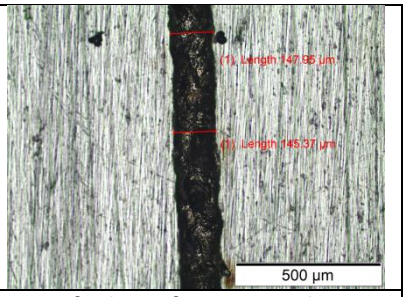

Track 19 - top bottom - 147.95µm

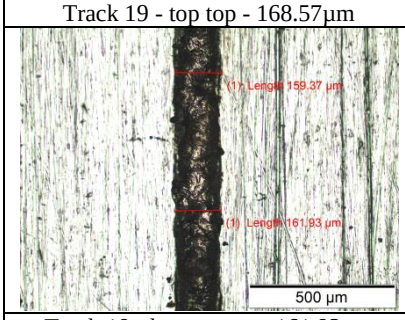

Track 19 - bottom top - 161.93µm

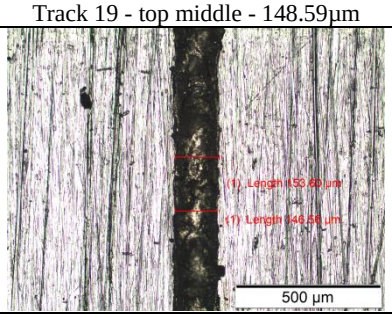

Track 19 - bottom middle - 153.60µm

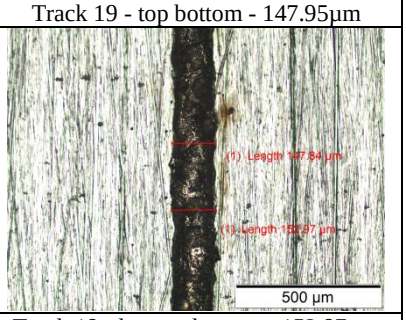

Track 19 - bottom bottom - 152.97µm

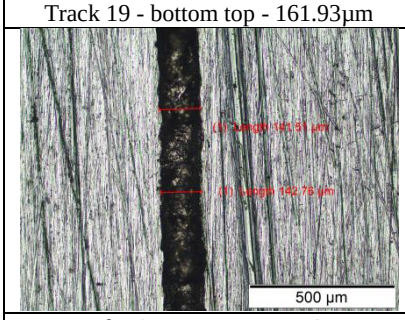

Track 20 - top top - 142.76µm

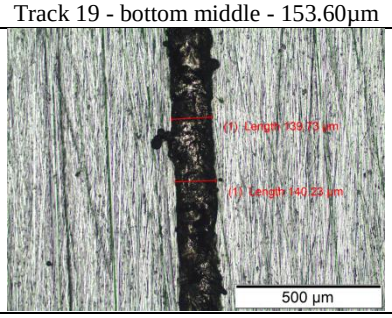

Track 20 - top middle - 140.23µm

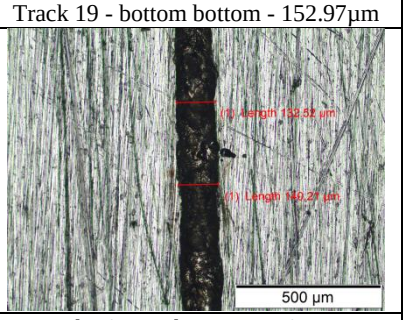

Track 20 - top bottom - 140.21µm

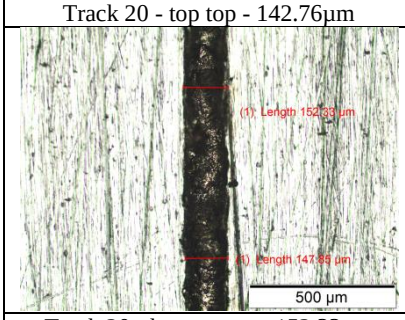

Track 20 - bottom top - 152.33µm

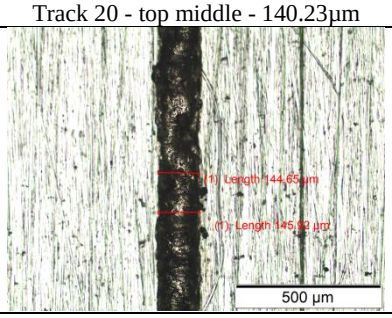

Track 20 - bottom middle - 145.92µm

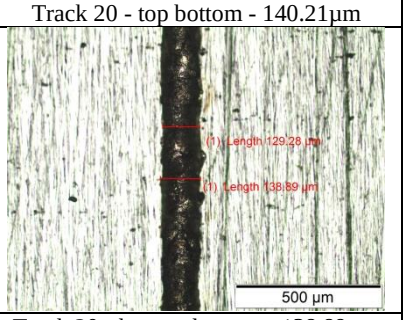

Track 20 - bottom bottom - 138.89µm

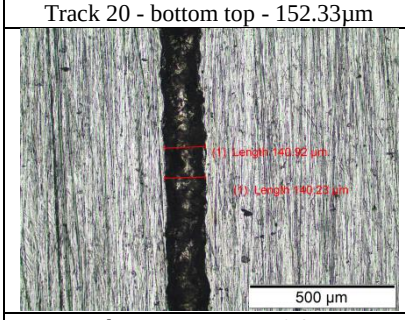

Track 21 - top top - 140.92µm

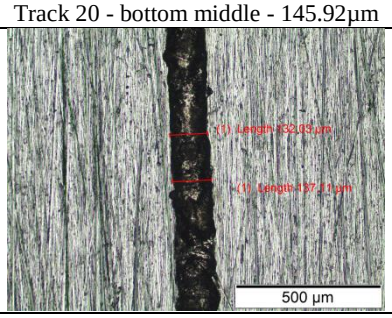

Track 21 - top middle - 137.11µm

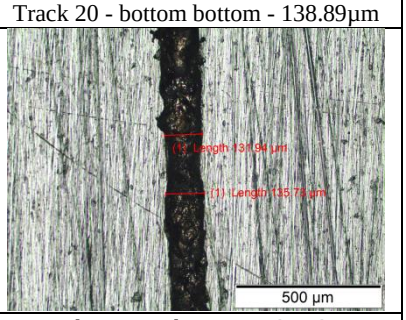

Track 21 - top bottom - 135.73µm

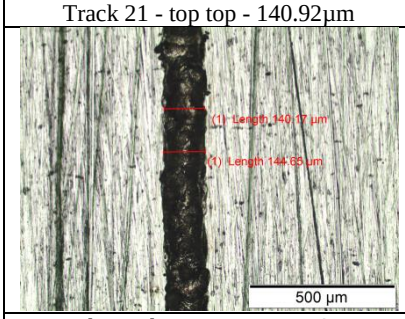

Track 21 - bottom top - 144.65µm

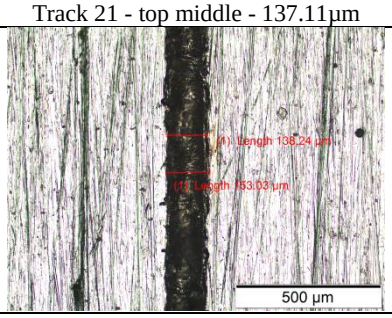

Track 21 - bottom middle - 153.03µm

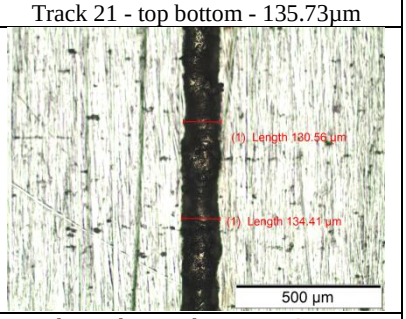

Track 21 - bottom bottom - 134.41µm

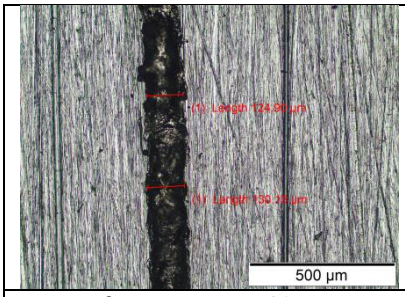

Track 22 - top top - 130.15µm

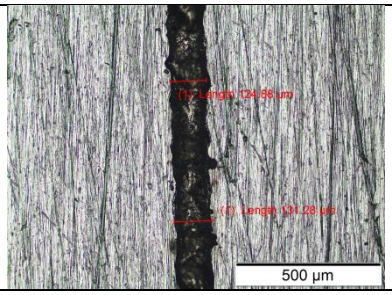

Track 22 - top middle - 131.28µm

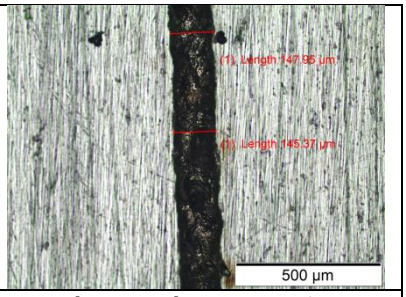

Track 22 - top bottom - 147.95µm

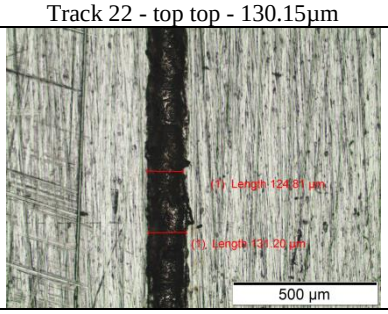

Track 22 - bottom top - 131.20µm

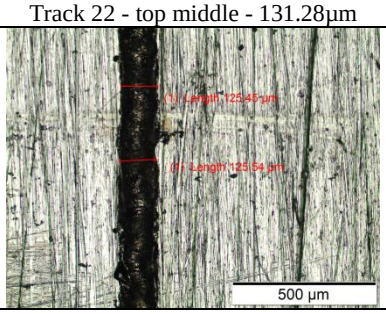

Track 22 - bottom middle - 125.54µm

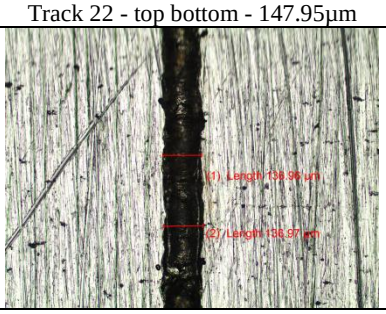

Track 22 - bottom bottom - 136.97µm

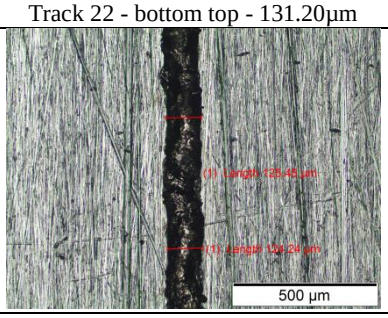

Track 23 - top top - 125.45µm

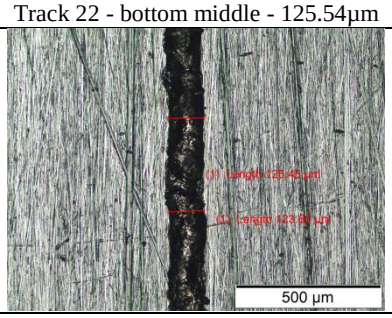

Track 23 - top middle - 125.45µm

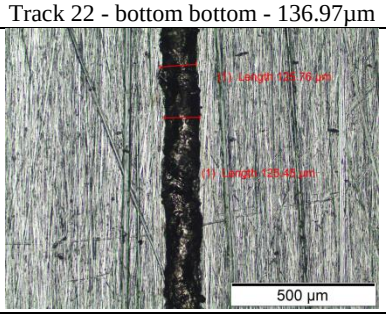

Track 23 - top bottom - 125.76µm

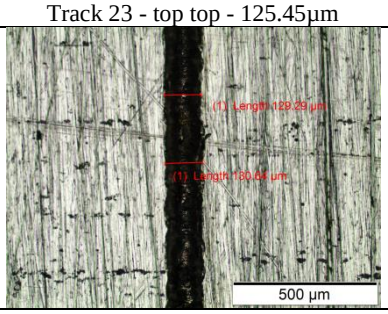

Track 23 - bottom top - 130.64µm

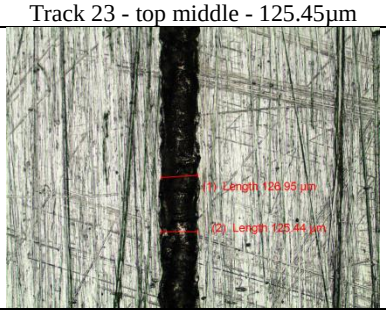

Track 23 - bottom middle - 126.95µm

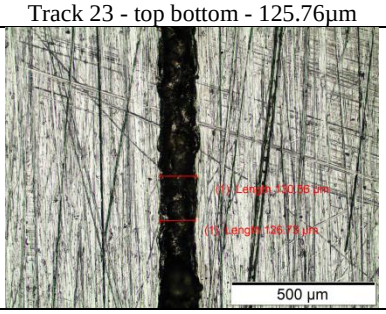

Track 23 - bottom bottom - 130.56µm

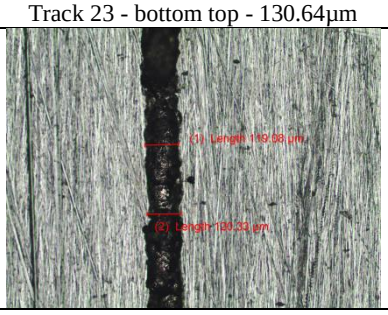

Track 24 - top top - 120.33µm

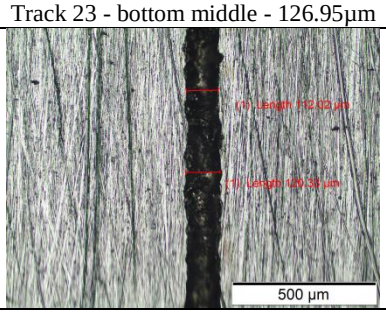

Track 24 - top middle - 120.33µm

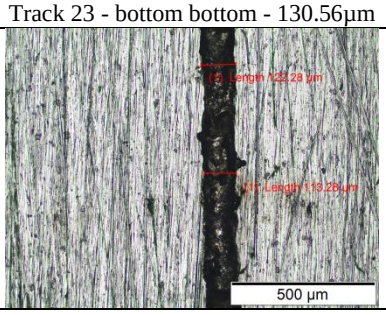

Track 24 - top bottom - 122.28µm

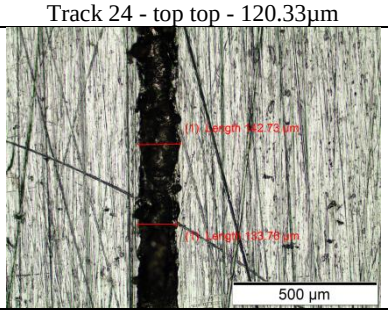

Track 24 - bottom top - 142.73µm

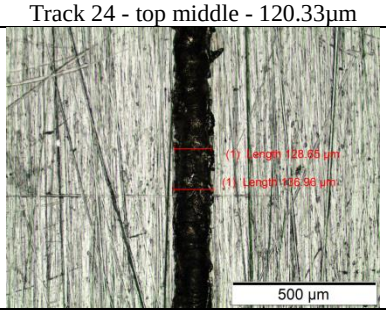

Track 24 - bottom middle - 136.96µm

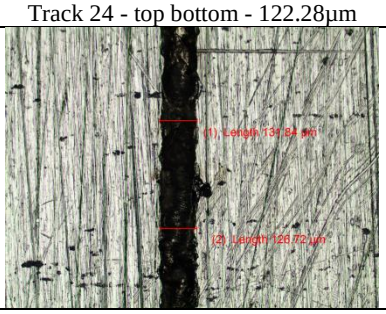

Track 24 - bottom bottom - 131.84µm

Appendix K: Laser Penetration Depth Measurements - Tool Steel Base Plate

Table K1: Experimental scan track penetration depth of the WC-12Co on the tool steel base plate.

Parameter set/ scan track number	Power [W]	Scanning speed [mm/s]	Energy density [J / mm^2]	Depth measurements [µm] 1	2	3	4	5	Average width [µm]
1	50	60	208.33	71.89	108.41	68.25	57.41	56.36	72.46
2	50	80	156.25	69.54	91.81	64.70	52.52	52.76	66.27
3	50	100	125.00	62.20	81.43	52.92	49.21	48.95	58.94
4	50	120	104.17	55.87	73.64	46.91	48.21	45.77	54.08
5	50	140	89.29	36.53	60.13	48.87	41.21	35.38	44.42
6	50	160	78.13	35.15	49.48	41.69	37.61	24.79	37.74
7	50	180	69.44	26.23	45.41	39.36	41.02	10.24	32.45
8	50	200	62.50	17.51	41.00	40.81	35.86	11.77	29.39
9	150	400	93.75	72.40	115.67	129.50	122.16	116.61	111.27
10	150	600	62.50	59.00	74.33	76.82	69.51	54.75	66.88
11	150	800	46.88	41.99	68.37	69.23	69.16	39.44	57.64
12	150	1000	37.50	41.22	59.50	54.10	58.18	34.52	49.50
13	150	1200	31.25	39.72	52.54	38.00	48.79	28.28	41.47
14	150	1400	26.79	35.75	36.95	34.91	48.86	17.48	34.79
15	150	1600	23.44	30.97	35.33	30.55	33.79	21.98	30.52
16	150	1800	20.83	25.07	48.77	25.38	35.86	19.44	30.90
17	300	1000	75.00	66.70	65.23	78.90	104.23	88.82	80.78
18	300	1200	62.50	60.70	60.65	76.37	93.59	73.06	72.87
19	300	1400	53.57	52.65	60.00	73.29	73.28	63.88	64.62
20	300	1600	46.88	41.45	53.58	60.13	62.77	43.72	52.33
21	300	1800	41.67	39.45	53.17	51.67	58.36	37.45	48.02
22	300	2000	37.50	30.90	42.51	49.22	40.27	37.34	40.05
23	300	2200	34.09	29.05	42.37	38.96	38.60	34.58	36.71
24	300	2400	31.25	25.54	37.01	37.45	35.31	33.08	33.68

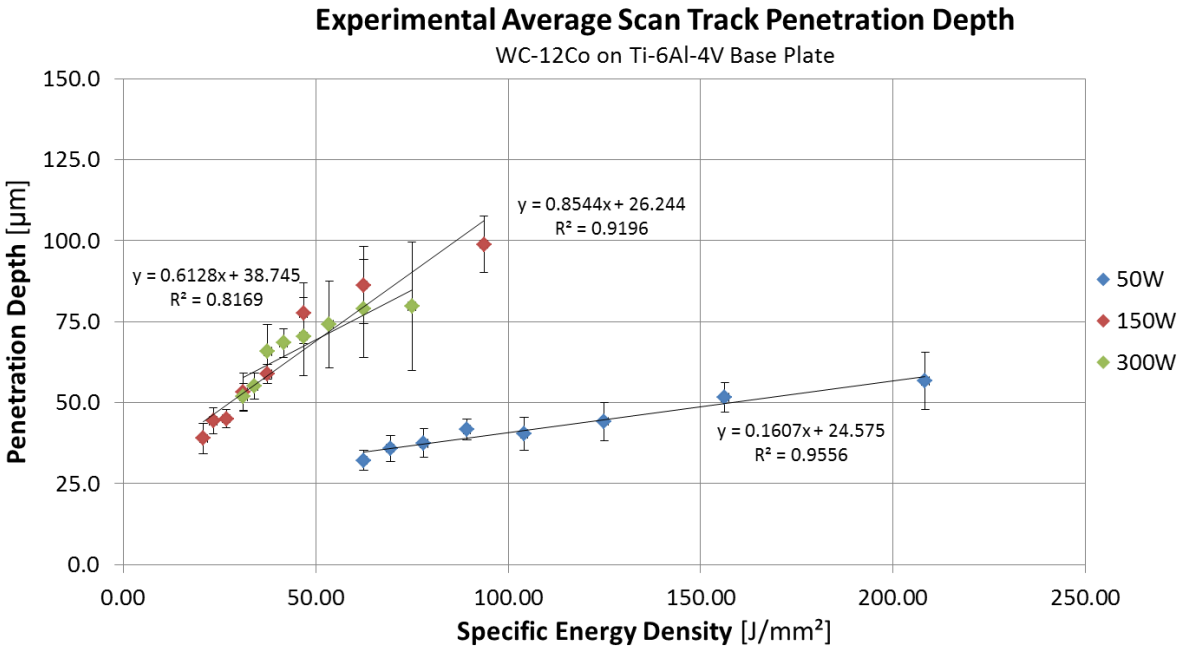

Figure K1: The average penetration depth of 24 scan tracks on the tool steel base plate measured at different specific energy density values.

Track 1 P = 50 W V = 60 mm/s	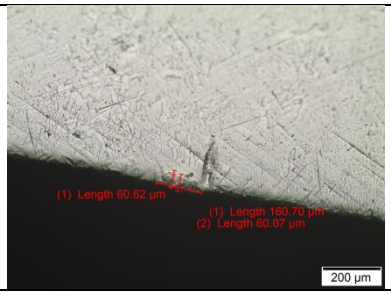	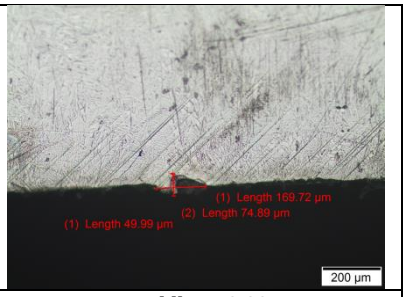
	top top - 60.62µm	top middle - 49.99µm
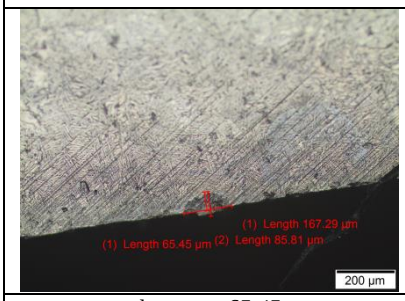	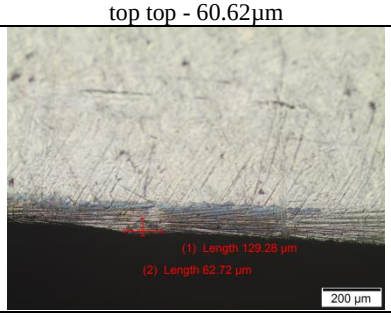	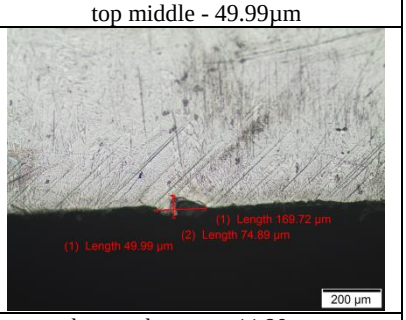
top bottom - 65.45µm	bottom top - 62.72µm	bottom bottom - 44.80µm
Track 2 P = 50 W V = 80 mm/s	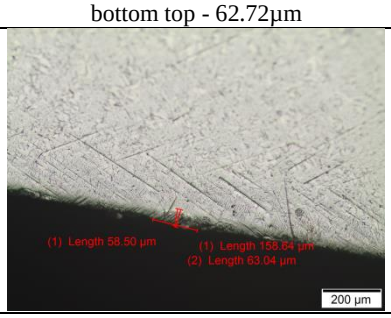	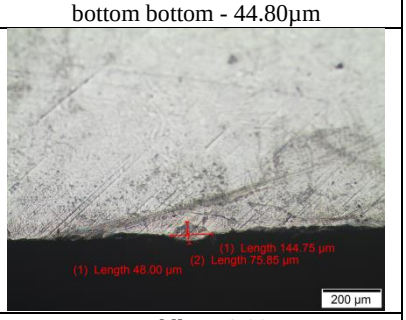
	top top - 58.50µm	top middle - 48.00µm
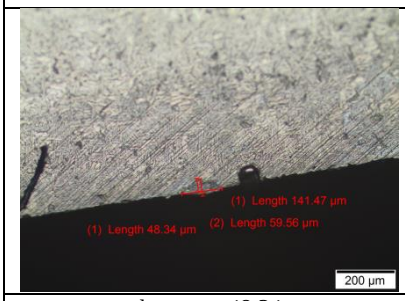	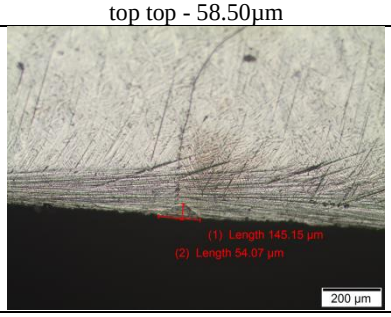	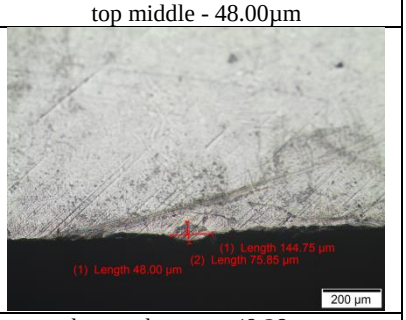
top bottom - 48.34µm	bottom top - 54.07µm	bottom bottom - 49.28µm
Track 3 P = 50 W V = 100 mm/s	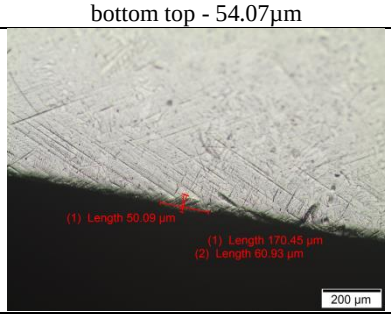	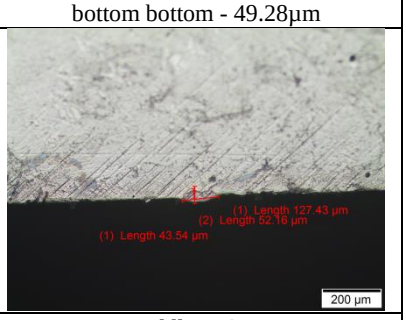
	top top - 50.09µm	top middle - 43.54µm
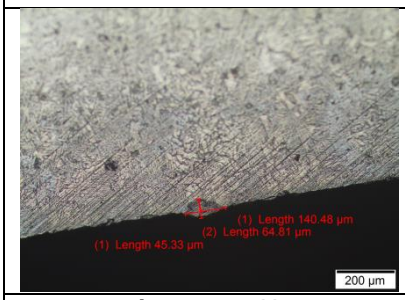	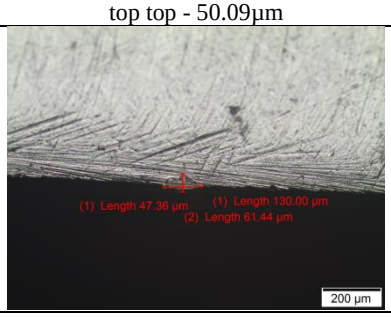	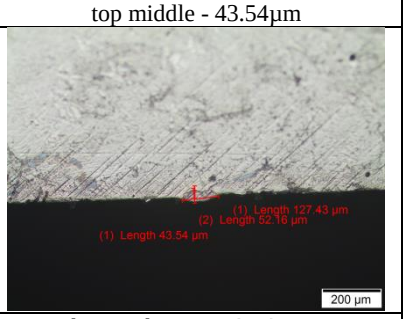
top bottom - 45.33µm	bottom top - 47.36µm	bottom bottom - 34.65µm

Track 4 P = 50 W V = 120 mm/s	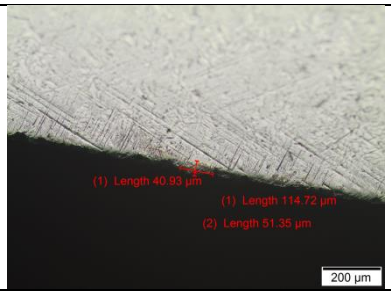	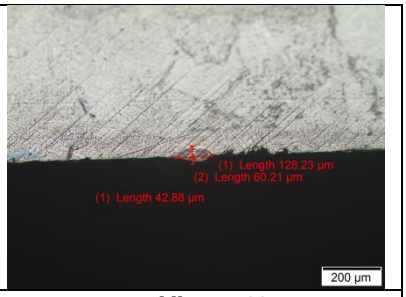
	top top - 40.93µm	top middle - 42.88µm
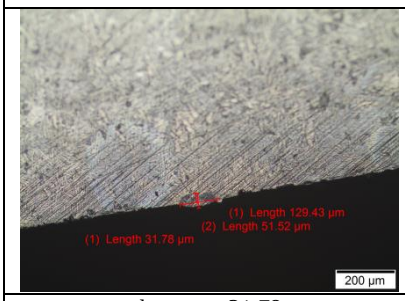	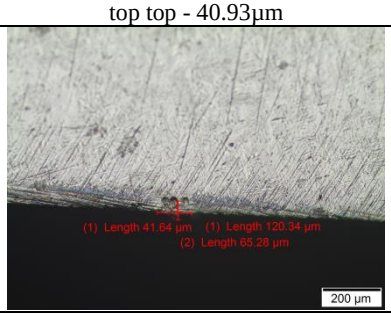	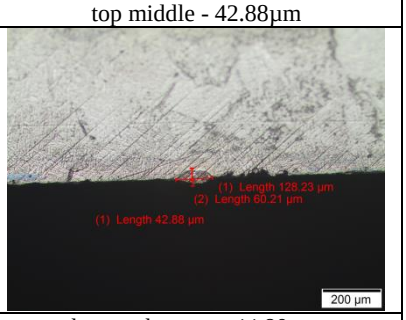
top bottom - 31.78µm	bottom top - 41.64µm	bottom bottom - 44.80µm
Track 5 P = 50 W V = 140 mm/s	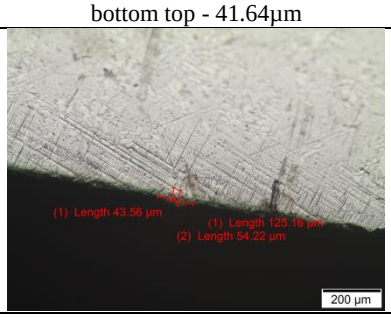	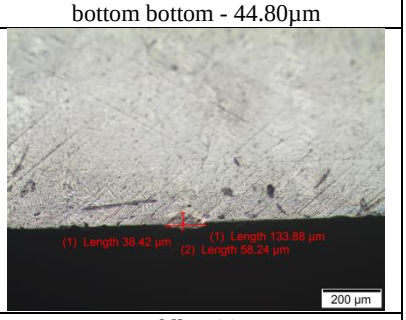
	top top - 43.56µm	top middle - 38.42µm
	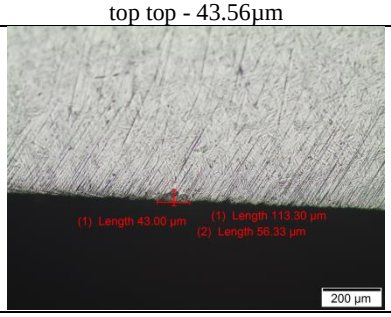	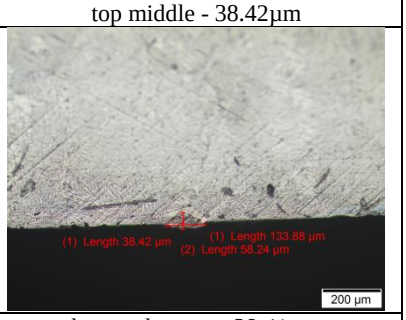
top bottom - 45.25µm	bottom top - 43.00µm	bottom bottom - 38.41µm
Track 6 P = 50 W V = 160 mm/s	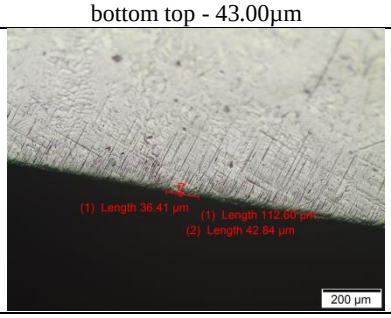	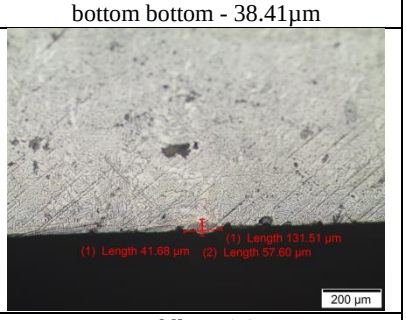
	top top - 36.41µm	top middle - 40.37µm
	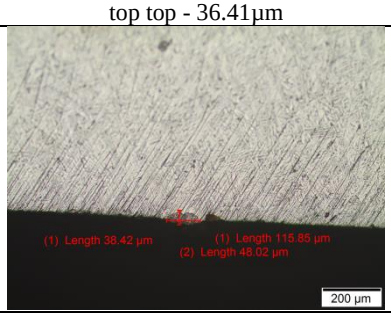	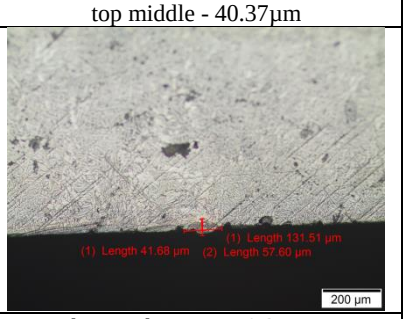
top bottom - 30.41µm	bottom top - 38.42µm	bottom bottom - 40.37µm

Track 7 P = 50 W V = 180 mm/s	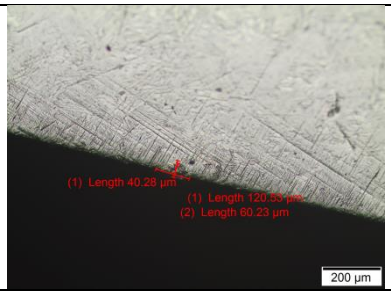	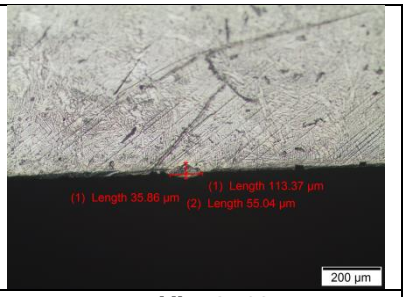
	top top - 40.28µm	top middle - 35.86µm
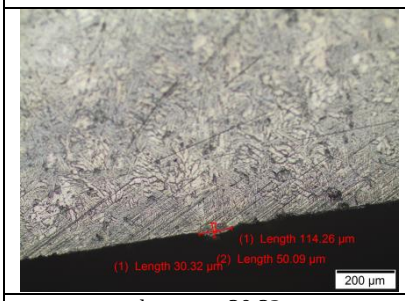	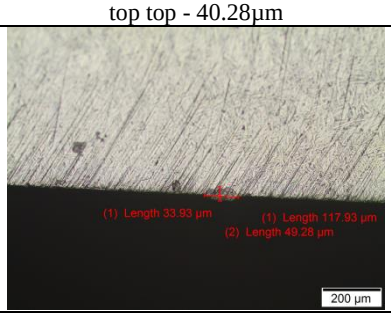	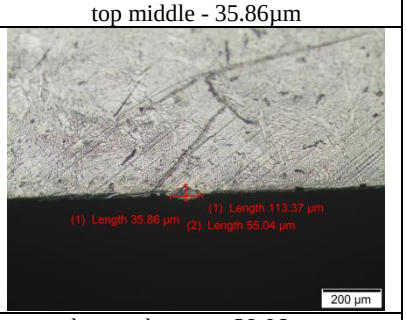
top bottom - 30.32µm	bottom top - 33.93µm	bottom bottom - 39.06µm
Track 8 P = 50 W V = 200 mm/s	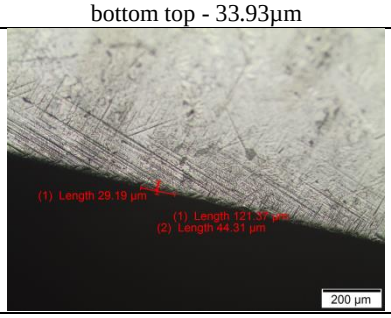	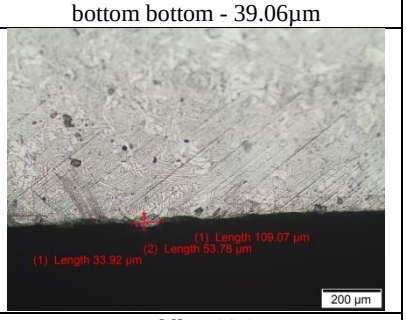
	top top - 29.19µm	top middle - 33.92µm
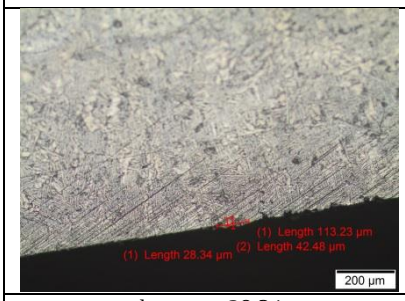	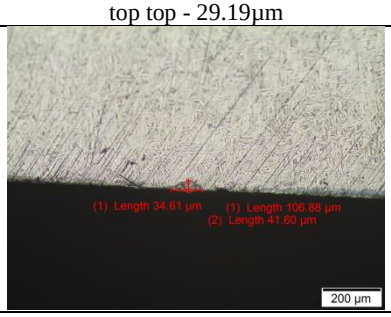	
top bottom - 28.34µm	bottom top - 34.61µm	bottom bottom - 34.56µm
Track 9 P = 150 W V = 400 mm/s	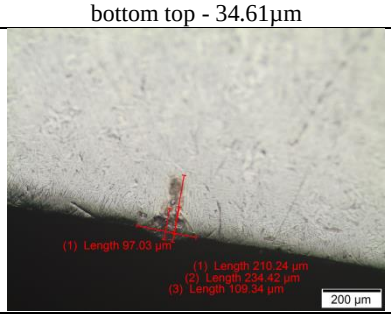	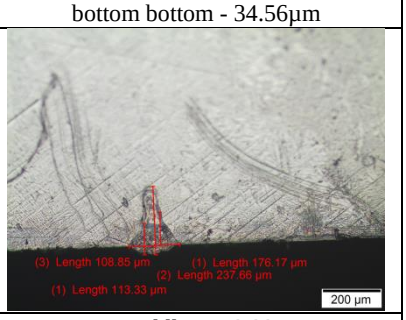
	top top - 97.03µm	top middle - 113.33µm
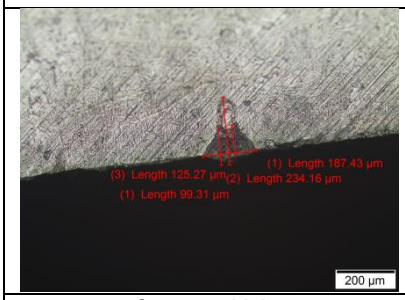	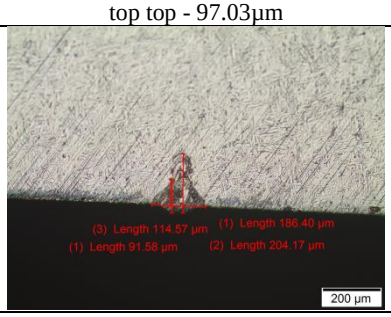	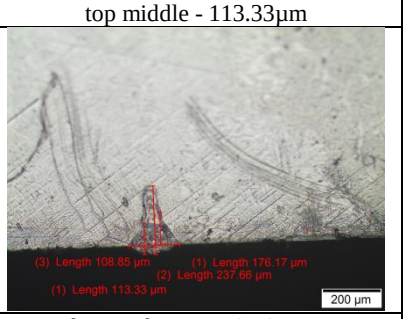
top bottom - 99.31µm	bottom top - 91.58µm	bottom bottom - 92.82µm

Track 10 P = 150 W V = 600 mm/s	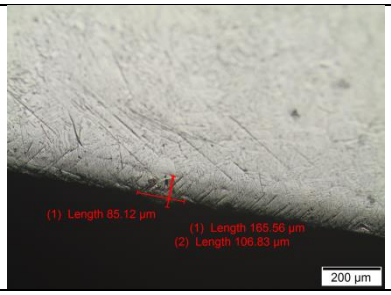	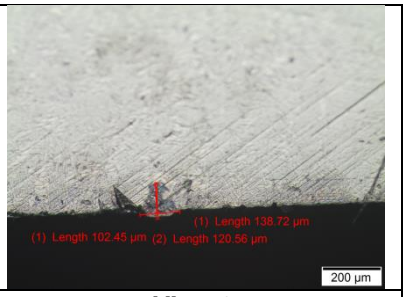
	top top - 85.12µm	top middle - 102.45µm
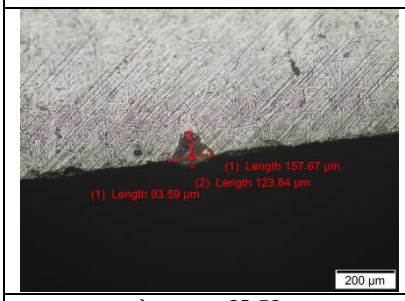	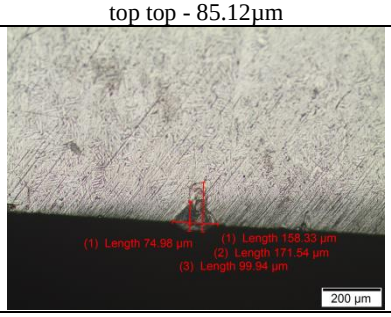	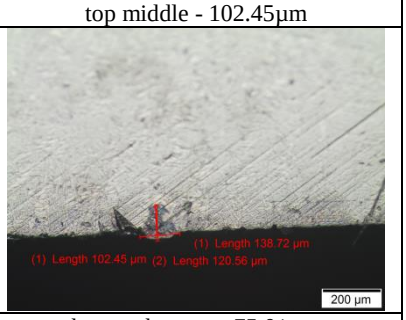
top bottom - 93.59µm	bottom top - 74.98µm	bottom bottom - 75.01µm
Track 11 P = 150 W V = 800 mm/s	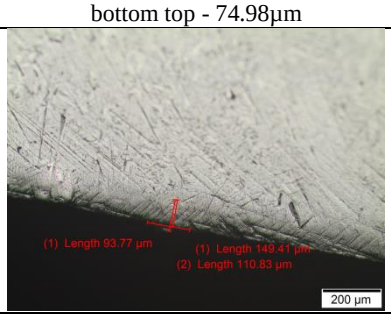	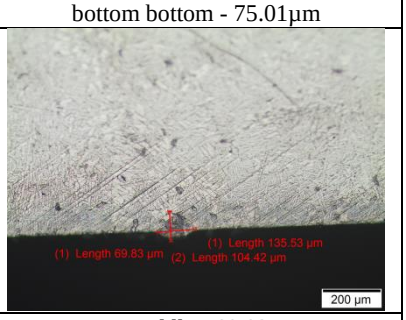
	top top - 93.77µm	top middle - 69.83µm
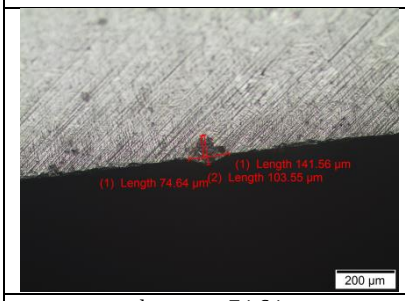	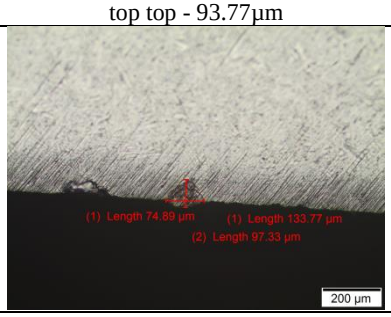	
top bottom - 74.64µm	bottom top - 74.89µm	bottom bottom - 74.38µm
Track 12 P = 150 W V = 1000 mm/s	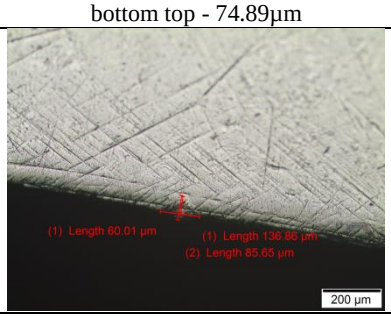	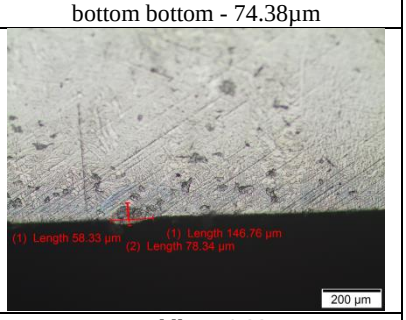
	top top - 60.01µm	top middle - 58.33µm
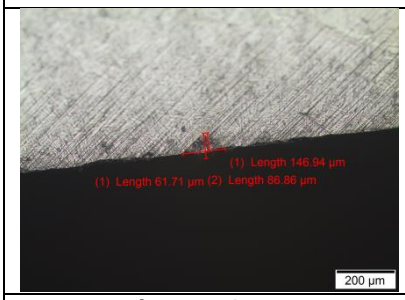	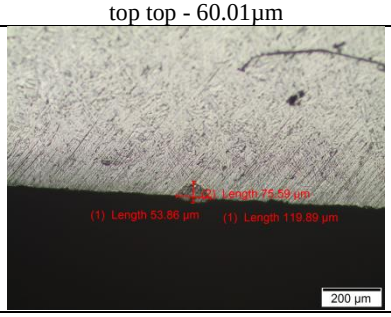	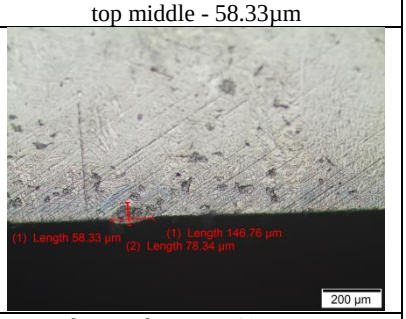
top bottom - 61.71µm	bottom top - 53.86µm	bottom bottom - 60.21µm

Track 13 P = 150 W V = 1200 mm/s	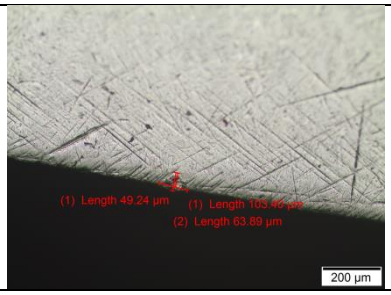	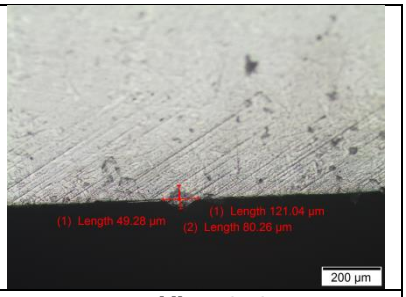
	top top - 49.24µm	top middle - 49.28µm
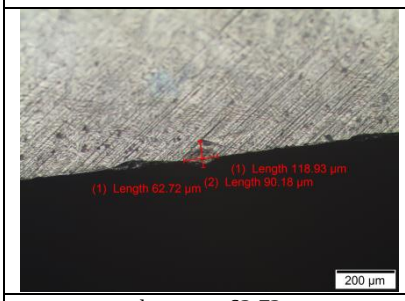	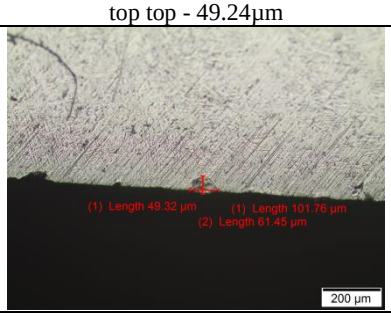	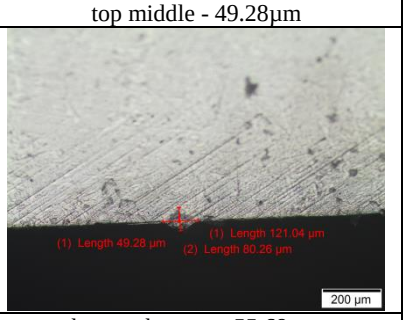
top bottom - 62.72µm	bottom top - 49.32µm	bottom bottom - 55.69µm
Track 14 P = 150 W V = 1400 mm/s	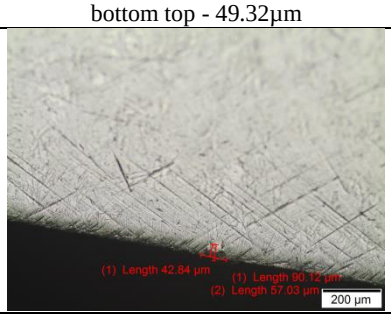	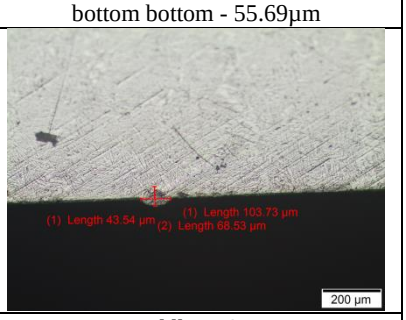
	top top - 42.84µm	top middle - 48.11µm
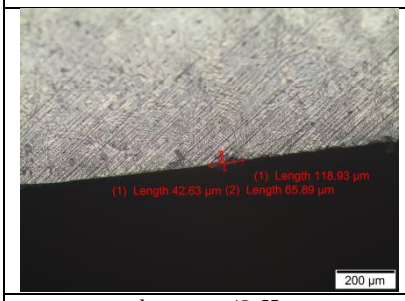	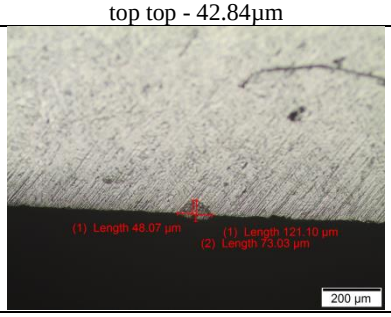	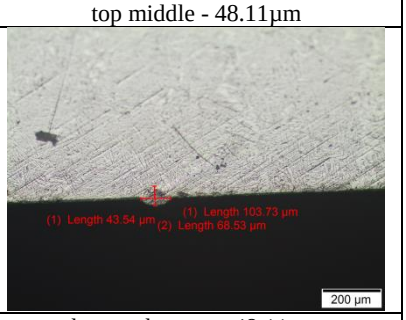
top bottom - 42.63µm	bottom top - 48.07µm	bottom bottom - 48.11µm
Track 15 P = 150 W V = 1600 mm/s	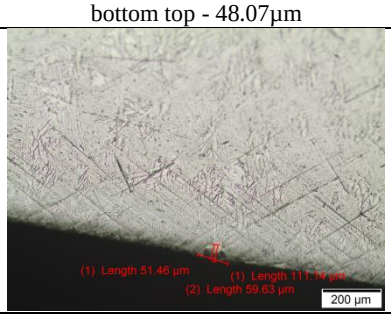	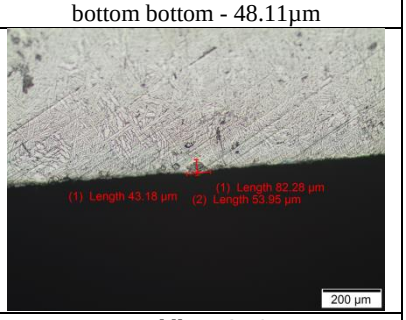
	top top - 51.46µm	top middle - 43.18µm
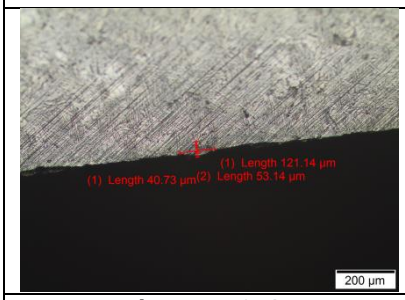	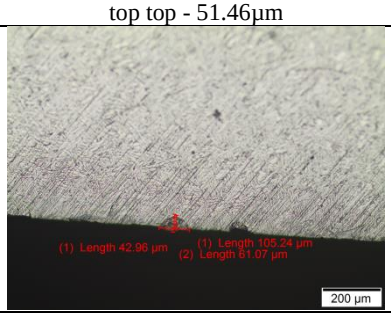	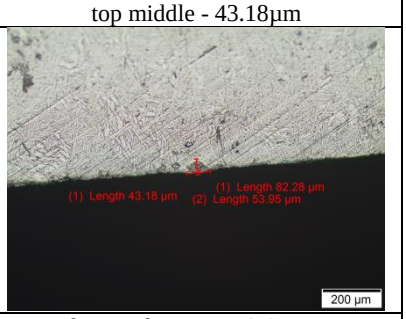
top bottom - 40.73µm	bottom top - 42.96µm	bottom bottom - 43.64µm

Track 16 P = 150 W V = 1800 mm/s	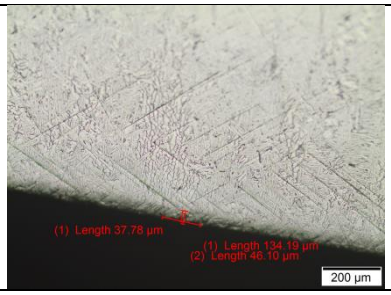	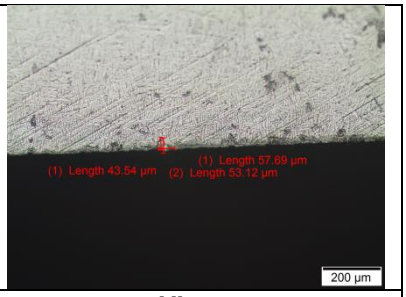
	top top - 37.78µm	top middle - 41.72µm
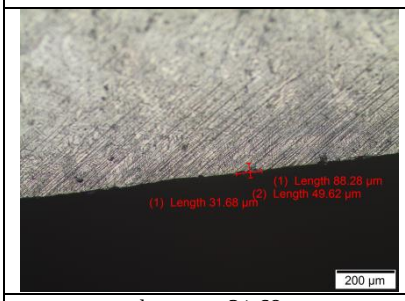	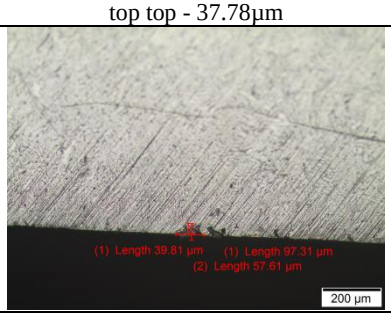	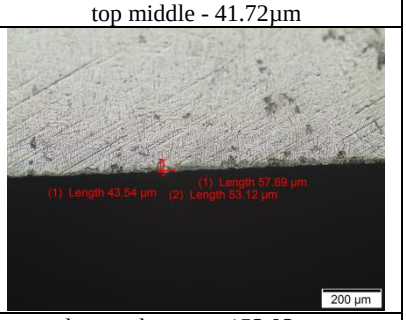
top bottom - 31.68µm	bottom top - 39.81µm	bottom bottom - 153.03µm
Track 17 P = 300 W V = 1000 mm/s	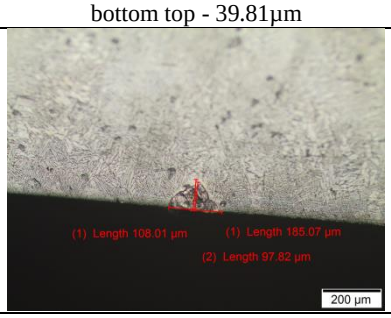	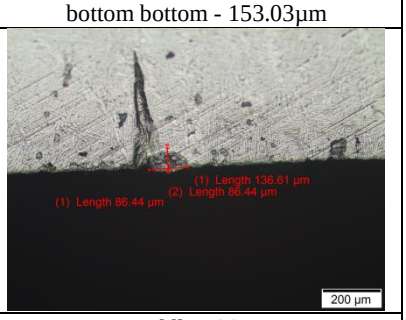
	top top - 108.01µm	top middle - 86.44µm
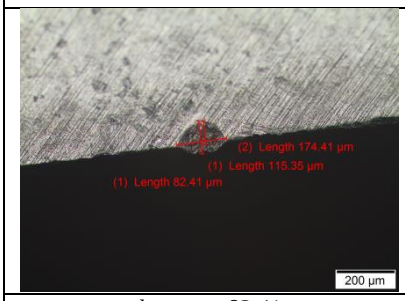	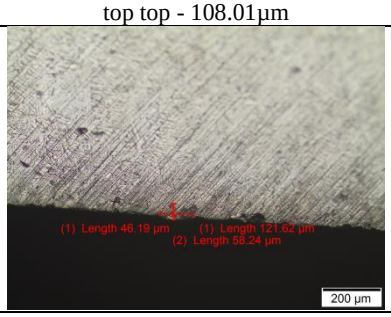	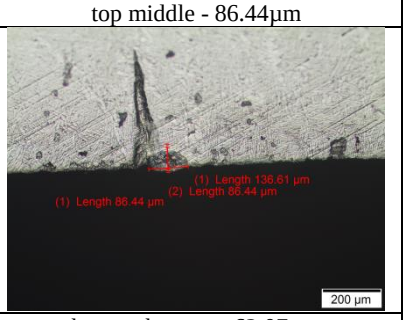
top bottom - 82.41µm	bottom top - 46.19µm	bottom bottom - 62.07µm
Track 18 P = 300 W V = 1200 mm/s	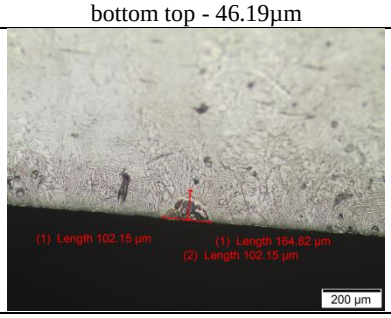	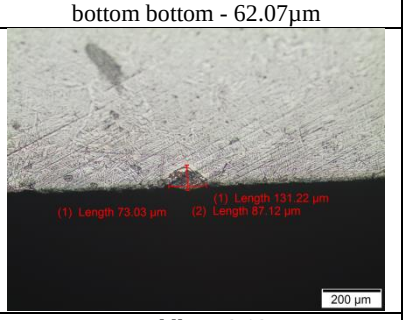
	top top - 102.15µm	top middle - 73.03µm
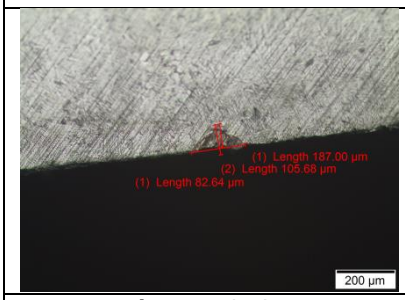	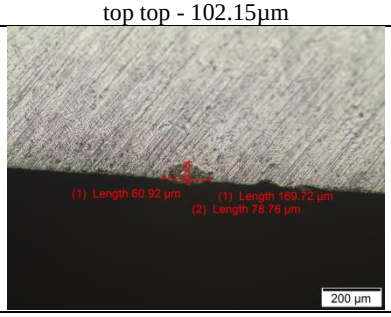	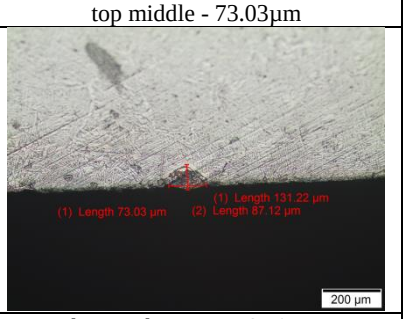
top bottom - 82.64µm	bottom top - 60.92µm	bottom bottom - 76.20µm

Track 19 P = 300 W V = 1400 mm/s	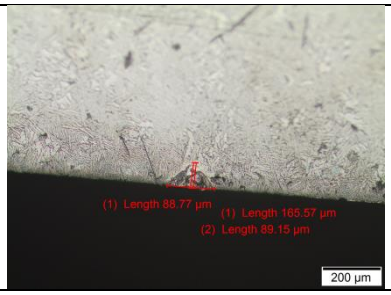	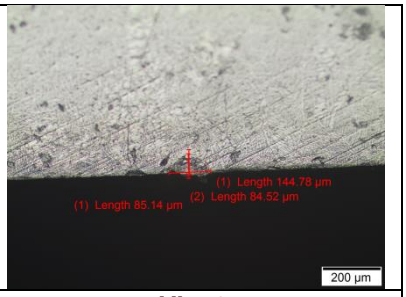
	top top - 88.77µm	top middle - 85.14µm
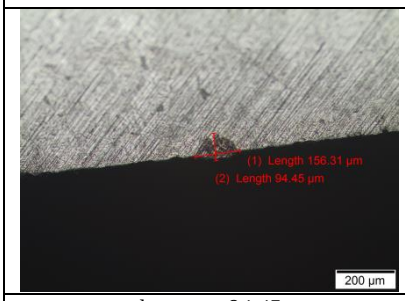	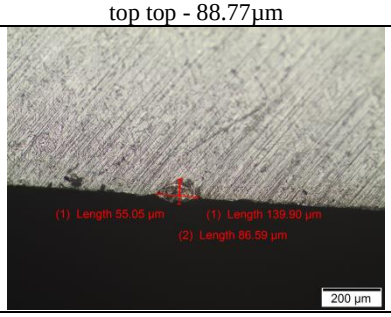	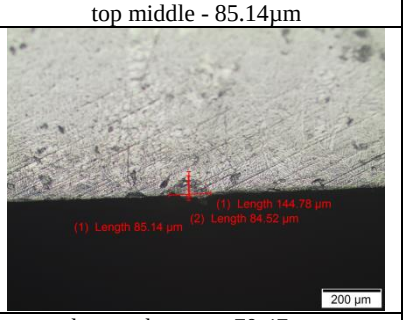
top bottom - 94.45µm	bottom top - 55.05µm	bottom bottom - 70.47µm
Track 20 P = 300 W V = 1600 mm/s	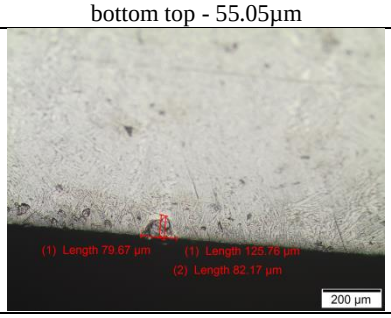	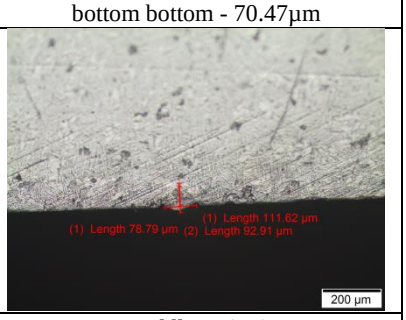
	top top - 79.67µm	top middle - 78.79µm
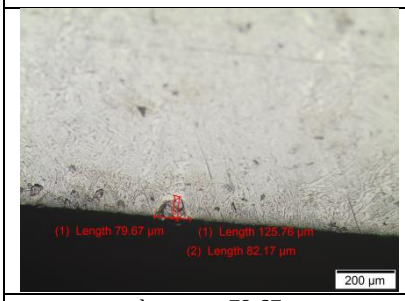	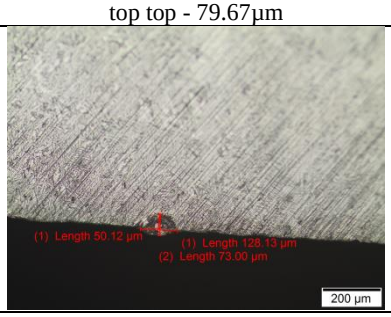	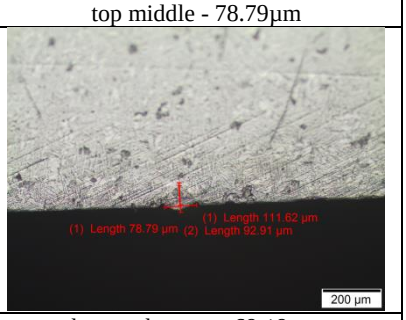
top bottom - 79.67µm	bottom top - 50.12µm	bottom bottom - 69.19µm
Track 21 P = 300 W V = 1800 mm/s	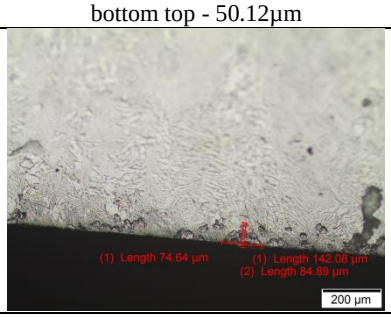	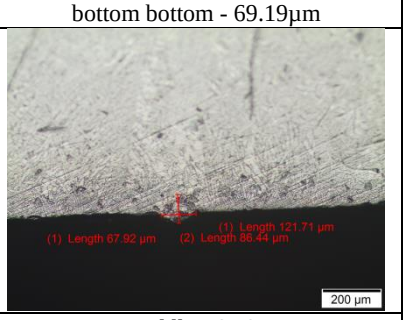
	top top - 74.64µm	top middle - 67.92µm
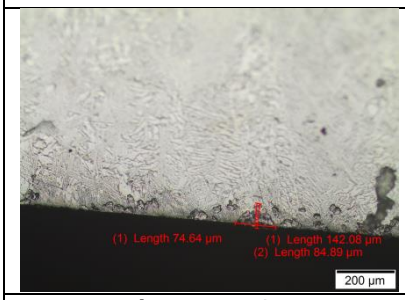	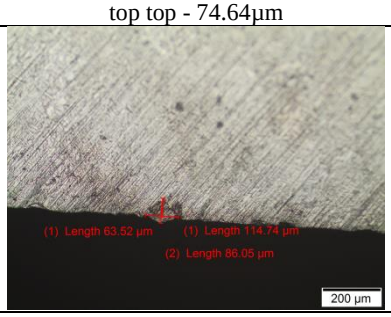	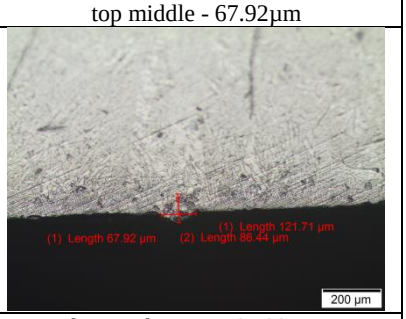
top bottom - 74.64µm	bottom top - 63.52µm	bottom bottom - 65.33µm

Track 22 P = 300 W V = 2000 mm/s	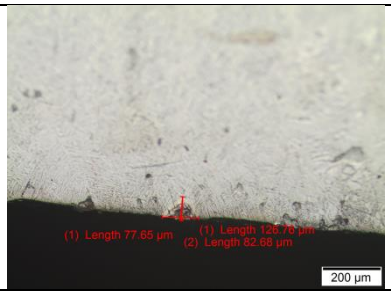	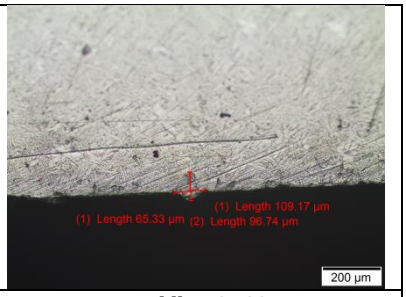
	top top - 77.65µm	top middle - 65.33µm
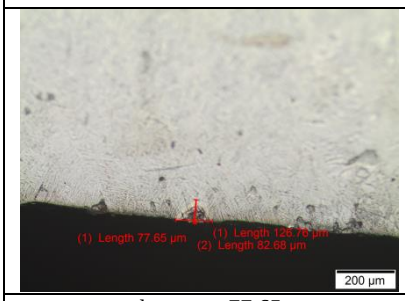	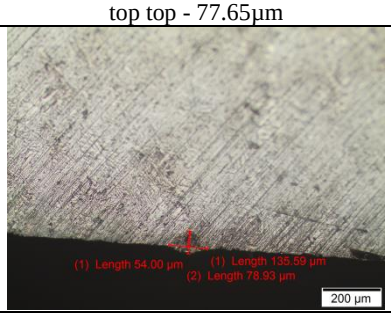	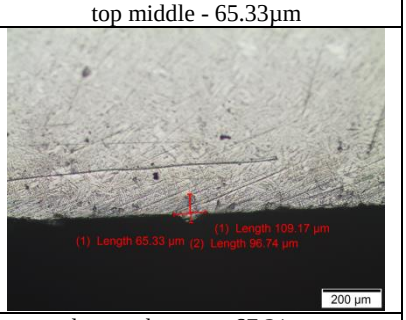
top bottom - 77.65µm	bottom top - 54.00µm	bottom bottom - 67.21µm
Track 23 P = 300 W V = 2200 mm/s	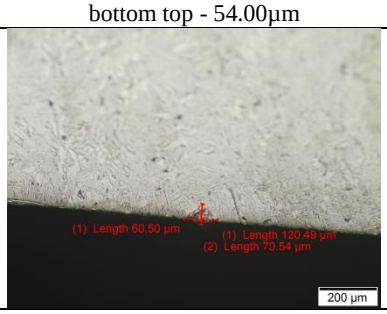	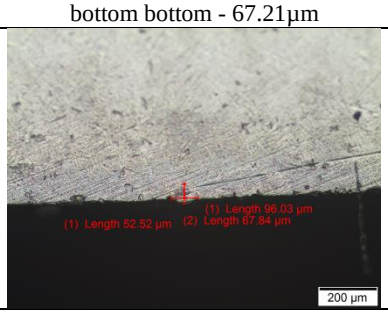
	top top - 60.50µm	top middle - 52.52µm
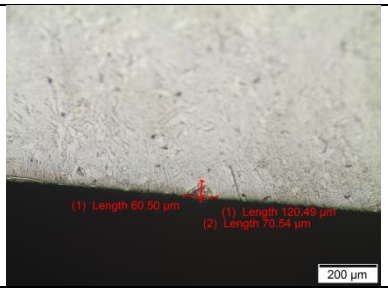	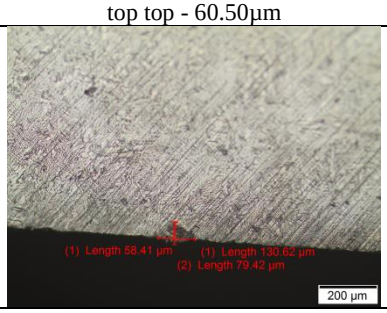	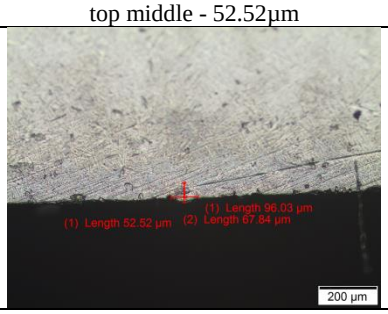
top bottom - 60.50µm	bottom top - 58.41µm	bottom bottom - 53.14µm
Track 24 P = 300 W V = 2400 mm/s	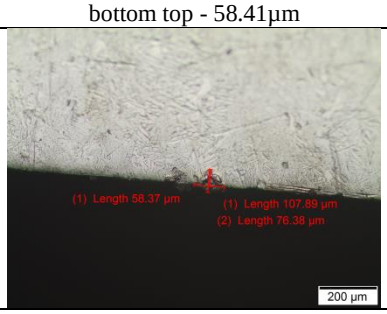	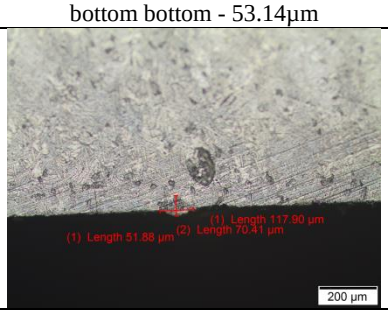
	top top - 58.37µm	top middle - 51.88µm
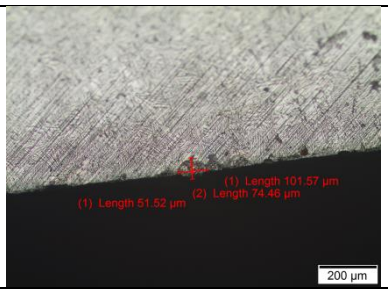	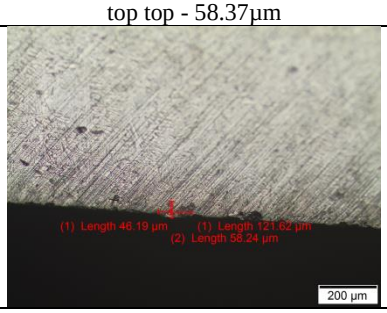	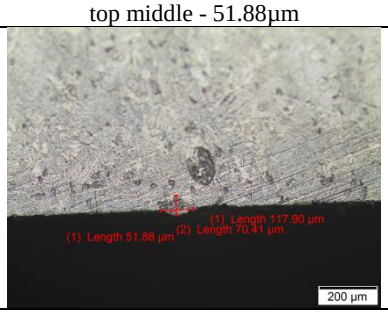
top bottom - 51.52µm	bottom top - 46.19µm	bottom bottom - 50.62µm

Appendix L: EOS Machine Technical Data

M-Solutions

Laser sintering system **EOSINT M 280**
for the production of tooling inserts, prototype parts
and end products directly in metal

Technical Data	
Building volume (including building platform)	250 mm x 250 mm x 325 mm (9.85 x 9.85 x 12.8 in)
Laser type	Yb-fibre laser, 200 W or 400 W (optional)
Precision optics	F-theta-lens, high-speed scanner
Scan speed	up to 7.0 m/s (23 ft./sec)
Variable focus diameter	100 - 500 µm (0.004 - 0.02 in)
Power supply	32 A
Power consumption	maximum 8.5 kW / typical 3.2 kW
Nitrogen generator	integrated
Compressed air supply	7,000 hPa; 20 m^3/h (102 psi; 706 ft^3/h)
Argon supply	4,000 hPa; 100 l/min (58 psi; 3.5 ft^3/min)
Dimensions (B x D x H)	
System	2,200 mm x 1,070 mm x 2,290 mm (86.6 x 42.1 x 90.1 in)
Recommended installation space	min. 4.8 m x 3.6 m x 2.9 m (189 x 142 x 114 in)
Weight	approx. 1,250 kg (2,756 lb)
Data preparation	
Software	EOS RP Tools; EOSTATE Magics RP (Materialise)
CAD interface	STL. Optional: converter for all standard formats
Network	Ethernet